Optical control of individual spins in magnetic and charged quantum dots

Lucien Besombes

Université de Grenoble, spécialité Physique

Optical control of individual spins in magnetic and charged quantum dots

Lucien BESOMBES

Habilitation à diriger des recherches

Soutenue publiquement le 18/01/2013

Composition du Jury:

Rapporteurs:	**Thierry Amand** **Denis Scalbert** **Paul Voisin**
Examinateurs:	**Marc Sanquer** **Dmitri Yakovlev**

Institut Néel, dpt Nanosciences, CNRS Grenoble
Equipe CNRS-CEA-UJF, "Nanophysique et semiconducteurs"

Contents

Part I

Spins in II-VI quantum dots

General introduction

The ability to control individual spins in semiconductors nanostructures is an important issue for spintronics and quantum information processing. It is a key but very challenging step for any spin-based solid-state quantum computing device. In the last ten years, efficient optical techniques have been developed to control the spin of individual carriers [123] or ensemble of nuclei [85, 64] in semiconductor quantum dots (QDs). Thanks to the increase of purity of semiconductor materials, the study of one single dopant spin also became possible. For example, the nitrogen-vacancy centers in diamond [82], or a single phosphorous dopant in a nano-FET [71] are possible ways to study single dopant spin properties. These examples may be viewed as the initial demonstrations of model single spin devices, which requires considerable additional fundamental study.

The desirable features of single dopants, such as reproducible quantized properties, make them ideal objects for further scientific study and robust applications. However, it is still a challenge to control single dopants because their properties strongly depend on their local environment (strain, electronic, magnetic and optical fields). Nevertheless, single atom quantum devices, i.e., systems whose macroscopic properties depend on the quantum state of a single atom, have been demonstrated in several systems [75]. These systems permit to test matter at a fundamental scale and, in some instances, already have practical applications like room temperature magnetometry with nanometer resolution [102]. A controlled upscale of these primary units would permit to test new physical phenomena and to find new applications. In this regard, the study of chains of a few magnetic atoms deposited on a metal is already giving promising results along this line [94]. We will discuss here possible progress in that direction in the case of magnetic atoms (Mn) in semiconductor QDs.

Thanks to their expected long spin coherence time, Mn atoms in a semiconductor host could be an alternative media to store quantum information in the solid state. However, in bulk material, as these localized spins interact weakly with their environment, individual Mn cannot be probed or controlled by electrical or optical methods and only collective phenomena were observed. Recently, QDs containing individual Mn atoms have been observed both in II-VI [11] and III-V [81] compounds. In these systems, since the confined carriers and Mn wavefunctions become strongly mixed (see Fig 0.1), the optical excitation of the QD strongly affects the spin state of the Mn atom through the exchange interaction offering a possibility of full optical control [127]. Despite the structural similarity

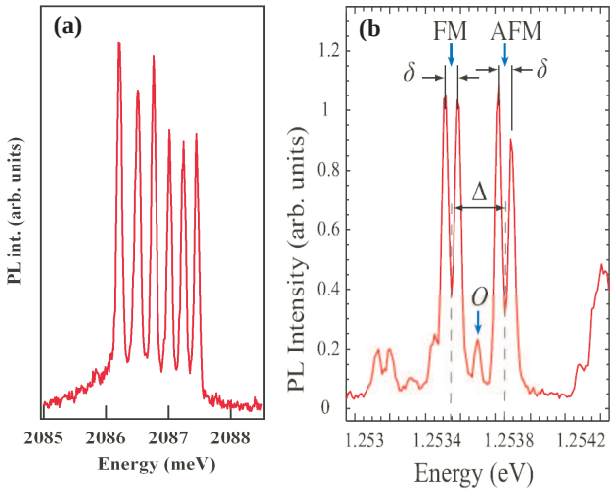

Figure 0.1 Low temperature (5K) photoluminescence at zero magnetic field of a CdTe/ZnTe (a) and an InAs/GaAs (b) (from reference [81]) quantum dot containing an individual Mn atom.

of II-VI and III-V magnetic QDs (an individual Mn atom in a self-assembled quantum dot) the spin properties of these systems are quite different. In a II-VI compound the magnetic impurity is an isoelectronic center in a $3d^5$ configuration with spin S=5/2. The QD photoluminescence reflects the Mn spin state when the exciton recombines (Fig 0.1(a)). Mn in a III-V matrix is a deep acceptor and the dominant center is the neutral acceptor A^0. It corresponds to the $3d^5+h$ configuration where h is a hole bound to the Mn ion. The ground state of this hybrid spin system has a total spin J=1 (Fig 0.1(b)) [79] and its dynamics is likely to be affected by the hole component [6]. In this manuscript, we will focus on the II-VI system giving access to the intrinsic properties of the Mn atom in ist host semiconductor matrix.

II-VI diluted magnetic semiconductor quantum dots

Carrier-Mn coupling was initially studied in bulk diluted magnetic semiconductor (DMS) made of II-VI semiconductors in which Mn impurities was introduced [52, 53]. In these materials, Mn impurities substitute the cations from column II (Zn, Cd or Hg) up to 100%. If not interacting, these localized spins follow Maxwell-Boltzmann statistics, resulting in a magnetization induced by an applied field given by a Brillouin function. Optical spectroscopy around the bandgap of DMS reveals the so-called "giant Zeeman effect", with a spin splitting proportional to the Mn magnetization [54]. Several studies have demonstrated this proportionality and measured the strength of the coupling [143]. Magneto-optical spectroscopy is now a very sensitive method for measuring locally the magnetization of the Mn system [17]. Altogether, this excellent knowledge of II-VI DMS,

and of the coupling between the localized spins and carriers, constitutes a very firm basis for the studies of individual Mn spins described in this manuscript.

In a magnetic QD, the exchange interaction takes place with a single carrier or a single electron-hole pair. However, besides effects related to the carriers-Mn exchange interaction, it was found that even a small content of Mn introduced in a II-VI semiconductor material can strongly suppress photoluminescence if the energy gap exceeds the energy of the Mn internal transition. This strongly limits the study of individual DMS QDs [28]. The first studies of individual QDs doped with Mn atoms were reported by Maksimov et al [99]. They studied CdMnTe QDs inserted in CdMgTe barriers in which the optical transition energies are lower than the energy of the internal transition of the Mn atom. This system allowed observing the formation of quasi zero-dimensional magnetic polaron.

Another way to reduce the non-radiative losses was to introduce the magnetic atoms in the QDs barriers. This was realized for large self-assembled CdSe dots embedded in ZnMnSe barriers by Seufert et al. [130]. In this system, the interaction between the confined exciton and the magnetic atoms is due to the spread of the wave function in the barriers and to a small diffusion of the magnetic atoms in the QDs. In these structures, the formation of a ferromagnetically aligned spin complex was demonstrated to be surprisingly stable as compared to bulk magnetic polaron [96, 152] even at elevated temperature and high magnetic fields. The photoluminescence of a single electron-hole pair confined in one magnetic QD, which sensitively depends on the alignment of the magnetic atoms spins, allowed to measure the statistical fluctuations of the magnetization on the nanometer scale. Quantitative access to statistical magnetic fluctuations was obtained by analyzing the linewidth broadening of the single dot emission. This all optical technique allowed to address a magnetic moment of about 100 μ_B and to resolve changes in the order of a few μ_B [5, 37, 67]. We will show here how self-assembled CdTe/ZnTe QDs can be used to optically probe an control individual Mn atoms.

A large effort has also been done to incorporate magnetic ions in chemically synthesized II-VI nanocrystals [116]. The incorporation of the magnetic atoms is strongly dependent on the growth conditions and controlled by the adsorption of atoms on the nanocrystal surface [43]. The doping of nanocrystals with magnetic impurities also leads to interesting magneto-optical properties [14] but once again, in these highly confined systems, the transfer of confined carriers to the Mn internal levels strongly reduces their quantum efficiency and prevents the optical study of individual Mn-doped nanocrystals. However, by looking to magnetic circular dichroism absorption spectra, it is possible to observe a giant excitonic Zeeman splitting and to deduce directly the strength of the exchange interaction [3]. Recently, a very robust light induced spontaneous spin polarization [8] was also obtained in large CdSe nanocrystals containing a few percent of Mn and emitting at lower energy than the internal transition of the Mn. Further development of such structure could lead to the observation of individual Mn spins at much higher temperature than self-assembled QDs.

Carriers and nuclear spins in II-VI semiconductor quantum dots

Individual electron spins in QDs are a promising system for quantum computing due to the suppression of some spin relaxation channels by the confinement. However, in the commonly studied III-V semiconductor QDs in the absence of external magnetic field, the hyperfine interaction of the electron with the fluctuating nuclear spins governs the time scale on which an electron spin can be stored. Continuous pumping of electrons can generate through hyperfine mediated spin flip-flop a dynamical nuclear polarization [42]. It has been proposed that a full polarization of the nuclei could cancel the decoherence of the electron induced by the fluctuating hyperfine field. Efficient optical coherent control protocols have been implemented on individual electron spins but the complexe dynamics of the coupled electron-nuclei system is a real limit to the practical use of III-V QDs in a quantum computing scheme [83]. A hole spin interacts much weakly with the nuclear spin bath [138], and recent optical coherent control experiments show that the nuclear spin feedback on the hole spin coherent dynamics is suppressed [33]. However, hole spin relaxation is still affected by nuclear spin fluctuations and additional channels of spin relaxation appears when increasing the temperature [51].

Alternatively, nuclear spins could be suppressed completely by using for instance QDs based on isotopically purified II-VI materials since Zn, Cd, Mg, Se and Te all have dominant isotopes without nuclear spins. As highlighted in reference [45] and [2], the interaction between a confined electron in a II-VI QD and the low density of nuclear spins I=1/2 in a QD volume ten times smaller than InAs/GaAs QDs can lead to some spin dynamics which is fundamentally different from the one observed in III-V systems. Due to the small QD size and low density of nuclear spins, the electron-nuclei dynamics in II-VI QDs is ruled by a large Knight field and significant nuclear spin fluctuations despite a small Overhauser field. Consequently, the nuclei-induced spin decoherence of the electron is also an issue in II-VI QDs. However, the built-up of a nuclear spin polarisation at B=0T, can be much faster than the relaxation induced by the dipole interaction between nuclear spins allowing the creation of a strong non-equilibrium nuclear spin polarisation [45]. Under these conditions, decoherence of the electron should be efficiently suppressed. Experimental study of the electron-nuclear dynamics in II-VI QDs are few. We will provide here a summary of experimental studies of this system at a single dot level and compare it with the commonly studied III-V QDs.

Outline of the manuscript

This manuscript is organized as follows: In Part One, the main properties of Mn-doped and singly charged II-VI QDs are presented. In chapter 1 we will describe their energy level structure. We will then analyze in detail the influence of the QD symmetry and of the valence band mixing on the spin structure of QDs containing an individual carrier and one or two Mn atoms. We will finally show

how the tuning of the charge state of a QD can be used to control the magnetic properties of a Mn atom.

In chapter 2, we will focus on the spin dynamics of these few interacting spins. We will first analyse the dynamics of coupled electron and diluted nuclear spins in these II-VI QDs. We will, in particular, show that the electron spin dephasing by the low density of fluctuating nuclear spins is efficiently suppressed at zero field by a dynamic nuclear spin polarization. We will then focus on the dynamics of coupled carriers and Mn spins. We will first show how the injection of spin polarized carriers can be used to prepare by optical pumping the spin state of one or two Mn atoms. We will then discuss the mechanism controlling the efficiency and the dynamics of this optical pumping. We will finally show how the strong coupling between a laser field and the optical transitions of a Mn-doped QD can be used to optically tune the energy of any spin state of a Mn atom.

Part Two (Chapter 3) is devoted to the presentation of ongoing work and perspectives on the coherent dynamics of interacting electron, nuclei and Mn spins in II-VI semiconductor QDs. We will, for instance, discuss the possibility of using the strong coupling with a resonant laser field to control the coherent dynamics of coupled electronic and nuclear spins of a Mn atom.

1

Mn doped and singly charged II-VI semiconductor quantum dots

We will present in this chapter the energy levels structure and optical properties of neutral, singly charged or Mn doped CdTe/ZnTe quantum dots (QDs). After a description of the sample growth we will discuss the influence of valence band mixing on the spin properties of neutral and charged QDs. We will then analyze in detail the exchange interaction between confined carriers and Mn atoms in a QD in under to describe the emission properties of singly and two Mn doped QDs. We will finally show how the tuning of the charge state of a QD can be used to control the magnetic properties of an individual Mn atom.

1.1 Spin structure of CdTe/ZnTe quantum dots

1.1.1 Quantum dots structure

Self-assembled semiconductor QDs can be manufactured by epitaxial growth methods, such as molecular beam epitaxy (MBE). To obtain epitaxial QDs, one grows a thin layer of one semiconductor on top of an other semiconductor (with a higher bandgap), to which it is not lattice-matched. As a result of the strain small islands are formed on top of a two-dimensional wetting layer (Stranski-Krastanow growth mode). The islands are overgrown subsequently by a layer of the high bandgap material, leading to a formation of buried QDs which confine carriers in all three directions. The quantum confinement is stronger in the growth direction (1-10 nm) than in the lateral direction (10-50 nm).

The samples used in all the studies presented in this manuscript are CdTe strained induced self-assembled QDs. They are all grown on ZnTe [001] substrates. A 6.5- monolayer-thick CdTe layer is deposited by atomic layer epitaxy on a ZnTe barrier grown by molecular beam epitaxy. The dots are formed by a Tellurium deposition/desorption process [140, 148] and protected by a 100-nm-thick ZnTe top barrier. The height of the QDs core is of few nanometers and their diameter is in the 10 to 20 nm range (Fig. 1.1). Single Mn atoms can be introduced in CdTe/ZnTe QDs during their growth adjusting the density of Mn atoms to be roughly equal to the density of QDs. Non-magnetic QDs and QDs containing a low number of magnetic atoms (1, 2, 3 Mn, ...) are then formed [97] [1]. In

[1] Single Mn doped quantum dots where first observed in sample designed for injection of spin polarized carriers from a DMS layer 10 monolayer below the QD plane. Diffusion of Mn atoms during the growth of the spacer layer leads to a low density of Mn atoms in the QD layer.

negatively charged samples used for the study of electron-nuclei spin dynamics, a 20 nm thick Al doped ZnTe layer is introduced 30 nm above the QDs.

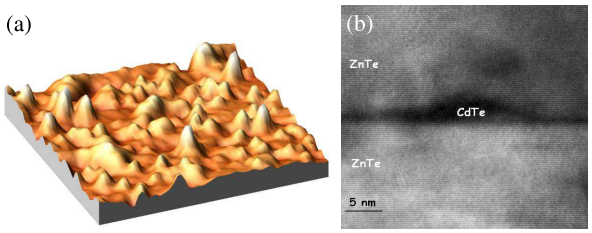

Figure 1.1 (a) AFM image (250nm × 250nm) of CdTe/ZnTe QDs before capping. The QD density is estimated to $\approx 3.10^{10} cm^{-2}$. (b) TEM image of a CdTe/ZnTe QD.

Optical addressing of individual QDs containing a single carrier or Mn atoms is achieved using micro-spectroscopy techniques. In most of our experiments, a high refractive index hemispherical solid immersion lens is mounted on the bare surface of the sample to enhance the spatial resolution and the collection efficiency of single-dot emission in a low-temperature ($T = 5K$) scanning optical microscope. Despite the quite large QD density ($\approx 10^{10} cm^{-2}$) and the large number of dots in the focal spot area, single QD transitions can be identified by their spectral signatures.

The low temperature photoluminescence (PL) of three QDs containing 0, 1, or 2 Mn atoms and a variable number of carriers are presented in Fig. 1.2. The different excitonic complexes observed in this spectrum (exciton, negatively charged excitons, biexciton) will be used to analyze the interaction between individual carriers and magnetic atoms and to access the spin dynamics of a resident electron coupled to a nuclear spin bath or an individual Mn spin coupled to its nuclear spin. We will first discuss the properties of neutral an singly charged QDs (top panel of Fig. 1.2) before describing in detail the spin structure of magnetic QDs.

1.1.2 Singly charged quantum dots

Charge tunable quantum dots

Non-intentionally doped CdTe/ZnTe QDs are p-type modulation doped by the transfer of holes from the p-doped ZnTe substrate and from surface states that act as acceptors [103, 15]. The occupation of the QDs by holes can be controlled by an external bias voltage V on an aluminium Schottky gate with respect to a back contact on the substrate. The bias dependent emission of a non-magnetic QD is presented in Fig. 1.3. For increasing V, the surface level states are shifted below the ground hole level in the QDs which results in the single hole charging. The optically generated excitons then form charged excitons with the bias induced extra hole in the QD. At zero bias or negative bias, the Fermi level is above the ground state and the QDs are likely to be neutral. However, the separated

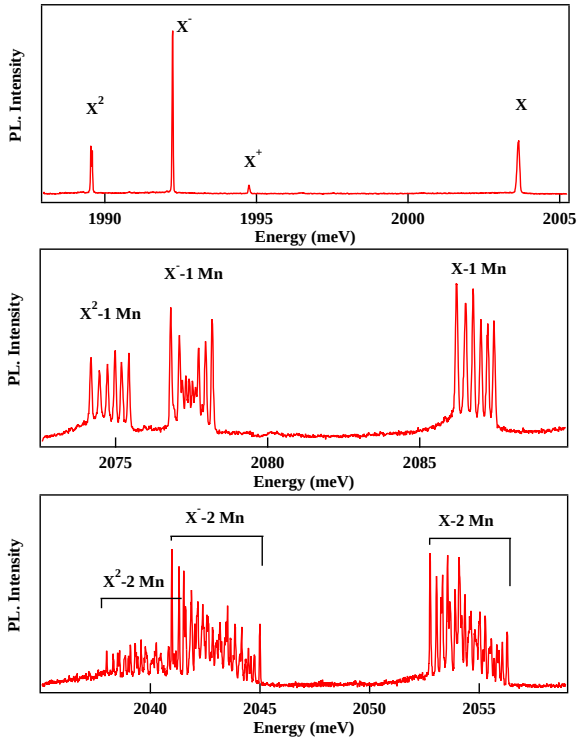

Figure 1.2 Low temperature (5K) PL spectra of CdTe/ZnTe QDs containing 0, 1, or 2 Mn atoms. All the spectra are obtain under resonant excitation on an excited state of the dots.

capture of photo-created electron or holes can sometimes charge the dots so that weak contributions of X^+ or X^- are observed in the zero bias spectra.

At zero bias, excess electrons can also be injected in the QD using resonant optical excitation into the excited levels. Under resonant excitation (energy below the band gap of the barriers), optical transitions from delocalized valence band states to the confined electron levels will preferentially create electrons in the QD [146]: the probability to find an excess electron in the QD is increased. As presented in Fig. 1.3(b), the negatively charged exciton emission is then seen for some discrete excitation energies. After the recombination of the charged exciton X^-, a single hole is likely to be captured to neutralize the QD and create a neutral exciton. This neutralization process is responsible for the simultaneous observation of charged and neutral species under resonant excitation.

Using this dynamic charging, the charge state of these dots can be optically tuned (Fig. 1.3(b)) to analyze the emission of non-magnetic or magnetic charged QDs. By combining a weak non-resonant excitation with the resonant one, a few carriers are created in the ZnTe barrier. They do not significantly contribute to the PL (lower PL spectra in Fig. 1.3(b)) but reduce the contribution of X^- in

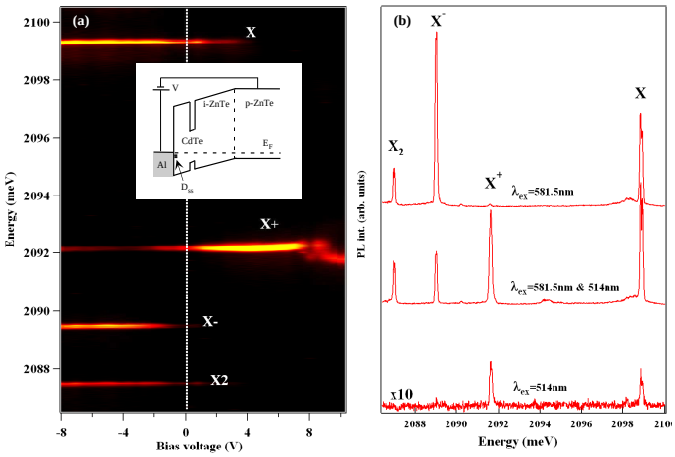

Figure 1.3 (a) Color-scale plot of the PL intensity of a QD in a Schottky structure as a function of emission energy and bias voltage. The emission lines can be assigned to the recombination of the neutral exciton (X), biexciton (X_2), positively charged exciton (X^+) and negatively charged exciton (X^-). (b) Detail of the PL of a single QD under resonant excitation (λ_{ex}=581.5nm), non-resonant excitation (λ_{ex}=514.5nm) and both resonant and non-resonant excitation.

favor of the neutral species. This evolution is characteristic of a photo-depletion mechanism in modulation doped QDs [66]. High energy photoexcited e-h pairs are dissociated in the space charge region surrounding the negatively charged QDs and neutralize the QDs.

Polarized fine structure of the charged exciton triplet in n-doped samples

To study the dynamics of coupled electron and nuclear spins, one needs a long-lived resident carrier. We use chemically n-doped samples and focus on the spectral feature of the negatively charged exciton (X^-) consisting of two electrons in a spin singlet state and one hole trapped in the QD. This charge complex has been shown to lead to a polarization of the nuclear spin system under circularly polarized excitation in both III-V [42] and II-VI QDs [2]. In order to prepare by optical pumping the spin state of a resident carrier or perform an optical orientation of a Mn spin, spin polarized electron-hole pairs have to be injected through circularly polarized excitation on a QD excited state.

Low power PL excitation (PLE) spectra on a singly negatively charged QD presented in Fig. 1.4 reveals intense absorption resonances for X^- with a strong polarization dependence. In general we find three distinctive features in these excitation spectra. The first is a set of lower energy resonances that are strongly co-polarized with the excitation laser. These transitions can be assigned to nominally forbidden transitions involving states with two *s*-shell electrons and an excited or delocalized hole. These transitions are particularly well observed in CdTe/ZnTe structures because of the weak valence band offset.

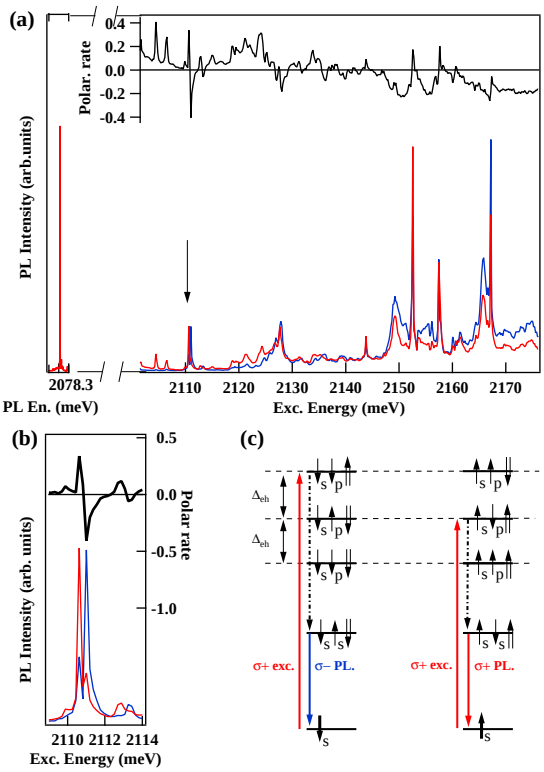

Figure 1.4 (a) PLE spectra resolved in circular polarisation under $\sigma+$ CW excitation with PL spectra in inset. (b) Zoom on the polarized doublet in the PLE spectra, the polarisation rate is also displayed. (c) Energy levels of the negative trion states. The electrons triplet state is split by the electron-hole exchange energy Δ_{eh}. The electrons singlet state, also part of the p-shell is not represented here. Left scheme: when exciting with $\sigma+$ light on the triplet state $|S = 1, S_z = -1\rangle$, photon absorption occurs only if the resident electron is down. As demonstrated by M.E. Ware [147], during the excited trion relaxation, an electron-hole flip-flop process allowed by anisotropic exchange interactions results in a $\sigma-$ PL. Right scheme: when exciting with $\sigma+$ light on the triplet state $|S = 1, S_z = 0\rangle$, photon absorption occurs only if the resident electron is up. Relaxation from this state leads to $\sigma+$ PL.

The second feature is a higher energy resonance that displays a fine structure doublet well resolved in circular polarization. As presented in Fig. 1.4(b), the PLE exhibits a strongly co- and then cross-polarized resonance as the laser energy increases around 2110 meV. As proposed by M.E. Ware *et al.* [147] we can assigned this doublet to the direct excitation of the two bright triplet states (see Fig. 1.4(c)) of the excited negatively charged exciton (X^{-*}). X^{-*} consists of an electron-hole pair in the s-shell and an electron in the p-shell. This doublet is a characteristic signature of the presence of a single electron in the QD ground state. We have found a triplet splitting Δ_0 around 400 μeV changing from dot

to dot. This is higher than the values found in InAs QDs, in agreement with the stronger exchange interaction in our II-VI system.

For an excitation above the X^{-*} triplet states, a series of excited states and an absorption background with a significant negative circular polarisation rate are observed. As we will discuss in chapter 2, this condition of excitation can be used to perform an optical pumping of the resident electron and analyze its spin dynamics in the diluted nuclear spin bath.

1.1.3 Valence band mixing in quantum dots

In flat self-assembled QDs with a relatively weak hole confinement, the bi-axial strains in the plane of the QD lift the degeneracy of the hole spin projections (heavy-hole/light hole splitting). In a first approximation, the optical properties of these QDs can be described by a heavy-hole exciton. However, several phenomena can lead to the mixing between light holes (lh) and heavy holes (hh).

First, the symmetry reduction due to the confinement geometry of the dot has to be considered. In this case, a hole band mixing appears through the non diagonal terms of the Luttinger-Kohn Hamiltonian. This mixing is responsible for the linear polarization rate observed in strongly confined quantum wires [16]. A large wave function anisotropy is indeed needed to reproduce the observed linear polarization [135]. Such anisotropy can only be obtained in a very elongated confining potential for the holes with large barriers. Another origin of hh-lh mixing is the coupling of the X and Y valence band states produced by the microscopic arrangement of chemical bonds at hetero-interfaces [30]. This contribution is expected to be weak in flat self-assembled QDs with almost symmetric interfaces. In self-assembled (strained induced) QDs, an in-plane anisotropy in the strain distribution can also be responsible for a strong hh-lh mixing. This mixing has striking effects on the hole spin anisotropy.

To describe in detail the optical properties of self-assembled QDs and then understand the interaction between confined carriers and a Mn spin, let us consider the general form of the Hamiltonian of a confined exciton. It consists of three parts:

$$\mathcal{H}_X = \mathcal{H}_{e-h} + \mathcal{H}_{band} + \mathcal{H}_{mag} \tag{1.1}$$

The last term, $\mathcal{H}_{mag}$ is the exciton magnetic coupling and will be discussed latter. The electron-hole exchange interaction, $\mathcal{H}_{e-h}$, contains two parts: the short range and the long range. The short range part can be describe by the Hamiltonian:

$$\mathcal{H}_{e-h,sr} = I_{eh}\,\overrightarrow{\sigma}.\overrightarrow{j} + \sum_i b_i \sigma_i j_i^3 \tag{1.2}$$

where $\overrightarrow{\sigma}$ ($\overrightarrow{j}$) is the spin operator for the electron (hole). The first term already exists in spherical symmetry whereas the second term takes into account the

reduction of the symmetry in a cubic crystal. The long range part mixes bright excitons confined in an anisotropic potential and can be represented in the heavy-hole exciton subspace ($J_z = +2,\ +1,\ -1,\ -2$) by:

$$\mathcal{H}_{e-h,lr} = \begin{pmatrix} 0 & 0 & 0 & 0 \\ 0 & 0 & \frac{1}{2}\delta_2 e^{-2i\phi_2} & 0 \\ 0 & \frac{1}{2}\delta_2 e^{2i\phi_2} & 0 & 0 \\ 0 & 0 & 0 & 0 \end{pmatrix} \tag{1.3}$$

where δ_2 is the splitting of the bright exciton induced by the exchange interaction.

The band Hamiltonian, $\mathcal{H}_{band}$, stands for the energy of the electron and the energy of the heavy-hole and light-hole. It has to take into account a possible valence band mixing. In bulk semiconductor, the spin orbit interaction is responsible for a splitting of the hole states. We only consider here the lowest energy holes with angular momentum $j = 3/2$. These $|j, j_z\rangle$ states can be simply defined using orbital (X, Y, Z) and spin $(\uparrow, \downarrow)$ eigenvectors :

$$\begin{aligned} |3/2, +3/2\rangle &= -\uparrow \frac{X + iY}{\sqrt{2}}, \\ |3/2, +1/2\rangle &= \sqrt{\frac{2}{3}} \uparrow Z - \downarrow \frac{X + iY}{\sqrt{6}}, \\ |3/2, -1/2\rangle &= \sqrt{\frac{2}{3}} \downarrow Z + \uparrow \frac{X - iY}{\sqrt{6}}, \\ |3/2, -3/2\rangle &= \downarrow \frac{X - iY}{\sqrt{2}}. \end{aligned} \tag{1.4}$$

Using these notations, a general form of Hamiltonian describing the influence of shape or strain anisotropy on the valence band structure can be written in the basis $(|\frac{3}{2}, +\frac{3}{2}\rangle, |\frac{3}{2}, +\frac{1}{2}\rangle, |\frac{3}{2}, -\frac{1}{2}\rangle, |\frac{3}{2}, -\frac{3}{2}\rangle)$ as:

$$\mathcal{H}_{vbm} = \begin{pmatrix} 0 & -S & R & 0 \\ -S^* & \Delta_{lh} & 0 & R \\ R^* & 0 & \Delta_{lh} & S \\ 0 & R^* & S^* & 0 \end{pmatrix} \tag{1.5}$$

with

$$\begin{aligned} S &= \delta_{xz} - i\delta_{yz} \\ R &= \delta_{xx,yy} - i\delta_{xy} \end{aligned} \tag{1.6}$$

where R describes the mixing induced by an anisotropy in the QD plane xy and S takes into account an asymmetry in the plane containing the QD growth axis z. This asymmetry can come from the shape of the QD or the strain distribution. Δ_{lh} is the splitting between lh and hh controlled by the in-plane bi-axial strain and the confinement.

In the case of a valence band mixing only induced by the strain anisotropy, Δ_{lh}, R and S can be linked to the deformation of the crystal ε_{ii} by the Bir and Pikus Hamiltonian [153, 21]:

$$\Delta_{lh} = 2b\left(\frac{\varepsilon_{xx}+\varepsilon_{yy}}{2} - \varepsilon_{zz}\right) \tag{1.7}$$

$$R = id\varepsilon_{xy} - b\frac{\sqrt{3}}{2}\left(\varepsilon_{xx}-\varepsilon_{yy}\right) \tag{1.8}$$

$$S = -\frac{d}{\sqrt{2}}\Big(\varepsilon_{zx} - i\varepsilon_{yz}\Big) \tag{1.9}$$

with b and d the Bir and Pikus parameters depending on the material.

Considering only an in-plane strain anisotropy (S=0) and using the hh band as the origin of the energies, the valence band Hamiltonian reads:

$$\mathcal{H}_{vbm,xy} = \begin{pmatrix} 0 & 0 & \rho_s e^{-2i\theta_s} & 0 \\ 0 & \Delta_{lh} & 0 & \rho_s e^{-2i\theta_s} \\ \rho_s e^{2i\theta_s} & 0 & \Delta_{lh} & 0 \\ 0 & \rho_s e^{2i\theta_s} & 0 & 0 \end{pmatrix} \tag{1.10}$$

This notation allows us to introduce useful parameters to describe the strain effects, namely the strain coupling amplitude ρ_s and the strain induced anisotropy axis in the QD plane defined by the angle θ_s with respect to the x (100) axis.

In the limit of weak valence band mixing ($\rho_s \ll \Delta_{lh}$), the ground states of the holes can be written:

$$\begin{aligned} \left|\widetilde{\Uparrow}\right\rangle &\propto |+3/2\rangle - \frac{\rho_s}{\Delta_{lh}} e^{2i\theta_s}\,|-1/2\rangle \\ \left|\widetilde{\Downarrow}\right\rangle &\propto |-3/2\rangle - \frac{\rho_s}{\Delta_{lh}} e^{-2i\theta_s}\,|+1/2\rangle \end{aligned} \tag{1.11}$$

A development of the hole angular momentum operator $\overrightarrow{j}$ in this subspace gives in the first order of $\frac{\rho_s}{\Delta_{lh}}$:

$$\tilde{j}_+ = \frac{\rho_s}{\Delta_{lh}} \begin{pmatrix} 0 & -2\sqrt{3}e^{-2i\theta_s} \\ 0 & 0 \end{pmatrix} \tag{1.12}$$

$$\tilde{j}_- = \frac{\rho_s}{\Delta_{lh}} \begin{pmatrix} 0 & 0 \\ -2\sqrt{3}e^{2i\theta_s} & 0 \end{pmatrix} \tag{1.13}$$

$$\tilde{j}_z = \begin{pmatrix} 3/2 & 0 \\ 0 & -3/2 \end{pmatrix} \tag{1.14}$$

the pseudo spin ladder operator $\tilde{j}_+$ and $\tilde{j}_-$ flip the hole spin whereas the z component $\tilde{j}_z$ confirms that these states are mainly hh. This pseudo-spin description

of the hole ground states is often sufficient to describe the main consequences of valence band mixing in self-assembled QDs.

1.1.4 Valence band mixing and optical polarization anisotropy

Fig. 1.1.4 presents the polarization resolved emission spectra for different charged states of the same QD presenting a very large valence band mixing: the neutral species (exciton and biexciton) and two charged excitons (positive and negative). Whatever the charged state, the emission of the QD is partially linearly polarized along a constant direction. In this case the linear polarization rate ρ_L equals 40%. A significant linear polarization rate is observed for most of the CdTe/ZnTe QDs but with polarization directions changing from dot to dot.

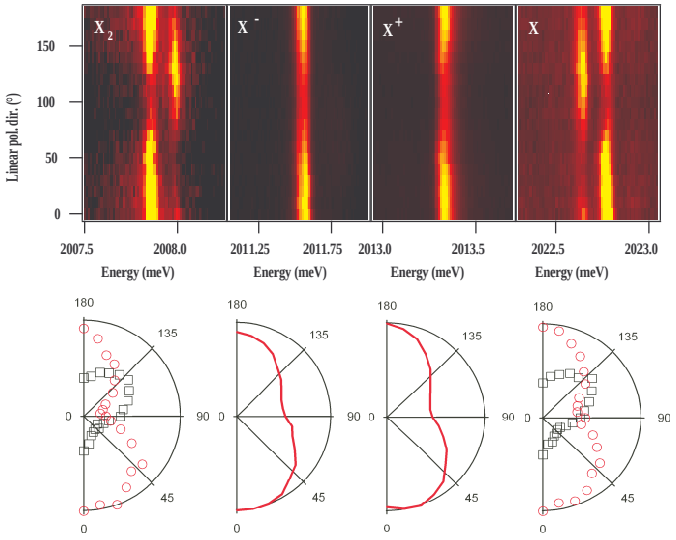

Figure 1.5 Linear polarization dependence of the PL intensity of X, X_2, X^- and X^+ in the same quantum dot. The polar plots depict the emission intensity for different positions of the polarization analyzer relative to [110] direction. For the exciton (biexciton), the high (low) energy line intensity is plotted with open circles and the low (high) energy line intensity is plotted with open squares.

To understand this effect, we first consider the simplest case of a charged exciton where exchange interactions do not play a role because the hole is interacting with an electron spin singlet. The oscillator strength $\Omega(\alpha)$ of the transition (where the vector $\vec{e}_\alpha = \cos(\alpha)\vec{e}_x + \sin(\alpha)\vec{e}_y$ is the polarization of the detection) is given by:

$$\begin{aligned}\Omega(\alpha) &\propto \left|\left\langle \uparrow |\cos(\alpha)p_X + \sin(\alpha)p_Y| \uparrow\downarrow \widetilde{\Uparrow}\right\rangle\right|^2 \\ &= 1 + A^2 + 2A\cos(2(\theta_s - \alpha))\end{aligned} \tag{1.15}$$

with $\overrightarrow{p} = -i\hbar\overrightarrow{\nabla}$ the impulsion operator and $A = 1/\sqrt{3}(\rho_s/\Delta_{lh})$. Contrary to what is expected in the hh approximation, the charged exciton can have a strong linear component, depending on the strength of the lh-hh mixing.

In the QD presented in Fig. 1.1.4, the linear polarization rate $\rho_l = 2A/(1 + A^2) \approx 40\%$, which corresponds to a very strong lh-hh mixing of $\rho_s/\Delta_{hh-lh} \approx 0.75$). Experimentally, there are no correlation between the polarisation axis of different QDs, even if they are spatially close to each other (and of course no correlation with the crystallographic axis). Such behaviour can be explained considering the anisotropic relaxation of strain during the growth. A similar behaviour is observed in III-V compounds at low QD density (near the 2D to 3D transition). Again, it is attributed to the effect of strains [44]. For this III-V system, this hypothesis is supported by AFM studies showing that, in such growth conditions, the dots are preferentially nucleating near structural defects [119]. In the case of II-VI materials, a strained-induced heavy hole / light hole mixing is not surprising as the dislocation formation energy is lower in this system [140].

For neutral excitons, the competition of the long range exchange interaction (which tends to favor linear emission along ϕ_2 and $\phi_2 + 90\,^\circ$) and the effect of strains (which tends to favor linear emission along θ_s and $\theta_s + 90\,^\circ$) explains that the angle between the two linearly polarized exciton lines is not equal to $90\,^\circ$ (Fig. 1.1.4). Moreover, the valence band mixing results in a fine structure splitting through the short-range exchange interaction that can either enhance or decrease the fine structure splitting due to long range exchange interaction. In order to illustrate our point, we consider only the isotropic part of the short-range exchange interaction between the electron and the light or heavy hole:

$$H_{e-h,sr} = I_{eh}\vec{\sigma}.\vec{j} \tag{1.16}$$

where $3/2I_{eh}$ corresponds to the energy splitting between bright and dark excitons due to the short-range exchange interaction. The coupling between the bright states $\left|\downarrow \widetilde{\Uparrow}\right\rangle$ and $\left|\uparrow \widetilde{\Downarrow}\right\rangle$ through $H_{e-h,sr}$ can be calculated using the pseudo spin operators 1.12 and 1.13:

$$\left\langle \downarrow \widetilde{\Uparrow} |H_{e-h,sr}| \uparrow \widetilde{\Downarrow} \right\rangle = \frac{1}{2\sqrt{3}} I_{eh} \frac{\rho_s}{\Delta_{lh}} e^{-2i\theta_s} \tag{1.17}$$

Hence, valence-band mixing through the short-range interaction splits the bright states into two linearly polarized states along axis defined by the strain angle θ_s. This add a contribution to the splitting produced by the long range exchange interaction in an anisotropic potential. As a result of the competition between this effect and the long-range exchange interactions which wants to impose an angle Φ_2, the angle between the two linearly polarized states is not necessarily 90° as observed in the emission of CdTe/ZnTe QDs [93] and recently in InAs/GaAs QDs [141].

1.1.5 Valence band mixing and magnetic anisotropy

To have a better understanding on the influence of the valence band mixing on the spin properties of confined carriers, magnetic field studies where performed. A combination of data obtained for magnetic fields in Faraday and Voigt configurations (Fig. 1.6(a)) allows a full determination of the magnetic properties of a given QD. In Faraday configuration (B‖z) X, X^+, X^- and X_2 split into doublets. In the heavy hole approximation, these doublets should be composed of two lines with opposite circular polarizations $\sigma+$ and $\sigma-$. Experimentally, we only observe circular polarization rates from 75 to 85% at 11T as illustrated in Fig. 1.6(d-e) for the charged excitons. This is not surprising because a magnetic field of a few Teslas has no influence on the valence band mixing produced by the strain anisotropy. Considering a valence band mixing efficiency ρ_s/Δ_{lh} of about 0.75, it appears that each line of the doublets should have elliptic polarizations with linear polarization rates of 40% and circular polarization rates of 90%. In other words, a 40% linear polarization of the QD emission is conserved whatever the charge state and whatever the magnetic field configuration.

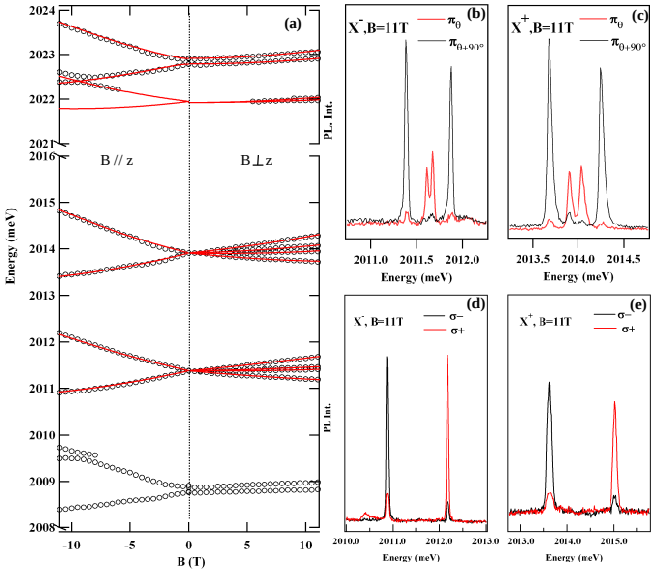

Figure 1.6 (a) Fine structure under magnetic field of X, X^+, X^- and X^2 in both Voigt ($B_\perp z$) and Faraday ($B_\parallel z$) configurations. (b) and (c) show respectively the linearly polarized PL spectra of X^- and X^+ in a transverse magnetic field B=11T. (d) and (e) show the circularly polarized PL spectra of X^- and X^+ in Faraday configuration (B=11T). The observed different splitting directly reveal a variation of the g-factor with the charged state of the QD.

For the exciton, an anticrossing of the bright and dark exciton states is observed around 9T allowing a full determination of the electron and hole g factors. This

anticrossing can be understood only by considering non zero trigonal shear strains (S term in the Hamiltonian (1.5)). In this case, the full Bir-Pikus Hamiltonian must be used and one obtains hole eigenfunctions that are linear combinations of $|3/2\rangle$, $|1/2\rangle$ and $|-1/2\rangle$ on one side and $|-3/2\rangle$, $|1/2\rangle$and $|-1/2\rangle$ on the other side. In this new basis, the Zeeman Hamiltonian in Faraday configuration is no more diagonal. Thus it couples these hole states producing anticrossings when they get close to each other as observed experimentally.

	X	X^+	X^-
$g_{e\perp}$	-0.40	-0.35	-0.35
$g_{h\perp}$	0.16	0.19	0.17
$g_{e\parallel}$	-0.45	-0.45	-0.45
$g_{h\parallel}$	0.53	0.60	0.53

Table 1.1 *g factors extracted from the magneto-optics measurements presented in Fig. 1.6.*

In Voigt configuration (B⊥z), the splitting of the exciton doublet slightly increases and at hight field a contribution of the dark exciton states is also observed on the low energy side of the spectra (Fig. 1.6). By contrast the charged excitons split into quartets of linearly polarized lines (Fig. 1.6(b) and 1.6(c)) with an intensity difference between the linearly polarized components corresponding to the polarization degree measured at zero field [7]. This spectral feature is a direct consequence of the presence of the strong hh-lh mixing detailed previously.

The magnetic coupling of the exciton in a D_{2d} geometry is given by:

$$\mathcal{H}_{mag} = g_e \mu_B \overrightarrow{B}.\overrightarrow{\sigma} + \mu_B(\kappa \overrightarrow{j}.\overrightarrow{B} + q \overrightarrow{j}^3.\overrightarrow{B}) + \gamma B^2 \tag{1.18}$$

where g_e is the electron Lande factor, κ and q describe the hole magnetic coupling and γ is a diamagnetic coefficient. As it has been shown in CdSe QDs [77], in presence of hh-lh mixing, the κ term of the hole magnetic Hamiltonian leads to magnetic coupling between the hole states for B⊥z, resulting in a non-zero value of the in-plane hole g-factor and in QD PL emission polarized parallel and perpendicular to the QD strain axis. We will see in the following deviations from these results in CdTe/ZnTe QDs.

Magneto-optical experiments enable a determination of the electron and hole g factors parallel and perpendicular to the growth axis. A summary of the g factors deduced from the magnetic field evolution of the different charged states observed in Fig. 1.6 are presented in table I. A larger hole g factor is found for X^+ in both Faraday and Voigt configurations. This variation of g_h reflects the expected variation of the hole confinement in the different excitonic species. Because of the weak valence band offset between CdTe and ZnTe, for X or X^-, a significant fraction of the confinement of the hole comes from the Coulomb attraction of the electrons present in the initial state of the optical transitions.

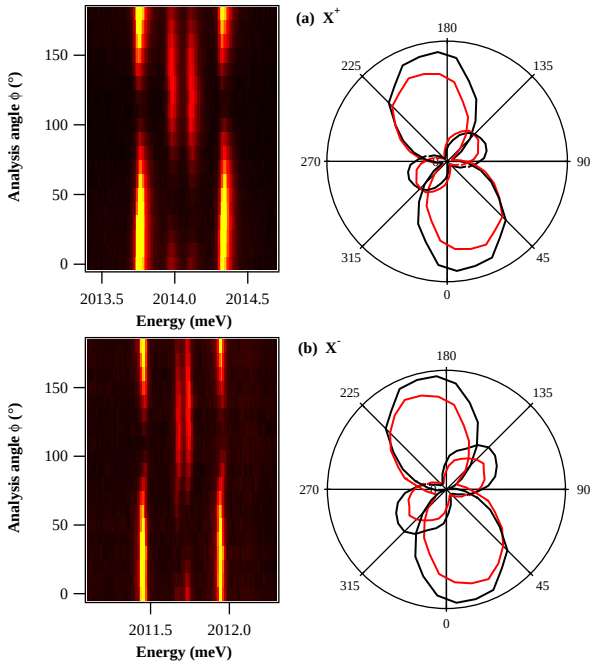

Figure 1.7 Polarization resolved fine structures of X^+((a)) and X^- ((b)). Polar graphs of the line intensities are plotted on the right panel. Black lines correspond to the low energy lines and red lines to the high energy lines.

By contrast, in the final state of X^+ there is no electron to attract the hole, resulting in a delocalization of the hole wave function in the ZnTe barrier and to a modification of its g-factor.

As observed for the linearly polarized exciton doublet at zero field, the charged exciton quadruplets under transverse magnetic field presents polarization axes which are not orthogonal. This can be seen in Fig. 1.7 where the polarization resolved spectra of charged excitons are plotted for a transverse magnetic field $B_\perp$ =11T. Not only the inner and outer doublets polarizations are not perpendicular to each other but there are also differences in the polarization directions of each doublet.

In the first part of this section, we have seen that a competition can arise between the strain distribution and the shape of the dots that define two different anisotropy axis in the QD plane. This competition has consequences on the exciton splitting and polarization features. Thus, for magneto-optical experiments in Voigt configuration, one can expect that the spectral features of the charged exciton emission will be influenced by a competition between the strain distribution and the in-plane anisotropy produced by the magnetic field.

As illustrated in Fig. 1.8, the emission spectra and polarization directions of a negatively charged exciton have been measured for two orientations of the in-plane magnetic field. It appears that the orientation of the magnetic field in the

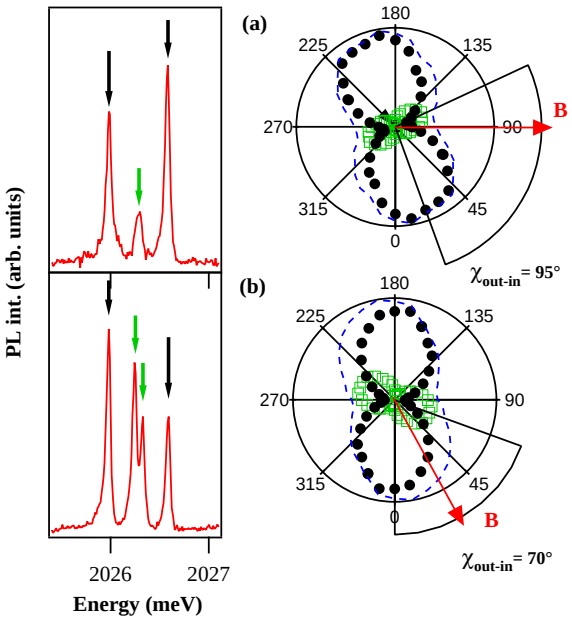

Figure 1.8 Fine structures and polar graphs of the emission intensity of a negatively charged exciton for two orientations of the transverse magnetic field (11 T) : (a) $\theta_B = 90°$ and (b) $\theta_B = 30°$ while $\theta_s = 10°$ in both cases. In the polar graphs, the intensity of the inner doublet is plotted with open green squares. The intensity of the outer doublet is plotted with full black circles. The dashed blue lines represent the total emission intensity.

QD plane has a significant impact on the Zeeman splitting and on the polarization directions of the inner and outer doublets. When the in-plane magnetic field is perpendicular to the (110) axis (Fig. 1.8(a)), the charged exciton splitting only enables us to observe a triplet structure and the inner and outer doublets are roughly perpendicular with directions defined by the strain distribution as explained in reference [77]. In the second case presented in Fig. 1.8(b) where θ_B=30°, the splitting has changed so that a quadruplet is observable. The angle χ_{out-in} between the inner and outer doublets is now only 70°. This confirms that the charged exciton behavior under transverse magnetic field is non trivial. A competition between the strain anisotropy axis and the magnetic field direction governs the hole states.

Such a competition can be qualitatively modeled by considering only the linear term of the hole magnetic coupling in equation (1.28) and a description of the valence band by equation (1.10). The calculated energy levels of a charged exciton presented in Fig. 1.9(a) show that for some magnetic field orientations, one can have either an acute or obtuse angle χ_{out-in} between the linear polarization directions of the inner and outer doublet. The angle χ_{out-in} (right panel of Fig. 1.9(a)), as well as the Zeeman splitting (left panel of Fig. 1.9(a)) present

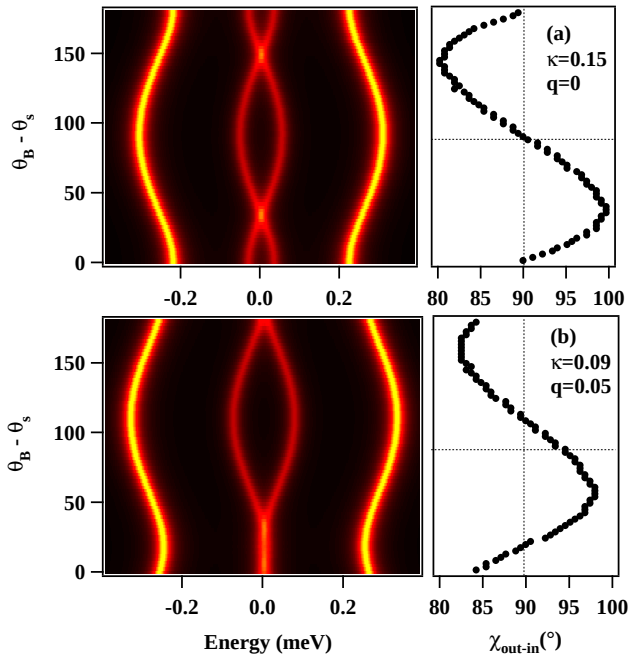

Figure 1.9 Calculated dependence of the fine structure and of χ_{out-in} on the magnetic field direction θ_B for two different sets of parameters: (a) κ =0.15, q =0; (b)κ =0.09, q =0.05. These parameters are chosen to reflect the experimental in-plane hole g factor. The strain parameters are: Δ_{lh} = 30 meV, ρ_s/Δ_{lh} =0.75 and θ_s = 10°. The other parameters are B=11T, I_{eh}=-550 μeV and δ_2=250μeV.

both an amplitude which strongly depends on the transverse magnetic field orientation. In particular, extremal splitting values and orthogonality of the doublet directions are obtained for magnetic field orientation parallel to the strain direction. Let's note that these modulations cannot be seen in the pseudo spin model (used for instance by Koudinov *et al.* [77]) in which the reduction to a 2x2 matrix cancels the phase of the coupling elements.

Fig. 1.9(b) shows that sharing the hole g factor between the linear and the cubic components ($q \neq 0$) modifies the splitting and angle variations. In particular, we observe an angular shift of the modulation shapes. However, a comparison with the experimental data do not permit to independently extract the values of κ and q. They may both contribute to the observed behavior. The presented model is also not able to reproduce the dephasing between the two inner lines on one side and the two outer lines on the other side. In order to improve the model, the g factor anisotropy due to the shape of the confinement and valence band mixing due to Luttinger hamiltonian should probably be considered.

1.2 Mn atoms in a II-VI quantum dot

Now that we have analyzed the basic magneto-optical properties of neutral and charged excitonic complexes in CdTe/ZnTe QDs, we will study their interaction with magnetic atoms (Mn). We will first remember some properties of II-VI DMS before describing in detail the coupling between confined carriers and an individual Mn atom. We will show that in QDs with a cylindrical symmetry, there is a direct correspondance between the state of a photon (energy and polarization) absorbed or emitted by the QD and the spin state of the Mn atom. We will discuss the limit of this direct correspondance in QDs presenting a shape and/or strain anisotropy.

1.2.1 A Mn atom in a zinc blende II-VI semiconductor

Carrier Mn coupling in a diluted magnetic semiconductor

In order to understand the effect of adding a Mn atom in a CdTe QD, a good starting point is to consider a Mn atom in a CdTe crystal and hence the case of DMS at the limit of low concentrations which have been intensively studied for the past decades. In such case, we can consider that the band states of the crystal are the ones of a pure crystal without the Mn impurity, while the presence of the Mn atom introduces localized d electronic states around the Mn nucleus.

When the Mn atom ($3d^5 4s^2$) replaces a Cd atom ($3d^{10} 4s^2$), the 2 electrons of the s shell participate to the crystal bond, while the 5 electrons of the d shell remain localized around the Mn^{2+} ion. Consequently, the presence of the Mn impurity in a II-VI crystal does not strongly modify the crystal potential seen by free carriers contrary to a Mn impurity in a III-V semiconductor where the Mn atom is also an acceptor (The Mn^{2+} ion, which is a negatively charged center in the III-V crystal, binds a hole from the valence band to form a hydrogenic-like state [81]).

The half filled $3d$ shell of the Mn atom in the ground electronic state satisfies according to Hund's rule $S = 5/2$ and $L = 0$: each electron occupies a d orbital ($L_z = -2, -1, 0, 1, 2$) with parallel spins. The lowest excited state $3d^{5*}$ with $S = 3/2$ and $L = 4$ (which corresponds schematically to the inversion of one of the electron's spin) lies $2.2eV$ above the electronic ground state. These intra-ionic optical transition (observed in ZnMnTe [90]) should be forbidden by parity rules and spin-conservation but are dipole allowed by the lack of inversion symmetry of the tetrahedral crystal field and spin-orbit interaction. The same mixing is responsible for spin-lattice relaxation of an isolated Mn spin. Since this mixing is small, we can consider that the Mn is a $S = 5/2$ pure spin.

In DMS, a strong spin-dependent coupling was discovered in 1977 [76] between the free carriers (electron from the s band and holes from the p band) and the localized d electrons of the Mn atom called $sp - d$ exchange. One of the most striking consequences of these interactions is the so-called giant Zeeman effect: the splitting produced by a magnetic field is more than an order of magnitude larger

than the intrinsic Zeeman splitting of the exciton optical transitions, reflecting an energy shift of the conduction and valence band edge.

In order to explain it, a shift induced by the effective field created by polarized Mn atoms needs to be considered. Since carriers near the band edge are delocalized, a mean field approximation is performed (it is the so-called virtual-crystal approximation): the carriers are only sensitive to the mean value of the Mn spins $\langle S_z \rangle$, and to their average density xN_0 where x is the percentage of Mn in the alloy, and where N_0 is the number of unit cells in a normalized volume (i.e. $N_0 = \frac{4}{a_0^3}$ where a_0 is the size of the cubic cell in the zinc-blende structure.). This $sp-d$ exchange-induced shift was found to be proportional to the Mn magnetization:

$$\begin{aligned} E_{sd} &= -N_0 x\alpha \langle S_z \rangle \sigma \\ E_{pd} &= -N_0 x\frac{\beta}{3} \langle S_z \rangle j_z \end{aligned} \tag{1.19}$$

α (resp. β) is a coupling constant between the s carriers (resp. p carriers) and the d electrons of the Mn spin. In CdTe, $N_0\alpha \approx 0.2eV$ and $N_0\beta \approx -0.88eV$. These values in bulk materials can be extracted from reflectivity measurements under magnetic field thanks to the presence of both light holes and heavy holes excitons which split proportionally to $N_0(\alpha+\beta/3)$ and $N_0(\alpha-\beta)$ [40, 52]. The law (1.19) is well satisfied in II-VI DMS with moderate band gap and a Zinc-Blende structure such as (Cd,Mn)Te, (Zn,Mn)Te or (Zn,Mn)Se. Generally, $N_0\alpha$ is fairly independent from the material, while $N_0\beta$ is large, negative and proportional to N_0 (i.e. increases as the size of a unit cell shrinks, for e.g. $N_0 |\beta_{CdTe}| < N_0 |\beta_{ZnTe}|$).

These spin-dependent coupling result from short-range exchange interactions between the carriers (electron from the s band at a position $\vec{r}_e$ and holes from the p band, at $\vec{r}_h$) and the localized d electrons at position $\vec{R}$ which take a Kondo-like form[2]:

$$H_{sp-d} = -J_{sd}(\vec{R}-\vec{r}_e)\vec{\sigma}_e \cdot \vec{S} - J_{pd}(\vec{R}-\vec{r}_h)\vec{\sigma}_h \cdot \vec{S} \tag{1.20}$$

Two mechanism contribute to this exchange coupling:

1. A ferromagnetic coupling resulting from direct exchange interaction: Two electrons with parallel spins tend to avoid each other due to the Pauli exclusion principle, thus the Coulomb repulsive interaction is reduced compared to the case of anti-parallel spins.
2. A spin-dependent hybridization of the Mn electrons with the free carriers which results in an anti-ferromagnetic coupling between the free carrier and the Mn spin, called kinetic exchange.

The hybridization is forbidden for an electron from the s band at $k = 0$ because

[2] Following the conventional notations, the Kondo Hamiltonian is expressed as a function of the pure spin of the free carriers, but it can also be expressed as a function of $\vec{j}$ by replacing $\vec{\sigma}_h \mapsto \vec{J}$ and $J_{pd} \mapsto J_{pd}/3$.

of symmetry (s and d wave-functions are orthogonal in zinc-blende structures). The s-d exchange is only governed by direct exchange and the coupling between s electrons and the Mn spin is ferromagnetic. But p-d hybridization is allowed, and has the main contribution to the hole-Mn exchange: the holes and Mn spins coupling is anti-ferromagnetic.

Mn spin fine and hyperfine structure

To fully describe a Mn atom in a zinc-blende semiconductor, we have also to notice that all the stable Mn isotopes (^{55}Mn) carries a nuclear spin I=5/2 which couples through hyperfine interaction to the electronic spin S=5/2. The d orbital of the Mn is also sensitive to the electric field produced by the neighboring atoms (crystal field) in the zinc-blende lattice. A distortion of the lattice and consequently a change in the crystal field will also affect the d orbital. The complete Hamiltonian of the coupled electronic and nuclear Mn spins in a strained zinc-blende layer grown along [001] is known from magnetic resonance measurements [124]. It reads:

$$\begin{aligned}\mathcal{H}_{Mn} = \mathcal{A}\overrightarrow{I}.\overrightarrow{S} + \frac{1}{6}a[S_x^4 + S_y^4 + S_z^4 - \frac{1}{5}S(S+1)(3S^2+3S-1)] \\ +\mathcal{D}_0[S_z^2 - \frac{1}{3}S(S+1)] + E[S_x^2 - S_y^2] \\ +g_{Mn}\mu_B\overrightarrow{B}.\overrightarrow{S}\end{aligned} \quad (1.21)$$

The term $\mathcal{A}$ in this Hamiltonian is the hyperfine coupling which results from the magnetic dipolar interaction between the Mn 5 d electrons forming the total spin $\vec{S}$ and the spin of the Mn nucleus $\vec{I}$. The hyperfine constant $\mathcal{A}$ is equal to $+0.7\mu eV$ [22]. The second term of the Hamiltonian results from cubic crystal symmetry and mixes different S_z of the Mn spin. We have $a = 0.32\mu eV$ according to [22].

The term $\mathcal{D}_0$, commonly called 'magnetic anisotropy' arises from the existence of bi-axial strains. These strains induce an additional component to the crystal field which has an axial symmetry. We can estimate the maximum D_0 expected in our samples. The lattice constant of an unstrained CdTe crystal is $a_{CdTe} \approx 0.648nm$ while for a ZnTe crystal, $a_{ZnTe} \approx 0.610nm$. According to [124], the magnetic anisotropy D_0 for a strained layer grown along the [001] axis is given by:

$$D_0 = -\frac{3}{2}G_{11}\left(1 + \frac{2C_{12}}{C_{11}}\right)\frac{a_{xy} - a_{CdTe}}{a_{CdTe}} \quad (1.22)$$

where G_{11} is the spin-lattice coefficient describing the energy-shift of spin levels per unit strain, C_{11} and C_{12} are elastic constants, and a_{xy} is the common in-plane lattice constant of the strained-layer. According to [22], $G_{11}/(2\pi\hbar c) = 0.46cm^{-1}$, and according to [63], $C_{11} = 5.62 \cdot 10^{10}N.m^{-2}$ and $C_{12} = 3.93 \cdot 10^{10}N.m^{-2}$ at 77K. Considering that a_{xy} is determined by the ZnTe lattice parameter, we can estimate $D_0 \approx 12\mu eV$. This is the maximum value we can expect for a fully strained CdTe QD matched on a ZnTe substrate.

An anisotropy of the strain in the xy plane can also, through the crystal field, mix different S_z components. This coupling is described in the Hamiltonian (1.21) by its characteristic energy E.

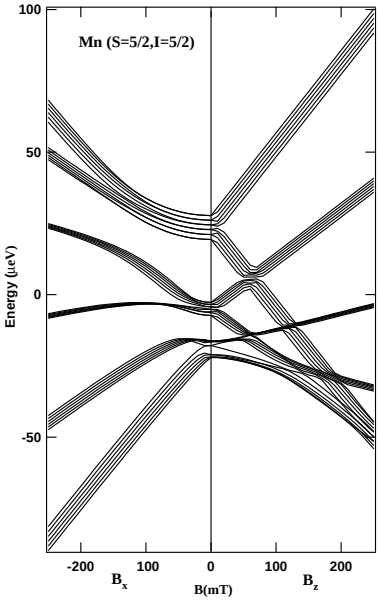

Figure 1.10 Magnetic field dependence of the fine structure of the Mn spin with a field along [001] (right) or perpendicular to [001] (left). The calculation are performed with $A = 0.7$ μeV, $D_0 = 7$ μeV, g_{Mn}=2 and a crystal field parameter $a = 0.32$ μeV.

The resulting fine and hyperfine structure of the Mn under a magnetic field applied along z or in the plane xy is shown in Fig. 1.10. At zero field, the Mn electronic spin is quantized along the growth axis and the different electronic spin doublets are separated by an energy proportional to D_0. The doublets S_z=$\pm$5/2 and S_z=$\pm$3/2 are further split into six lines by the hyperfine coupling with the nuclear spin I=5/2. For the doublet S_z=$\pm$1/2, the isotropic coupling with the nuclear spin I=5/2 results in two levels with total spin M=2 and M=3. The harmonic spacing between the electronic spin levels is restored for a large magnetic field (B$\geq$1T) along the z axis [001].

1.2.2 Coupling between confined carriers and a Mn spin

In Fig. 1.11, PL spectra of an individual Mn-doped QD are compared to those of a non-magnetic CdTe/ZnTe reference sample. In non-magnetic samples, the emission of neutral QDs is split by the e-h exchange interaction and usually a linearly polarized doublet is observed [9]. On the over hand, most of the individual emission peaks of magnetic single QDs are characterized by a rather large linewidth of about 1 meV. For some of these QDs, a fine structure can be resolved and six

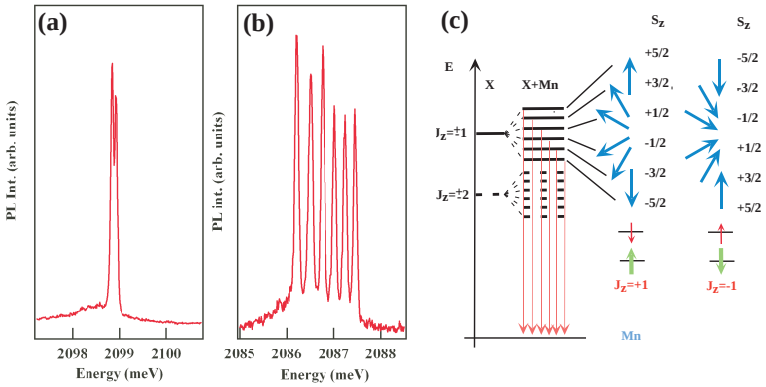

Figure 1.11 Low temperature (T=5K) PL spectra obtained at B=0T for an individual CdTe/ZnTe QD (a) and a Mn-doped QD (b). (c) Scheme of the energy levels of the Mn-exciton coupled system at zero magnetic field. The exciton-Mn exchange interaction shift the energy of the exciton depending on the S_z component of the Mn spin.

emission lines are clearly observed at zero magnetic field. The measured splitting changes from dot to dot. This fine structure splitting as well as the broadening is obviously related to the influence of the Mn atoms located within the spatial extent of the exciton wave function. The broadening observed in magnetic QDs has been attributed by Bacher *et al.* to the magnetic fluctuations of the spin projection of a *large number* of Mn spins interacting with the confined exciton [5]. In the low concentration Mn-doped samples, the observation of a fine structure shows that the QD exciton interacts with a single Mn spin.

As we have seen, the bi-axial strains in the plane of the QD lift the degeneracy of the hh and lh. In a first approximation, this system can be described by a hh exciton confined in a symmetric QD, in interaction with the six spin projections of the Mn atom [61]. The spin interaction part of the exciton-Mn Hamiltonian is then given by:

$$\mathcal{H}_{int} = I_{eMn}\overrightarrow{\sigma}.\overrightarrow{S} + I_{hMn}j_z.S_z + I_{eh}\overrightarrow{\sigma}.\overrightarrow{j} \tag{1.23}$$

where I_{eMn} (I_{hMn}) is the Mn-electron (-hole) exchange integral, I_{eh} the electron-hole exchange interaction and σ (j, S) the magnetic moment of the electron (hole, Mn). As the carrier-Mn exchange interaction is short-range, in first approximation, we can consider that the exchange constants are proportional to the probability of presence of the carrier at the Mn location $\vec{R}$:

$$\begin{aligned} I_{eMn} &= -\alpha \left|F_e(\vec{R})\right|^2 \\ I_{hMn} &= -\beta/3 \left|F_h(\vec{R})\right|^2 \end{aligned} \tag{1.24}$$

For a better understanding of the exchange interactions, the Hamiltonian of the electron-Mn interaction for instance can be rewritten in the form:

$$\mathcal{H}_{e-Mn} = I_{eMn} S_z.\sigma_z + \frac{I_{eMn}}{2}(S_+.\sigma_- + S_-.\sigma_+) \tag{1.25}$$

Here the ladder operators $S_\pm = S_x \pm iS_y$ for the Mn and $\sigma_\pm = \sigma_x \pm i\sigma_y$ for the electron have been introduced. The first part of the Hamiltonian $S_z.\sigma_z$ is an Ising type interaction and thus called Ising term. It is diagonal in the chosen basis and leads to energy shifts of the states $|X, S_z\rangle$. The second part $(S_+.\sigma_- + S_-.\sigma_+)$ contains the ladder operators. This term allows the electron to exchange spin with the Mn. For example, the electron spin flips from up to down and the Mn spin increases by one or vice versa. This part is called flip-flop term.

The exciton-Mn levels (initial states of the optical transitions) are obtained from the diagonalisation of the spin Hamiltonian $\mathcal{H}_{int}$ in the subspace of the hh exciton and Mn spin components $|\pm 1/2\rangle_e|\pm 3/2\rangle_h|S_z\rangle_{Mn}$, with $S_z = \pm 5/2, \pm 3/2, \pm 1/2$. Since the dipolar interaction operator does not affect the Mn d electrons, the final states involve only the Mn states $|S_z\rangle_{Mn}$ with the same spin component [11]. At zero magnetic field, the QD emission presents a fine structure composed of six doubly degenerate transitions roughly equally spaced in energy. The lower energy bright states, $|+1/2\rangle_e|-3/2\rangle_h|+5/2\rangle_{Mn}$ and $|-1/2\rangle_e|+3/2\rangle_h|-5/2\rangle_{Mn}$ are characterized by an anti-ferromagnetic coupling between the hole and the Mn atom. The following states are associated with the Mn spin projections $S_z = \pm 3/2, \pm 1/2$ until the higher energy states $|-1/2\rangle_e|+3/2\rangle_h|+5/2\rangle_{Mn}$ and $|+1/2\rangle_e|-3/2\rangle_h|-5/2\rangle_{Mn}$ corresponding to ferromagnetically coupled hole and manganese. In this simple model, the splitting between bright excitons at zero field $\delta_{Mn} = \frac{1}{2}(3I_{hMn} - I_{eMn})$ depends only on the exchange integrals I_{eMn} and I_{hMn} and is thus related to the position of the Mn atom within the exciton wave function. The overall splitting of the bright exciton sextuplet is simply given by $\delta_{Mn} = \frac{5}{2}(3I_{hMn} - I_{eMn})$.

When an external magnetic field is applied in the Faraday geometry (Fig. 1.12), each PL peak is further split and twelve lines are observed, six in each circular polarization. The relative intensities of the six emission lines observed in each circular polarization strongly depend on the applied magnetic field. The emission intensity, which is almost equally distributed over the six emission lines at zero field, is concentrated on the high energy side of the $\sigma-$ emission and on the low energy side of the $\sigma+$ emission at high magnetic field.

As presented in Fig. 1.13, the Zeeman effect of the Mn states is identical in the initial and final states of the optical transitions. The six lines in a given polarization follow the Zeeman and diamagnetic shift of the exciton, as in a non-magnetic QD. The parallel evolution of six lines is perturbed around 7T in $\sigma-$ polarization by anti-crossings observed for five of the lines.

The electron-Mn part of the interaction Hamiltonian $I_{eMn}\overrightarrow{\sigma}.\overrightarrow{S}$ couples the dark ($J_z = \pm 2$) and bright ($J_z = \pm 1$) hh exciton states. This coupling corresponds to a simultaneous electron and Mn spin flip changing a bright exciton into a dark

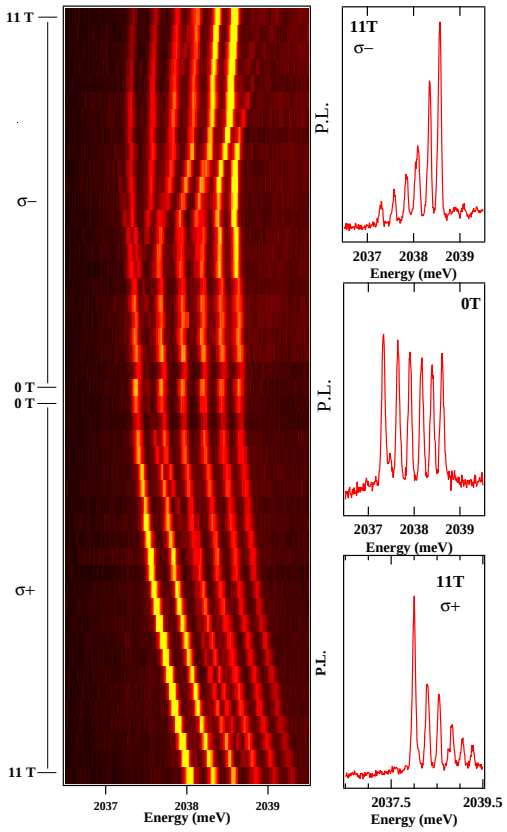

Figure 1.12 Magnetic field dependence of the emission of a Mn-doped QD recorded in $\sigma+$ and $\sigma-$ polarisation. Anticrossing of the bright and dark states appears around 7T in $\sigma-$ polarisation.

exciton. Because of the hh-lh splitting, a similar Mn-hole spin flip scattering is not allowed in a first approximation. The electron-Mn spin flip is enhanced as the corresponding levels of bright and dark excitons are brought into coincidence by the Zeeman effect. An anti-crossing is observed around 7T for five of the bright states in $\sigma-$ polarization (experiment: Fig. 1.12 and theory: Fig. 1.13). It induces a transfer of oscillator strength to the dark states. In agreement with the experimental results, in the calculations the lower energy state in $\sigma-$ polarization ($|+1/2\rangle_e|-3/2\rangle_h|+5/2\rangle_{Mn}$) does not present any anti-crossing. In this spin configuration, both the electron and the Mn atom have maximum spin projection and a spin flip is not possible.

The minimum energy splitting at the anti-crossing, $\sqrt{5}I_{eMn}$, is controlled by the electron-Mn exchange integral. In Fig. 1.12, the splitting measured for the higher energy line in $\sigma-$ polarisation, $\Delta E = 150\mu$eV gives I_{eMn} ≈-65μeV. From the overall splitting measured at zero field ($1.3meV$) and with this value of I_{eMn}, we obtain I_{hMn} ≈150μeV.

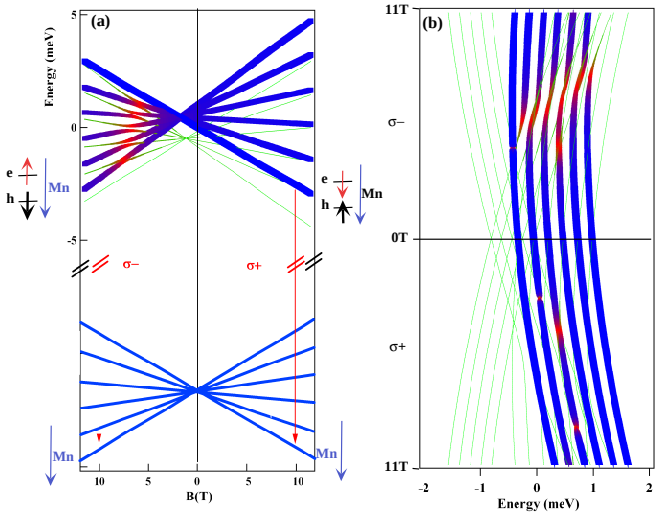

Figure 1.13 (a) Scheme of the energy levels of the initial and final state involved in the optical transitions of a quantum dot containing a Mn atom. (b) Modlisation of the optical transition obtained from the diagonalisation of an effective spin Hamiltonien including the e-h exchange interaction, the exciton-Mn exchange interaction, the Zeeman and the diamagnetic energies. The contribution of the dark states appears in green.

The ratio of the exchange integral, $(3I_{hMn})/I_{eMn}$ ≈-6 for the discussed QD does not directly reflects the ratio of the $sp-d$ exchange constants $\beta/\alpha \approx -4$ measured in bulk CdMnTe alloys [52]. Such deviation likely comes from the difference in the electron-Mn and hole-Mn overlap expected from the difference in the electron and hole confinement length but it could also be due to a change of the exchange parameters induced by the confinement [105].

The spin Hamiltonien (1.23) does not reproduce the observed non uniform zero field splitting between consecutive lines (Fig. 1.11) and some anticrossings under magnetic field (Fig. 1.12). As we will see in the following, a more accurate model has to take into account the full valence band structure and the hh-lh mixing as well as coupling with the QD excited states.

1.2.3 Spin effective Hamiltonian of a Mn doped quantum dot

We will in the following analyze in details with a complete spin effective Hamiltonian the optical spectrum of a singly Mn doped QD taking into account hh and lh and possible shape and strain anisotropy. For generality, we will also include the fine and hyperfine structure of the Mn and see in which condition it could be detected in the optical spectrum. We will then analyze the influence of the QD excited state on the energy spectrum of the ground exciton-Mn complex. In the last part we will discuss the emission of QDs containing two Mn atoms.

For a sufficiently small number of Mn atoms (1 or 2 in this work, including elec-

tronic (S=5/2)) and nuclear (I=5/2) spins) the size of the Hilbert space permits to obtain the spectra from the exact numerical diagonalization of the Hamiltonian of the system. The complete exciton-Mn Hamiltonian consists of five parts [46]:

$$\mathcal{H}_{X-Mn} = \mathcal{H}_{c-Mn} + \mathcal{H}_{mag} + \mathcal{H}_{e-h} + \mathcal{H}_{band} + \mathcal{H}_{Mn} \tag{1.26}$$

$\mathcal{H}_{band}$, $\mathcal{H}_{e-h}$ and $\mathcal{H}_{Mn}$ have been described in the previous section. The carrier-Mn exchange interaction, $\mathcal{H}_{c-Mn}$, describes the coupling of the electron and hole with the Mn spin.

$$\mathcal{H}_{c-Mn} = \mathcal{H}_{e-Mn} + \mathcal{H}_{h-Mn} = I_{eMn}\,\overrightarrow{S}.\overrightarrow{\sigma} + I_{hMn}\,\overrightarrow{S}.\overrightarrow{j} \tag{1.27}$$

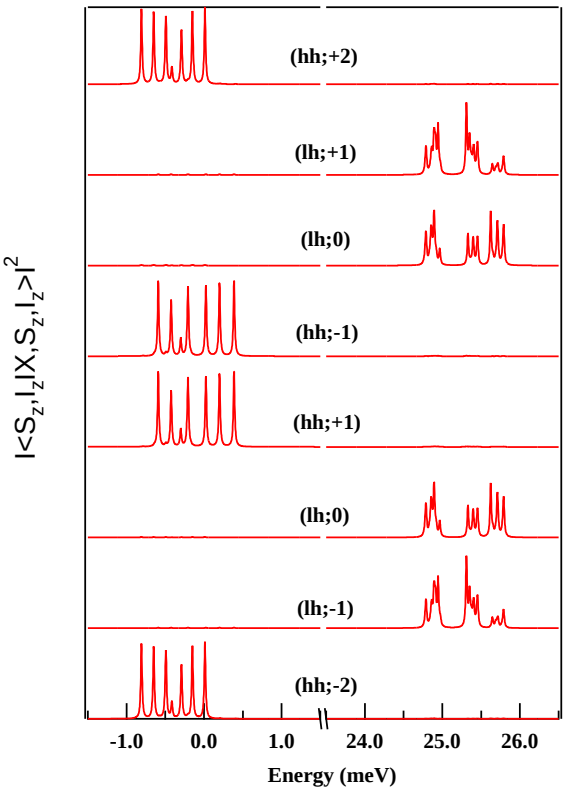

Figure 1.14 Calculated energy levels in a Mn doped quantum dot. The parameters used in the calculation are: $A = 0.7$ μeV, $D_0 = 7$ μeV, $a = 0.32$ μeV, $I_{eh} = -200$ μeV, $I_{eMn} = -30$ μeV, $I_{hMn} = 120$ μeV, Δ_{hh-lh}=25 meV, δ_{xz}=δ_{yz}=0, δ_{xy}=0, $\delta_{xx,yy}$=2.5 meV, $\delta_2 = 50$ μeV, ϕ_2=0, b_x=b_y=b_z=0.

An external magnetic field couples via the standard Zeeman term to both the Mn spin and carriers spins and a diamagnetic shift can also be included:

$$\mathcal{H}_{mag} = g_{Mn}\mu_B \overrightarrow{B}.\overrightarrow{S} + g_e\mu_B \overrightarrow{B}.\overrightarrow{\sigma} + \mu_B(\kappa \overrightarrow{j}.\overrightarrow{B} + q \overrightarrow{j}^3.\overrightarrow{B}) + \gamma B^2 \quad (1.28)$$

Using the Hamiltonian of the excited state $\mathcal{H}_{X-Mn}$ and the Hamiltonian of the ground state $\mathcal{H}_{Mn}$, we can compute the spectrum of a neutral QD containing a Mn atom. They are obtained calculating the matrix elements $|\langle S_z, I_z|X, S_z, Iz\rangle|^2$ where X, S_z and I_z stands for the 8 possible exciton states, the electronic and the nuclear Mn spin respectively.

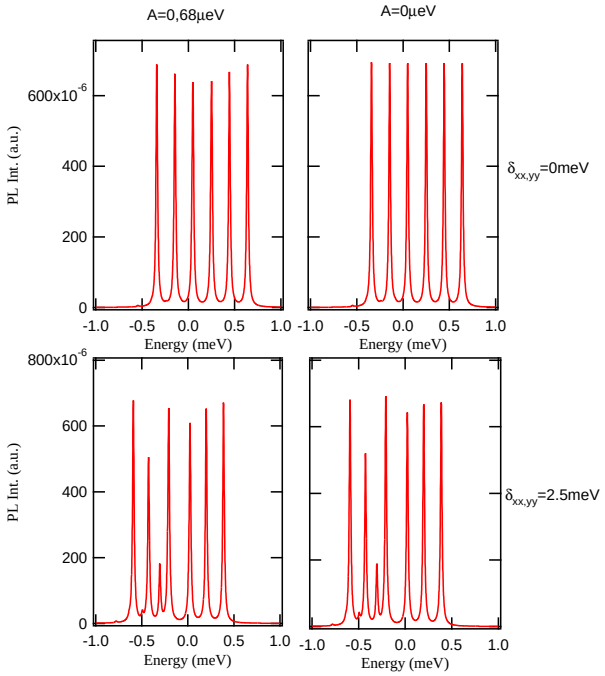

Figure 1.15 Calculated spectrum of the ground state of a Mn doped QD in circular polarisation with (lower panels) and without (upper panels) valence band mixing for A=0.7μeV (left panels) and A=0μeV (right panels). The other parameters are the same as in Fig. 1.14.

An example of calculated spectrum of a Mn doped QD is presented in Fig. 1.14. The parameters used for this calculation are listed in the caption. The appearance of a seventh line in the spectrum of the bright hh levels is characteristic of the presence of hole-Mn spins flips which couple bright and dark excitons. These spin flips are allowed by a mixing with lh produced by an anisotropy in the QD plane ($\delta_{xx,yy} \neq 0$ for instance).

Detail of the calculated optical emission of the bright hh exciton coupled with a Mn spin are presented in Fig. 1.15. A careful analysis reveals a small influence

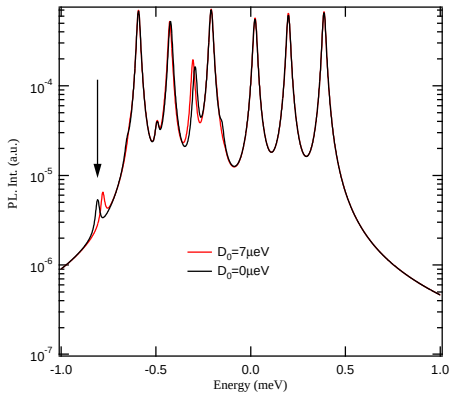

Figure 1.16 Calculated spectrum of the ground state of a Mn doped quantum dot in circular polarisation with D_0=0 and D_0=7μeV. The other parameters are the same as in Fig. 1.14.

of the fine and hyperfine structure of the Mn on the spectrum. In the case of a neutral QD, as the Mn spin S_z is conserved during the optical transition, one expect no signature of $\mathcal{D}_0$ in the optical spectra of the bright excitons. On the other hand, the hyperfine coupling $\mathcal{A}$ mixes the different spin state of the Mn in the ground state (*i.e.* without exciton). This isotropic coupling is partially blocked by the magnetic anisotropy $\mathcal{D}_0$ except for the states S_z=$\pm$1/2 where flip-flop with the nuclear spin are completely allowed. Depending on the relative value of $\mathcal{D}_0$ and $\mathcal{A}$, an influence of the Mn fine and hyperfine structure on the exciton-Mn emission is expected.

This is illustrated in Fig. 1.15. In the absence of valence band mixing, an influence of $\mathcal{A}$ is obtained in the intensity distribution of the calculated spectrum: a decrease of the intensity of the center lines corresponding to S_z=$\pm$1/2 is observed. This apparent decrease of intensity is indeed produced by the slight broadening of the lines as in the ground state of these optical transitions the states $S_z = \pm 1/2$ are mixed and split by the hyperfine coupling.

Such modulation of intensity is also observed in the presence of a significant valence band mixing but in this case, the intensity distribution is mainly controlled by the coupling with lh and the specific influence of $\mathcal{A}$ is difficult to observe experimentally. One way to tune the influence of the hyperfine coupling is to apply a magnetic field in the Faraday configuration. When the Zeeman energy of the Mn dominates the hyperfine energy (typically under B_z=0.5T), a quantization axis along z is restored for the Mn alone. The influence of $\mathcal{A}$ on the emission spectrum vanishes. This tiny effect of the hyperfine interaction has not been observed until now in the spectrum of real QDs dominated by shape or strain anisotropy.

As presented in Fig.1.16, the magnetic anisotropy term $\mathcal{D}_0$ influence the position of the emission of the "dark" exciton states. These dark states are mixed with the bright exciton through an electron-Mn or a hole-Mn flip-flop. Their optical recombination involve a Mn spin flip and is then sensitive to the Mn energy

levels in the final state of the transition. This energy shift, though tiny, should be taken into account for an accurate description of the energy of the dark exciton levels in Mn doped QDs.

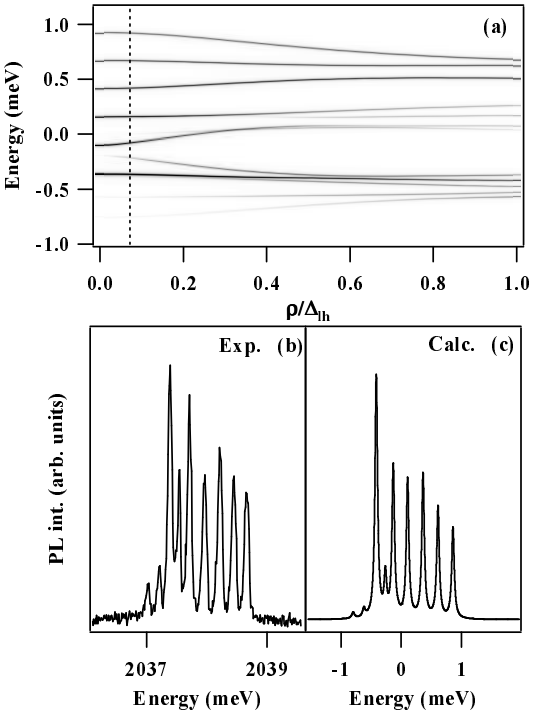

Figure 1.17 (a) Dependence of the exciton-Mn energy spectrum on the strength of the valence band mixing ρ_s/Δ_{lh}. Parameters are chosen to reproduce the features of the QD emission plotted in (b): I_{eMn}=-70 μeV, I_{eh}=-400 μeV, I_{hMn}=170 μeV, Δ_{lh}=30 meV and variable $\rho_s/\Delta_{lh} = 0.07$. The dotted line corresponds to the situation of the QD presented in (b) with $\rho_s/\Delta_{lh} = 0.07$. (c) is the corresponding calculated emission spectra.

1.2.4 Quantum dot symmetry and exciton Mn coupling

Let's now consider in detail the interplay between shape and strain anisotropy in the spectrum of Mn doped QDs. The effect of an increasing valence band mixing on the excitonic emission spectrum of a QD is presented on Fig. 1.17(a). We have seen in the case of non-magnetic QDs that, in first approximation, the only effect of the valence band mixing combined with the short range e-h exchange interaction is to couple bright excitons states together. For magnetic QDs, bright states associated with the same Mn spin projection are thus coupled. This coupling mainly concerns the energy levels associated with Mn spin projections S_z=$\pm$1/2 because they are only slightly split by the exciton-Mn exchange interaction. An

increase of the valence band mixing will thus open a slight gap in the middle of the bright exciton fine structure (around 0.25 meV in Fig. 1.17(a)).

Another gap appears on the low energy side of the structure because of the hole-Mn interaction. As a matter of fact, simultaneous hole-Mn spin flips couples bright and dark states associated with consecutive Mn spin projections. The exciton-Mn exchange interaction induces an overlap of the bright and dark exciton fine structure. Exciton-Mn states coupled by h-Mn spin flips are therefore quite close to each other and an increase of the valence band mixing, that is to say an increase of the h-Mn spin flip efficiency, will open a gap between them. This can be observed on Fig. 1.17(a) around - 0.1 meV. Finally, the overall splitting of the structure decreases as the valence band mixing increases because of the decrease of the weight of the heavy-hole in the exciton ground state.

Such coupling between bright and dark excitons is observed in the spectrum the QD presented in Fig. 1.17(b). In this QD, the valence band mixing is quite weak and the gaps induced by the e-h exchange and the h-Mn exchange can be hardly resolved in the exciton spectrum. Nevertheless, the h-Mn spin flips induced bright-dark coupling is large enough to give non negligible oscillator strengths to the dark states. Three "dark" states are then observed in the emission spectrum. The value ρ_s/Δ_{lh} can be estimated to 0.07. Using, this parameter we can calculate the exciton emission spectrum. The result is plotted on Fig. 1.17(c). The exciton-Mn system is partially thermalized during the exciton lifetime. This results in the increase of the intensity of the lines as their energy decreases. In the calculation we thus consider that the system has relaxed and that it is characterized by an effective spin temperature T_{eff}. In Fig. 1.17(c), $T_{eff} = 15$ K. With this effective temperature, "dark" states appears in the calculated spectrum but their intensity is weaker than in the experiment. Moreover, comparing the intensities of the bright lines in the calculation and in the experiment, we note that we cannot fit the data with an effective temperature smaller than 15K in order to increase the "dark" states intensity. These features show that we should not consider a total thermalization in the exciton-Mn system. As under non-resonant excitation bright and dark excitons are created with the same generation rate, if the spin relaxation is partially blocked, the intensities of the associated transitions can be comparable even though they have different oscillator strengths. These effects of thermalization will be discussed in detail in chapter 2.

We finally consider the neutral exciton fine structure of Mn-doped QDs that present an anisotropic in-plane shape. Fig. 1.18 presents the linear polarization dependence of the emission spectrum of such QD. The experimental spectrum show the main characteristics of a quite strong valence band mixing as detailed in Fig. 1.17(a). The spectrum presents an overall linear polarization rate of about 25% orientated at $\theta_s = 110°$ from the cleaved edge of the sample and dark states appear on the low energy side of the structure. Two gaps can also be observed: One between the two first main lines and the other between the third and the fourth lines. However, if these peculiarities were only due to the combined effect of the valence band mixing and short range e-h exchange, one could expect the third and the fourth lines to be polarized parallel and perpendicular to the strain

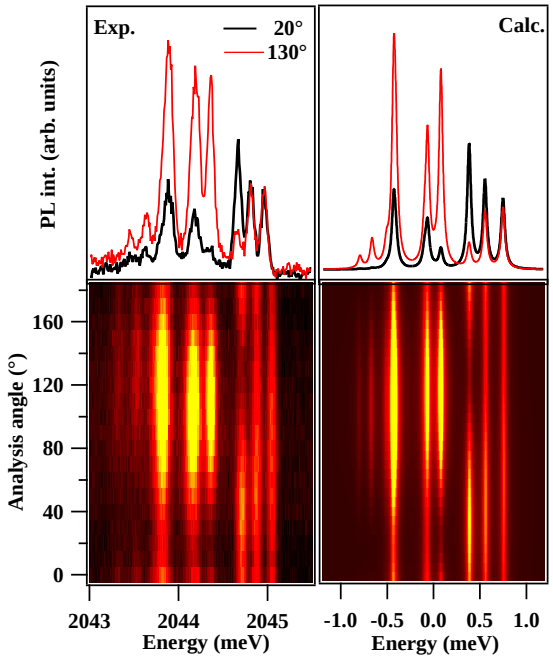

Figure 1.18 Experimental and calculated polarization resolved photoluminescence of an anisotropic quantum dot. The intensity maps present the dependence of the emission on the analyser angle. The emission spectrum are presented for orthogonal linear analyzer directions (red and black curves).

direction (110°). It is not the case and surprisingly, the emission spectrum also presents non-orthogonal linear polarization directions.

These polarization directions are the signature of a competition between a valence band mixing and long range electron-hole exchange interaction. The calculation of the emission spectrum (right panels of Fig. 1.18) gives a good agreement with the experiment using the following parameters: I_{eMn} = -60μeV, I_{hMn} = 135μeV, I_{eh}=-400μeV, δ_2 = 450μeV, Δ_{lh} = 30meV, ρ_s/Δ_{lh} = 0.25 and T_{eff} = 20K. The strain direction and the dot shape direction must be roughly perpendicular (80°) to fit the experiment.

In anisotropic QDs, the interplay between the electron-hole and exciton-Mn exchange interactions is confirmed by magneto-optical measurements (Fig. 1.19). The typical Zeeman splitting of the six lines is clearly observed in the data at all fields, with a strong intensity gradient at the highest fields resulting from a rather strong Mn spin polarization. For this clearly anisotropic dot, the central gap in the emission structure is maintained in both circular polarizations, with a small quadratic diamagnetic energy shift. This behavior is explained as follows: The dot anisotropy leads to successive anticrossings of the ± 1 bright exciton states associated with given Mn spin projections ($-1/2$, $-3/2$ and $-5/2$) as a function

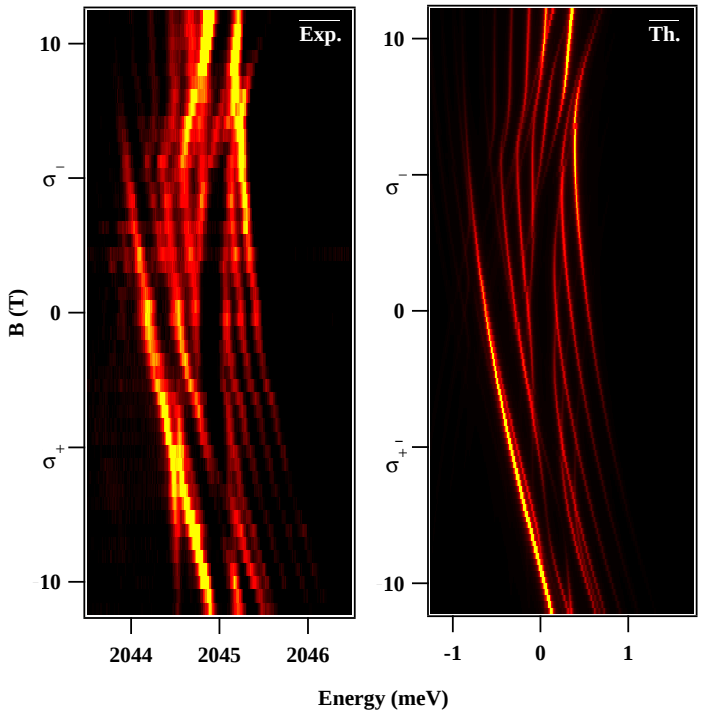

Figure 1.19 (left) Intensity map of magnetic field dependence of the emission spectrum of anisotropic Mn-doped QD, for circular polarization $\sigma+$ and $\sigma-$. (right) Optical transitions obtained from the diagonalization of the spin effective Hamiltonian with the parameters: $I_{eh} = -400$ μeV, $I_{eMn} = -60$ μeV, $I_{hMn} = 135$ μeV, $\delta_2 = 450$ μeV, $\rho_s/\Delta_{lh} = 0.25$, $g_e = -0.1$, $\kappa = 0.3$, $\gamma = 2.4$ μeVT^{-2}, T$_{eff}$ = 15K, $\theta_s = 110°$, $\phi_2 - \theta_s = 80°$.

of magnetic field : As B increases, transitions associated with the $J_z = +1$ exciton shift up in energy whereas the $J_z = -1$ transitions shift down. The anisotropic part of the electron-hole exchange interaction mixes successively the $J_z = \pm 1$ exciton states associated with $S_z = -1/2$, then with $S_z = -3/2$ and finally with $S_z = -5/2$ at successively higher B. For the QD presented in Fig. 1.19, these anticrossings are observed successively at 2.5T, 7T and 11T.

To fully understand the rich magnetic behavior of these anisotropic QDs, we calculated the optical transitions under magnetic field by diagonalizing the complete Hamiltonian of the electron-hole-Mn system (including the exchange, Zeeman and diamagnetism Hamiltonians). Calculated transitions are presented in Fig. 1.19. The fitted Landé factors of the electron ($g_e = -0.1$), the hole ($g_h = 0.3$) and the Mn atom ($g_{Mn} = 2.0$), the splitting between $J_z = \pm 1$ and $J_z = \pm 2$ excitons (= 1meV) and the diamagnetic factor ($\gamma = 2.4 \mu$eV.T^{-2}) agree well with previous work [52, 9]. Parameters δ_2, I_{eMn} and I_{hMn} were adjusted to fit the zero field data, as explained earlier.

Comparison between calculation and data explains most of the details of the magneto-optic properties. In particular, around 7T, the central gap is perturbed in both circular polarizations. In $\sigma-$, this is due to anticrossings induced by the mixing of $\mid 1/2, -3/2, S_z >$ states and $\mid -1/2, -3/2, S_z + 1 >$ states by the electron-Mn exchange, i.e. corresponding to simultaneous spin-flips of electron and Mn spin.

To summarize these geometrical effects, it comes out from this study that an anisotropic strain distribution in the growth plane and a QD shape anisotropy induce a valence band mixing which strongly modifies the emission spectra of a single Mn doped QDs. The main observed effects are: (i) the appearance of anti-crossings related to possible Mn-hole spin-flips, (ii) the separation of the six lines structures into two sets of lines partially linearly polarized, and (iii) the variation of the linear polarization directions which are no longer perpendicular for the exciton fine structure of a given QD. The last feature clearly evidences the competition between two types of anisotropy, one coming from the confinement potential (shape anisotropy) and one coming from the local strain distribution into the dot.

1.2.5 Influence of the quantum dot excited states on the exciton-Mn coupling.

One important characteristic of the experimental spectra is not yet described by the previous spin effective Hamiltonian: the irregular spacing between the six emission lines. To understand this energy distribution one has to consider the influence of the scattering of carrier to an excited state of the QD induced by the carrier-Mn coupling acting as a perturbation on the exciton wave function. A detail description of this effect requires a model for the confinement potential and to calculate the ground and excited state wave function before considering their perturbation by the exchange coupling with the Mn. This has been recently done by Trojnar *et al.* considering a parabolic confinement potential [142].

To understand qualitatively this effect, let us consider the case of a hh coupled to one Mn. The hole-Mn would be the dominant contribution as in CdTe QDs most of the exciton Mn interaction energy is coming from the hole-Mn Hamiltonian and the energy splitting between the confined hole states is expected to be much weaker than for the electrons.

To deduce the general form of the perturbation, we assume the hole can occupy two spin degenerated levels, a (ground state) and b (excited state). b could be for instance a p or d state confined in the QD. The energy difference between a and b, δ, is assumed to be bigger than the exchange energy scale with the Mn, J. The eigenstates of the h-Mn Hamiltonian are the product of the fermion state (hole in our case) and the spin states of the Mn.

$$|\Psi\rangle = |\varphi\rangle_{fer} \otimes |S_z\rangle \tag{1.29}$$

where $|\varphi\rangle_{fer}$ are all the possible state of the fermion in the two levels. We define

Label	a↑a↓ b↑b↓	Energy	M_z
1	1 0 0 0	$0 + j_{aa}S_z$	+3/2
2	0 1 0 0	$0 - j_{aa}S_z$	-3/2
3	0 0 1 0	$\delta + j_{bb}S_z$	+3/2
4	0 0 0 1	$\delta - j_{bb}S_z$	-3/2

Table 1.2 *Possible states and energy of one fermion in two levels. First column: label for each fermion state in the two levels. Second column: occupation of the single particule levels a↑a↓ b↑b↓. Third column: single particule energy associated to the states including the diagonal exchange interaction. Last column: fermion spin along the z axis, M_z.*

$$j_{aa} = J|\varphi_a(\overrightarrow{r_I})|^2, j_{bb} = J|\varphi_b(\overrightarrow{r_I})|^2, j_{ab} = J\varphi_a^*(\overrightarrow{r_I})\varphi_b(\overrightarrow{r_I}) \tag{1.30}$$

where J is the exchange coupling constant of the material (either α for electrons or β for holes).

In this simplified picture where we consider only one excited state, each of the 4 fermion states (see table 1.2) can combine with the 6 Mn spin states, S_z. Therefore, there are as much as 6 times 4 states. In the case of a heavy hole we can ignore, to first order, all the spin-flip terms in the Hamiltonian. In that case, the 24 by 24 Hamiltonian can be written as 6 blocks of 4 by 4. Each block has a well defined S_z.

In a multi-level system, the general form of the hole-Mn Hamiltonian reads [26]:

$$\mathcal{H}_{h-Mn} = \sum_{i,j} \frac{3}{2} j_{ij}(\overrightarrow{r_I})[h_{i,\uparrow}^\dagger h_{j,\uparrow} - h_{i,\downarrow}^\dagger h_{j,\downarrow}].S_z \tag{1.31}$$

where $h_{i,\uparrow}^\dagger$ ($h_{i,\uparrow}$) is the creation (annihilation) operator of a spin up hole in the state i. $h_{i,\uparrow}^\dagger h_{i,\uparrow}$ is then the number of spin up hole in state i (either 0 or 1). This Hamiltonian describes the scattering of the hole by the Mn ion considered as a perturbation while conserving the hole spin, $j_{ij}(\overrightarrow{r_I})$ being the exchange matrix element leading to scattering of a hole from state i to state j by the Mn ion at position $\overrightarrow{r_I}$. This scattering process depends on the spin state of the Mn, S_z.

In the two levels models (a and b), each 4 by 4 blocks of the total Hamiltonian can then be written as the sum of two terms, the intra-level part and the inter-level part. The intra-level part comes both from the non-magnetic terms of the Hamiltonian (energy δ in our simple model) and the magnetic terms proportional to either j_{aa} or j_{bb}:

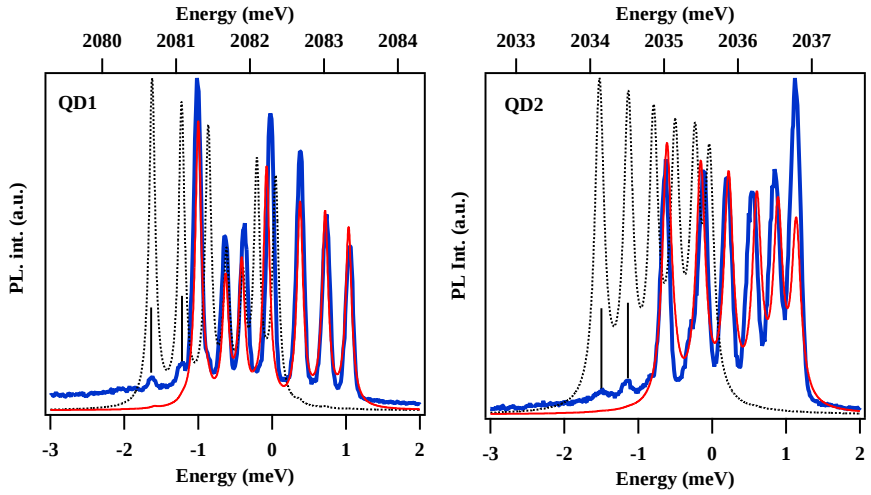

Figure 1.20 Comparaison of theoretical and experimental spectra for two QDs. Blue line: experiment circularly polarized spectrum. Dotted black line: calculated dark exciton (hh,-2). Red line: calculated bright exciton (hh,+1). The parameters used in the calculation are for QD1: $A = 0.7$ μeV, $D_0 = 7$ μeV, $a = 0.32$ μeV, $I_{eh} = -550$ μeV, $I_{eMn} = -70$ μeV, $I_{hMn} = 245$ μeV, Δ_{hh-lh}=25 meV, δ_{xz}=δ_{yz}=0, δ_{xy}=0, $\delta_{xx,yy}$=2.5 meV, $\delta_2 = 0$ μeV, ϕ_2=0, b_x=b_y=b_z=0, $\eta = 20\mu$eV and for QD2: $A = 0.7$ μeV, $D_0 = 7$ μeV, $a = 0.32$ μeV, $I_{eh} = -700$ μeV, $I_{eMn} = -50$ μeV, $I_{hMn} = 215$ μeV, Δ_{hh-lh}=25 meV, δ_{xz}=δ_{yz}=0, δ_{xy}=0, $\delta_{xx,yy}$=1.5 meV, $\delta_2 = 0$ μeV, ϕ_2=0, b_x=b_y=b_z=0, $\eta = 25\mu$eV. For both QDs, a thermalization among the exciton-Mn energy levels with a temperature of T=40K is used. The intensity distribution of the experimental spectrum of QD2 is affected by a spin selectivity in the absorption of the QD excited state.

$$\mathcal{H}_0(S_z) = \frac{3}{2}\begin{pmatrix} j_{aa}S_z & 0 & 0 & 0 \\ 0 & -j_{aa}S_z & 0 & 0 \\ 0 & 0 & \delta + j_{bb}S_z & 0 \\ 0 & 0 & 0 & \delta - j_{bb}S_z \end{pmatrix} \tag{1.32}$$

The inter-level Hamiltonian contains the terms by which a hole from level a scatters to level b conserving the spin, since we ignore spin-flip terms:

$$\mathcal{V}(S_z) = \frac{3}{2}j_{ab}S_z \begin{pmatrix} 0 & 0 & 1 & 0 \\ 0 & 0 & 0 & 1 \\ 1 & 0 & 0 & 0 \\ 0 & 1 & 0 & 0 \end{pmatrix} \tag{1.33}$$

It is possible to obtain simple analytical expressions from these Hamiltonian doing non-degenerated perturbation theory. The unperturbed Hamiltonian of each of the 4 by 4 blocks is $\mathcal{H}_0(S_z)$ and the perturbation is $\mathcal{V}(S_z)$. Through this per-

turbation, this interaction with the excited state renormalizes the energies of the ground state exciton-Mn complex. The standard expressions for the perturbed energy levels reads:

$$\delta E_i(S_z) = \sum_j \frac{|\langle i|\mathcal{V}(S_z)|j\rangle|^2}{E_i^0(Sz) - E_j^0(S_z)} \tag{1.34}$$

In our two levels case we obtain:

$$\delta E_1(S_z) = (\frac{3}{2} j_{ab})^2 S_z^2 \frac{1}{3/2 j_{aa} S_z - (\delta + 3/2 j_{aa} S_z)} \tag{1.35}$$

therefore, to lower order in S_z, we can write:

$$\delta E_1(S_z) = -\frac{9/4|j_{ab}|^2}{\delta} S_z^2 \tag{1.36}$$

The origin of (1.36) are the virtual transitions of the holes from the low energy level a to the higher energy level b.

This simplified model shows that, in first order, the energy correction coming from scattering to excited states can be described in a spin effective Hamiltonian by an additional term $-\eta S_z^2$ with $\eta > 0$. The zero field spectrum of two CdTe Mn doped QDs obtained with the total spin effective Hamiltonian including the $-\eta S_z^2$ correction are compared in Fig. 1.20 with experimental spectrum. A very good agreement is obtained, especially for the irregular spacing between the bright exciton lines which is a direct consequence of the Mn induced scattering to excited states.

1.2.6 Two Mn spins (or more) in a quantum dot.

Now that we have a detail understanding of the energy levels in a singly Mn-doped QD, let us consider the case of two Mn atoms localized in the same QD. As we will see in chapter 3, such system could be interesting for the design of device allowing controlling optically the interaction between localized spins.

The spin structure of a 2 Mn QD is illustrated by the detailed spectrum of an exciton presented in Fig. 1.21. The highest and lowest PL lines in the spectrum of the exciton correspond to the total spin projection of the 2 Mn $M_z = S_{z,1} + S_{z,2} = \pm 5$ coupled to the bright excitons (± 1). The next lines correspond to the situation where the less coupled Mn spin has flipped its spin projection component by one unit ($M_z = \pm 4$). The emission structure becomes more complex as M_z decreases (towards the center of the emission structure) because different configurations of the 2 Mn spins interacting with the exciton spin are very close in energy

This spectrum is compared in Fig. 1.21 to a model based on an effective spin Hamiltonian. The spin interacting part of the Hamiltonian of a QD describing the coupling of the electron spin $\vec{\sigma}$, the hole spin $\vec{j}$, and two Mn spins $\vec{S}_{1,2}$ reads:

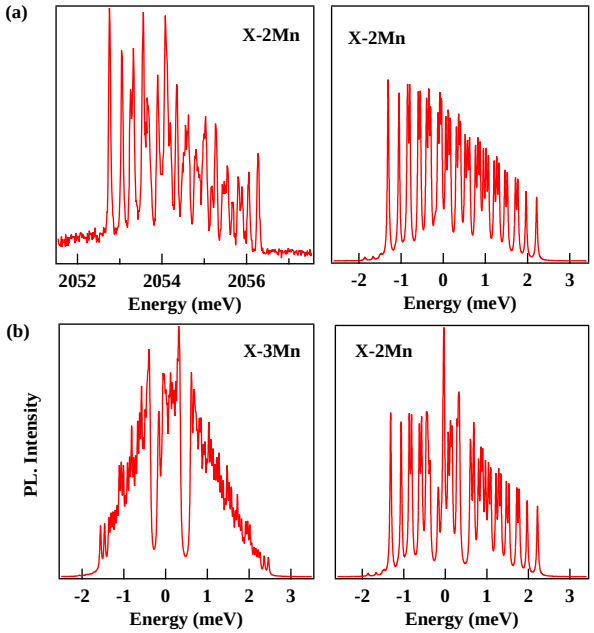

Figure 1.21 (a) Experimental (left panel) and calculated (right panels) spectra of an exciton exchanged coupled to 2 Mn in a QD. See text for details of the calculations performed with $I_{e,1}$=-55 μeV, $I_{h,1}$=150 μeV, $I_{e,2}$=-90 μeV, $I_{h,2}$=270 μeV, $I_{eh} = -600$ μeV, an effective valence band mixing parameter ρ_s/Δ_{lh}=0.025 and $\theta_s = 0$. A thermalization (effective temperature T=40K) is included for X-2Mn. A broadening of the lines of 40 μeV is included in the calculated spectra. (b) presents the calculated spectra of X coupled to 2 Mn with ρ_s/Δ_{lh}=0.1 (right panel) and when a third Mn atom with $I_{e,3}$=-20 μeV and $I_{h,3}$=60 μeV is introduced in the QD (left panel).

$$\mathcal{H} = \vec{\sigma} \cdot \left(I_{eMn,1}\vec{S_1} + I_{eMn,2}\vec{S_2} \right) + \vec{\tilde{j}} \cdot \left(I_{hMn,1}\vec{S_1} + I_{hMn,2}\vec{S_2} \right) + I_{eh}\vec{\sigma}.\vec{\tilde{j}} + I_{12}\vec{S_1}.\vec{S_2} \tag{1.37}$$

where the hole pseudo-spin operators $\tilde{j}_+$, $\tilde{j}_-$ and $\tilde{j}_z$, represented in the basis of the two low energy hh states, are given in equations (1.12), (1.13) and (1.14). $I_{hMn,i}$ ($I_{eMn,i}$) is the exchange integral of the hole (electron) with the Mn atom i, I_{eh} the electron-hole exchange interaction and I_{12} the short ranged anti-ferromagnetic Mn-Mn interaction. This latter coupling is only comparable with the carrier-Mn energy when the two Mn are positioned closed to each other ($I_{Mn,Mn}$=0.5meV for neighboring atoms [52, 126]): it is neglected in the following because the carrier-Mn interaction is different for the two atoms indicating that they are far apart in the QD.

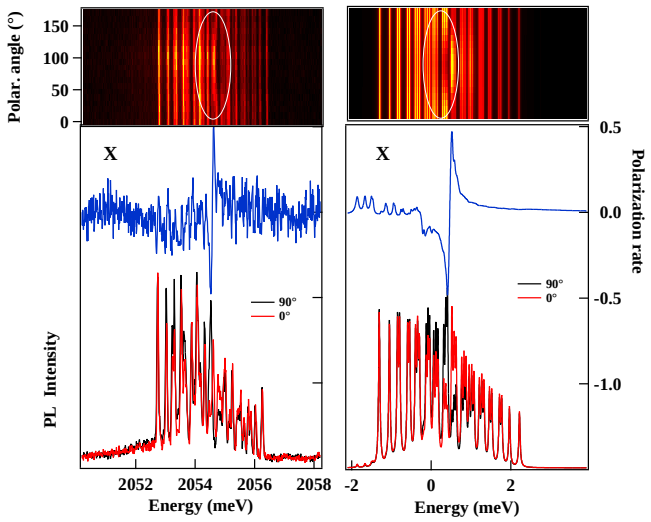

Figure 1.22 Left panel: Experimental linear polarization dependence of the PL intensity of X exchanged coupled to 2 Mn atoms. The polarization angle is relative to the [110] direction. The PL are presented for orthogonal linear analyzer directions (red and black curves) and the linear polarization rate is presented in blue. Right panel: Calculated linear polarization dependence of the PL intensity of X with the same parameters as the one given in Fig.1.21.

The main feature (*i.e.* overall splitting, position of PL lines, linear polarization) of the experimental spectra can be well reproduced by this spin effective model. The QD presented here corresponds to a situation where the coupling with one Mn is about twice the coupling with the other. This can be deduced from a qualitative analysis of the structure of the low (or high) energy side of the PL spectrum of the exciton. Starting from the low energy line ($M_z = \pm 5$), the second PL line, 280 μeV above, corresponds to a spin-flip of the less coupled Mn spin (S_1) by one unit ($M_z = \pm 4$). Then a group of two lines, very close in energy, are observed at slightly higher energy. The line which sits 560 μeV above the low energy states corresponds to $M_z = \pm 3$ where S_1 has flip by two units. It is very close in energy to the states $M_z = \pm 4$ corresponding to a spin flip by one unit of the Mn spin which is the most coupled to the exciton (S_2), 500 μeV above the low energy state.

From this analysis of the splitting of the low energy lines, we can estimate in the pure hh approximation (*i.e.* ρ_s/Δ_{lh}=0) the exchange energy of the bright exciton with each Mn spin S_1 and S_2: E_{S_1}=1/2($3I_{h,1} - I_{e,1}$) $\approx$ 280μeV and E_{S_2}=1/2($3I_{h,2} - I_{e,2}$) $\approx$ 500μeV. However, these values do not gives an exact measurement of the exchange energies. Indeed, these splitting are slightly perturbed by the influence of the scattering of carriers to an excited state of the QD by the carrier-Mn coupling acting as a perturbation on the exciton wave function [142]. Such perturbation is also present in the 2 Mn case.

From these PL measurements at zero magnetic field, we cannot deduce the ratio I_h/I_e and the electron-hole exchange interaction energy I_{eh}. In the model we chose typical values for I_h/I_e and I_{eh} measured in singly Mn doped QDs [11, 92]. All the parameters used in the calculation are listed in the caption of Fig. 1.21. To reproduce the overall splitting of the exciton (given in the hh approximation by $5(1/2(3I_{h,1}-I_{e,1})+1/2(3I_{h,2}-I_{e,2}))$) and match the splitting of the lines observed on both the low and high energy side of the exciton spectrum, we use $I_{e,1}$=-50 μeV, $I_{h,1}$=150 μeV, $I_{e,2}$=-90 μeV and $I_{h,2}$=270 μeV. A good agreement is obtained with the energy distribution of the lines observed in the experimental spectra confirming the presence of 2 Mn atoms exchanged coupled with the exciton. If a third Mn atom interacts with the exciton, 6×36 emission lines are expected. As the typical PL linewidth in CdTe/ZnTe QDs is larger than 50 μeV, the detail of the emission structure of such QD cannot be resolved. A broad emission line is obtained (calculated spectra presented in Fig. 1.21(b)) and the 3 Mn case can be hardly distinguished from a QD containing a larger number of magnetic atoms.

To reproduce the intensity distribution in the PL spectra, a thermalization on the X-2Mn levels with an effective temperature T=40K is included in the model. This effective temperature not far from the lattice temperature suggests a carrier-Mn spin relaxation time longer but close to the lifetime of the exciton (let's note that an infinite temperature would corresponds to an absence of spin relaxation and an effective temperature equal to the temperature of the lattice would mean a spin relaxation much shorter than the exciton lifetime).

Figure 1.22 reveals the linear polarization rate which is observed in the center of the X-2Mn PL spectra. This polarization can be explained by the presence of a valence band mixing. Like in 1 Mn doped QDs, this mixing, combined with the short range electron-hole exchange interaction, couples the bright excitons +1 and -1 associated with the same Mn spins configurations and creates linearly polarized eigenstates. This mechanism is more efficient in the center of the X-2Mn PL structure where M_z is smaller and the +1 and -1 exciton close in energy. The linear polarization rate is well reproduced by the spin effective model (Fig. 1.22 (right panel)) for X-2Mn if a weak effective valence band mixing ρ_s/Δ_{lh}=0.025 is introduced. For large valence band mixing (with typically ρ_s/Δ_{lh} >0.1, which is often the case in CdTe/ZnTe QDs), the valence band mixing also permit direct coupling between bright and dark excitons through a hole-Mn spin flip. The model shows (Fig. 1.21(b)) that in the 2 Mn case, such valence band mixing perturbs the low energy side of the exciton emission spectrum. Additional PL lines mixed with the bright exciton levels and energy gaps appear giving rise to a more complex emission structure difficult to accurately compare with experiments.

1.3 Carrier controlled magnetism of individual Mn atoms.

We will discuss the influence of confined carriers on the magnetic properties of the Mn atom. After a analysis of the emission of Mn-doped QDs in a transverse magnetic field giving information on the anisotropy of the hole-Mn interaction,

we will consider the effect on the Mn spin splitting of progressively adding carriers in the QD.

1.3.1 Magnetic anisotropy of a Mn doped quantum dot

The effects of hole spin anisotropy on X-Mn coupling have been considered in collective phenomena such as the formation of magnetic polaron involving individual carriers and a large number of magnetic atoms [37, 133]. The observation of the spin state of a single Mn atom interacting with a single exciton in a transverse magnetic field allowed to monitor the orientation of the Mn spin in the exchange field of the hole. This progressive orientation is responsible (i) for the decrease of the overall splitting of the X-Mn structure and (ii) for the appearance of optical recombination occurring with multiple spin flips within the Zeeman split ground state of the Mn. This transverse magnetic field dependence is well modeled by the evolution of the stationary states of a single Mn spin in the exchange field of a heavy hole exciton.

The anisotropy of the exchange interaction in a Mn-doped QD is directly revealed when comparing the magnetic field dependence of the emission in Faraday and Voigt configurations. These are presented in Fig. 1.23(a) and (b). Under a longitudinal magnetic field ($B_{ext} \parallel z$), the quantization axis along the growth direction is conserved (see Fig. 1.23(c)). The Mn spin projection is conserved during the optical transition and there is no influence of the Mn Zeeman energy on the emission spectrum. Only the exciton Zeeman splitting is observed for each of the six zero field lines leading to the typical magnetic dependence observed in Fig. 1.23(b).

The magnetic field dependence in Voigt configuration (Fig. 1.23(a)) is totally different, revealing the anisotropy of the magneto-optic response of the system. When increasing the transverse magnetic field ($B_{ext} \parallel x$), each of the six lines splits in a large fan. Many lines appear, crossing and then joining in different sets. Five sets can clearly be observed: a central one that progressively takes all the intensity and four replicas which linearly shift with B_{ext}. The intensity of the replicas is very weak compared to the central line and decreases with the increase of B_{ext}. The energy spacing between these sets corresponds to an integer number n of the Zeeman energy of the Mn atom ($g_{Mn}\mu_B B_{ext}$). The linear shift of the replicas is well reproduced with a Mn g-factor g_{Mn}=2.0 (left inset of Fig. 1.24). At high transverse field, an additional emission line (X_d) appears about 0.7 meV below the central set (Fig. 1.24). Its intensity increases with increasing the magnetic field and its energy follows the central set. Finally, the overall splitting of each line set decreases progressively when increasing B_{ext}. This effect is particularly clear for the central group of emission lines.

This complex magneto-optic behavior can be qualitatively explained by considering the precession motion of a single Mn spin in external and exchange fields. Let us consider the demonstrative extreme case of a pure hh exciton interacting with the Mn spin. It is convenient to introduce the two effective exchange fields induced by the electron ($B^e_{ex,Mn} = I_e\sigma/g_{Mn}\mu_B$) and the hole

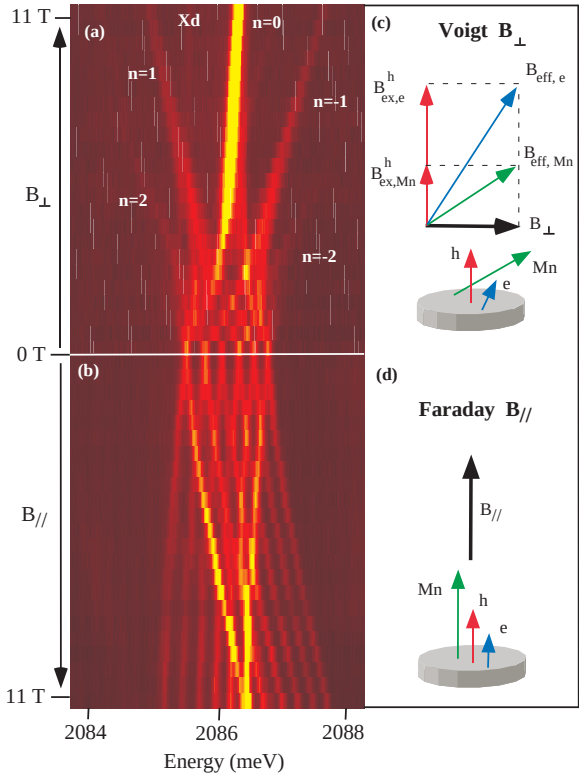

Figure 1.23 (a) and (b) are contour plots presenting the magnetic field dependence of a Mn-doped quantum dot emission. ((a) Voigt configuration, (b) Faraday configuration) (yellow or light gray: high intensity; red or dark gray: low intensity). (c) and (d) are schemes of the spin orientations of the electron (blue), the hole (red) and the Mn atom (green) in Voigt and in Faraday configuration respectively.

($B^h_{ex,Mn} = I_h j / g_{Mn}\mu_B$). In this framework, the spin effective Hamiltonian can be rewritten as $g_{Mn}\mu_B((B^e_{ex,Mn} + B^h_{ex,Mn} + B_{ext}).S)$ where we can define a resulting effective magnetic field acting on the Mn spin $B_{eff} = B^e_{ex,Mn} + B^h_{ex,Mn} + B_{ext}$. Typical values of these exchange fields for the studied QDs are $B^e_{ex,Mn} \approx 0.3T$ and $B^h_{ex,Mn} \approx 1.8T$.

Such exchange fields can also be defined to describe the electron behavior. The e-Mn and the e-h exchange interactions are equivalent to effective magnetic fields $B^{Mn}_{ex,e} \simeq 3$T and $B^h_{ex,e} \simeq 11$T respectively. The e-Mn exchange interaction is small compared to the other exchange energies and we can neglect its influence on the spin orientation of the particles (electron and Mn). In this way, we can easily define the total effective magnetic fields for the electron and for the Mn spin (see Fig. 1.23(c))). Whereas the hh spin is blocked along the growth axis, the electron and the Mn spins rotate about **y** when an external in-plane magnetic field B_{ext} is applied along the **x** axis.

The orientation of the Mn spin is the key point in the understanding of the

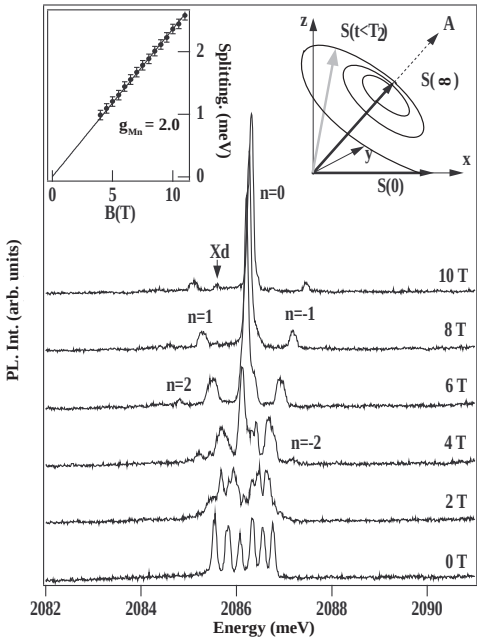

Figure 1.24 PL spectra under magnetic field in Voigt geometry. The left inset presents the magnetic field dependence of the energy splitting between the emission replicas n=1 and n=-1. This linear evolution corresponds to a Mn g-factor $g_{Mn} = 2.0$. The right inset is an illustration the precession motion of S in $B_{eff} = B_{ext} + B^h_{ex,Mn}$.

Voigt magneto-optic behavior. Under an external magnetic field in Voigt geometry ($B_{ext} \parallel x$), the Mn spin is oriented along **x**. After the creation of a confined exciton, the Mn spin is rotated away from the **x** axis by the strong exchange field of the hole $B^h_{ex,Mn} \parallel z$ and begins to precess with Larmor frequency around the resulting effective field $B_{eff} = B_{ext} + B^h_{ex,Mn}$ (right inset of Fig. 1.24) [152]. The component of $S(t)$ transversal to the field B_{eff} relaxes within the time T_2 which corresponds to the dephasing time of the coherent precession of the magnetic ion spin. The X-Mn complex will then further relax its energy within the time T_1. Under non-resonant excitation, because of the spin-spin coupling with the created free carriers, T_1 is found to be shorter than the exciton lifetime τ_r [13]. After T_1, the X-Mn complex reaches its stationary state with the Mn spin directed along the effective field B_{eff}. When the exciton recombines, after a delay τ, the projection of the Mn spin on B_{ext}, $S_x(\tau)$, differs from the initial value $S_x(0) = S(0)$ [152]. The energy of the emitted light in the recombination process is modified by the energy spent (or win) to reorient the Mn spin, which is an integer number n of energy steps of a single spin flip. These spin flips are responsible of the replicas observed in the luminescence in Voigt geometry.

The probability of these spin-flips depends on the change in the quantization axis direction during the recombination process. When an exciton is present in

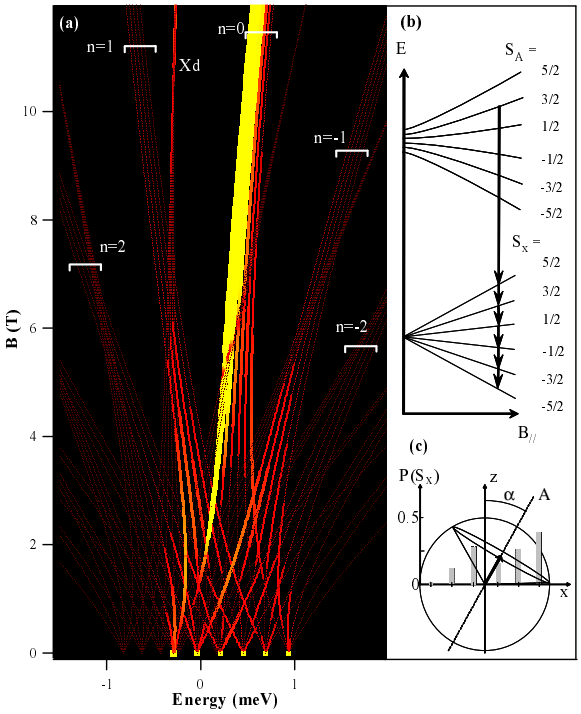

Figure 1.25 (a) Simulation of the magnetic field dependence of a quantum dot emission in Voigt configuration. Under high field, several sets of lines are observed, spaced by the Zeeman energy of the Mn atom. (b) Energy level diagram of the Mn-doped quantum dot in a transverse magnetic field. The quantization axis in the initial state (A) differs from the quantization axis in the ground state (x). (c) Illustration of the rotation of a spin 5/2 with a projection S_A=3/2 by an angle α from an axis A to the x axis.

the QD we can define an effective quantization axis for the Mn spin, called A axis, orientated along the sum of external and exchange fields. During the recombination, the Mn spin has to pass from an eigenstate of $\mathbf{S}_A$ to an eigenstates of $\mathbf{S}_x$. This corresponds to the projection of a spin 5/2 (Fig. 1.25(c)). The probability of transition from a given spin state along the A axis, noted S_A, to the S_x state is given by the spin 5/2 rotation matrix [154]. Every excitonic state associated with a given S_A Mn spin can recombine on any of the S_x final Mn spin states, excepted when the two quantization axes are identical. Considering the energy level diagram presented in Fig. 1.25(b), one notes that now the Mn Zeeman splitting influences the emission spectrum: Six optical transitions take place without any influence of the Mn Zeeman energy (conservation of the Mn spin projection), forming the $n = 0$ set; five with a $g_{Mn}\mu_B B_{ext}$ shift (and five with $-g_{Mn}\mu_B B_{ext}$) forming $n = \pm 1$ sets; four with a $2g_{Mn}\mu_B B_{ext}$ shift ...*etc.* Under high transverse magnetic field ($B_{ext} \gg B^h_{ex,Mn}$), the initial and final quantization axes merge, the spin blockade is restored and only the transitions in which the Mn spin projection

is conserved become possible. As observed in the experimental data, the replicas disappears.

The rotation of the Mn spin in the fixed exchange field of the hole progressively cancel the h-Mn exchange energy. Under high transverse magnetic field, electron and Mn spins are both aligned with the **x** axis and only the e-Mn exchange remains. This orientation of the Mn spin explains the decrease of the X-Mn splitting clearly observed in the central set of emission lines. Moreover, as the electron spin rotates and tends to be aligned with the **x** axis, radiative and non-radiative excitons can no longer be defined. As in non-magnetic QDs, under transverse magnetic field, *dark* exciton states (noted X_d in Fig. 1.24) progressively take some oscillator strength and appear on the low energy side of the bright exciton structure.

A more quantitative model of the Voigt magneto-optic response can be performed with Hamiltonian (1.23). As the optical recombination occurs after a stationary state of the X-Mn system has been reached, a simulation of the emission structure can be obtained by diagonalizing the Hamiltonian of the X-Mn system in the subspace of a pure hh exciton. The obtained optical transitions are presented in Fig. 1.25(a). The e-Mn ($I_{eMn} = -50\mu$eV) and the h-Mn ($I_{hMn} = 140\mu$eV) exchange interactions are extracted from the magneto-optic behavior in Faraday configuration. The e-h exchange integral $I_{eh} = -460\mu$eV (corresponding to $\delta_0 = 700\mu$eV directly observed under transverse magnetic field). For the magnetic field dependence we choose pure isotropic electron ($g_e = -0.25$) and Mn ($g_{Mn} = 2.0$) g-factors. The hole g-factor is completely anisotropic with $g_h^z = -0.15$ and $g_h^x = g_h^y = 0$. A diamagnetic factor $\gamma = 1.45\mu\text{eV/T}^2$ is also introduced. The initial and final eigenstates are calculated in the $\mathbf{S}_z$ basis. In order to obtain each transition intensity, we calculated the projection of the bright exciton part of each eigenstate of the X-Mn system on the final state (Mn in a transverse field). A thermal distribution in the excited states is also taken into account with an effective temperature of T=30K. There is a good agreement between the experimental data and this simple model. The main characteristics are well reproduced, namely the different sets of lines, their intensity evolution, the number of line within each set and the appearance of the *dark* states at high magnetic fields.

These experiments and modeling show that in the hh approximation or in the limit of weak valence band mixing, the injection of a single exciton (or a hole) in a QD doped with a single magnetic atom acts as a pulse of magnetic field along the growth axis. This pulsed exchange field could be used to control the dynamics of a single magnetic atom embedded in a QD.

1.3.2 Carriers induced spin splitting of a single Mn atom.

As a first step in the study of the influence of the number of carriers on the magnetic properties of the Mn atom, we will compare the fine structure of the exciton and biexciton in a single Mn-doped QD. Figure 1.26 shows the emission spectra of one of these Mn-doped QD for various excitation densities. At low

excitation, the spectrum is dominated by the six line fine structure of X-Mn. The three additional lines, observed at low excitation intensity in the low energy side of the emission structure (enlarge view in the inset of Fig. 1.26) are due to the dark excitons.

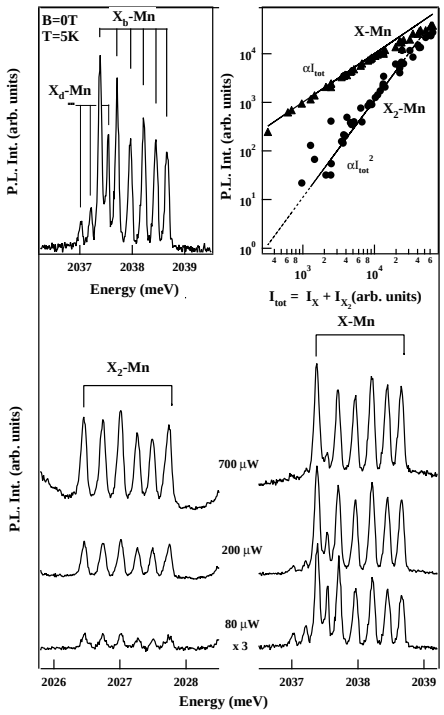

Figure 1.26 PL spectra of a single Mn-doped QD for different excitation intensity. X-Mn denotes the exciton-Mn emission while X_2-Mn corresponds to the recombination of the biexciton-Mn states. The insets give a detail of the X-Mn emission spectra at low excitation density (X_b-Mn corresponds to the bright excitons and X_d-Mn corresponds to the dark excitons) and the evolution of the integrated intensities of X-Mn and X_2-Mn as a function of the total emission intensity.

On increasing the excitation intensity, the emission of the biexciton coupled with the Mn (X_2-Mn) appears 11 meV below the exciton lines. Simultaneously, the contribution of the transitions associated with the dark exciton states progressively vanishes. This evolution, already observed in non-magnetic QDs [10], is due to the longer lifetime of the dark exciton states. The formation of the biexciton acts as an efficient recombination channel for the dark exciton states and decreases their direct PL contribution.

The magnetic field dependence of the exciton-Mn and biexciton-Mn transitions energies are presented as a contour-plot in figure 1.27. For X-Mn, six lines are observed in each circular polarization. Their energy follow the Zeeman and diamagnetic shift of the exciton in non-magnetic QDs. The excitonic transitions

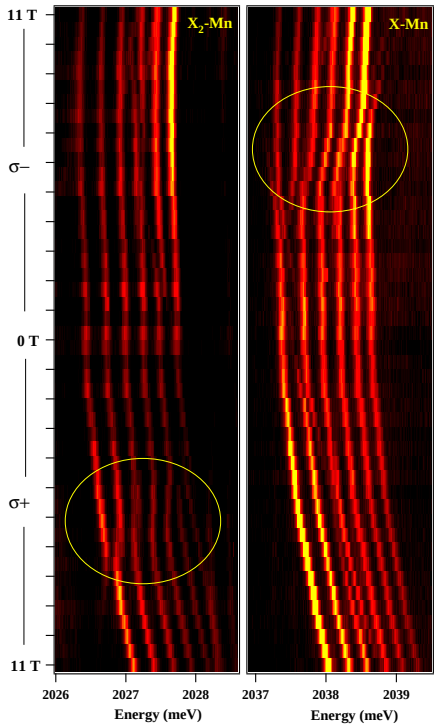

Figure 1.27 Intensity contour plot of the magnetic field dependence of the excitonic and biexcitonic transitions of a single Mn-doped QD. The bright areas corresponds to the high PL intensity. The anti-crossings observed for the exciton are symmetrically reproduced on the biexciton transitions.

present also around 7T anti-crossings coming from the mixing of the bright and dark exciton states induced by a simultaneous e-Mn spin flips. The fine structure of the exciton-Mn and the biexciton-Mn systems under magnetic field present a perfect mirror symmetry. The anti-crossings observed on the high energy lines of X-Mn in $\sigma-$ polarization are symmetrically observed on the low energy lines and in $\sigma+$ polarization for X_2-Mn (circles in Fig. 1.27) [91].

In a QD, the biexciton ground state is a spin-singlet state (J=0) and cannot be split by the magnetic field or the spin interaction part of the carriers-Mn Hamiltonian [9]. In this simplified picture, the creation of two excitons in the same QD cancels all the exchange interaction terms with the Mn. Thus, the fine structure of the biexciton-Mn transitions is controlled by the final state of the recombination of the biexciton, *i.e.* the eigenstates of the exciton-Mn coupled system. The optical transitions directly reflect this mirror symmetry of the energy levels. Moreover, the intensity distribution of the X-Mn and X_2-Mn transitions are both controlled by the spin polarization of the Mn. The spin of the Mn is orientated by the applied magnetic field. At high field, when the biexciton recombines, the probability to leave in the QD an exciton coupled with a Mn spin component

S_z=-5/2 is enhanced. Therefore, in the two photons cascade occurring during the recombination of a biexciton, the polarization of the Mn spin will enhance the intensity of the high energy biexcitonic transition in $\sigma-$ polarization and the one of the low energy single-exciton transition in $\sigma+$ polarization. Symmetrically, the emission intensity is concentrated in the low energy biexcitonic transition in $\sigma+$ polarization and in the high energy single-exciton transition in $\sigma-$ polarization.

Let us consider more in details the exciton and the biexciton transitions at zero magnetic field (Fig. 1.28(a)). As we have seen, if only the spin interaction part of the carrier-Mn Hamiltonian is considered, the six bright X-Mn transitions should be equally spaced in energy. In fact, an irregular structure is observed and the energy spacing decreases from the low energy side to the high energy side of the emission pattern. In the framework of the effective spin Hamiltonian model, the transitions energies of X_2-Mn are controlled by the energies of the X-Mn levels. This means that the structure of the X-Mn and X_2-Mn transitions should be perfectly symmetric. Surprisingly, the X-Mn and X_2-Mn transitions are found to be almost identical and not symmetric. This directly shows that the biexciton-Mn levels remain split and that their fine structure are not completely controlled by X-Mn in the final state of the biexciton-exciton transitions.

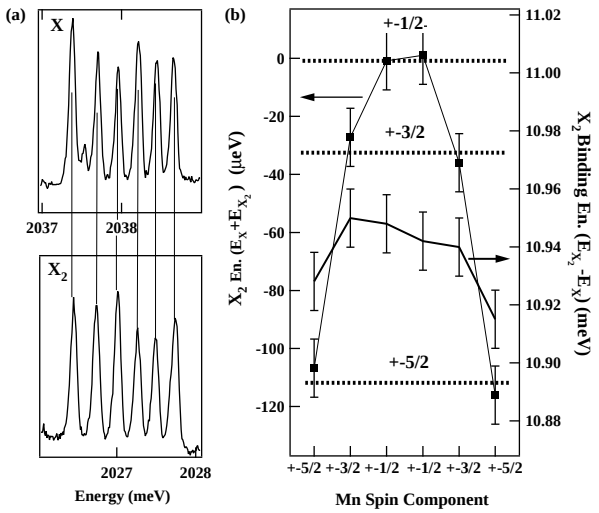

Figure 1.28 (a) Detail of the exciton-Mn and biexciton-Mn transitions at zero magnetic field showing the irregular spacing of the transition energies. (b) Biexciton energies (E_{X_2}+E_X) and biexciton binding energies (E_{X_2}-E_X) deduced from the optical transitions presented in (a). The biexciton energies scale is translated by 4065.225 meV.

The irregular spacing observed for X-Mn comes from a correction to the exchange energy terms due to a perturbation of the electron and hole wave functions. It scales as $-\eta S_z^2$ (equation (1.36)). This perturbation also affects the biexciton-Mn energies. Due to the presence of two electron-hole pairs, the perturbation of

X_2-Mn is twice the perturbation of X-Mn, as already noticed for the diamagnetic shift. The biexciton-exciton transition will then reproduce exactly the perturbed structure of the exciton-Mn system, as observed in the PL spectra at zero field.

For a given Mn spin component, the total energy of the biexciton-Mn complexes can be directly deduced from the X-Mn and X_2-Mn transitions energies at zero field. For instance, in the case S_z=+5/2, this energy is given by ${E_{X_2}}^{\sigma-}$+${E_X}^{\sigma+}$. The result obtained for all the different spin components are presented in Fig. 1.28(b). As expected from the qualitative model developed in section (1.2.5), three biexciton energy levels are obtained with an overall splitting of about 110μeV. The most stable biexcitonic complex is associated with a Mn spin projection S_z=$\pm$5/2 corresponding to the largest exchange coupling with the exciton and consequently, the largest perturbation in the exciton wave functions. This perturbation corresponds to a parameter $\eta \approx 18\mu$eV. Despite this perturbation, the binding energy of the biexciton (${E_X}^{\sigma-}$-${E_{X_2}}^{\sigma-}$) is found to be almost constant. This binding energy comes from the balance of the attractive and repulsive Coulomb terms and is not significantly affected by the presence of the Mn.

In summary, the analysis of the biexciton fine structure shows that the optical injection of a controlled number of carriers in an individual QD allows to control the spin splitting of a magnetic atom. The exchange interaction with a single exciton acts as an effective local magnetic field which splits the Mn levels in zero applied magnetic field. The injection of a second exciton almost completely cancels the carriers Mn exchange interaction and the Mn spin splitting is significantly reduced. Let us now analyze the interaction with an individual carrier.

1.3.3 Electrical control of the magnetic anisotropy of single Mn atom.

The two charge control mechanisms discussed for non-magnetic QDs (bias voltage and resonant excitation combined with photo-depletion) presented in Fig. 1.29 allow to independently probe the interaction between individual carriers (electron or hole) and an individual magnetic atom. Let us first consider the negatively charged exciton. Fig. 1.30(a) presents a detail of the recombination spectrum for X^- coupled with a single Mn atom obtained at zero bias under resonant excitation. Eleven emission lines are observed with intensity decreasing from the outer to the inner part of the emission structure.

A simple effective spin Hamiltonian quantitatively accounts for the emission spectrum shown in Fig. 1.30(a). The emitting state in the X^- transition has two conduction band (CB) electrons and one hole coupled to the Mn. The effect of the two spin-paired electrons on the Mn is zero. Thereby, the spin structure of the X^- state is governed by the interaction of the hole with the Mn. Let us, in a first stage, neglect the valence band mixing. Later we will show its influence. The twelve eigenstates of $\mathcal{H}_{h-Mn}$ are organized as six doublets (Fig. 1.30(a)(b)) with well defined S_z and j_z (Mn and hole spin along the z axis). We label these states as $|S_z, j_z\rangle$. Recombination of one of the CB electrons with the hole of the X^- state leaves a final state with a single CB electron coupled to the Mn. The

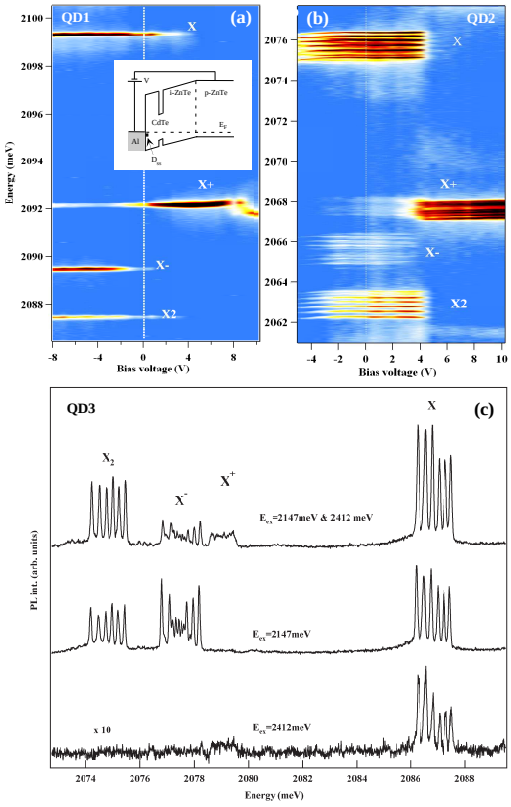

Figure 1.29 Color-scale plot of the PL intensity of a non-magnetic QD (a) and a single Mn-doped QD (b) in a Schottky structure as a function of emission energy and bias voltage. The series of emission lines can be assigned to QD s-shell transitions, namely the recombination of the neutral exciton (X), biexciton (X^2), positively charged exciton (X^+) and negatively charged exciton (X^-). Detail of the PL of a single Mn-doped QD under resonant excitation (E_{ex}=2147 meV), non-resonant excitation (E_{ex}=2412 meV) and both resonant and non-resonant excitation.

spin Hamiltonian of this system is the ferromagnetic Heisenberg model, $\mathcal{H}_{e-Mn} = I_{eMn}\vec{S}\cdot\vec{\sigma}$. The twelve eigenstates of the Mn-electron complex are splitted into a ground state septuplet (total spin $J = 3$) and a five-fold degenerate manifold with $J = 2$. We label them all as $|J, J_z\rangle$.

Thereby, for each of the six doublets of X^- there are two possible final states after annihilation of an e-h pair, with either $J = 2$ or $J = 3$. From this consideration alone, we would expect twelve spectrally resolved lines. Their weight is given by both optical and spin conservation rules. Since electrons and holes reside in s and p bands respectively, the $\Delta L = 1$ optical selection rule is immediately satisfied. The polarization of the photon imposes an additional selection rule on ΔM which is accounted for by the spin of the electron and hole. The Mn spin

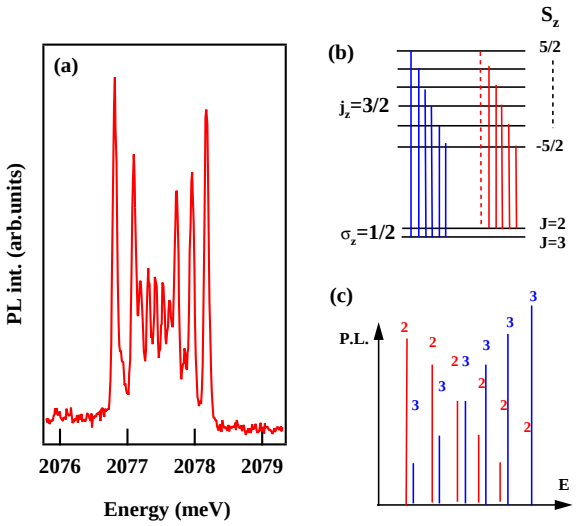

Figure 1.30 (a) Detail of the unpolarized emission spectrum of the negatively charged exciton (X^-) coupled with the Mn atom in QD3. (b) Scheme of the $\sigma+$ optical transitions of (X^-,Mn) and their respective PL intensity distribution (c).

is not affected by the transition. The weight of optical transitions between the initial state $|i\rangle = (\uparrow,\downarrow)_e \times |S_z, j_z\rangle$ and the final state $|f\rangle = |J, J_z\rangle$ is proportional to: $|\langle f| \sum_\sigma P(\sigma, j_z) c_\sigma d_{j_z} |i\rangle|^2$ where c_σ annihilates a CB electron with spin σ, and d_{j_z} annihilates a VB hole with angular mommentum j_z. Here $P(\sigma, j_z)$ is given by the polarization selection rule.

Let us consider, for instance, $\sigma+$ recombination transitions where the $(\downarrow_e, \Uparrow_h)$ e-h pair is annihilated. Each of the six doublets, characterized by their Mn spin projection S_z, can be an initial state. After the electron-hole annihilation, the resulting state is $|S_z, \uparrow_e\rangle$ which, in general, is not an eigenstate of $\mathcal{H}_{e-Mn}$. The intensity of the optical transition to a given final state $|J, J_z\rangle$ is proportional to the overlap $\langle J, J_z | S_z, \uparrow_e\rangle$, which is nothing but a Clebsh-Gordan coefficient which appears in the composition of a spin 1/2 with a spin 5/2. The highest energy transition, with $\sigma+$ polarization, would correspond to the initial state $(\uparrow,\downarrow)_e \times |+5/2, \Uparrow_h\rangle$ and a low energy final state $|J = 3, J_z\rangle$. After the photon emission, the state of the system is $|S_z = +5/2, \uparrow_e\rangle$ which is identical to $|J = 3, J_Z = +3\rangle$ and thereby gives the highest optical weight (Fig. 1.30(b)). In contrast, emission from that initial state to $|J = 2, J_z\rangle$ is forbidden. The other five doublets have optical weights lying between 1/6 and 5/6 with both $|J = 2, J_z\rangle$ and $|J = 3, J_z\rangle$ final states. Thereby, the number of spectrally resolved lines in this model is 11.

The relative weight of the emission lines is accounted for by the model. According to the final state, the transitions belong to either the $J = 2$ or the $J = 3$ series. As the initial S_z decreases, the overlap of $|\uparrow_e S_z\rangle$ to the $J = 3$ ($J = 2$) states decreases (increases). As presented in Fig. 1.30(c), the PL of X^- can be seen

as a superposition of two substructures: six lines with intensities increasing with their energy position (transitions to J=3 states) and five lines with intensities decreasing with increasing their energy position (transitions to J=2 states).

Reversing the role of the initial and final states, and neglecting the small coupling of two holes to the Mn spin, this model should account for the emission from X^+ states. Actually, different energy splittings are observed for the different excitonic species in the same QD. For instance, in Fig. 1.29(c) one measured $\Delta E_X = 1.23$ meV, $\Delta E_{X-} = 1.36$ meV and $\Delta E_{X+} = 0.95$ meV. The energy splitting is mostly due to the Mn-hole exchange coupling, which in turn is inversely proportional to the volume of the hole wave function. The difference between ΔE_{X+} and ΔE_{X-} indicates that a significant fraction of the confinement of the hole comes from the Coulomb attraction of the 2 electrons in the initial state of the X^- emission. In contrast, in the final state of the X^+ emission, there is no electron to attract the hole, resulting in a spread of the hole wave function and a smaller exchange energy. This difference appears directly in the emission structure shown in Fig. 1.29, where the peak structure of X^+ is not well resolved.

In Fig. 1.31(a) we show the intensity of X^- emission as a function of the direction of a linear analyser. It is apparent that the central lines are linearly polarized. This polarization can only be understood if we allow for some spin-flip interaction between the Mn and the hole induced by the valence band mixing. Provided that $\rho_s/\Delta_{lh} << 1$, the effect of this interaction is small both on the wave function and on the degeneracy of all the doublets except the third, which is split, as illustrated in the inset of Fig. 1.31. The split states are the bonding and antibonding combinations of $|S_z = -1/2, \Uparrow_h\rangle$ and $|S_z = +1/2, \Downarrow_h\rangle$. These states are coupled, via linearly polarized photons, to the $|2,0\rangle$ and $|3,0\rangle$ e-Mn complex and four linearly polarized lines should be observed on the emission spectra as shown in the insets of Fig. 1.31(c) and (d). Polarization directions are controlled by the distribution of strains through the Bir-Pikus Hamiltonian.

We can obtain numerical values of I_{hMn}, I_{eMn} and ρ_s/Δ_{lh} for the charged excitons comparing the transition probabilities calculated with the model (Fig. 1.31(c)) to the experimental data. The electron-Mn exchange integral I_{eMn} is deduced from magneto-optics measurements on the neutral exciton. I_{hMn} is then chosen to reproduce the overall splitting of the two charged species emission structure. There is a good agreement between the experimental data (QD presented in Fig. 1.29(c)) and the spin effective model with I_{eMn}=-40μeV, I_{hMn}(X)=150μeV, $\mathrm{I}_{hMn}(\mathrm{X}^+)$=95$\mu$eV and $\mathrm{I}_{hMn}(\mathrm{X}^-)$=170$\mu$eV. The different values of I_{hMn} directly reflect the expected variation of the confinement of the hole. The main characteristics of the emission spectra are well reproduced, namely the number of emission lines, their intensity distribution and the linear polarization structure, with a slight valence band mixing coefficient $\rho_s/\Delta_{lh} = 0.05$. This small value of the valence band mixing coefficient shows that hole-Mn exchange interaction remains highly anisotropic.

When a magnetic field is applied along the growth axis, the complex fine structure of the charged exciton observed at zero field progressively disappears and an emission structure similar to the exciton under magnetic field is restored: six lines

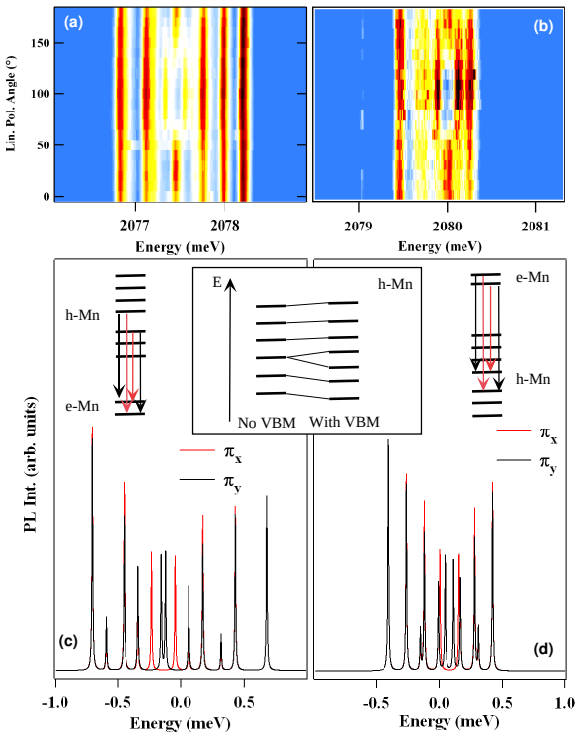

Figure 1.31 Color scale plot of the dependence of the PL of (X^-,Mn) (a) and (X^+,Mn) (b) on the direction of a linear analyzer, in QD3. Three lines in the center of the structure are linearly polarized. (c) and (d): calculated linearly polarized PL spectra of (X^-,Mn) and (X^+,Mn) with exchange integrals I_{eMn} and I_{hMn} chosen to reproduce the overall splitting for X^+ and X^- presented in (a) and (b). Transitions are arbitrarily broadened by 10μeV. The schemes in (c) and (d) show energy levels involved in (X^-,Mn) and (X^+,Mn) recombination with valence band mixing. The central inset presents the energy level scheme of the h-Mn system without and with valence band mixing (VBM).

are observed in each circular polarisation. This change in the emission structure is due to the influence of the magnetic field on the coupled electron and Mn spins.

A longitudinal magnetic field ($B_{ext} \parallel z$) conserves the quantization axis imposed by the hole spin in the initial state of X^- optical transition. The six energy levels in the initial state are only split by the g-factor of the Mn and the g-factor of the hole. However, in the final state (e coupled to Mn), the increase of the external magnetic field perturbs the electron and Mn spins exchange coupling. When the Zeeman splitting of the Mn exceed the e-Mn exchange energy, the spherical symmetry of the e-Mn system is destroyed and the electron and Mn spins are quantized along the external magnetic field. At high field, both the hole-Mn and the electron-Mn systems are quantized along the external magnetic field (growth direction). The Mn spin projection S_z is conserved during the op-

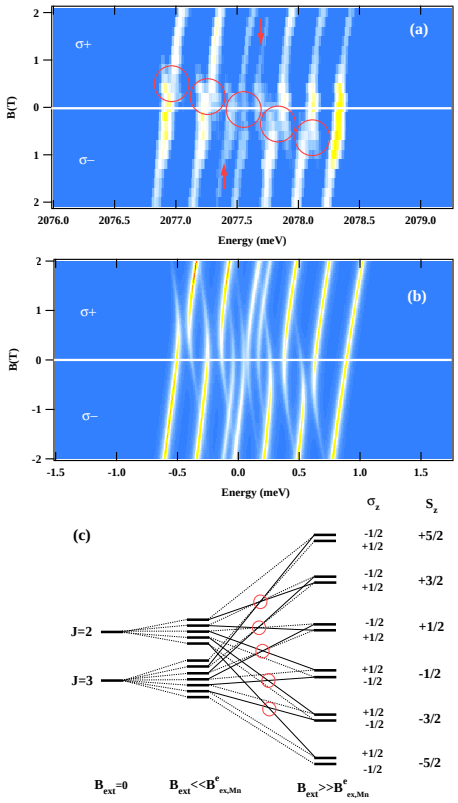

Figure 1.32 (a) Contour plot presenting the magnetic field dependence of the negatively charged exciton in QD3 in Faraday configuration (yellow: high intensity, blue: low intensity) in σ^+ and $\sigma-$ polarization. (b) Calculated magnetic field dependence using the effective spin Hamiltonian described in the text. (c) Scheme of the e-Mn energy levels for different condition of magnetic field. The red circles indicates the levels coupled by a simultaneous e-Mn spin flip.

tical transition and, as for the exciton, six emission lines are expected in each circular polarization.

At intermediate field, when B_{ext} is almost equal to the effective exchange field induced by the electron ($B^e_{ex,Mn} = I_e\sigma/g_{Mn}\mu_B$), there is a transition between the isotropic e-Mn coupled system at B_{ext}=0 and the fully quantized system at high field. In this intermediate regime, anticrossings are successively observed on five of the emissions lines (red circles in Fig. 1.32(a)). These anticrossings are due to simultaneous spin-flip of the electron and Mn spins coupling two sates of the form $|S_z, \uparrow_e\rangle$ and $|S_z + 1, \downarrow_e\rangle$. These states are split by the e-Mn exchange coupling and at B_{ext}=0T belong to the J=2 or J=3 sets. As illustrated in Fig. 1.32(c) these two sets are split by the magnetic field and conserve their J=2 and J=3 behavior as long as the Zeeman energy is weaker than the e-Mn exchange energy.

When $B_{ext} \approx B^{e}_{ex,Mn}$, the spherical symmetry is broken and the states $|S_z, \uparrow_e\rangle$ and $|S_z + 1, \downarrow_e\rangle$ are mixed, giving rise to the anticrossing observed in the emission of X^-.

This magnetic field dependence is well described by the spin effective Hamiltonian $\mathcal{H}_{h-Mn} + \mathcal{H}_{e-Mn} + \mathcal{H}_{mag}$, where $\mathcal{H}_{mag}$ gives the Zeeman energy of the electron, hole and Mn. The results of the calculation using the parameters deduced from the zero field structure of X^- (Fig. 1.31) are presented as a contour plot in Fig. 1.32(b). The overall structure and the five anticrossings are well reproduced.

1.4 Summary and conclusion

Through the study of the structure of the emission of neutral (exciton, biexciton) and charged (positively and negatively) excitonic complex, we have shown that the magnetic properties of a Mn atom strongly depends on the number of carriers confined in the QD. For a neutral QD, there is a direct correspondance between the state of a photon emitted by the QD and the spin state of the embedded Mn atom. However, this direct correspondance can be perturbed by valence band mixing induced by the shape and strain anisotropy of the QD. We will see in the next chapter how we can use these optical properties to optically control the spin state of on individual Mn atom and probe its dynamics.

2

Optical control of spins in a quantum dot: from diluted nuclear spins to an individual magnetic atom.

In Chapter 1, we discussed the basic optical properties of neutral, singly charged and magnetic II-VI QDs. We will show now how individual QDs can be used to control and access the spin dynamics of an individual carrier, an individual Mn atom or an ensemble of nuclear spins. Optical spin injection from a QD excited state will first be used to perform an optical orientation of a resident electron spin and of the diluted nuclear spin bath in singly charged QDs. The spin dynamics of coupled electron and diluted nuclear spins I=1/2 will be discussed. We will then show that the injection of spin polarized carriers in a QD can be an efficient tool to prepare the spin state of one or two Mn atoms. After an analysis of the influence of the quantum fluctuation of an individual Mn spin on the statistics of the photon emitted by a QD, we will present optical orientation and resonant optical pumping experiments allowing probing the dynamics of an individual Mn spin. We will in particular show that the efficiency of optical preparation and the spin memory of the Mn atom at weak magnetic field is mainly controlled by the fine and hyperfine structure of the Mn atom. We will finally demonstrate that we can use the optical Stark effect under a strong resonant optical field to optically modify the fine structure of the Mn atom. This strong coupling with the laser field is an additional tool to influence the Mn spin dynamics.

2.1 Electron-nuclei spin dynamics in a II-VI quantum dot

We summarize here an experimental study of the dynamics of coupled electron and nuclear spins in a CdTe/ZnTe QD and compare it with the commonly studied III-V QDs. In contrast to gated structures where the number of resident charges is controlled by an applied voltage, we use the characteristic spectral feature of the charged exciton triplet state observed in PLE to identify QDs containing a single resident electron. Non-resonant circularly polarized excitation of the negatively charged exciton will be used throughout this study to build-up and probe dynamic nuclear spin polarization (DNSP). In II-VI QDs, the Overhauser shift is much smaller than the photoluminescence linewidth and cannot be observed directly: The nuclear field will be detected through the polarization rate of the resident electron which is controlled by the nuclear spin fluctuations (NSF).

We will first present a model for the expected nuclear spin-polarisation in II-VI QDs and derive orders of magnitude for the effective hyperfine fields encountered in this system. Secondly, we will discuss the mechanism of build-up of negative

circular polarization in singly charged CdTe/ZnTe QDs. We will then describe how the polarization of nuclear spins influences the spin dynamics of the confined electron. The dynamics of nuclear spin polarization will then be considered. Finally, we will present and discuss results of coupled electron/nuclei spin decay in the absence of optical excitation.

2.1.1 Nuclear spin polarization in II-VI quantum dots

In a singly charged QD under the injection of spin polarized electrons, a nuclear spin polarization builds up by integration over many mutual spin flip-flops of the confined electrons and the lattice nuclei. This nuclear magnetic field modifies the coherent electron spin dynamics and consequently the average polarization of the PL of the X^-. The knowledge of the nuclear spin polarization can then be used to estimate the resident electron spin polarization. In this section, we want to estimate the order of magnitude of the nuclear spin polarization that can build-up in a II-VI QD and its influence on the spin dynamics of a confined electron.

The dominant contribution to the coupling between the confined electron and the nuclear spins originates from a Fermi contact hyperfine interaction. This interaction can be written as [118]:

$$H_{hf} = \nu_0 \sum_i A_i^I |\psi(R_i)|^2 (I_z^i \sigma_z + \frac{I_+^i \sigma_- + I_-^i \sigma_+}{2}) \tag{2.1}$$

where R_i is the position of the nuclei i with spin I^i and hyperfine interaction constant A_i^I. σ and I^i are the spin operators of the electron and nuclei respectively. ν_0 is the volume of the unitary cell containing Z=2 nuclei (one Cd and one Te). This Hamiltonian can be decomposed in a static part affecting the energy of the electron and nuclear spins and a dynamical part proportional to $(I_+^i \sigma_- + I_-^i \sigma_+)$, allowing for the transfer of angular momentum between the electron and nuclear spin system. The static part of the hyperfine interaction leads to the notion of effective magnetic field, either seen by the electron due to the spin polarized nuclei (Overhauser field $\overrightarrow{B}_N$), or by a nucleus at position R_i due to a spin polarized electron (Knight field $\overrightarrow{B}_e^i$). These fields are defined by the electron-nuclei interaction energy:

$$H_{hf} = g_e \mu_B \overrightarrow{\sigma}.\overrightarrow{B}_N = -\sum_i \mu_I^i \overrightarrow{I}^i.\overrightarrow{B}_e^i \tag{2.2}$$

where g_e is the Lande factor of the electron and μ_I^i the magneton of nucleus i with spin I^i defined by $\mu_I^i = \hbar \gamma_I^i I$ with γ_I^i the gyromagnetic ratio of the nucleus i.

Overhauser field in a CdTe/ZnTe quantum dot

The maximum Overhauser field resulting from a complete polarization of the nuclei, B_N^{max}, is defined by intrinsic parameters characterizing the material and the hyperfine interaction inside the material [137, 100]. The Overhauser field can be written as:

$$B_N = \frac{\nu_0}{g_e \mu_B} \sum_i^{N_I} A_i^I |\psi(R_i)|^2 \langle I_z^i \rangle \tag{2.3}$$

where the sum runs over N_I, the number of nuclei carrying a spin I. When all the Cd and Te nuclear spins are polarized and if we assume a homogeneous electron wave function $\psi(R) = \sqrt{2/(\nu_0 N_L)}$, with N_L the total number of nuclei in the QD, the nuclear field reads:

$$B_N^{max} = \frac{1}{g_e \mu_B} (I^{Cd} A^{Cd} p^{Cd} + I^{Te} A^{Te} p^{Te}) \tag{2.4}$$

The nuclear spin of Cd and Te are I^{Cd}=I^{Te}=1/2 and their corresponding abundance $p^I = N_I/N_L$ are $p^{Cd} = 0.25$ and $p^{Te} = 0.08$ (see table 2.1). Taking the hyperfine coupling constants A^{Cd} ≈-31μeV, A^{Te} ≈-45μeV from [137] and an average electron Lande factor $g_e \approx -0.5$ [9, 93], we obtain B_N^{max} ≈200mT.

Table 2.1 *Isotopic abundance, nuclear spin I and magneton of the nucleus μ_I for Cd and Te alloys [62]. μ_I is given in unit of the nuclear magneton μ_N.*

	Abundance (%)	I	μ_I
^{111}Cd	12.75	1/2	−0.5943
^{113}Cd	12.26	1/2	−0.6217
^{123}Te	0.87	1/2	−0.7357
^{125}Te	6.99	1/2	−0.8871

The Overhauser field really obtained in a QD under optical pumping, B_N, is proportional to the average nuclear spin polarization $\langle I_z \rangle$ and reaches B_N^{max} when $\langle I_z \rangle$=1/2. As the electron Lande factor in CdTe/ZnTe QDs is negative and the hyperfine constants are negative, the sign of B_N is fixed by the sign of $\langle I_z \rangle$ which is given by the average electron spin polarization [104, 137] $\langle S_z \rangle$ along the QD growth axis z ($\langle S_z \rangle$=1/2 for fully polarized spin up electrons). In the present study, the resident electron is pumped down ($\langle S_z \rangle \leq$0) for a $\sigma+$ excitation (spin $|\downarrow\rangle$ electron) in the presence of a positive external magnetic field. Thus, a $\sigma+$ excitation leads to an Overhauser field, B_N, antiparallel to the applied magnetic field ($B_N < 0$).

Knight field in a CdTe/ZnTe quantum dot

At zero external magnetic field, the formation of a nuclear spin polarization is only possible if the effective field induced by the electron spin on the nuclei exceeds the local field B_l created by the nuclear dipole-dipole interaction [104]. The Knight field is inhomogeneous across the nuclear ensemble because the electron wave function is not constant across the QD. In the core of the QD where the Knight field is the strongest, the spin diffusion induced by the nuclear dipole-dipole coupling is suppressed and it is there that the nuclear spins may become polarized. The magnitude of the time averaged Knight field for a nucleus with a hyperfine constant A^I at the position R_i is given by

$$B_e^i = -\nu_0 \frac{A^I}{\mu_I} |\psi(R_i)|^2 (\langle S_z \rangle f_e) \tag{2.5}$$

where f_e is the probability that the dot is occupied by an electron. Considering a constant electron/nuclei overlap (homogeneous wave function $\psi(R) = \sqrt{2/(\nu_0 N_L)}$) one can obtain [118, 98] the maximum Knight field for nuclei with a hyperfine constant A^I:

$$B_e^{max} = -\frac{A^I}{N_L \mu_I} \tag{2.6}$$

With $\mu_{Cd} \approx -0.6$ and a total number of nuclei in the QD assumed to be $N_L \approx 8 \times 10^3$, $B_e^{max} \approx 100$ mT is derived for Cd nuclei. A Knight field of 10mT is typical for InAs/GaAs QDs [84]. The difference is a consequence of the smaller QD size in II-VI materials. However, B_e follows the distribution of the electron wave function in the dot leading to a nuclear site-dependent field varying across the dot and in optical pumping experiments, only a weighted-averaged value of the Knight field can be accessible.

Dynamic nuclear spin polarization

Under circularly polarized CW excitation, the rate equation describing the nuclear spin polarization I_z in a singly negatively charged QD can be written as [1]:

$$\frac{\partial I_z}{\partial t} = \frac{1}{T_{1e}} \left(\frac{4}{3} I(I+1) S_0 - I_z\right) - \frac{1}{T_{dd}} I_z - \frac{1}{T_r} I_z \tag{2.7}$$

The last term on the right side of the equation accounts for any spin relaxation mechanism except the dipole-dipole interaction between nuclei which is described by the relaxation time T_{dd}. The first term corresponds to the transfer of angular momentum between the spin of the electron and the nuclear spin bath, with S_0 the polarization rate of the injected electrons and T_{1e} the probability of an electron/nuclei spin "flip-flop" given by [136]:

$$\frac{1}{T_{1e}} = \frac{1}{T_{1e}^0} \frac{1}{1 + (\Delta E_{eZ}/\hbar)^2 \tau_e^2} \tag{2.8}$$

τ_e is the correlation time of the electron/nuclear spin interaction [1]. $\Delta E_{eZ} = g_e \mu_B (B_{ext} + B_N)$ is the electron Zeeman splitting which depends on the external magnetic field, B_{ext}, and the effective nuclear field B_N. This term provides a feedback process mechanism between the spin transfer rate and the nuclear polarization leading to the enhancement of flip-flop processes when B_N reduces the electron Zeeman splitting. This feedback is responsible for the bi-stability in the nuclear spin polarization observed under magnetic field in InAs/GaAs QDs [42, 136, 100]. T_{1e}^0, is given by:

$$\frac{1}{T_{1e}^0} = f_e \tau_e (\frac{E_{hf}}{\hbar})^2 \tag{2.9}$$

with

$$E_{hf} = \nu_0 A_i^I |\psi(R_i)|^2 \tag{2.10}$$

the interaction energy between the electron and nuclear spin I at position R_i. T_{1e}^0 corresponds to the nuclear spin relaxation induced by the electron at zero electron splitting. For a homogeneous electron wave function ($\psi(R) = \sqrt{2/(\nu_0 N_L)}$), we obtain $1/T_{1e}^0 = f_e \tau_e (2A_i^I/(N_L \hbar))^2$.

The contribution of the dipole-dipole interaction to the relaxation process is given, in the presence of an external magnetic field, B_{ext}, by:

$$\frac{1}{T_{dd}} = \frac{1}{T_{dd}^0} \frac{B_l^2}{(B_{ext} + B_e)^2 + B_l^2} \tag{2.11}$$

where B_l is the local field describing the nuclear spin-spin interaction and T_{dd}^0 the characteristic time of this interaction at zero field [40, 27, 55]. This formula describes the acceleration of the nuclear spin relaxation when an applied magnetic field compensates the Knight field.

The magnetic field dependence of the nuclear spin polarization for a single family of nuclei with an average hyperfine coupling A_{av}=-40μeV and abundance p_{av}=16% obtained by a numerical determination of the steady state of the rate equation (2.7) is presented in Fig. 2.1. In this model, the electron wave function is described by a Gaussian function in the QD plane and a constant function in the z direction:

$$\psi(\rho, z) = \frac{1}{\sqrt{L_z}} \frac{1}{\xi\sqrt{\pi}} e^{-\frac{\rho^2}{2\xi^2}} \tag{2.12}$$

where L_z is the thickness of the QD and ξ the lateral extension of the electron wave function. For the numerical calculation, the Gaussian wave function is approximated by a 7 steps function (inset of Fig.2.1) and the 7 coupled differential

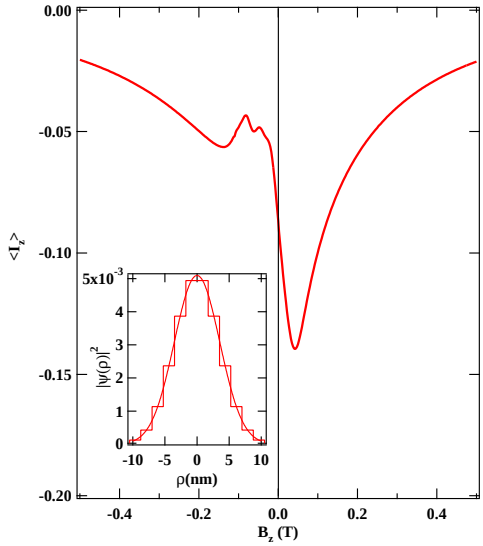

Figure 2.1 Nuclear spin polarization obtained from equation (2.7) for a single family of nuclei with an average hyperfine coupling A_{av}=-40μeV and abundance p_{av}=16% and with the parameters: f_e=0.4, S_0=-0.4, T^0_{dd}=5μs, B_l=2.5mT, d=2.5nm, ξ=5nm, τ_e=5ns, T_r=5ms. The inset shows the approximation of the Gaussian electron density with ξ=5nm and L_z=2.5nm by a step function used in the numerical calculation.

equations corresponding to the 7 families of nuclear spins (*i.e.* with different Knight fields) are solved simultaneously.

The acceleration of the dipole-dipole interaction between the nuclear spins when the external field compensate the Knight field is responsible for the decrease of the nuclear spin polarisation observed at low negative magnetic field (between $B_z \approx -50mT$ and $B_z \approx -100mT$). The position of this minimum depends on the average electron spin polarization and is a measurement of the mean value of the Knight field. The nuclear spin polarization does not drop to zero because of the inhomogeneity of the Knight field: the condition $B_{tot} = 0$ is satisfied only for a small number of nuclei at any given B_{ext}. Provided $B_e \gg B_l$, the majority of nuclei experience negligible change in depolarization.

The feedback process occurring when the Overhauser field compensates the applied magnetic field leads to a strong increase of the nuclear spin polarization at low positive magnetic field ($B_z \approx 50mT$). This resonant effect is enhanced by a long electron correlation time τ_e, *i.e.* a weak broadening of the electron transition. This time of free coherent electron-nuclei precession is likely to be controlled in our experimental condition (*i.e.* chemically doped QDs under CW excitation) by the non-resonant optical injection of an electron-hole pair: we chose $\tau_e = 5ns$ in the calculation presented in Fig.2.1.

The important variations of the nuclear spin polarization observed in Fig. 2.1

for a small varying magnetic field around B_z=0T are expected to significantly influence the spin dynamics of the resident electron. In particular, an increase of the relaxation rate of the electron spin should be observed when the external magnetic field compensates the Overhauser field increasing the influence of the fluctuating nuclear field.

2.1.2 Electron spin optical orientation

As a probe of the resident electron spin orientation, we use the amplitude of the negative circular polarization of the charged QDs for an excitation above the triplet states of the charged exciton [31, 68, 19, 131]. In the case of X^-, the circular polarization of the emitted light reflects both the spin of the resident electron before the absorption of a photon and the spin of the hole before emission. Negative polarization of X^- implies that the hole spin has flipped prior to recombination and that a spin flipped hole contributes to the X^- formation with a higher probability than a non-flipped hole. This process can also lead to an optical pumping of the resident electron spin [89]. The observation of negative circular polarization does not necessarily mean that the resident electron is polarized but a variation of its polarization will cause a change in the negative circular polarization rate.

The presence of optical pumping of the resident electron is confirmed by the power dependence of the negative circular polarization rate obtained under CW excitation (Fig. 2.2(a)). As the pump power intensity is increased, we observe a rapid growth of the negative circular polarization with a saturation at about -55%. This reveals the progressive orientation of the resident electron spin by the exciting beam.

This electron spin memory can be significantly erased by a weak magnetic field (see Fig. 2.2(b)) applied in the plane of the QD. At $B_x \approx 0.1T$, all the contribution of the electron spin polarization to the negative circular polarization rate has disappeared. Despite the weak transverse component of the hole g-factor, a further increase of the transverse magnetic field can induce a precession of the confined hole spin during the lifetime of the negatively charged exciton. At high field, this precession depolarizes the hole spin and finishes to destroy the average negative circular polarisation of the X^-. This effect is observed in Fig. 2.2(b) as an oscillation of the polarization rate for a transverse field larger than 0.1T. This oscillation corresponds to the first period of precession of a spin polarized hole injected at $t = 0ns$. The decrease of the polarization rate at long time delay corresponds to the late recombination of spin flipped holes stored as dark excitons in the triplet state of X^{-*} (see reference [89] for discussion of spin injection).

The dynamics of the pumping and relaxation of the resident electron spin can be estimated through the time evolution of the polarization rate when the QD is excited by a sequence of two circularly polarized *ps* laser pulses. The results of the experiments using equal intensities for the two pulses are shown in Fig. 2.2(c). When the QD is excited with circularly co-polarized pulses (ii), a large average negative circular polarization is observed for both PL pulses. However, in the case

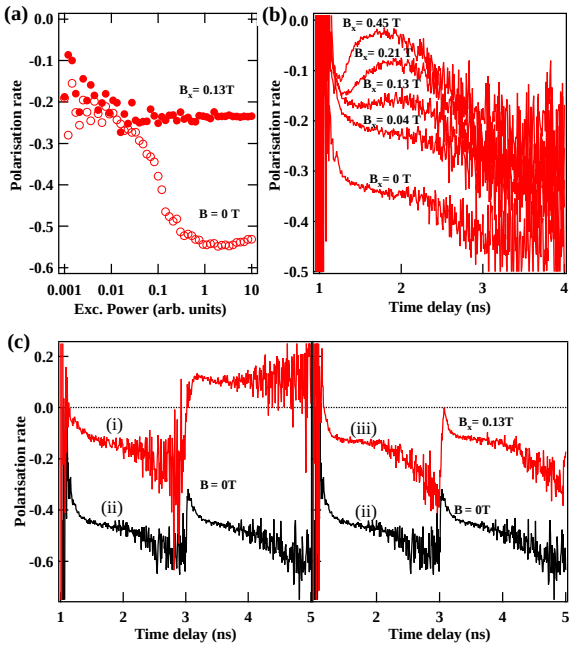

Figure 2.2 (a) Evolution of the degree of circular polarisation as a function of CW excitation power. Empty circles are zero field measurements, filled circles are measurements in a transverse magnetic field B_x=0.13T. (b) Time-evolution of the degree of circular polarisation under pulsed (2ps) quasi-resonant excitation for different transverse magnetic fields. (c) Time-evolution of the degree of circular polarisation with a two-pulse-excitation sequence: the pulses are separated by 2ns. (i) is obtained with cross-polarized pulses at zero field. (ii) is obtained with co-polarized pulses at zero field. (iii) is obtained with co-polarized pulses and a transverse magnetic field B_x=0.13T.

of excitation by cross-polarized beams (i), the average PL polarization vanishes. These results directly demonstrate that the spin orientation created by the first pulse affects the polarization of the PL excited by the second one. It means that after recombination of the e-h pair, the information about the polarization of the excitation is stored in the orientation of the resident electron spin. In addition, we notice that the polarization rate is identical for the two pulses in the excitation sequence. As these pulses are separated in time by either $2ns$ or $11ns$ this suggest that the relaxation time of the electron exceeds by far the laser pulses repetition rate ($\approx 13ns$). Consequently, the resident electron can be fully depolarized by a weak transverse magnetic field. A significant decrease of the negative polarisation rate is observed for both pulses in a transverse field B_x=0.13T (iii) confirming the influence of the optical pumping of the electron spin on the negative polarization rate.

Dynamics of the electron spin orientation

In the presence of optical pumping, the degree of negative circular polarization of X^- reflects the spin polarisation of the resident electron. The dynamics of its optical orientation can then be revealed by the observation of the negative polarization rate under modulated circularly polarized excitation. As presented in Fig. 2.3(a), the negative polarisation strongly depends on the modulation frequency: an increase of the degree of circular polarisation when the modulation frequency is decreased is observed at B=0T. This modulation frequency dependence is canceled by a magnetic field of B_z=0.16T applied along the QD growth axis. As already observed in InAs QDs, this behavior is a fingerprint of the coupling of the electron to a fluctuating nuclear field [110].

The QD contains a finite number N_I of nuclei carrying a spin, which means that statistically, the number of spins parallel and antiparallel in any given direction differs by a value $\sqrt{N_I/3}$. The result is an effective magnetic field B_f, oriented in a random direction. This field will induce a precession of the spin of the electron for every B_f not aligned along the QD growth axis z. B_f can be estimated, for a CdTe QD. Assuming a homogeneous envelope-function for the electron ($\psi(R) = \sqrt{2/(\nu_0 N_L)}$), B_f is given by [40]:

$$B_f^2 = \frac{2}{(g_e \mu_B \sqrt{N_L})^2}(I_{Cd}(I_{Cd}+1)A_{Cd}^2 p_{Cd} + I_{Te}(I_{Te}+1)A_{Te}^2 p_{Te}) \tag{2.13}$$

Forom our estimation of $N_L = 8000$ one obtain $B_f \approx 12mT$. The electron spin precession frequency in the frozen nuclear spin fluctuation B_f ≈12mT is ≈80MHz. This frequency can be smaller than the rate of optical injection of the spin polarized carriers at high excitation intensity allowing an optical pumping of the electron spin even in the presence of nuclear spin fluctuations.

At high modulation frequency of the polarisation and low excitation intensity, a dynamic nuclear spin polarisation does not have time to build-up. Over time scales less than 1 μs, the electron is exposed to a snapshot of B_f where the nuclear spin configuration remains frozen. In the absence of an external magnetic field, only this internal field B=B_f acts on the electron. For a randomly oriented nuclear spin system, the electron spin polarization quickly decays to 1/3 of its initial value due to the frozen nuclear field [106]. This decay is not a real relaxation process as the electron coherently evolves in a frozen nuclear spin configuration. On an averaged measurement, a fast decay of the electron polarization on a characteristic timescale $t \approx h/(g_e \mu_B B_f)$ is expected [106]. In the absence of nuclear spin polarization, the influence of the fluctuating nuclear field can be suppressed by applying an external magnetic field. For sufficiently large external fields, the nuclear spin fluctuations does not contribute significantly to the total field, B_{tot}=B_{ext}+B_f, and the electron-spin polarization is preserved.

At small modulation frequencies of the polarization or under CW excitation, nuclei can be dynamically oriented through flip-flop with the spin polarized res-

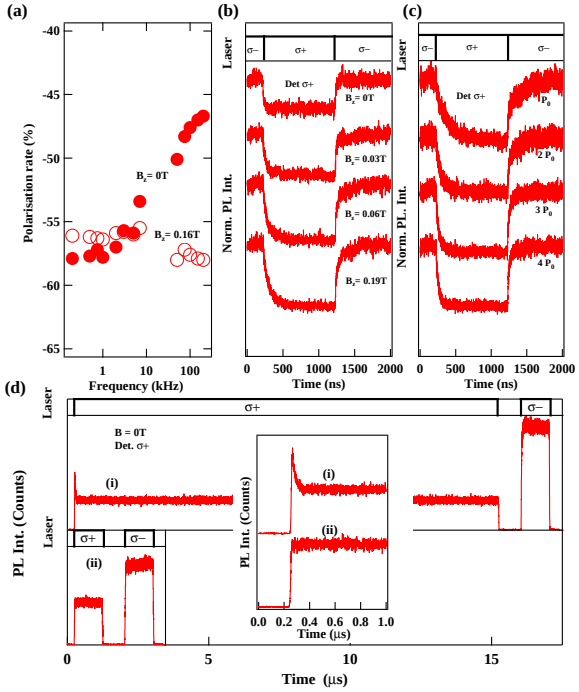

Figure 2.3 (a) Evolution of the NCP with the frequency of the $\sigma+/\sigma-$ modulation of the excitation laser tuned on an excited state above the charged exciton triplet states at zero magnetic field and at a field B_z=0.16T applied along the QD growth axis z. Time-evolution of the $\sigma+$ PL excited alternatively with $\sigma+$ or $\sigma-$ light for different magnetic fields applied in Faraday geometry (b) and for different excitation intensities and a fixed magnetic field B_z=0.19T (c). (d) Time-evolution of the $\sigma+$ PL excited alternatively with $\sigma+$ and $\sigma-$ light trains. The excitation sequence are displayed above the spectrum. The inset is a zoom on the fast transient at short time delay.

ident electron. This nuclei orientation leads to the formation of an Overhauser field, B_N along the z axis, which may be much larger than the in-plane component of the fluctuating field (B_f). The electron now precesses around a nuclear field whose z component dominates: the result is an increase of the average electron spin polarization compared to the case of a totally randomly oriented nuclear spin system. The effect of the Overhauser field is similar to an applied magnetic field along the z axis allowing an optical orientation of the electron spin even at low excitation power.

This influence of the nuclear spin fluctuations on the optical pumping of the electron is confirmed by the magnetic field dependence of the time resolved polarisation rate obtained at high modulation frequency (Fig. 2.3(b)). The increase of the polarization rate and the appearance of a transient with an applied external magnetic field along z reflects an increase of the optical pumping efficiency of the

electron [45]. This optical pumping, which takes place in a few tens of ns, is promoted by the presence of the external field which can dominate the fluctuations of the Overhauser field [121]. This short timescale component in the dynamics of the polarization of the spin of the electron becomes faster with the increase of the optical generation rate of spin polarized carriers and reach the ns range (Fig. 2.3(c)).

Similarly to the application of an external magnetic field, the build-up of a DNSP favors the electron spin polarization. This is confirmed by the following experiment: in Fig. 2.3(d), the $\sigma+$ PL has been time-resolved using the two different excitation sequences displayed on each spectrum. In the sequence (ii), the excitation pulses are of equal length and power, and are short enough to prevent the creation of DNSP. In sequence (i), the difference of pulses length allows the creation of DNSP. The measurements show two striking differences. First, the average circular polarisation, given by the difference of the PL intensity obtained under $\sigma-$ and $\sigma+$ excitation, is higher in (i) than in (ii). Second, the PL of (i) exhibits a fast PL transient at short delay reflecting an optical pumping of the electron spin (detail of this transient is shown in the inset of Fig. 2.3(d)). These two features demonstrate that the Overhauser field created in (i) is strong enough to block the longitudinal decay of the electron spin by the fluctuating nuclear field.

2.1.3 Nuclear spin optical orientation

Built-up of the nuclear spin polarization

Direct evidence of the build-up of a DNSP can be observed using sequences of pulses of long duration (tens of μs). As displayed in Fig. 2.4(a), the $\sigma+$ PL recorded under $\sigma+$ excitation presents first a fast transient with a drop of the intensity due to the orientation of the resident electron spin (a zoom of the transient at short delay is presented in Fig. 2.4(b)). Then, a slower transient is observed: the $\sigma+$ PL increases during a few μs reflecting a decrease of the absolute value of the negative polarisation (*i.e.* of the spin polarization of the resident electron) before it decreases again. This evolution has been predicted by M. Petrov *et al.* [122] and results from a destruction of the Overhauser field created at the end of the $\sigma-$ excitation pulse, and a build-up of an Overhauser field in the opposite direction under $\sigma+$ excitation. During this process, the amplitude of the Overhauser field becomes zero and the electron spin is strongly affected by the nuclear spin fluctuations B_f.

As presented in Fig. 2.4(d), the speed of the destruction and build-up of the nuclear polarization strongly increases with the increase of the excitation power. Simultaneously, the average negative polarisation of the X^-, given by the intensity difference of the PL obtained under $\sigma+$ and $\sigma-$ excitation, increases. This effect is also directly observed in the modulation frequency dependence of the polarization rate displayed in Fig. 2.4(c). The modulation frequency required to suppress the nuclear spin polarisation (*i.e.* to decrease the absolute value of the

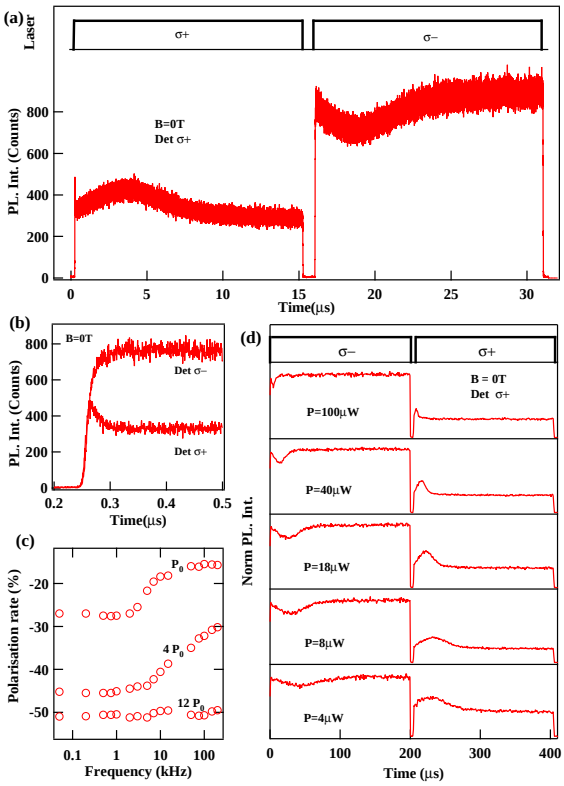

Figure 2.4 (a) Time-evolution of the $\sigma+$ PL excited alternatively with $\sigma+/\sigma-$ light trains. The excitation sequence is displayed above the spectrum. (b) Zoom on the transient corresponding to the optical pumping of the electron. The time-evolution of the $\sigma-$ PL recorded in the same conditions of excitation is also displayed.(c) Dependence of the the degree of circular polarisation of the QD PL on the frequency of the $\sigma+/\sigma-$ modulation of the light for different excitation power. (d) Time-evolution of the $\sigma+$ PL excited alternatively with $\sigma+/\sigma-$ light for different excitation power.

polarization) increases with the excitation intensity. At low excitation intensity, a formation time of the nuclear spin polarization of about $50\mu s$ can be estimated from the modulation frequency dependence of the negative circular polarization [110]. This is faster than in InAs/GaAs QDs where a pumping time ranging from a few hundreds μs to 10 ms have been reported depending on the experimental conditions [100, 38]. At hight excitation power, the pumping rate of the nuclei becomes faster than the polarization modulation frequency and a stable negative polarization of about -50% is obtained (Fig. 2.4(c)). An increase of the value of the negative polarization with the excitation intensity is also observed suggesting an increase of the average nuclear spin polarization and Overhauser field with the excitation intensity.

Magnetic field dependence of the nuclear spin polarisation

A typical magnetic field dependence of the polarization rate of a singly charged QD under CW circularly polarized excitation, in the optical pumping regime, is presented in Fig. 2.5: Fig. 2.5(a) focuses on the Faraday geometry while the Voigt geometry and the influence of the modulation frequency of the polarization of the excitation beam are presented in Fig. 2.5(b). The asymmetry of the response in the Faraday geometry is a fingerprint of the presence of a nuclear spin polarization induced by the helicity of the excitation beam.

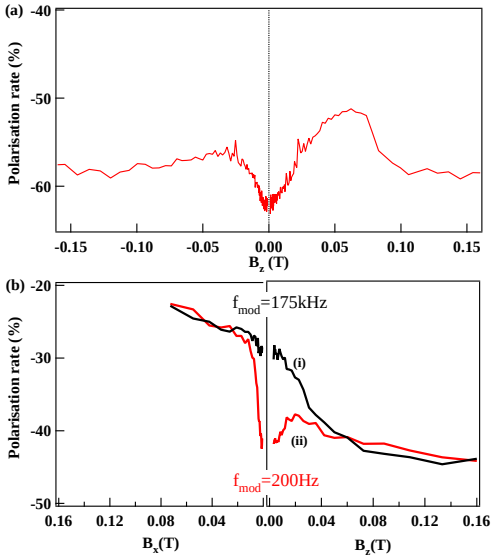

Figure 2.5 (a) Magnetic field dependence in Faraday configuration of the negative polarization rate under $\sigma+$ CW excitation. (b) Magnetic field dependence of the negative polarization rate, on a different QD, in Voight (left) and Faraday (right) configuration under $\sigma+/\sigma-$ modulated excitation at low (f_{mod}=200Hz) and high (f_{mod}=175kHz) modulation frequency.

A striking feature of this magnetic field dependence is the small increase of the absolute value of the negative polarization around B=0T. This is in opposition to what is usually observed in III-V semiconductor QDs where a decrease of the electron spin polarisation occurs at weak magnetic field because of the dominant contribution of the fluctuating nuclear field B_f. As presented in curve (i) of Fig. 2.5(b), a standard increase of polarisation with magnetic field is restored in the absence of nuclear polarisation (*i.e.* under polarization modulated excitation). This shows that the increase of the electron polarization around $B = 0T$ observed under CW excitation is linked to the DNSP: the nuclear spin fluctuations are strongly suppressed by the build-up of a large Overhauser field.

The experiment presented in Fig. 2.5(a) was carried out under CW $\sigma+$ excitation, pumping the resident electron down. This leads to an average polarization of nuclei with $\langle I_z \rangle < 0$ and an Overhauser field $B_N \leq 0$. For $B_z \geq 0$, we observe

around 50mT an increase of the circular polarization rate of 10% which reflects a depolarization of the resident electron. This behavior is attributed to the compensation of the Overhauser field by the external Faraday field ($B_z = -B_N$). As the electron precesses around the total field $B_{tot} = B_z + B_N + B_f$, the electron dynamics is then governed by the nuclear spin fluctuations B_f, resulting in a depolarization of the resident electron.

Considering the left panel of Fig. 2.5(a) (corresponding to $B_z \leq 0$), we observe at $B = 0T$ a maximum in the electron polarization, then a decrease of about 5% in the first 25 mT followed by a small increase at larger fields. This extremum around $B_z = -25mT$ also reflects a depolarization of the resident electron spin. This depolarization is attributed to a compensation of the Knight field by the external magnetic field. The nuclear field is then close to zero and the electron dynamics is ruled by the sum of $B_z \approx 25mT$ and the nuclear spin fluctuations B_f. The effect of B_f is not negligible at $25mT$. As observed in the experiment of Fig. 2.3(b), in the absence of DNSP, the polarization of the PL continuously increases as the Faraday magnetic field is increased from 0 to $60mT$.

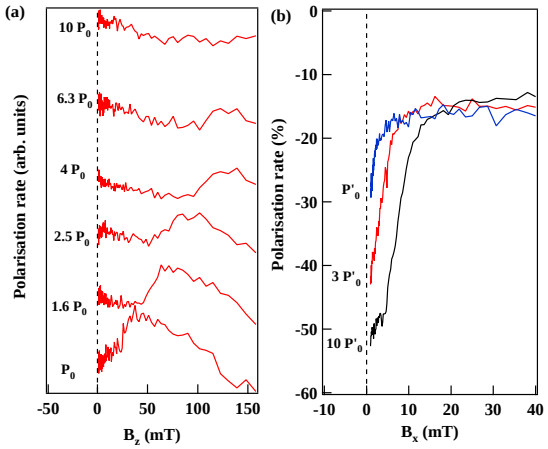

Figure 2.6 Excitation power dependence of the negative polarization rate under magnetic field. (a) Faraday configuration under $\sigma+$ CW excitation. (b) Voigt configuration.

This influence of the Knight and Overhauser fields is further-confirmed by the following experiment: We present on the right panel of Fig. 2.5(b) a measurement, were we have studied the polarization rate as a function of the magnetic field B_z under modulated excitation. The light is modulated $\sigma + /\sigma-$ at two different rates: (i) 175 kHz ($\approx 3\mu s$ of $\sigma+$ exc., then $\approx 3\mu s$ of $\sigma-$ exc. of equal intensity) and (ii) 200 Hz ($\approx 2500\mu s$ for a given polarization). Hence, at low power of excitation, DNSP is achieved in (ii) and not in (i). The detection is done on an APD synchronized with the modulation, and for a fixed circularly polarized detection. We measure a polarization rate by varying the excitation polarization and not the detection. Hence, this polarization rate is an average of the polarization rates

measured in Fig. 2.5(a) for B_z and $-B_z$. The magnetic field dependence for (ii) is consistent with the one observed in the CW regime, with an evolution ruled by the competition between the B_z, B_N, B_e and B_f. On the other hand the magnetic field dependence (i) is only controlled by the competition between B_z and B_f. For sufficiently large external fields, the nuclear spin fluctuations B_f do not contribute to the total field and the electron-spin polarization does not decay. The width at half maximum is $25 \pm 5mT$. This gives an order of magnitude of the fluctuating Overhauser field.

The magnetic field dependence of the polarization rate under CW excitation has been performed for $B_z > 0$ for different excitation powers (Fig. 2.6(a)). With increasing power, the minimum in the electron polarization is shifted to higher magnetic field, evidencing an increase of the polarization of the nuclei and of the resulting Overhauser field. At high excitation intensity, a significant portion of the nuclei are polarized and the minimum of electron polarization is observed around $B_z = -B_N = 100mT$ which would correspond to 50% of the maximum Overhauser field. However, the parameters of II-VI QDs used to estimate this maximum field are not known with precision and this percentage is subject to caution.

2.1.4 Dynamics of coupled electron and diluted nuclear spins.

Electron-nuclear spin system in a transverse magnetic field

A transverse magnetic field dependence of the polarization rate of X^- is presented in the left panel of Fig. 2.5(b). As the transverse magnetic field is increased, we observe in the absence of DNSP (black curve, corresponding to fast $\sigma + /\sigma -$ modulation), a progressive decrease of the negative polarization rate over the first $80mT$. For a spin polarized electron and in the absence of nuclear spin polarization, two processes can contribute to the observed Hanle depolarization of X^-. The first is a depolarization of the resident electron governed by the transverse relaxation time of the spin of the electron, T_2, in an unpolarized nuclear spin bath (standard Hanle depolarization). This T_2 should give rise to a half width of the Hanle curve $B_{1/2} = B_f \approx 25mT$, deduced from the Faraday measurement in Fig. 2.5(b). The second mechanism is a precession of the hole during the charged exciton life-time. This process is expected to play a role above $50mT$ as we have seen in the time resolved polarization rates presented in Fig. 2.2(b). It is not possible to discriminate between the two mechanisms as, because of the weak polarization of the electron, they are both responsible of a small decrease of few % of the circular polarization rate.

More interesting is the comparison with the data where a DNSP is created (red curve on the left panel of Fig. 2.5(b)). In this later case, a fast decrease of the negative polarization rate is observed when increasing the transverse field from 0 to $10mT$. The half width at half maximum of the depolarization curve is $\approx 5mT$. This efficient depolarization of the resident electron is due to the precession of the coupled electron-nuclei system [104, 117, 27]. After this fast depolarization

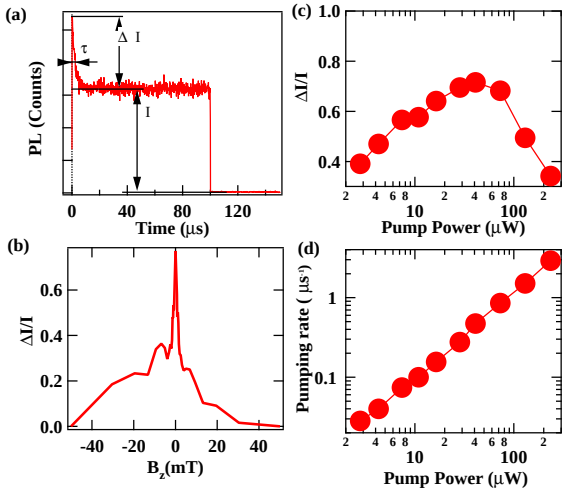

Figure 2.7 Variation of the amplitude (c) and characteristic time (d) of the DNSP transient under $\sigma+$ excitation (an exemple is presented in (a)) as a function of the excitation intensity at B_z=0mT with a constant dark time $\tau_{dark} = 50\mu s$. (b) Variation of the amplitude of the DNSP transient with a magnetic field applied along the QD growth axis.

of the electron, the negative polarization rate reaches the value observed in the absence of DNSP (*i.e.* under fast $\sigma+/\sigma-$ modulated excitation, black curve). This is also observed in the modulation frequency dependence of the polarization rate presented in Fig. 2.2(a).

We observe that the depolarization curve in transverse magnetic field in the presence of nuclear spin polarization (Fig. 2.6(a)) strongly depends on the excitation power and deviates from a Lorentzian shape at high excitation power. For the later case, the negative polarization rate seems to be weakly affected by the first few mT of transverse magnetic field, and then decreases abruptly.

The width of such depolarization curve is typically 50mT in a singly charged InAs/GaAs QDs in the presence of nuclear spin polarization [35]. In InAs QDs, an influence of the magnetic anisotropy of the nuclei produced by the in-plane strain is also observed in the transverse magnetic field dependence of the Overhauser field [41, 78]. This cannot be the case in CdTe QDs as the nuclear spins I=1/2 for Cd and Te.

The power dependence observed in our system could arise as the electron is pumped faster than the precession in the transverse applied ($\tau^e_{press} = 4ns$ at $B_x = 5mT$). At hight excitation intensity, the resident electron is replaced by an injected spin polarized electron faster than the precession in the transverse magnetic field. The depolarization of the electron spin is then given by the power dependent Hanle curve $S_z(\Omega) = S_z(0)/(1+(\Omega\tau)^2)$ with $\Omega = g_e\mu_B B/\hbar$ and $1/\tau = 1/\tau_p + 1/\tau_s$ with $1/\tau_p$ the pumping rate and $1/\tau_s$ the electron spin relaxation rate.

However, this power broadening does not explain the slight deviation form the Lorentzian shape we observed at high excitation intensity in (Fig. 2.6(b)).

The creation of DNSP could also be faster than the nuclei precession ($\tau^N_{press} = 5\mu s$ at $B_x = 5mT$). The decrease of the electron polarization in a transverse magnetic field can then be influenced by the decrease of the steady state nuclear field. As a result of this decrease, the total in-plane component of the magnetic field which controls the electron precession increases more slowly than the external field B_x: the precession of the electron would be efficiently blocked by the Overhauser field, and the electron polarization would be conserved. Such a scenario would be specific to II-VI quantum dots, where the build-up of DNSP is fast enough to block the precession of nuclei. This point requires further investigation.

Dynamics of the nuclear spin polarization

In order to analyze quantitatively the build-up time and the characteristic amplitude of the polarization transient induced by the DNSP, we performed a time-resolved measurement using a $100\mu s$ pulse of a $\sigma+$ helicity, followed by a $50\mu s$ dark time during which the DNSP relaxes partially (quantitative analysis of this relaxation will be done in the next section and is indeed found to occur on a time-scale shorter than $50\mu s$ for $B_z < 5mT$). This experimental configuration enables us to fit the observed DNSP transient by an exponential variation, permitting to extract a characteristic rate $1/\tau$ and amplitude ΔI (Fig. 2.7(a)).

We observe in Fig. 2.7(d), a linear increase of the pumping rate with the excitation power. While the build up of DNSP takes a few ms in III-V materials at $B = 0T$ [100], it occurs in the μs range in our case. This results from the strong localization of the electron in II-VI quantum dots: the built-up rate of DNSP scales as[107] $|\Psi_e|^4$ so that we typically expect $\tau_{II-VI}/\tau_{III-V} \approx 8000^2/(10^5)^2 \approx 5.10^{-3}$.

The amplitude of the pumping transient ($\Delta I/I$) presented in Fig. 2.7(c) increases linearly at low excitation power, reaches a maximum and decreases at high power. The increase is attributed to an increase of the nuclear spin polarization. The reduction at high excitation power likely comes from a decoupling of the dynamics of the electron spin from the fluctuating nuclear spin. As we have already seen in Fig. 2.4(c), at high excitation intensity, optical pumping of the electron spin becomes faster than the precession in the fluctuating field of the nuclear spin B_f and the measured polarisation rate of the X^- becomes less sensitive to the polarization of the nuclei. A similar decrease of the amplitude of the transient is observed under a magnetic field of a few mT applied along the QD growth axis.

The magnetic field dependence, of $\Delta I/I$ is shown in Fig. 2.7(b). We observe an important decrease of $\Delta I/I$ as soon as a few mT are applied along the QD growth axis z. This fast decrease mainly comes from the increase of the relaxation time of the DNSP under magnetic field (this increase of the relaxation time is evidenced in Fig. 2.9 and will be further discussed): As the nuclear spin polarization does not fully relax during the dark time, the amplitude of the pumping transient decreases. This increase of the relaxation time explains the general shape at fields lower than a few mT. At larger fields, a decrease also occurs when the static

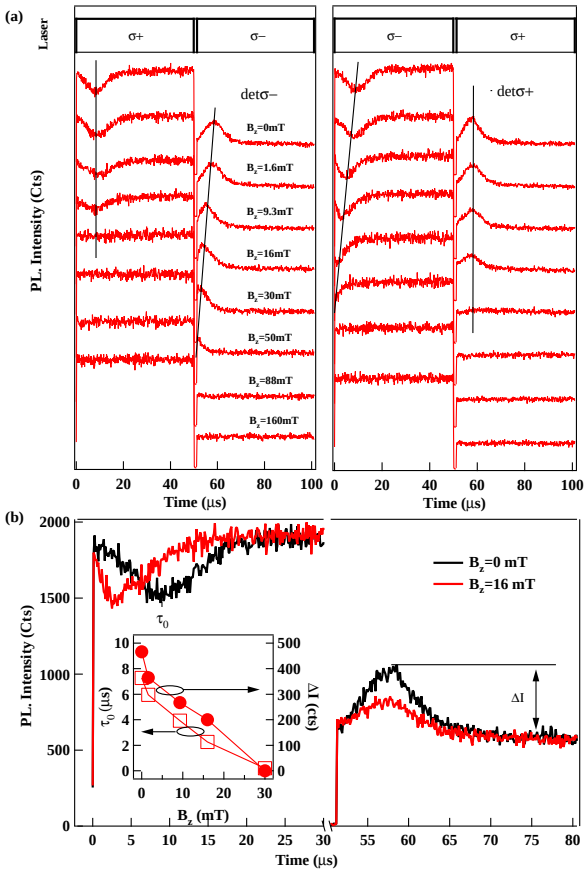

Figure 2.8 (a) Magnetic field dependence of the destruction and build-up of the nuclear spin polarisation observed under $\sigma+/\sigma-$ modulated excitation (left: detection $\sigma-$, right: detection $\sigma+$). A detailed vue of the transients is presented in (b). The inset shows the magnetic field dependence of the transient amplitude (ΔI) and position (τ_0).

magnetic field exceed the fluctuating nuclear field. The magnetic field dependence of $\Delta I/I$ presents an asymmetry as the magnetic field is reversed. Similarly to the calculated asymmetry presented in Fig. 2.1 and the observed asymmetry presented in Fig. 2.5(a), this is the signature of the creation of an effective internal field with well defined direction. The faster drop of $\Delta I/I$ in a positive magnetic field comes from the increase of the influence of the fluctuating nuclear field B_f when the external magnetic field compensates the Overhauser field. Such behavior has already been observed on ensemble of negatively charged CdSe/ZnSe QDs [2].

Our study of the DNSP build-up time scales was complemented by adding a magnetic field in the Faraday configuration in the time resolved pumping experiments. Under $\sigma+/\sigma-$ modulated excitation, each switching of the polariza-

tion results in an instantaneous (on the time-scale of the nuclear spin dynamics) change in the electron spin polarization followed by a slow evolution due to the re-polarization of the nuclei. This re-polarization process is responsible for the minimum observed in the time evolution of the negative polarization rate. Under a magnetic field, an asymmetry between the cases of $\sigma+$ and $\sigma-$ excitation is observed in the dynamics of the coupled electron-nuclei spin system (Fig. 2.8). Under $\sigma+$ excitation, as expected, the application of a magnetic field along z progressively decreases the influence of the nuclear spin fluctuations on the electron-spin dynamics and the minimum in the electron polarization rate vanishes.

The behavior of the electron polarization is different under $\sigma-$ excitation: we observe an acceleration with the increase of B_z of the destruction of the DNSP at the beginning of the $\sigma-$ pulse. This is illustrated in the inset of Fig. 2.9(b): The position of the minimum of polarization, τ_0, linearly shift from $\tau_0 \approx 8\mu s$ at $B_z = 0mT$ to $\tau_0 \approx 0\mu s$ at $B_z \approx 30mT$.

At the end of the $\sigma+$ light train, the polarized light has created a nuclear field $B_N^{\sigma+}$ anti-parallel to B_z. At some time after switching to $\sigma-$ excitation, B_N decreases and approach -B_z. At this point, the non-linear feed-back process in the electron-nuclei "flip-flops" starts and accelerates the depolarization until the DNSP vanishes. Simultaneously, the absolute value of the negative polarization reaches a minimum. Then the nuclei are re-polarized by the $\sigma-$ excitation until B_N reaches $B_N^{\sigma-}$ parallel to B_z. Consequently, as observed in Fig. 2.8(b), under $\sigma-$ excitation the destruction of the DNSP is expected to be faster than its buildup. However, it is not clear why such a magnetic field dependent acceleration is not observed during the build-up of the DNSP at the end of the transient in $\sigma+$ polarization when $B_N^{\sigma+}$ reaches -B_z. To fully understand this behavior, a complete model of the coherent dynamics of coupled electron and nuclear spins in a weak Faraday magnetic field should be developed. Such model at zero field has already shown that the minimum of $\langle S_z \rangle$ can apparently be shifted from the point $\langle I_z \rangle$=0 [122].

Nuclear spin polarization decay

In order to investigate the variation with magnetic field of the relaxation time in the dark of the DNSP, we follow the protocol shown in Fig.2.9. For a given magnetic field, we prepare a DNSP and measure after a time τ_{dark} the amplitude of the transient, corresponding to the partial relaxation of the nuclear polarization. As τ_{dark} is increased, this amplitude saturates, demonstrating the full relaxation. The variation of the amplitude of the transient with τ_{dark} is used to estimate the relaxation time of the DNSP at a given magnetic field.

The evolution of this relaxation time is presented in Fig.2.9(b). It ranges from $14\mu s$ at $B = 0T$ to $170\mu s$ at $B = 16mT$. The relaxation rate is one order of magnitude faster than the one observed by Feng *et al.* on ensemble of CdSe/ZnSe QDs[45], and the one expected from nuclear dipole-dipole interactions. Furthermore, in InAs/GaAs Schottky structure the decay in electron charged dots occurred in a millisecond time scale [100] while nuclear spin lifetime in an empty dot has been shown to exceed 1 hour. [101].

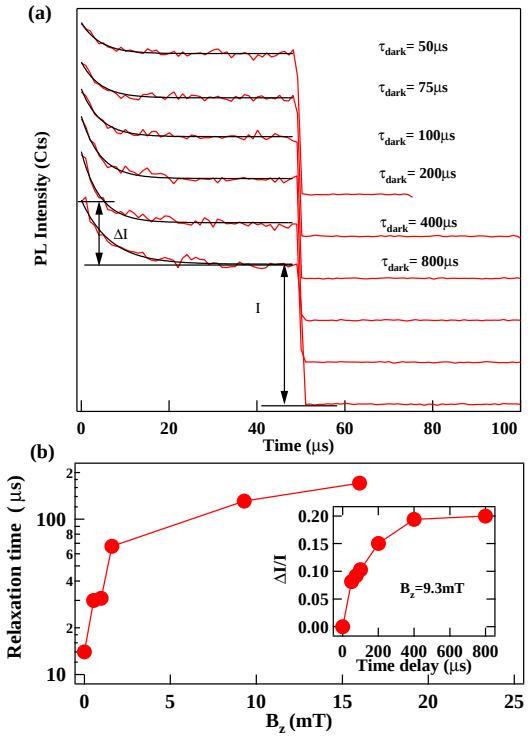

Figure 2.9 (a) Evolution of the DNSP transient, under a magnetic field B_z=9.3mT, with the variation of the dark time introduced between circularly polarized light trains of constant length. (b) Magnetic field dependence of the nuclear spin relaxation time. The inset show the evolution of amplitude of the DNSP transient with the dark time for B_z=9.3mT.

The magnetic field dependence of the DNSP relaxation presents a significant increase of the decay time over the first few mT. It has been demonstrated that a magnetic field of $1mT$ efficiently inhibits nuclear dipole-dipole interactions in III-V materials [100]. Since this interaction is expected to be smaller in our system with diluted nuclear spins, we can definitely rule out dipole-dipole interaction as a major cause of DNSP relaxation.

Co-tunneling to the close-by reservoir could be responsible for this depolarization. Via hyperfine-mediated flip-flop, the randomization of the electron spin creates an efficient relaxation of the nuclei. Following Merkulov *et. al.* [107], this relaxation time is given by:

$$T_{1e}^{-1} = \frac{2\left\langle \omega^2 \right\rangle \left\| s \right\|^2 \tau_c}{3[1+(\Omega\tau_e)^2]} \tag{2.14}$$

In this expression, ω is the precession frequency of the nuclei in the Knight field, τ_e is the correlation time of the electron (in the dark), Ω is the precession

frequency of the electron in the Overhauser field. At last, $\|s\|^2$ is equal to $s(s+1) = 3/4$. The fastest relaxation we expect from this process can be estimated taking $\Omega = \Omega_{fluc} = 2\pi/2ns^{-1}$ and $\tau_c = 10ns$. We obtain $T_{1e} \approx 200\mu s$ which is not fast enough. Therefore, we are tempted to conclude that co-tunneling alone cannot explain the observed dynamics.

Another mechanism to consider is the depolarization resulting from an electron-mediated nuclear dipole-dipole interaction. This results in exchange constants between the nuclei which typically scale as $A^2/(N^2\epsilon_z)$. The resulting rate of nuclear-spin depolarization is $T_{ind}^{-1} \approx A^2/(N^{3/2}\hbar\epsilon_z)$, where ϵ_z is the Zeeman splitting of the electron. This mechanism could explain a depolarization of the nuclei on a μs scale [73]. However, this expression gives only a minor bound to the relaxation time because the inhomogeneity of the Knight field can strongly inhibit this decay [34, 23]. A magnetic field along the z axis is expected to affect this process, progressively decoupling the nuclei from the indirect coupling created by the electron, as observed in our experiments in the first few mT (Fig.2.9). The electron-induced nuclear depolarization was demonstrated in reference [100] where the ms relaxation was completely suppressed using a voltage pulse on a Schottky diode in order to remove the resident electron.

2.1.5 Conclusion on electron-nuclei spin dynamics in II-VI quantum dots

We have shown that the optical injection of spin polarized carriers above the triplet states of the charged exciton can be use to pump the resident electron on a time-scale of $10 - 100ns$ and to create a dynamic nuclear spin polarization. At $B = 0T$, the creation of the DNSP can be as fast as a few μs, and the decay of the nuclear polarization, attributed to an electron mediated relaxation, is $\approx 10\mu s$. The measured dynamics are $\approx 10^3$ faster than the ones observed in III/V QDs at $B = 0T$. The relaxation time of the coupled electron-nuclei system is increased by one order of magnitude under a magnetic field of about 5mT. The magnetic-field dependence of the PL polarization rate revealed that the nuclear spin fluctuations are the dominant process in the dephasing of the resident electron. We demonstrated that this dephasing is efficiently suppressed by a large dynamic nuclear spin polarization at $B = 0T$. In these II-VI diluted nuclear spin QDs, the observed Overhauser field is 10 to 50 time smaller than in InAs/GaAs QDs. This should permit much simpler optical coherent control protocols of the electron spin similar to hole spins in III-V structures [83, 33].

2.2 Optical probing of the spin fluctuations of a Mn atom

We will show now how the injection of spin polarized photo-carriers in an individual QD can also be efficiently used to optically prepare the spin state of a individual Mn atoms. We will analyze, using time resolved optical pumping experiments, the main mechanisms responsible at low magnetic field for the spin dynamics a Mn atom localized in a QD.

Let us first estimate in which extend the distribution intensity in the PL of a Mn doped QD can be used to probe the spin state of the Mn atom. We will then present high resolution auto-correlation measurements allowing probing the spin quantum jumps of an individual Mn atom exchange coupled with a confined exciton.

2.2.1 Thermalization of the exciton-Mn complex

The exciton as a probe of the Mn spin state?

As illustrated in Fig. 1.12, in a Mn doped QD the relative intensities of the six emission lines observed in each circular polarization depends strongly on the applied magnetic field. The emission intensity, which is almost equally distributed over the six emission lines at zero field, is concentrated on the high energy line for the $\sigma-$ emission and on the low energy line for the $\sigma+$ emission at high magnetic field.

As the magnetic field increases, the Mn atom is progressively polarized. In time-averaged experiments, the probability to observe the recombination of the bright excitons coupled with the $S_z = -5/2$ spin projection is then enhanced. Two states dominate the spectra: $|-1/2\rangle_e|+3/2\rangle_h|-5/2\rangle_{Mn}$ in the low energy side of the $\sigma+$ emission and $|+1/2\rangle_e|-3/2\rangle_h|-5/2\rangle_{Mn}$ in the high energy side of the $\sigma-$ polarization. Changing the temperature of the Mn spin will affect the distribution of the exciton emission intensities. The PL of the exciton is then a direct probe of the magnetic state of the Mn.

The effective temperature of the Mn in the presence of the exciton, T_{Mn}, is found to depend of course on the lattice temperature but also on the laser excitation density (Fig. 2.10). For a fixed temperature and a fixed magnetic field, the asymmetry observed in the emission intensity distribution progressively disappears as the excitation intensity is increased (Fig. 2.10(a)). The variation of T_{Mn} deduced from the emission rates, is presented in the inset of Fig. 2.10(c) (7T) and Fig. 2.10(d) (0T) as a function of the excitation density. A similar excitation intensity dependence of T_{Mn} is observed in DMS quantum wells and is attributed to the heating of the Mn through their spin-spin coupling with the photo-created carriers [72]. The photo-carriers have excess energy. Via spin-flip exchange scattering they pass their energy to the Mn and elevate their spin temperature. The energy flux from the Mn to the lattice, determined by the spin lattice relaxation, will tend to dissipate this excess energy. Under steady-state photo-excitation, the resulting temperature of the magnetic ions T_{Mn} exceeds the lattice temperature. The effect of this spin-spin coupling is strongly enhanced in our system since the isolated Mn is only weakly coupled to the lattice and hardly thermalize with the phonon bath [129].

Under non-resonant excitation, the injection of an exciton changes the spin distribution of the magnetic atom. As illustrated in Fig. 2.10(b), at 0T and at low excitation intensity, an asymmetry is observed in the emission intensity distribution. This polarisation shows that a spin flip of the exciton-Mn system can

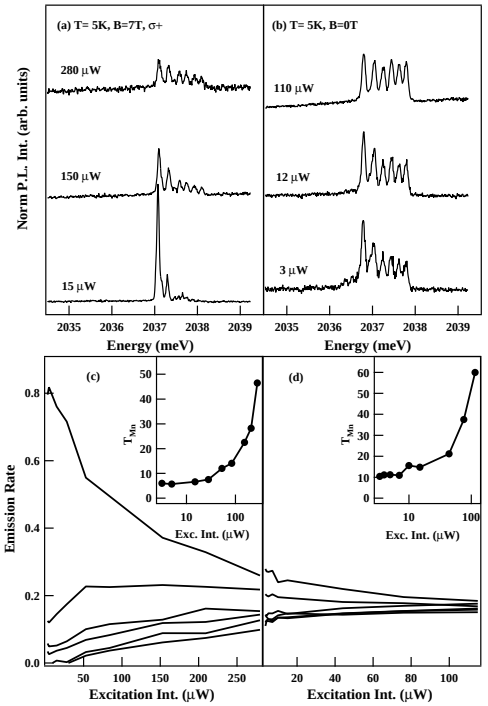

Figure 2.10 (a) Normalized PL (PL spectra divided by the total integrated intensity) in $\sigma+$ polarization versus excitation intensity for a fixed temperature (5K) and magnetic field (7T). (b) Excitation intensity dependence of the zero magnetic field emission of a single Mn-doped QD for a fixed lattice temperature T=5K. (c) and (d): extracted emission rates of each PL lines as a function of the excitation intensity at 7T (c) and 0T (d). The inset plots the extracted Mn effective temperature.

occur during the lifetime of the exciton. The exchange interaction with the exciton acts as an effective magnetic field which splits the Mn levels in zero applied field, allowing a progressive polarization of its spin distribution.

Resonant excitation of electron-hole pairs directly in the QD limits the exciton-Mn spin relaxation. This is illustrated in Fig. 2.11(b) and Fig. 2.11(c) where the emission intensity of the ground state of a Mn doped QD is presented as a function of the detection energy when the laser excitation energy is scanned through the resonant absorption of an excited state identified in a PLE spectra (Fig. 2.11(a)) [57]. This excitation energy scan reveals that the intensity distribution of the emission strongly depends on both the wavelength and on the polarization of the excitation laser. This dependence confirms that under resonant excitation there is not a complete spin relaxation of the exciton-Mn complexe during the lifetime of the exciton. As shown in Fig. 2.11(d), this long spin relaxation time combined with the fine structure of the excited states permits to create selectively a given

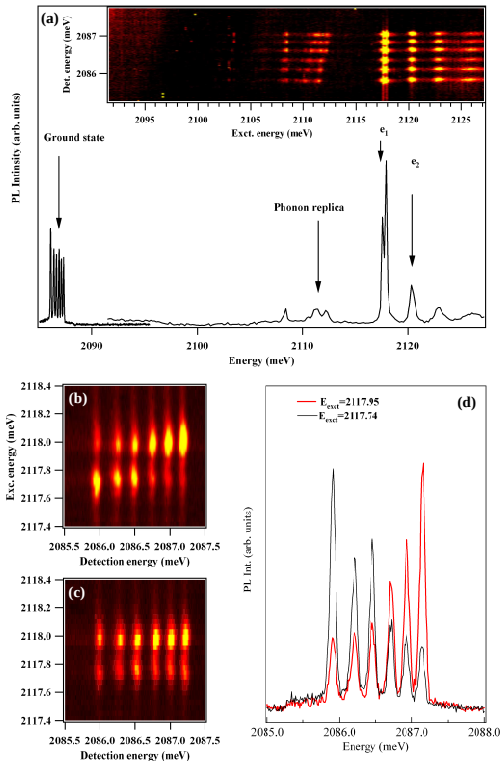

Figure 2.11 (a) Experimental PL and PLE spectra of a Mn-doped quantum dot exciton. The inset shows the contour plot of the multi-channel PLE. (b) and (c): PLE contour plots for excited state e_1 obtained for co-polarized (b) and cross-polarized (c) circular excitation and detection. (d) Resonant PL spectra obtained in co-polarized circular excitation and detection for two different excitation wavelength on e_1

spin configuration of the exciton-Mn complex by tuning the polarization and wavelength of the excitation laser.

Exciton-Mn spin flips

A direct signature of the exciton-Mn spin dynamics can be observed in the PL decay of the X-Mn complex. Figure 2.12 presents the PL decay of three different transitions of the X-Mn complex under quasi-resonant excitation by *ps* pulses. These transitions present a biexponential decay. The fast component corresponds to the radiative lifetime of the exciton, as already measured in non magnetic QDs. The long component is associated with the existence of the dark excitons [132]. Direct recombination of the dark exciton can be observed in some Mn-doped QDs because of a slight admixture of the bright states with the dark ones induced by a valence band mixing. However, the dark excitons mainly contribute to the signal by undergoing a spin flip to become bright excitons which decays radiatively. The PL decay is then determined by both radiative decay and excitons spin-

flips. The exciton decay, and particularly the amplitude of the slow component, depends strongly on the energy level observed. For the high energy lines, the slow component makes a negligible contribution to the time integrated signal. Conversely, for the low energy lines, the secondary component makes a significant contribution while the primary lifetime remains constant. In this regime, the secondary lifetime can be associated either with the dark exciton lifetime or the exciton spin flip time.

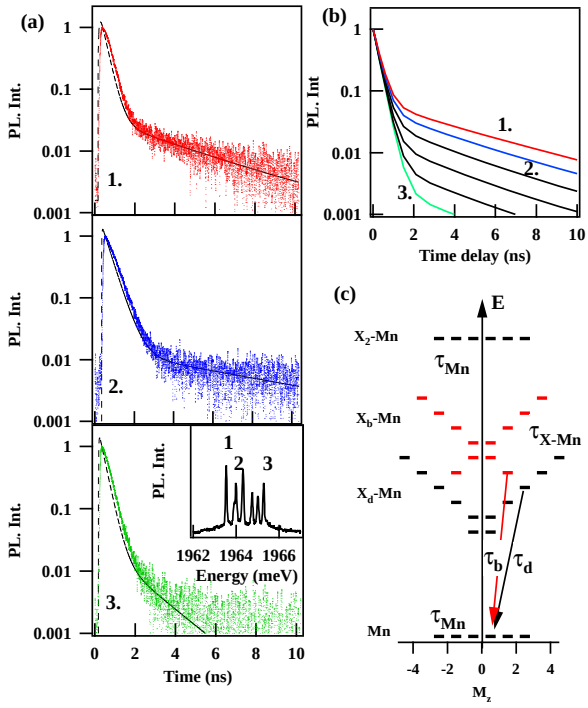

Figure 2.12 (a) Experimental time resolved PL recorded on three different energy lines (labeled 1, 2 and 3) of an X-Mn complex. The inset shows the corresponding time integrated PL spectrum. The dotted lines are the PL decay after deconvolution from the response of the set-up. (b) PL decay time calculated using the parameters T=5K, τ_b=280ps, τ_d=8ns, τ_{X-Mn}=25ns. (c) Energy levels involved in the rate equation model described in the text displayed as a function of their total angular momentum M_z.

To extract these two parameters from the PL decay curves, we compare the experimental data with a rate equation model describing the time evolution of the population of the 24 X-Mn spin levels (Fig. 2.12(c)) after the injection of a single exciton [60]. Different spin-flips times are expected depending on wether the transitions among the X-Mn levels occur with or without conservation of the energy or of the total spin. However, we consider in first approximation that the X-Mn spin-flips can be described by a single characteristic time τ_{X-Mn}. We consider, in agreement with A. Govorov *et al.* [60], that at finite temperature,

the intraband relaxation rates $\Gamma_{\gamma\to\gamma'}$ between the different spin states of the exciton-Mn complex depend on the energy separation $E_{\gamma\gamma'} = E_{\gamma'} - E_{\gamma}$. Here we use $\Gamma_{\gamma\to\gamma'}=1/\tau_{X-Mn}$ if $E_{\gamma\gamma'} < 0$ and $\Gamma_{\gamma\to\gamma'}=1/\tau_{X-Mn}e^{-E_{\gamma\gamma'}/k_BT}$ if $E_{\gamma\gamma'} > 0$. This describes a partial thermalization of the X-Mn system during the lifetime of the exciton (bright or dark). In this model, we also neglect the influence of the valence band mixing on the oscillator strength and consider that all the excitonic bright (dark) states have the same lifetime τ_b (τ_d). Because of possible hole spin-flips during the phonon assisted relaxation of the unpolarized injected carriers, we consider that the excitons with spins ±1 and ±2 are excited with the same probability at $t = 0$.

The PL decay curves can be well reproduced by this simplified rate equation model using $\tau_b = 280ps$, $\tau_d = 8ns$ and $\tau_{X-Mn} = 25ns$ (Fig. 2.12(b)). The value of τ_d controls the decay time of the long component whereas τ_{X-Mn}, larger than τ_d, reproduces the emission energy dependence of the amplitude of the long component very well. With this faster spin relaxation for the X-Mn complex than for the Mn alone, we will see in the following that the injection of spin polarized carriers can be exploited to prepare the spin state of the atom.

2.2.2 Optical probing of spin quantum jumps of a Mn atom

High resolution autocorrelation of a Mn-doped quantum dot

To directly observe the time fluctuations of the Mn spin interacting with the injected carriers, we can analyze the statistics of the photons emitted by a Mn-doped QD. This statistics is deduced from an intensity correlation function of the QD emission. Fig. 2.13(a) shows the intensity correlation function $g^{(2)}(\tau)$ of the circularly polarized ($\sigma+$) low energy line of a Mn-doped QD compared with the correlation function obtained for the overall PL of the QD. The auto-correlation function obtained for all the photons emitted by the QD is characteristic of a single photon emitter with a dip at short delay. The width of this antibunching signal is given by the lifetime of the emitter and the generation rate of excitons and its depth is limited by the time resolution of the setup. A similar experiment performed on one of the single line of the X-Mn complex still presents a reduced coincidence rate near τ=0, but it is mainly characterized by a large bunching signal with a half width at half maximum (HWHM) of about 10ns. This bunching reflects an intermittency in the QD emission. This intermittency comes from the fluctuations of the Mn spin.

To confirm this result, cross-correlation measurements were performed between different spin states of the X-Mn complex. Cross-correlation of the $\sigma+$ and $\sigma-$ photon emitted by the low energy line (Fig. 2.13(b)) shows an antibunching with $g^{(2)}(0)$=0.2 and a HWHM of about 5ns. These two different behaviors, namely the bunching of the auto-correlation signal and the antibunching of the cross-correlation signal, demonstrate unambiguously that the statistic of the QD emission is completely governed by the Mn spin fluctuations. Whereas the auto-correlation probes the time dependence of the probability for the spin of the Mn

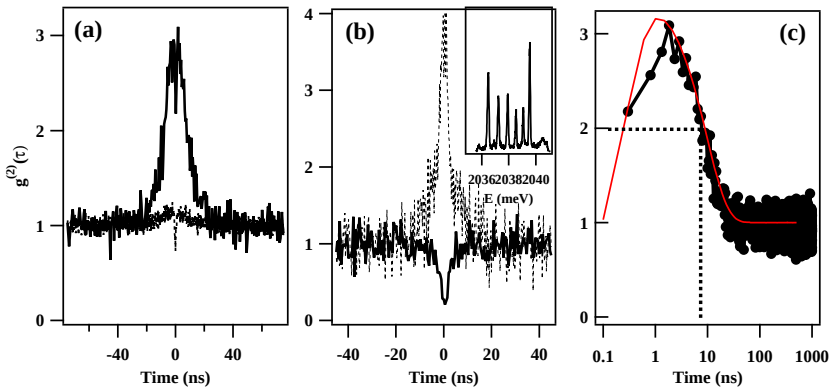

Figure 2.13 (a) Auto-correlation function of the intensity collected in $\sigma+$ polarisation on the low energy line of the X-Mn complex (solid line) and on the overall PL spectra (dotted line). (b) Circularly polarized cross-correlation function (solid line) and auto-correlation (dotted line) on the same line as in (a) but for a larger excitation intensity. The inset shows the PL spectrum of the corresponding QD. (c) Experimental auto-correlation function and theoretical function calculated with the rate equation model described in the text with parameters T=5K, τ_b=280ps, τ_d=8ns, τ_{X-Mn}=25ns, τ_{Mn}=50ns and g=0.05x10^{-3}ps^{-1}.

to be conserved (S_z =+5/2 at τ=0 in Fig. 2.13(a)), the cross-correlation presented in Fig. 2.13(b) is a probe of the spin transfer between +5/2 and -5/2.

As observed in the time resolved PL measurements, fluctuations of the Mn spin occur during the lifetime of an exciton. However, they can also take place when the QD is empty. As the spin relaxation rate of the Mn is expected to be influenced by the presence of carriers in the QD, we have to consider in a simplified model at least two relaxation times, τ_{Mn} for an empty dot and τ_{X-Mn} for a dot occupied by an exciton. Their relative contributions to the observed effective relaxation time will depend on the generation rate of excitons.

The rate equation model described previously can be extended to extract an order of magnitude of the parameters τ_{Mn} and τ_{X-Mn} from the correlation experiments. Six biexciton states are added to the 24 (X-Mn)+6 (Mn) levels system (see Fig. 2.12(c)). A continuous generation rate g is considered to populate the exciton and biexciton states. The initial state of the system is fixed on one of the six Mn ground states and one monitors the time evolution of the population of the corresponding bright X-Mn state. When normalized to one at long time delay, this time evolution accounts for the correlation function of the transition associated with the considered Mn spin state.

The time evolution of the correlation function calculated using this model are presented in Fig. 2.13(c) and compared with the experimental data. At low generation rate, when the average time between two injected excitons is longer than any spin relaxation rate, τ_{Mn} and τ_{X-Mn} have distinguishable effects on the calcu-

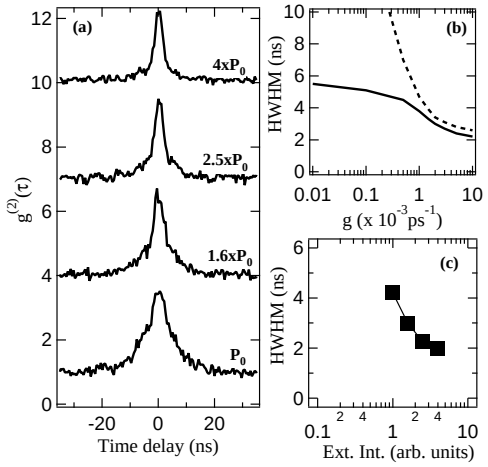

Figure 2.14 (a) Power dependence of the autocorrelation function of the hight energy line of an X-Mn complex. (b) Calculated power dependence of the HWHM of the autocorrelation function of the hight energy line. The parameters used in the model are: τ_b=280ps, τ_d=8ns, τ_{X-Mn}=20ns, and τ_{Mn}=40ns (plain line) or τ_{Mn}=4μs (dotted line). (c) Experimental HWHM of the autocorrelation signals presented in (a).

lated correlation curves. In average, the relaxation of the Mn alone (controlled by τ_{Mn}) is only perturbed by the injection of the exciton used to probe the Mn spin projection. During the lifetime of this exciton, the system relaxes with the relaxation rate τ_{X-Mn}. This produces a relaxation of the Mn spin proportional to the ratio of τ_{X-Mn} and the exciton lifetime. A reduction of τ_{X-Mn} then reduces the amplitude of the bunching curve expected for a Mn alone (because of the six available spin states, the maximum amplitude of the bunching should be six) without significantly changing its width controlled by τ_{Mn}. With the generation rate used in the measurements of Fig. 2.13(a) (a generation rate of about g=0.05x10^{-3}ps^{-1} can be deduced from the ratio of the exciton and biexciton amplitude), τ_{X-Mn} mainly affects the height of the bunching signal whereas τ_{Mn} preferentially controls its width. Then, with given values of g, τ_b and τ_d, it is possible to estimate a parameter pair (τ_{Mn},τ_{X-Mn}) that reproduces the bunching and anti-bunching curves. The bright and dark excitons lifetimes were estimated from the PL decay curves and the exciton generation rate can be estimated from the relative amplitudes of the exciton and biexciton emissions [12]. For the data presented in Fig. 2.13(c), the best fit is obtained with $\tau_{X-Mn} = 25ns$ and $\tau_{Mn} = 50ns$. The obtained X-Mn relaxation time is consistent with the value deduced from the PL decay curves. The relaxation time of the Mn alone (empty dot) appears to be 3 orders of magnitude shorter than expected from the extrapolation of measurements in bulk dilute CdMnTe under magnetic field [36].

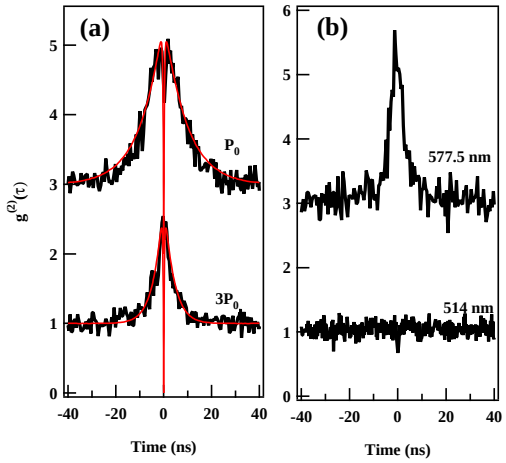

Figure 2.15 (a) Auto-correlation function on the low energy line of an X-Mn complex in $\sigma+$ polarization for excitation intensities P_0 and $3P_0$. Theoretical curves are presented in red. A reduction of τ_{X-Mn}(=15ns) and τ_{Mn}(=20ns) has to be included to describe the high excitation intensity autocorrelation curve. (b) Auto-correlation function on the low energy line of an X-Mn complex in $\sigma+$ polarization for two different excitation conditions: resonant on an excited state (577.5nm) and non-resonant (514nm).

Carriers induced Mn spin fluctuations

The observed Mn spin dynamics is not simply an intrinsic property of the localized Mn atom but depends on the optical excitation conditions. The power dependence of the correlation signal of the high energy transition of a X-Mn complex is presented in Fig. 2.14(a). Increasing the excitation power significantly reduces the width of the correlation signal. This reduction has two origins: first, when carriers are injected in the QD under quasi-resonant conditions (excitation on an excited state of the QD), increasing the carrier generation rate increases the probability of finding the QD occupied by an exciton. The spin relaxation time being shorter for an occupied dot than for an empty dot, the Mn spin fluctuates faster and the width of the auto-correlation curve decreases. This effect is illustrated by the power dependence of the HWHM of the calculated and experimental correlation curves presented in Fig. 2.14(b) and Fig. 2.14(c) respectively. At high generation rate, the width of the correlation signal is controlled by τ_{X-Mn} whereas at low excitation the photon statistics is ultimately determine by the spin fluctuations of the Mn alone. The width of the calculated correlation curves saturates at low excitation. This maximum width is controlled by τ_{Mn}. In the experiments, this saturation is not observed due to the limit in the accessible excitation power range.

However, this process is not sufficient to explain the observed excitation power dependence of the correlation signal. For instance, to reproduce the power dependence presented in Fig. 2.15(a), one has also to reduce the spin relaxation times

τ_{Mn} and τ_{X-Mn} at high excitation intensity. In Fig. 2.15(a) the best fit at high excitation power is obtained with $\tau_{Mn} = 25ns$ and $\tau_{X-Mn} = 15ns$ whereas at low excitation $\tau_{Mn} = 50ns$ and $\tau_{X-Mn} = 25ns$. This reduction of the relaxation time likely comes from the spin-spin coupling with carriers injected in the surroundings of the QD thought the background absorption observed in PLE spectra of these QDs [146].

The influence of the free carriers on the spin relaxation rate is shown by the correlation signals obtained on the same X-Mn transition for two different excitation wavelengths (Fig. 2.15(b)): resonant on an excited state (577,5nm) and non-resonant in the ZnTe barriers (514nm). These two signals are recorded with the same photon count rate, suggesting a similar occupation rate of the QD. The characteristic bunching signal observed under quasi-resonant excitation completely disappears when the excitation energy is tuned above the wetting layer absorption. As already observed in DMS quantum wells, this behavior reflects the extreme sensitivity of the localized Mn spin to the spin-spin coupling with the free carriers or the carriers relaxing in the QD [144].

For an isolated Mn atom, the spin relaxation τ_{Mn} comes only from the spin-lattice interaction [129] and a long spin relaxation time is expected. The Mn spin dynamics can be modified significantly by the presence of free carriers which are strongly coupled with both the magnetic atom and the phonons. These free carriers serve as a bypass channel for the slow direct spin-lattice relaxation.

Thermalization of the exciton-Mn complex.

The X-Mn complex is significantly coupled to the phonon bath. A partial thermalization of the X-Mn system appears directly in the amplitude of the correlation curves obtained on different energy levels of the X-Mn system (Fig. 2.16(a)) as well as in cross-correlation measurements (Fig. 2.16(b) and (c)). A finite temperature enhances the probability of the spin-flips involving an energy loss. This introduces a dissymmetry in the spin relaxation channels of the X-Mn complex. The consequence of this dissymmetry in the relaxation process is an energy dependence of the amplitude of the correlation signal. This is illustrated by the correlation curves obtained on the high ($|-1,-5/2\rangle$) and low energy states ($|+1,-5/2\rangle$) of X-Mn (Fig. 2.16(a)). For the high energy state, all the relaxation transitions within the X-Mn complex take place with an energy loss: The leakage probability is then maximum and the probability for this state to be re-populated by spin-flips from low energy states is very weak. A large bunching signal is then observed (Fig. 2.16(a)). On the opposite, the low energy level can be populated by a transfer from the high energy states, and some relaxation channels involving an absorption of energy are blocked at low temperature. The associated bunching signal is weaker (Fig. 2.16(a)).

This thermalization process directly appears if a cross-correlation of the intensity emitted by a low and a high energy levels is performed. Fig. 2.16(c) shows the correlation of the photons emitted by $|-1,-5/2\rangle$ (high energy line) and $|+1,-5/2\rangle$ (low energy line). At low excitation intensity, this correlation signal presents a clear dissymmetry. This cross-correlation measurement probe the time

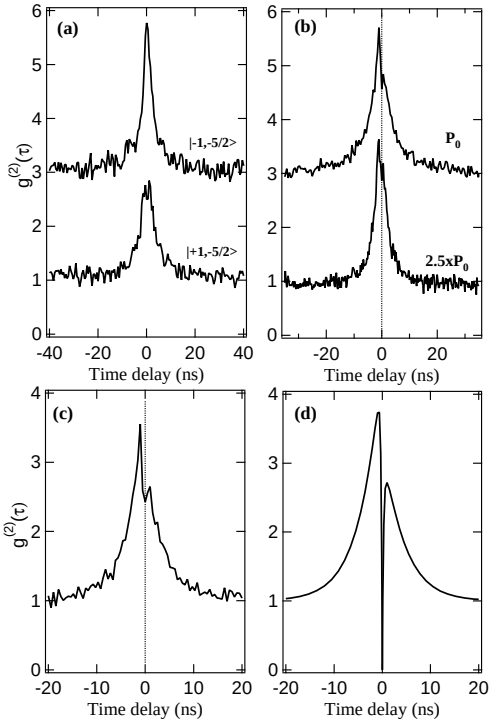

Figure 2.16 (a) Auto-correlation function of the emission intensity of the hight (upper trace) and low (lower trace) energy lines of a X-Mn complex recorded in the same circular polarization. (b) Cross-correlation function of the emission intensity of the high and low energy line recorded in $\sigma+$ and $\sigma-$ polarization respectively for two different excitation intensities. Detail of the experimental (c) and calculated (d) cross-correlation function.

dependence of the probability of finding an exciton (either $|+1\rangle$ or $|-1\rangle$) coupled with the Mn spin in the state S_z=-5/2. At positive time delay, $g^2(\tau)$ gives the probability to find the system in the state $|+1,-5/2\rangle$ knowing that at $\tau = 0$ the Mn spin projection was S_z=-5/2 (detection of a photon from $|-1,-5/2\rangle$). The situation is reversed for the negative delay where a photon from $|+1,-5/2\rangle$ acts as the trigger in the start-stop measurement and $g^2(\tau)$ gives the probability for the system to be in the high energy state $|-1,-5/2\rangle$. The dissymmetry in the cross-correlation curve reflects the difference in the spin relaxation channels available for the high ($|-1,-5/2\rangle$) and the low ($|+1,-5/2\rangle$) energy X-Mn states.

The dissymmetry in the relaxation processes is influenced by the excitation intensity: as observed in the PL decay measurements presented in Fig. 2.11, the low energy bright exciton states can be efficiently populated by spin-flips from the dark exciton states reducing the effective population loss of these states and consequently reducing the amplitude of the photon bunching. Increasing the excitation intensity decreases the effective lifetime of the dark excitons because

of the formation of the biexciton. This opens an efficient spin relaxation channel for the low energy bright X-Mn states: once a dark exciton has been created after a spin-flip, it is quickly destroyed by the injection of a second exciton with the formation of a biexciton. It can no longer flip back to the low energy bright state. This effect stop the refilling process and consequently increases the amplitude of the bunching signal. As observed in Fig. 2.16(b), increasing the excitation intensity decreases the difference in the amplitude of the corresponding bunching signal of the low and high energy lines.

These time resolved PL and photon-correlation experiments reveals a fast X-Mn spin relaxation in the range of a few tens of ns leading to a partial thermalization of the complex. Correlation measurements have to be performed under high excitation intensity and do not permit to access the intrinsic relaxation time of the Mn spin. A much longer relaxation time is expected for the Mn than for X-Mn. We will show now that this can be exploited for an optical preparation of the Mn spin.

2.3 Optical pumping of a Mn spin

We will show in this section that a high degree of spin polarization can be achieved for an individual Mn atom using quasi-resonant or fully-resonant optical excitation of the QD at zero magnetic field. Under quasi-resonant excitation, optically created spin polarized carriers generate an energy splitting of the Mn spin and enable magnetic moment orientation controlled by the photon helicity and energy. Monitoring the time dependence of the intensity of the fluorescence during a resonant optical pumping process allows to directly probe the dynamics of the initialization of the Mn spin: the optical initialization can take place in less than 100ns. The Mn spin state prepared by optical pumping is fully conserved for a few microseconds. These experiments suggest a complex carriers-Mn spin dynamics that we will analyze in the following section.

2.3.1 Optical orientation by spin polarized carriers

To optically pump the Mn spin, Mn-doped QDs were quasi-resonantly excited with a tunable CW dye laser. In order to record the dynamics of the preparation of the Mn spin (spin transients), the linear polarization of the excitation laser was modulated between two orthogonal states by switching an electro-optic modulator, and converted to circular polarization with a quarter-wave plate. Trains of resonant light with variable duration were generated from the CW laser using acousto-optical modulators with a switching time of 10 ns.

Signature of Mn spin optical orientation

Fig. 2.17 and 2.18 summarize the main features of the time-resolved optical orientation experiment. The PL of the exciton-Mn (X-Mn) complex was excited about 20 meV above the PL (top of Fig. 2.17(a)), on an excited state of the

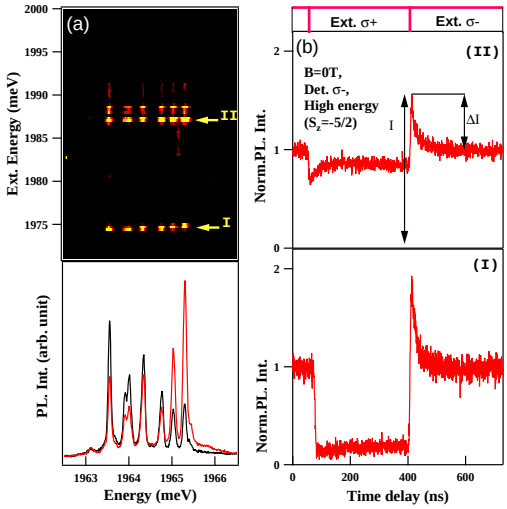

Figure 2.17 (a) PL and PLE of a Mn-doped QD (QD1) at $B = 0$ T and $T = 5$ K. The PL is detected in circular polarization under an alternate σ^-/σ^+ excitation at two different wavelengths: 1987.0 meV (black) and 1987.4 meV (red). (b) PL transient under polarization switching at $B = 0$ T. The PL is detected on the high energy line of X-Mn in σ^- polarization (Mn spin $S_z = -5/2$). Transient (I) (resp. (II)) was observed under resonant excitation at 1975 meV (resp. 1987 meV)

X-Mn complex [57]; the PL intensity was detected in circular polarization (*e.g.*, σ^-, corresponding to the recombination of the -1 exciton). The relative intensities of the six lines dramatically depend on the excitation energy (bottom of Fig. 2.17(a)): as each line corresponds to one value of the Mn spin projection S_z, the whole process creates a non-equilibrium occupation probability of the Mn spin states.

Under these conditions, switching the circular polarization of the excitation produces a change of the σ^- PL intensity (Fig. 2.17(b)) with two transients: first an abrupt one with the same sign for all six lines, reflecting the population change of the spin polarized excitons; then a slower transient reflecting an increase or a decrease of the occupation of the detected Mn spin state. This slow transient has an opposite sign for the two extreme PL lines (*i.e.*, when monitoring the Mn spin states $S_z = \pm + 5/2$, Fig. 2.18(b), and a characteristic time which is inversely proportional to the pump intensity (Fig. 2.18(a)). This is the signature of an optical pumping process which realizes a spin orientation of the Mn atom. We first discuss the details of this process, then use it to study the spin dynamics of the single Mn in the QD.

The relevant sub-levels of X-Mn and Mn are schematized in Fig. 2.18(c). For the sake of simplicity, we omit the dark exciton states which should be included for a quantitative analysis and consider that the dynamics can be described by two spin relaxation rates, one for the Mn alone $\Gamma_{Mn,G}$ and one within the X-

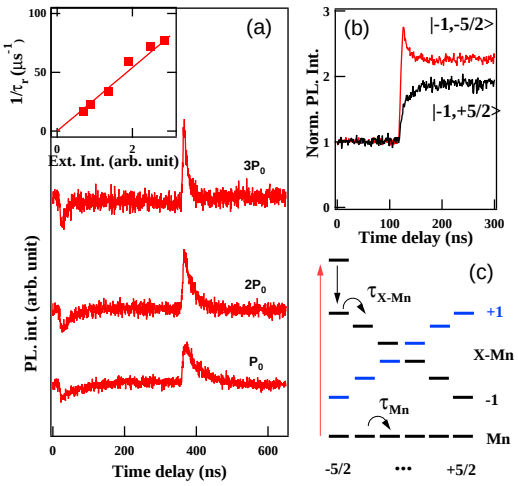

Figure 2.18 PL transients at different values of the excitation power obtained on QD1. Inset: power dependence of the inverse response time τ_r, taken at the $1/e$ point of the spin-related transient. (b) PL transients recorded in σ^- polarization on the high (S_z=-5/2) and low (S_z=+5/2) energy line of the X-Mn complex. (c) Simplified level diagram of a Mn-doped QD, as a function of Mn spin (X-Mn: bright exciton-Mn).

Mn complex Γ_{X-Mn} [60, 13]. As spin orientation results from a cumulative effect of relaxation in presence of the exciton, it can be performed only if Γ_{X-Mn} is faster than $\Gamma_{Mn,G}$. When exciting one of the low energy excited states of the QD, two mechanisms are expected to contribute to the observed spin orientation: the selective excitation of the QD can show a dependence on the Mn spin state [57], and the relaxation of the Mn spin within the X-Mn system is driven by the interaction with the spin polarized carriers which have been injected.

Under spin selective excitation, the spin relaxation of X-Mn tends to empty the spin state of the Mn which is most absorbant [60]. Under injection of spin polarized carriers, relaxation processes tend to anti-align the Mn spin with the X exchange field to reach a thermal equilibrium on the X-Mn levels [60]. Hence, optical pumping with σ^- photons for instance, tends to decrease the population of the spin state S_z=-5/2 and increase that of S_z=+5/2, as observed in Fig.2.18(b). Both mechanisms, absorption selectivity and spin injection, depend on the structure of the excited states, resulting in a pumping signal which depends on the excitation energy (Fig. 2.17). An efficient pumping of the Mn spin can be performed within a few tens of ns, showing that at $B = 0$T the spin relaxation time of the Mn alone is long enough compared to the X-Mn dynamics.

Mn spin relaxation.

Having established a method to prepare the Mn spin, we performed pump-probe experiments to observe how long the Mn polarization can be conserved (Fig. 2.19).

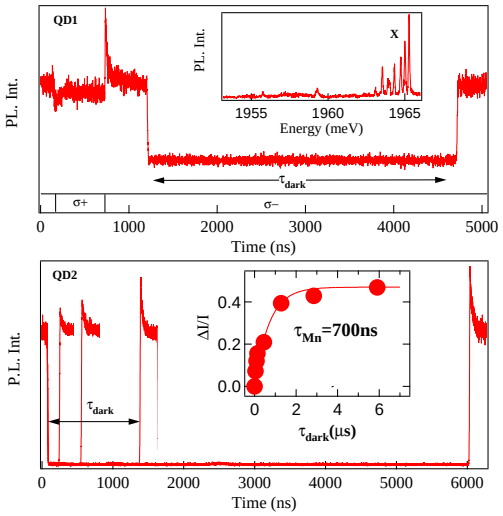

Figure 2.19 (a) PL transients recorded on QD1 (corresponding PL in the inset) under the optical polarization sequence displayed at the bottom of the plot. The spin distribution prepared by optical pumping is conserved during τ_{dark}=3.5μs. (b) PL transients recorded on QD2. The amplitude of the pumping signal is restored after $\tau_{dark}\sim$3μs. From the delay dependence of this amplitude we deduce a Mn relaxation time of ∼700ns.

We prepare a non-equilibrium distribution of the Mn spin with a $\sigma^{\pm}$ pump pulse. The pump laser is then switched off, and switched on again after a dark time τ_{dark}. The amplitude of the pumping transient after τ_{dark} depends on the Mn spin relaxation in the dark. For QD1 (Fig. 2.19(a)) no transients are observed after a dark time of 3.5μs. This demonstrates that in the absence of charges fluctuations (*i.e.* neutral QD (see inset of fig. 2.19(a))) the prepared Mn spin is conserved over μs. For QD2 (fig. 2.19(b)) the amplitude of the pumping signal is restored after $\tau_{dark}\sim$3μs. From the delay dependence of this amplitude we deduce a Mn relaxation time of ∼700ns. These two examples show that the measured spin relaxation is not intrinsic to the Mn spin but depends on its local environment (strain, presence of carriers...).

More information on the Mn local environment can be obtained from the magnetic field dependence of the optical pumping signal. For an isotropic Mn spin, the decoherence of the precessing spin in a transverse field gives rise to the standard Hanle depolarization curve with a Lorentzian shape and a width proportional to $1/T_2$ [113]. In the present case, a magnetic field in the Faraday configuration (B_z) does not change significantly the PL transients (Fig. 2.20(b)): a weak increase of the spin orientation efficiency is observed as soon as a field of a few mT is applied. By contrast, an in-plane field (B_x) induces a coherent precession of the Mn spin away from the optical axis (= QDs' growth axis), so that the average spin

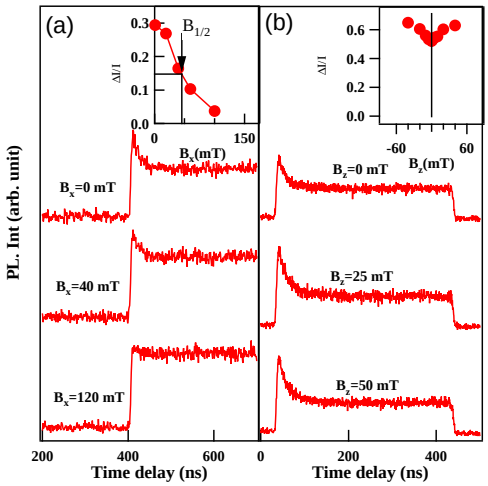

Figure 2.20 Mn spin transient as a function of a magnetic field applied in-plane (a) and out-of-plane (b) obtained on QD1. Inset: transverse field dependence of the transient amplitude $\Delta I/I$ (see Fig. 1). $B_{1/2}$ is the half width at half maximum.

polarization, and therefore the amplitude of the optical pumping signal, decays (Fig. 2.20(a)).

As we have seen in the first chapter, the ground state of the Mn presents a fine structure resulting from a hyperfine coupling with the Mn nuclear spin, the crystal field and a magnetic anisotropy $D_0 S_z^2$ induced by the biaxial strain. This fine structure controls the Mn spin dynamics at zero or weak magnetic field. At zero field, in the absence of anisotropy, the precession of the electronic spin of the Mn in its own hyperfine field should erase any information stored on the electronic spin [58]. In the presence of magnetic anisotropy, the precession of the Mn spin in the nuclear field is blocked even at $B = 0T$. The magnetic anisotropy also blocks the Mn spin precession in a weak transverse magnetic field. Then the magnetic field dependence of the optical pumping efficiency is controlled by the anisotropy D_0. We will come back to this point after a the discussion of the resonant optical pumping experiments.

Optical orientation of two Mn spins.

A similar optical orientation technique can be used to prepare the spin of two magnetic atoms embedded in the same QD. The QD is excited on resonance with an excited state. The relative intensity of the PL lines of X-2Mn depends strongly on the correlation between the polarization of the excitation and detection (Fig. 2.21(a)). As each line corresponds to a given M_z (total spin projection along z of the 2 Mn), this shows that the whole process of spin injection and relaxation creates a non-equilibrium distribution of the two Mn spin states. In opposition to the observation in QDs containing a large number of magnetic

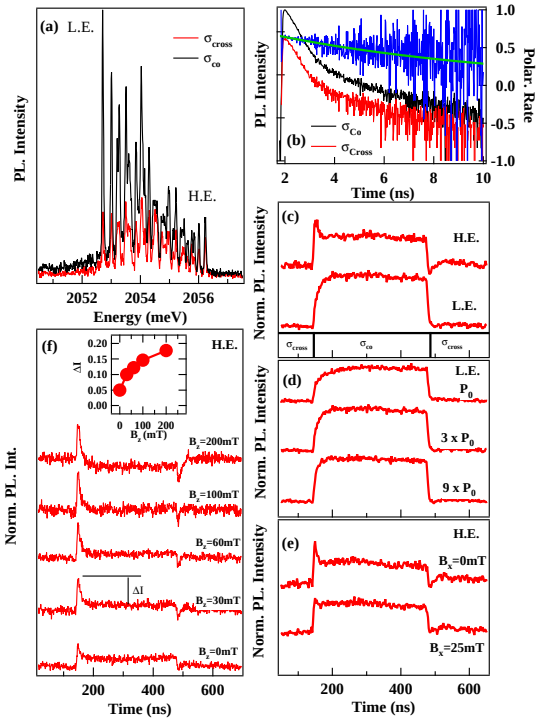

Figure 2.21 (a) PL of the exciton exchanged coupled to 2 Mn in a QD under circularly polarized excitation on an excited state (peak at 2143.5 meV in the inset of Fig. 1.1) and detected in co and cross circular polarization. (b) Time resolved polarization rate of the low energy line (L.E) under pulsed excitation at 2143.5 meV. (c) Optical orientation transients under polarization switching of the excitation detected in circular polarization on the low (L.E.) and high (H.E.) energy lines. (d) Excitation intensity dependence of the spin transients detected on the low energy line. (e) and (f) present the magnetic field dependence of the spin transients in Voight (e) and Faraday (f) configuration detected on the high energy line.

atoms [74], the polarization of X-2Mn is almost fully conserved during the lifetime of the exciton. Nevertheless, an exciton spin relaxation rate of about 10 ns can be extracted from the time decay of the circular polarization rate of the exciton (exponential fit in Fig. 2.21(b)).

The main features of time resolved optical orientation experiments performed on a QD containing 2 Mn are reported in Fig. 2.21(c-f). Switching the circular polarization of the laser produces a change of the PL intensity with two transients (Fig. 2.21(c)): first an abrupt one, reflecting the population change of the spin-polarized excitons; then a slower transient with opposite signs on the two extreme PL lines (Fig. 2.21(c)) (*i.e.*, when monitoring the Mn spin states M_z=+5 or M_z=-5) and a characteristic time in the 10 ns range which is inversely proportional

to the pump intensity (Fig. 2.21(d)). This is the signature of an optical spin orientation process which realizes a spin orientation of the two Mn atoms.

As shown in Fig. 2.21(e), the efficiency of the spin orientation increases as soon as a magnetic field, B_z, of a few tens of mT is applied in the Faraday configuration. By contrast, an in-plane magnetic field (B_x) induces coherent precession of the Mn spins away from the optical axis (QDs growth axis), so that the average spin polarization, probed by the amplitude of the optical pumping signal, decays. In this case, a transverse field of 25 mT is enough to erase the optical pumping (Fig. 2.21(f)). The timescale of the orientation of the 2 Mn as well as its magnetic field dependence are similar to what was observed for individual Mn atoms.

2.3.2 Resonant optical pumping of a Mn spin

As proposed by Govorov *et al.* [60], the direct resonant excitation of one optical transition of the ground X-Mn complex can be used to perform a direct and more efficient optical pumping of the Mn spin. In this optical pumping process, a laser drives resonantly one of the exciton-Mn transition ($|-1, S_z = -5/2\rangle$ in Fig. 2.22) with a Rabi frequency $\Omega = \mathcal{P}\mathcal{E}/\hbar$, $\mathcal{P}$ is the dipolar moment of the QD transition and $\mathcal{E}$ the amplitude of the electric field of the resonant laser. A photon absorption occurs only if the Mn spin in the QD is in the $S_z = -5/2$ spin state. The resultant exciton can radiatively recombine via the same channel, or a spin-flip process can project the X-Mn complex in a state with $S_z \neq -5/2$ with a rate $\Gamma_{Mn,X}$. After a few cycles of absorption-emission, the probability of detecting the Mn in the $S_z = -5/2$ state decreases. In this mechanism, we assume that the Mn spin is conserved once the exciton has recombined.

The conservation of the Mn spin between the recombination of an exciton and the absorption of a photon can be altered in two ways: either by a relaxation process involving an exchange of energy or by a coherent evolution [86, 59]. A coherent evolution can be neglected if the fine structure of the Mn atom is dominated by a large magnetic anisotropy along the growth axis. Otherwise, processes such as the coherent evolution of the Mn spin in the hyperfine field of the Mn nucleus or in the tetragonal crystal field leads to a change of the Mn spin state between the injection of two excitons. In that case, no optical pumping can occur. In the following, we will use $\Gamma_{Mn,G}$ to describe the characteristic rate at which the Mn spin state changes due to coherent or incoherent processes, when the QD is empty. This mechanism of Mn spin manipulation is similar to the pumping process used to prepare a single carrier spin in a QD [39, 56]. It involves an optically forbidden transition (*i.e.* spin flip of the Mn interacting with the exciton) and is based on the inequality $\Gamma_{Mn,X} > \Gamma_{Mn,G}$.

Signature of resonant optical pumping.

To demonstrate and test the efficiency of this optical pumping process, we developed a two wavelength pump-probe set-up allowing an optical initialization and read-out of the Mn spin [87]. In this experiment, a resonant circularly polarized CW laser (*resonant pump*) tuned on a X-Mn level pumps the Mn spin.

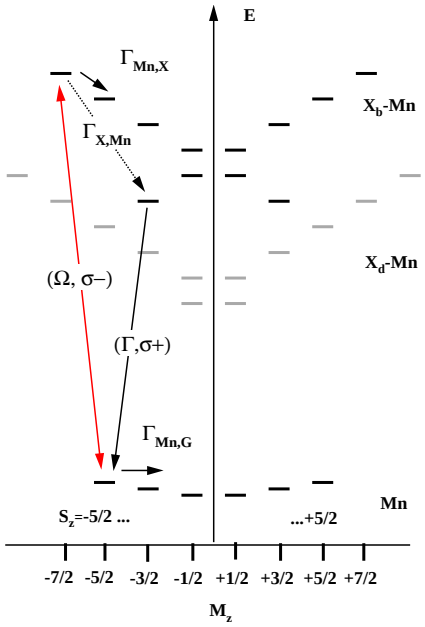

Figure 2.22 Energy levels of a Mn doped QD involved in the optical pumping mechanism described in the text (Black: bright excitons (X_b)); grey: dark excitons (X_d)). The sates are displayed as a function of their total angular momentum M_z and energy E. For the resonant optical pumping, the QD is resonantly driven on the state $S_z = -5/2$ with a $\sigma-$ laser pulse with a Rabi frequency Ω. The scattered photons obtained after a spin-flip of the exciton (rate $\Gamma_{X,Mn}$) are recorded in $\sigma+$ polarisation.

In the initial state at t=0, the Mn atom is in thermal equilibrium. The resonant creation of an exciton followed by a spin relaxation of the Mn in the exchange field of the exciton empties the spin-state under excitation. Then, a second laser train, linearly polarized and tuned on an excited state of the QD (*quasi-resonant probe*), injects excitons independently of the Mn spin state S_z. A spin relaxation of the X-Mn complex under these conditions of excitation drives the Mn atom back to an equilibrium where all spin states are equally populated. Recording one of the six PL lines under this periodic sequence of excitation, we monitor the time evolution of the probability of occupation of a given Mn spin state.

The main features of this experiment are presented in Fig. 2.23. In this example, $\sigma+$ PL signal is recorded on the low energy X-Mn line. The QD is resonantly excited on the high energy state of the X-Mn complex with $\sigma-$ photons. This excitation can only create an exciton in the dot if the Mn spin state is S_z=-5/2. After this pumping sequence, the resonant pump laser is switched off and followed by a linearly polarized excitation on an excited state (*quasi-resonant probe*). The amplitude of this quasi-resonant PL depends on the population of S_z=-5/2 and,

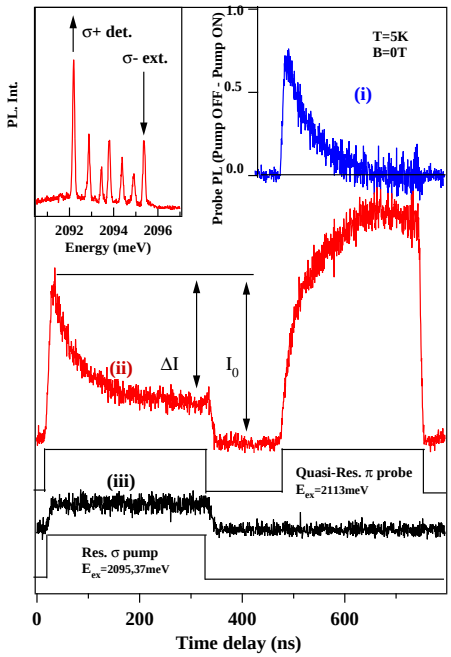

Figure 2.23 PL transients recorded on the low energy line of a Mn-doped QD (QD2) under the quasi-resonant (QD excited state: *probe*) and resonant (QD ground state: *pump*) optical excitation sequence displayed at the bottom. The inset presents the QD PL under non-resonant excitation and the configuration of the resonant excitation and detection. (i) Difference between the PL produced by the probe when the pump is OFF and when the pump is ON, (ii) PL from the pump and the probe and (iii) resonant PL produced by the pump alone. Because of the Mn spin memory in the absence of injected carriers, no signature of pumping is observed when the linearly non-resonant probe is OFF (iii). The optical pumping process is directly observed on the resonant fluorescence produced by the pump and latter on the PL from the probe laser. I_0 is the amplitude of the fluorescence at the beginning of the pump pulse and ΔI the amplitude of the transient. $\Delta I/I_0$ is the efficiency of the spin optical pumping.

at the beginning of the probe pulse, is a probe of the resonant pumping efficiency reached at the end of the pump pulse.

This is illustrated in Fig. 2.23(i) which presents the difference of the two PL signals produced by the probe when the resonant pump laser was OFF or ON in the pump-probe sequence presented underneath the curve 2.23(ii). The difference of the two PL signals reflects the population difference between a sequence with optical pumping and a sequence where $S_z = -5/2$ is evenly populated. The height of the difference signal at the beginning of the probe pulse, which reaches 75% gives a direct measurement of the efficiency of the spin optical pumping. The PL transients observed during the probe pulse corresponds to the progressive destruction of the non-equilibrium distribution prepared by the pump. This reset

process is produced by the injection of unpolarized excitons and its rapidity depends on the intensity of the probe laser.

A more direct way to probe the optical pumping process is to monitor the time evolution of the fluorescence signal observed during the resonant excitation. Excitation transfer can occur within the X-Mn complex during the lifetime of the exciton and gives rise to a weak PL on all the QDs levels. Whatever the spin relaxation processes involved in this excitation transfer, this signal depends on the absorption of the pump laser which is controlled by the occupation of S_z=-5/2: it monitors the spin selective absorption of the QD and is then a direct probe of the pumping efficiency of the Mn spin. The pumping efficiency is then given by $\Delta I/I_0 \approx 75\%$ (see Fig. 2.23), in agreement with the pumping efficiency measured on the probe sequence.

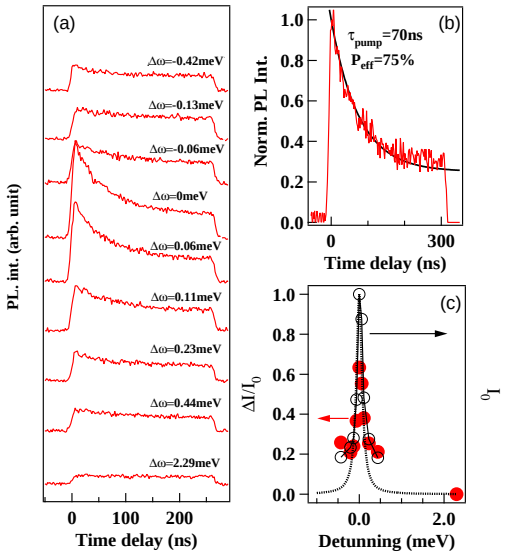

Figure 2.24 (a) Excitation energy dependence of the resonant fluorescence signal obtained on QD2 for cross circular excitation-detection on the high and low energy exciton line respectively (positive detuning corresponds to an excitation on the hight energy side of the line). (b) Detail of the resonant fluorescence transient recorded during the optical pumping process. The exponential fit (black line) gives an optical pumping efficiency P_{eff}≈75% and a pump time of 70 ns. (c) Amplitude of the resonant fluorescence signal as the excitation is tuned around the high energy line of X-Mn. The Lorentzian fit give a full width at half maximum of $80\mu eV$.

The time evolution of the PL detected on the low energy state of X-Mn under a resonant excitation on the high energy state is presented in Fig. 2.23(ii) and 2.23(iii) for two different pump-probe sequences: probe ON and probe OFF respectively. When the probe laser is switched ON, an equilibrium distribution of the Mn spin is restored by the non-resonantly injected unpolarized excitons

before each pumping pulse. The absorption, and then the amplitude of the resonant fluorescence signal is maximum at the beginning of the pump pulse and progressively decreases as the state S_z=-5/2 is emptied by the optical pumping process. When the probe laser is switched OFF in the pump-probe sequence, the resonant fluorescence transients during the pump pulse disappears and a weak constant PL is observed. This disappearance of the transient is a signature of the perfect conservation of the Mn spin distribution during the dark time between each pumping pulse. The steady state PL depends on the optical pumping efficiency which is controlled by the ratio of the relaxation rates for the Mn spin in the exchange field of the exciton and the relaxation and coherent evolution of the Mn spin in an empty dot.

Time resolved resonant fluorescence of a Mn doped QD.

The resonant fluorescence signal can be used to analyse the influence of the excitation power, wavelength and polarisation on the efficiency of the Mn spin optical pumping [87]. A detail of the time resolved resonant fluorescence signal obtained with the pump laser tuned strictly on resonance with the high energy level is presented in Fig. 2.24(b). A decrease of about 75% of the resonant PL is observed during the optical pumping process with a characteristic time of τ_{pump}=70 ns. This exponential decay reflects the decrease of the absorption of the QD induced by the decrease of the population of the state S_z=-5/2 and shows it takes a few tens of ns to initialize the Mn spin. Alternatively, one can say that the transition can be recycled for a few tens of ns before the laser induces a Mn spin-flip event. After a few tens of ns the PL reaches a steady state intensity.

Fig. 2.24(a) and 2.24(b) present the amplitude and time evolution of the fluorescence signal detected on $|+1, S_z = -5/2\rangle$ for different *pump* wavelength around the high energy level $|-1, S_z = -5/2\rangle$. A clear resonant behavior is observed in the initial amplitude I_0 of the fluorescence signal (Fig. 2.24(c)). This reflects the wavelength and excitation power dependence of the absorption of the QD. The measured width of the resonance ($\sim 80\mu eV$) is a convolution of the width of the QD's absorption in the non-linear regime and of the linewidth of the excitation laser.

As displayed in Fig. 2.25, the characteristic time and the amplitude of the optical pumping signal also depends on the excitation intensity. In the low excitation regime, as expected for a spin optical pumping process, the transient characteristic time (τ_{pump}) is inversely proportional to the pump laser intensity. A saturation behavior is clearly observed for the amplitude and the characteristic time of the resonant fluorescence transient. The saturation of the optical pumping process results from a saturation of the absorption of the resonantly excited excitonic level. Indeed, the population of a two level system driven by a resonant excitation laser is given by [49]: $n_{eq} = \Omega^2(\frac{T_1}{T_2})/2(\Delta\omega^2 + \frac{1}{T_2^2} + \Omega^2\frac{T_1}{T_2})$, where Ω is the Rabi frequency, $\Delta\omega$ the detuning between the excitation laser and the excitonic transition, T_1 and T_2 the lifetime and the coherence time of the exciton respectively. The rate of the spin optical pumping process, which is

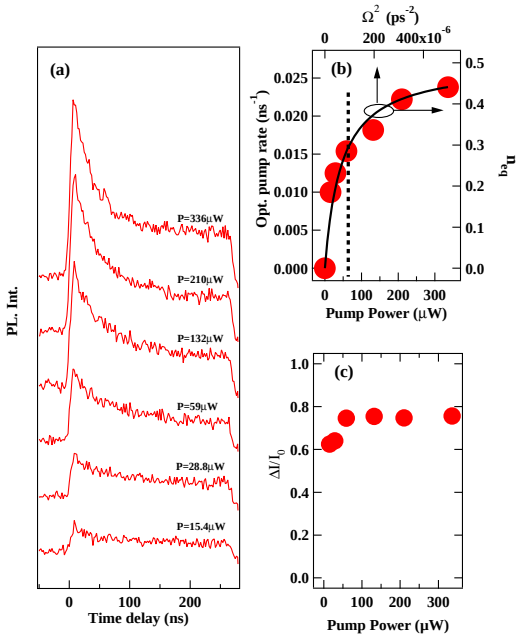

Figure 2.25 (a) Excitation power dependence of the resonant fluorescence signal of QD2. (b) Excitation power dependence of the optical pumping rate. The vertical dotted line shows the excitation power range used in the optical pumping wavelength dependence presented in Fig. 32.24. (c) Excitation power dependence of the optical pumping effieciency. The solid lines in (b) represent the calculated evolution of the population of a resonantly excited two level system as a function of the square of the Rabi frequency which is proportional to excitation intensity. In this calculation, T_1=180ps, T_2=50ps and Ω^2 is adjusted to reproduce the observed saturation.

proportional to n_{eq}, is expected to increase with the excitation Rabi frequency until it reaches a saturation value when the Rabi frequency is larger than the spontaneous emission rate ($\Omega \gg T_1^{-1}$). n_{eq} obtained with T_1=180ps, T_2=10ps [120] and $\Delta\omega$=0 is compared with the optical pumping signal in Fig. 2.25(b) and 2.25(c). A good agreement with this simple model describing the population of a two level system resonantly excited by a CW laser is obtained. The efficiency of the optical pumping (Fig. 2.25(c)) is almost constant over the covered excitation intensity range showing that even at low excitation intensity, the Mn spin relaxation time remains much longer than the optical pumping rate.

In the saturation regime, if $S_z = -5/2$ the QD is in the $|-1, S_z = -5/2\rangle$ state half of the time in average. Taking for granted that $\Gamma_{Mn,X} \gg \Gamma_{Mn,G}$, the rapidity of the optical pumping process is no longer controlled by the rate at which excitons are injected but depends only on the relaxation rate from the state $|-1, S_z = -5/2\rangle$ to other X-Mn levels with $S_z \neq -5/2$. Therefore, the pumping rate in the saturation regime gives an estimation of the spin-flip rate of the Mn in the exchange field of the exciton $\Gamma_{Mn,X}/2 \approx \Gamma_{pump}$ and a relaxation

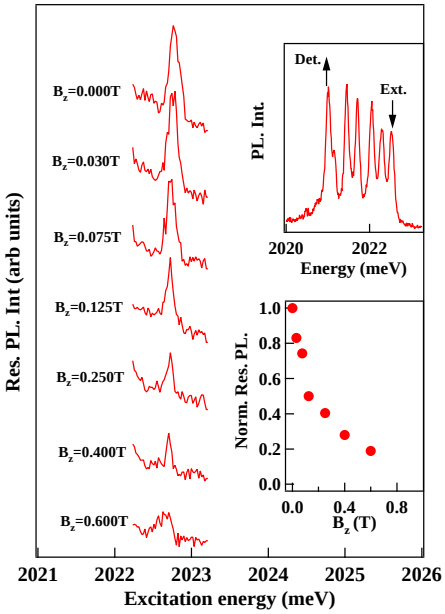

Figure 2.26 Magnetic field dependence of the photoluminescence excitation (PLE) spectra obtained on the ground state of a Mn doped QD (QD3) under circularly cross-polarized excitation-detection. The insets presents a PL spectra of QD3 (arrows point the excitation and detection wavelength) and the magnetic field (B_z) dependence of the amplitude of the resonant PL signal.

time $\tau_{Mn,X} \approx 20ns$ in agreement with the value deduced from photon correlation measurements [13].

For a given Mn spin state, the amplitude of the resonant fluorescence depends on an applied external magnetic field. This is illustrated in Fig. 2.26 where the PLE spectra detected on the low energy line when the excitation laser is tuned around the high energy level are presented for different magnetic fields in Faraday geometry. The PL intensity is divided by two for a magnetic field of about 0.1T. This reduction could either be explained by a reduction of the spin flip rate of the exciton or an increase of the efficiency of the optical pumping of the Mn spin. The Zeeman energy of the exciton in this weak magnetic field is not significant compared to the exchange field with the Mn: the dynamics of the exciton coupled with the Mn is unlikely to be affected by this small energy change. Indeed, the Zeeman splitting of the Mn in an empty dot cancels the nondiagonal coupling induced by the tetragonal crystal field or an anisotropic strained distribution at the Mn atom location [124, 86]. It improves the Mn spin conservation thus accounting for the increase of the optical pumping efficiency in a weak magnetic field. A model of optical pumping taking into account the Mn spin coherent dynamics and its magnetic field dependence will be presented in the next section.

2.4 Carriers and Mn spin dynamics in a quantum dot

The optical orientation and optical pumping experiments we have presented require an efficient Mn spin relaxation in the presence of an exciton in the QD. They also suggest a strong influence of the Mn fine and hyperfine structure of the Mn on the pumping process and its magnetic field dependence. We will analyze in this section the influence of the coherent dynamics of the Mn on the efficiency of optical pumping and discuss some possible origin of the fast carrier-Mn spin dynamics in order to explain the optical pumping dynamics.

2.4.1 Influence of the Mn coherent dynamics on the optical pumping

We first consider the coherent evolution of coupled electronic and nuclear spins optically coupled to a single exciton-Mn state (see Fig. 2.27). The states (S_z=+5/2,I_z) of the Mn are coupled by a resonant laser to the exciton states (J_X=-1,S_z=+5/2,I_z). This situation corresponds to the optical pumping experiments performed under resonant optical excitation of one transition of X-Mn.

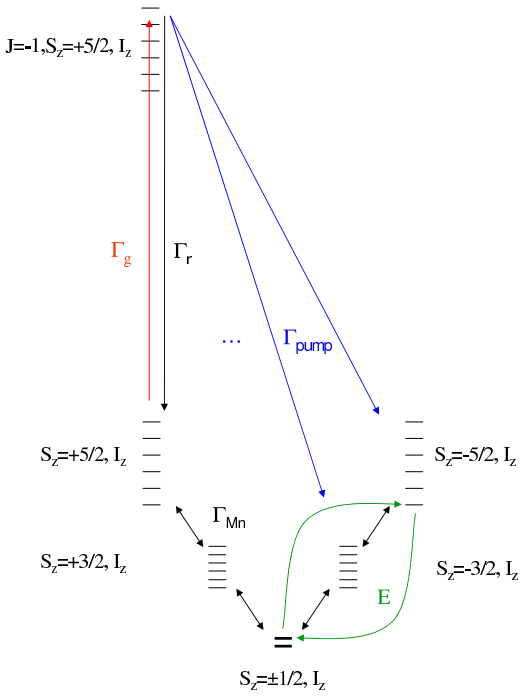

Figure 2.27 Scheme of the energy levels and transitions rates involved in the resonant excitation model. Ω is the coupling with the laser, γ_d is a pure dephasing of the exciton, Γ_{Mn} is the relaxation rate of the Mn, Γ_r is the optical recombination rate of the exciton. An effective relaxation rate of the exciton-Mn complex Γ_{pump} can be introduced for a description of the optical pumping effect.

The Hamiltonian of the coupled electronic and nuclear Mn spins in the ground state is given in equation (1.21) of Chapter 1. We consider only one exciton state $|+1\rangle$ laser coupled with one state of the Mn $|S_z = +5/2, I_z\rangle$ with a generation rate Γ_g. This approximation is justified in strongly confined QDs with a large X-Mn splitting resonantly excited by a narrow band laser. The exciton can relax to the ground state by conserving the Mn spin with a rate Γ_r. It can heve a pure dephasing γ_d. The relaxation of the Mn spin in the ground state is described by a relaxation rate Γ_{Mn} coupling one by one the different spin states S_z. We do not consider any spin relaxation for the nuclear spin which is considered to be frozen in the timescale of the data presented here. An effective spin relaxation rate ($\Gamma_{pump} = 1/T_{pump}$) for the exciton-Mn complex is introduce. It allows a transfer of population from the state $|J_z = -1, S_z = +5/2, I_z\rangle$ to any other spin state of the Mn $|S_z\rangle$ with I_z unchanged. This is a simplified effective way to describe the complex X-Mn spin dynamics at the origin of the optical pumping. The details of these relaxation channels will be discussed in the next section. At low magnetic field (lower than a few hundreds mT), we also consider that the hole Mn exchange interaction is much larger than the Mn Zeeman energy and we will neglect its influence on the exciton-Mn state.

We compute the time evolution of ϱ, the 42x42 density matrix describing the population and the coherence of the 36 nuclear (I_z) and Mn spins (S_z) in the ground state and 6 exciton sates (+1,S_z=5/2,I_z) in the excited state. The general form (Lindblad form) of the master equation which governs the evolution of ϱ is given by:

$$\frac{\partial \varrho}{\partial t} = -i/\hbar[H, \varrho] + L\varrho \tag{2.15}$$

$L\varrho$ separates into one contribution for each coupling or decay channel resulting from an interaction with the environment [145]:

1- The incoherent population transfer from level j to level i in an irreversible process associated with a coupling to a reservoir. It results in a one way exponential decay that can be described by the operator:

$$L_{inc,j\to i}\varrho = \frac{\Gamma_{j\to i}}{2}(2|i\rangle\langle j|\varrho|j\rangle\langle i| - \varrho|j\rangle\langle j| - |j\rangle\langle j|\varrho) \tag{2.16}$$

where $\Gamma_{j\to i}$ is the incoherent relaxation rate from level j to level i. This form of operator can describe the radiative decay of the exciton (irreversible coupling to the photon modes) or the relaxation of the Mn spin (irreversible coupling to the phonon modes). Such term can also be used to describe the optical generation of an exciton in the low excitation regime were one can neglect the energy shift induced by the strong coupling with the laser field. The influence of a strong coupling with the laser field will be discussed in chapter 3.

2- A pure dephasing (*i.e.* not related to an exchange of energy with a reservoir) can also be introduced and is described by an operator of the form:

$$L_{deph,jj}\varrho = \frac{\gamma_{jj}}{2}(2|j\rangle\langle j|\varrho|j\rangle\langle j| - \varrho|j\rangle\langle j| - |j\rangle\langle j|\varrho) \tag{2.17}$$

where γ_{jj} is a pure dephasing rate.

This model of Mn spin coherent dynamics under resonant optical excitation can be used to analyze the origin of the residual fluorescence signal observed under optical pumping conditions: Experimentally, the optical pumping efficiency nether reach 100% and a resonant fluorescence signal can be observed.

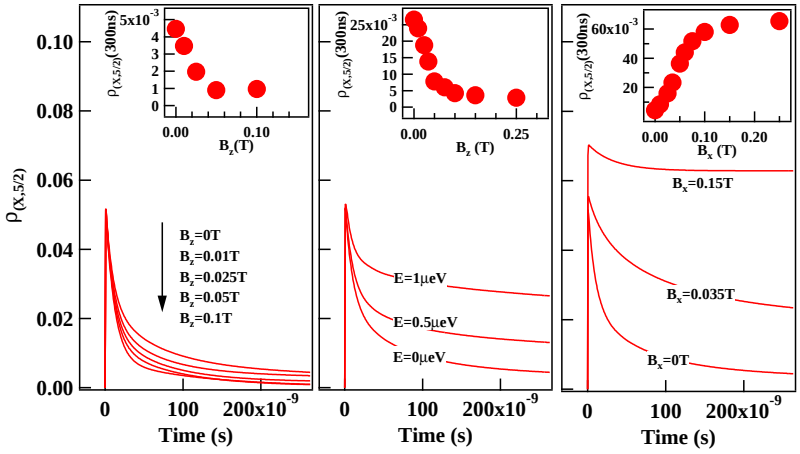

Figure 2.28 (a) Magnetic field dependence of the optical pumping transient calculated with D_0=5μeV and E=0μeV. The inset shows the amplitude of $\rho_{X,5/2}$ at 300ns as a function of a magnetic field applied along the QD growth axis B_z. (b) Optical pumping transients calculated for different values of E with D_0=5μeV. The inset shows the amplitude of $\rho_{X,5/2}$ at 300ns as a function of magnetic field B_z applied on a QD with $E = 1\mu$eV along z. (c) Optical pumping transients calculated for different values of transverse magnetic field B_x with D_0=5μeV and E=0μeV. The inset shows the amplitude of $\rho_{X,5/2}$ at 300ns as a function of the magnetic field B_x . In all the calculations A=0.7μeV and a=0.32μeV. The relaxation times used in the model are T_{pump}=20ns, T_g=0.5ns, T_{Mn}=1μs and T_r=0.25ns.

As confirmed by the calculated PL transients presented in Fig. 2.28(a), the coherent coupling with the nuclear spin prevents the optical pumping efficiency to reach 100%. This is particularly pronounced for a weak value of D_0. As observed experimentally, this effect can be suppressed by a weak magnetic field applied along the QD growth axis. This evolution is qualitatively reproduced by our simple model (Inset of Fig. 2.28(a)). When the Zeeman energy exceeds the hyperfine coupling and the tetragonal crystal field energies, the coherent precession is blocked and the efficiency of optical pumping is maximum.

An anisotropy in the strain distribution at the Mn spin location, resulting in a term $E(S_x^2 - S_y^2)$ in Mn fine structure, can also be responsible for a poor optical

pumping efficiency. This is illustrated in Fig. 2.28(b) where the influence of E on the optical pumping transient are presented. Even a weak anisotropy of the strain ($E = 0.5\mu$eV compared to the isotropic term D_0=5μeV) significantly reduces the efficiency of the optical pumping. In the presence of this anisotropy, a magnetic field along z has a strong influence on the optical pumping transient. The pumping is almost fully restored and the resonance fluorescence almost suppressed within the first 100mT, in good agreement with experimental data [87]. This model confirms that the presence of anisotropic strain at the Mn location is responsible for the magnetic field dependence of the resonance fluorescence signal and the poor efficiency of the optical pumping in most of the Mn doped QDs.

The fine and hyperfine structure of the Mn also control the transverse magnetic field dependence of the optical pumping. In this case, as we have already seen above in the optical orientation experiments (Fig. 2.20), the determinant parameter is the magnetic anisotropy D_0 which blocks the precession of the Mn spin at low magnetic field (Fig. 2.28(c). The width the depolarization curve in a transverse field is then controlled by D_0. A HWHM of about 50mT as observed experimentally corresponds to a magnetic anisotropy term $D_0 \approx$=6μeV [86]. This suggest a partial relaxation of strain in the QD plane (in a fully strain CdTe layer on ZnTe, D_0=12μeV).

2.4.2 Mechanism of photo-induced Mn spin orientation

We have observed in time resolved PL experiments, in photon correlation measurements and in optical pumping experiments (both non-resonant and resonant) a spin relaxation within the exciton-Mn complex in the tens of ns range. This fast exciton-Mn spin relaxation permits an optical preparation of the Mn spin. To understand the spin-flips involved in the mechanism of optical orientation, we will discuss here the main spin relaxation channels within the exciton-Mn complex. To observed these relaxation channels, we perform resonant excitation on a given line of the exciton-Mn complex, and detect the PL emitted on the other lines. The spectral distribution of the scattered photons under resonant excitation reveals the main spin-flip processes.

First, we report results on a QD presenting a very large splitting and a weak optical pumping at $B = 0T$. This poor efficiency of the optical pumping can be attributed to the local strain environment. This case is interesting for a study of the exciton-Mn dynamics: the QD line under resonant excitation is always absorbant and the scattered photons reflect the fastest spin relaxation channels. The large splitting also permits to observed the spin-flips channels among the bright exciton levels.

In Fig. 2.29(a), we present the following PLE measurements: the detection window is set on the low energy side of the X-Mn PL, while a circularly cross-polarized laser scans the high energy lines. A PL spectrum obtained under quasi-resonant excitation is displayed at the bottom to identify the lines. The three PLE detected on the low energy lines of X-Mn associated with the Mn spin states +5/2, +3/2 and +1/2 are presented as plain lines. In addition, PLE spectra detected on

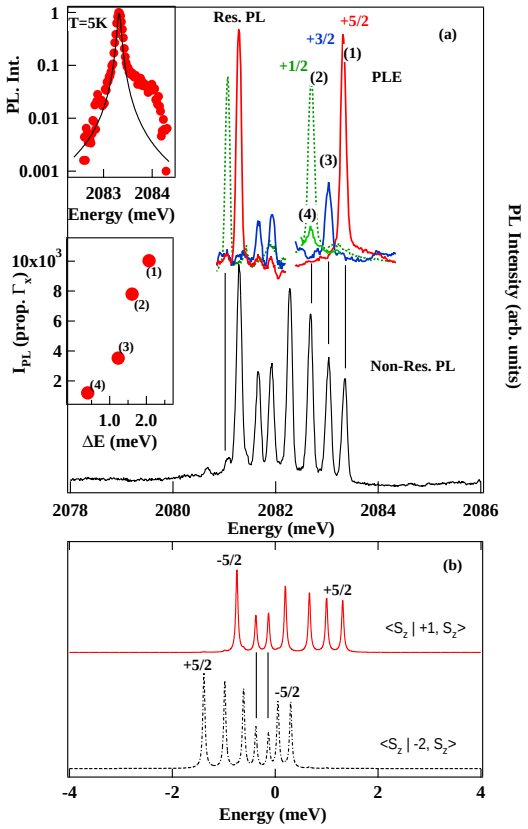

Figure 2.29 PLE spectra and resonant PL obtained on the ground state of a Mn doped QD. The resonant PL is obtained under circularly cross-polarized excitation-detection. The top-inset presents an enlarged view of the PLE obtained under excitation and detection on the S_z=+5/2 state. The black line is a Lorentzian fit with a half width at half maximum of 80μeV. The asymmetry of the absorption line comes from a coupling with acoustic phonons. The lower inset presents the evolution of the intensity of the PL as a function of the energy splitting between the two states involved in the transition. The labels (1-4) refer to the resonances given in the text. (b) Calculated bright $|+1\rangle$ and dark $|-2\rangle$ energy levels with I_{eMn}=-0.07 meV, I_{hMn}=0.245 meV, I_{eh}=-550 meV, $\rho_s/\Delta_{lh} = 0.11$, η=20μeV and $\delta_2 = 0$. Because of the large carrier-Mn exchange coupling, the dark exciton levels overlap with the bright excitons. The valence band mixing couples the states $|+1, -3/2\rangle$ and $|-2, -1/2\rangle$ and gives rise to an additional PL line.

a dark exciton state is also presented (dotted line). The corresponding resonant PL spectra obtained at the maximum of the PLE signal are displayed. To facilitate the attribution of the observed lines to the different bright or dark exciton states, a calculation of the energy levels is presented in Fig. 2.29(b). This QD presents some valence band mixing and a large overlap between bright and dark excitons

induced by the strong exciton-Mn coupling. Dark and bright excitons are then coupled by hole-Mn flip-flops and additional lines are observed in the low energy side of the spectrum.

From these PLE spectra and resonant PL spectra, it follows that the most efficient spin relaxation channels within the X-Mn system do conserve the Mn spin. For instance, an excitation with $\sigma+$ photons on the high energy line (state $|+1, S_z = +5/2\rangle$) produces $\sigma-$ PL mainly on the low energy state $|-1, S_z = +5/2\rangle$. A similar behavior is observed for an excitation on $|+1, S_z = +3/2\rangle$ which generate a PL on $|-1, S_z = +3/2\rangle$. In both cases, this excitation transfer corresponds to a spin flip of the exciton from $|+1\rangle$ to $|-1\rangle$ with a conservation of the Mn spin.

More surprising, an excitation on $|+1, S_z = +1/2\rangle$ produces the strongest PL on an exciton level formed mostly of a dark state with a weak oscillator strength (weak signal in the non-resonant PL plotted at the bottom of Fig. 2.29(a)). Using Fig. 2.29(b) we can attribute this dark state to either $|-2, S_z = +3/2\rangle$ or $|+2, S_z = -3/2\rangle$. A hole-Mn spin flip could explain a transfer to $|-2, S_z = +3/2\rangle$. Such kind of transition occurs with a change in the spin of the Mn and could be an important ingredient to explain the optical orientation of the Mn in the exchange field of the exciton. Before going to a more detailed discussion of these transitions to dark states, let us note that the intensity of the resonant PL (which reflects the probability of transfer during the life-time of the exciton) increases with the inter-level splitting of the two-states involved in the transition. This suggest that an acoustic phonon process is responsible for the efficient exciton spin flips.

To analyze more in detail the possible transfer to the dark states, we consider the spin-flip channels in a less split QD, where all the dark states are well separated from the bright states and can be observed at zero magnetic field on the low energy side of the PL spectra (Fig. 2.30). In the PLE experiments presented in Fig. 2.30, the detection window is set on the dark states while a circularly cross-polarized laser is scanned on the three high energy levels of the bright exciton. Let's describe the three successive resonances we observe.

(1): An excitation on $|+1, S_z = +1/2\rangle$ produces the dominant PL on a dark states associated with a Mn spin state $\pm 3/2$. As a Mn spin flip by two units is unlikely, we then attribute this PL to $|-2, S_z = +3/2\rangle$. The transfer between these states involves a hole-Mn spin flip. The second contribution comes from the state $|+2, S_z = +1/2\rangle$. It corresponds to a transfer conserving the Mn spin and involving a spin flip of the electron.

(2): An excitation on $|+1, S_z = +3/2\rangle$ produces the dominant PL on a dark states associated with a Mn spin state $\pm 5/2$. As discussed above, a Mn spin flip by four units is unlikely, we then attribute this PL to $|-2, S_z = +5/2\rangle$. The transfer involve a hole-Mn spin flip. The second contribution comes from the state $|+2, S_z = +3/2\rangle$. It corresponds to a conservation of the Mn spin and a spin flip of the electron.

(3): From an excitation on $|+1, S_z = +5/2\rangle$, the dominant PL comes from the state $|+2, S_z = +5/2\rangle$. It corresponds to a transfer with conservation of the Mn

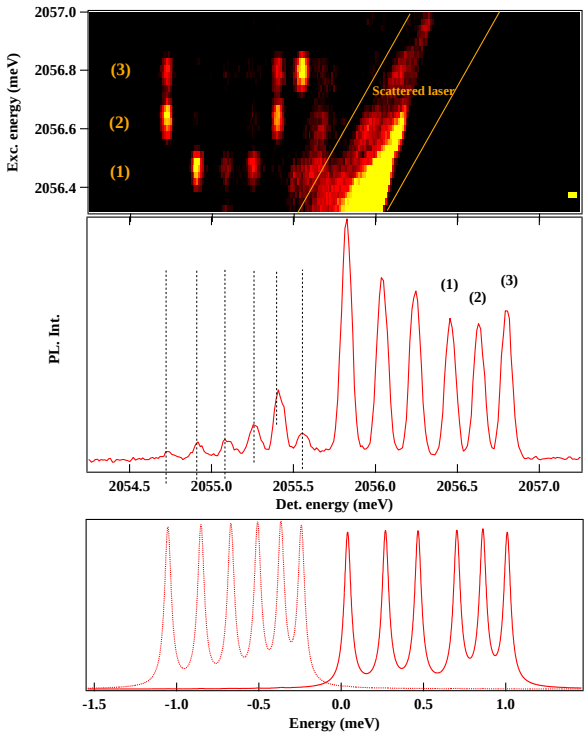

Figure 2.30 PLE intensity map detected on the dark states of a Mn-doped QD. The excitation laser is scanned across the three high energy bright states. Excitation and detection are circularly cross-polarized. The resonances (1-3) are discussed in the text. The bottom panel presents calculated bright $|+1\rangle$ (plain line) and dark $|-2\rangle$ (dotted line) energy levels with I_{eMn}=-0.03 meV, I_{hMn}=0.120 meV, I_{eh}=-780 meV, $\rho/\Delta_{lh} = 0.05$, η=10μeV and $\delta_2 = 0$.

spin and a spin flip of the electron. PL is also observed from $|-2, S_z = +5/2\rangle$ after a spin flip of the hole and from $|+2, S_z = +3/2\rangle$. The latter transfer involves an electron-Mn spin flip. Let's note that in the state $|+1, S_z = +5/2\rangle$ a hole-Mn flip-flop is forbidden (parallel hole and Mn spin).

If we resume the observed resonances in these two QDs, we can distinguish three types of spin transfer which occurs within the lifetime of the exciton:

- Transfer between bright states which involve a change of the spin of the exciton while the Mn spin state is unaffected.
- Transfer from a bright to a dark state involving a carrier-Mn flip-flop (hole-Mn seems to dominate). This produces a change of one unit of the Mn spin state.
- Transfer from a bright to a dark state involving a carrier spin-flip and conservation of the Mn spin. Electron spin flips are the most efficient in QD with a weak valence band mixing (case of QD presented in Fig. 2.30).

The two last processes involving a transfer to dark states can lead to an optical pumping of the Mn spin. Let us consider the case of a resonant excitation on $|+1, S_z = +5/2\rangle$ as in the experiments presented in section (2.3). The three possible relaxation path were observed: hole spin-flip, electron spin-flip and electron-Mn flip-flop (a hole-Mn flip-flop is forbidden). Starting from $|+1, S_z = +5/2\rangle$, an electron spin-flip leads to $|+2, S_z = +5/2\rangle$ which is not admixed to any other states: an optical recombination of this state will not produce any pumping of the Mn spin.

On the other hand, a hole spin-flip leads to $|-2, S_z = +5/2\rangle$. The optical recombination of this dark state can occur thought its small light hole component and emit a photon π_z linearly polarized along the QD growth axis. This does not occur with any change in the spin state of the Mn and can not explain the pumping. However, this dark state can also recombine through an admixture with bright states induced by a hole-Mn flip-flop (admixture with $|+1, S_z = +3/2\rangle$) or a electron-Mn flip-flop (admixture with $|-1, S_z = +3/2\rangle$). In both cases, the recombination of the dark state through its bright heavy-hole exciton part decreases the Mn spin by one unit. This pumping process was initially proposed by Cywinski [32] and numerical modeling were performed by Cao et.al. [21]. The modeling shows that for a large valence band mixing that can induce an efficient hole spin relaxation, this process could lead to a resonant optical pumping in the tens of ns range.

This mechanism is likely to be dominant for the optical orientation under non-resonant excitation. An efficient spin-flip of the hole is expected during the energy relaxation of the exciton. This leads to an injection of dark excitons. Let's consider the case of a $\sigma+$ excitation (injection of $|+1\rangle$ excitons). A spin flip of the hole during the relaxation of the exciton injects a $|-2\rangle$ dark exciton. Whatever the Mn spin state S_z, the recombination of this dark state through its bright heavy-hole exciton component (electron-Mn or hole-Mn spin-flip) decreases the Mn spin by one unit ($S_z \longrightarrow (S_z - 1)$). This is consistent with the observation in the optical orientation experiments of a progressive anti-ferromagnetic alignement of the exciton and Mn spins (i.e. increase of $S_z = -5/2$ population under $\sigma+$ excitation).

However, another mechanism is indeed possible and could contributes to the orientation of the Mn spin under resonant excitation where spin relaxation of the hole was not found to be the dominant relaxation channel (Fig. 2.30). Starting from the state $|+1, S_z = +5/2\rangle$, an electron-Mn spin relaxation leads to the dark state $|+2, S_z = +3/2\rangle$. From the state $|+2, S_z = +3/2\rangle$, we need to consider the two optical recombination path we discuss previously. Optical recombination through the admixture with bright heavy-hole exciton states (i.e. hole-Mn or electron-Mn spin flip) will bring back the Mn spin on $S_z = +5/2$ and not play any role in the optical orientation. However, recombination through the light-hole component (emission π_z) leaves in the QD ground state a Mn spin projection $S_z = +3/2$, differing by one unit from the initial one ($S_z = +5/2$): this recombination channel can also contribute to an optical pumping of the Mn spin.

An even more complex dynamics is expected for a resonant excitation on $\pm 3/2$

or $\pm 1/2$ where either an increase or decrease of S_z could be obtained depending on the chosen relaxation path. To discriminate the dominant pumping mechanism, one should perform the resonant optical pumping on different Mn spin states and in each case observe the Mn spin redistribution among the six levels. We will discuss the development of such experiments in chapter 3 and will see that other ingredients, such as pumping of the nuclear spin of the Mn, have to be taken into account to fully understand the behavior of the Mn spin under resonant optical excitation.

2.5 Optically dressed magnetic atoms: Towards an optical coherent control of a Mn spin

We have shown that the fine and hyperfine structure of the Mn atom was controlling its spin dynamics at low magnetic field. We will demonstrate now that we can optically modify this fine structure by a resonant excitation by a strong laser field. The consequences of this strong coupling with the laser field on the Mn spin dynamics will be discussed in chapter 3.

So far, only a few experiments have demonstrated the possibility to use a strong continuous wave laser field to create hybrid matter-field systems and manipulate QDs states in their solid environment. The strong coupling regime between a QD transition and a laser field has been observed for the first time by Kamada *et al.* [70]. The optical dressing of an exciton via the biexciton transition using absorption spectroscopy [69], the Autler-Townes effect in the fine structure of the ground state of a neutral [150] or charged [80] QD, the Mollow absorption spectrum of an individual QD [151] and the emission of optically dressed exciton-biexciton complex for a QD in a planar micro-cavity [111] have then been reported. It has also been demonstrated that the optical Stark effect can be used to compensate the exchange splitting in anisotropic QDs to produce entangled photon pairs [112]. All these experiments where performed on III-V QDs inserted in optical cavities to improve the signal collection. We show here that the energy of any spin state of an individual Mn atom embedded in a II-VI semiconductor QD, can be tuned using the optical Stark effect induced by a strong laser field [88].

2.5.1 Experimental evidence of optical Stark effect on a Mn spin

Only one spin state of the Mn is addressed when a control laser is circularly polarized ($\sigma\pm$) and tuned on resonance with an emission line of the exciton-Mn complex. As illustrated in Fig. 2.31, the splitting induced by the control laser tuned to the high energy line of X-Mn in $\sigma+$ polarization can be detected in $\sigma-$ polarization on the low energy line of X-Mn as both lines correspond to the same Mn spin. This is the equivalent of the Autler-Townes splitting observed in atomic physics [4].

The control laser field mixes the states with a Mn spin component S_z=+5/2 in the presence (X-Mn) or absence (Mn alone) of the exciton. At the resonance, the unperturbed states $|Mn\rangle \otimes |n\rangle$ and $|XMn\rangle \otimes |n-1\rangle$ can be dressed into pairs of

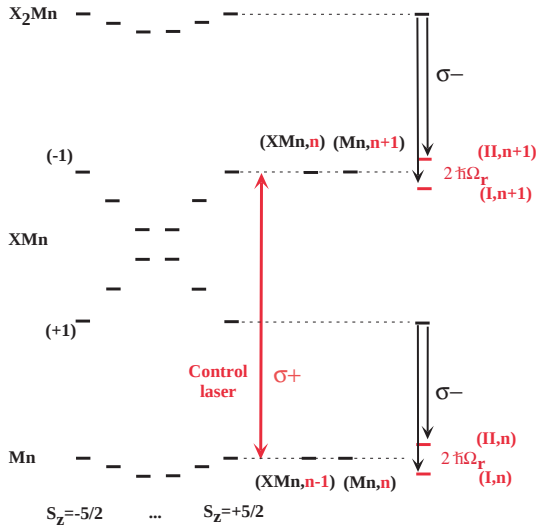

Figure 2.31 Energy scheme of a Mn-doped QD and formation of light-matter hybrid states by a laser field. In the absence of carriers, the Mn fine structure is dominated by the strained induced magnetic anisotropy which also splits the biexciton states (X_2-Mn). The bright exciton levels (X, with kinetic momentum ± 1) are split by the exchange interaction with the Mn (X-Mn levels). A pump laser tuned to a QD excited state is used to produce PL of any exciton and biexciton states. The Rabi splitting, $\hbar\Omega_r$, induced on the Mn state by the control laser (circularly polarized $\sigma+$) can be probed in the PL of the exciton while the splitting of XMn is observed in the PL of the biexciton. (I,n), (II,n), (I,n+1) and (II,n+1) are the optically dressed states produced by the mixing of the uncoupled states (XMn,n-1), (Mn,n), (XMn,n) and (Mn,n+1) where n is the number of photons in the control laser.

hybrid matter-field states $|I,n\rangle$ and $|II,n\rangle$ where $|n\rangle$ is a n-photons state of the control laser. These states can be written as [18]:

$$|I,n\rangle = c|Mn\rangle \otimes |n\rangle - s|XMn\rangle \otimes |n-1\rangle$$
$$|II,n\rangle = s|Mn\rangle \otimes |n\rangle + c|XMn\rangle \otimes |n-1\rangle$$

with corresponding energies $E_\pm = \frac{\hbar}{2}(\omega_c + \omega_0) \pm \frac{\hbar}{2}\Omega'_r$. Here, $c = \sqrt{\frac{1}{2}(1 - \frac{\delta}{\Omega'})}$ and $s = \sqrt{\frac{1}{2}(1 + \frac{\delta}{\Omega'})}$. $\delta = \omega_c - \omega_0$ is the laser detuning with ω_0 the resonance frequency of the unperturbed transition and ω_c the frequency of the control laser. $\hbar\Omega'_r = \hbar\sqrt{4\Omega_r^2 + \delta^2}$ defines the energy splitting of the dressed states where $\Omega_r = \mathcal{P}\mathcal{E}/\hbar$ is the Rabi frequency with $\mathcal{P}$ the dipolar moment of the QD transition and $\mathcal{E}$ the amplitude of the electric field of the control laser. A power dependent Autler-Townes type splitting is then expected for all transitions that share such an optically dressed state [4, 108].

Experimental data corresponding to a control laser tuned on $|+1,+5/2\rangle$ and the observation of an Autler-Townes splitting in the PL of the state $|-1,+5/2\rangle$

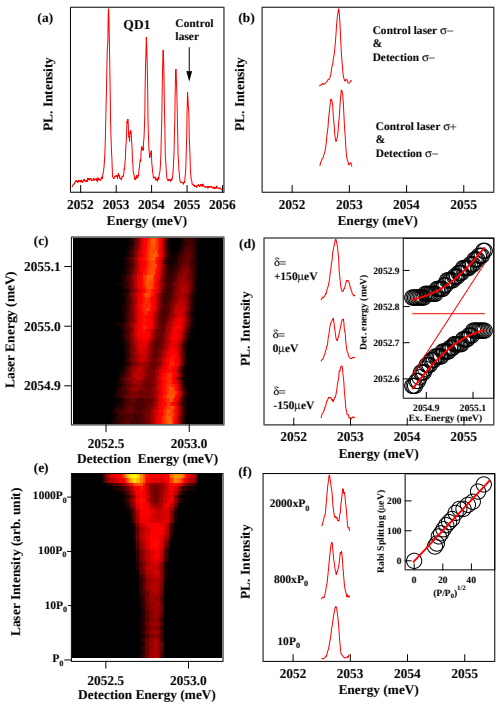

Figure 2.32 Autler-Townes splitting of the emission of $|-1,+5/2\rangle$ in a Mn-doped QD (QD1) resonantly excited on $|+1,+5/2\rangle$. (a) shows the non-resonant PL of the QD. The intensity map (c) shows the excitation energy dependence of the Rabi splitting. The corresponding emission line-shape is presented in (d). The inset shows the spectral position of the Autler-Townes doublet as a function of the pump detuning. The fit is obtained with a Rabi energy $\hbar\Omega_r = 180\mu eV$. The straight lines corresponds to the uncoupled exciton and laser energy. The excitation intensity dependence of the Autler-Townes doublet is presented in the intensity map (e). The corresponding emission line-shape are presented in (f). The inset shows the evolution of the Rabi splitting as a function of the square-root of the pump intensity. A linear increase is observed. (b) presents the circular polarisation dependence of the Rabi splitting obtained under resonant excitation.

are presented in Fig. 2.32. Particular care is given to the effect of the detuning of the control laser from the X-Mn resonance (Fig. 2.32(c) and 2.32(d)) and its intensity (Fig. 2.32(e) and 2.32(f)). At large laser detuning, the optically active transitions asymptotically approach the original excitonic transitions where the remaining energy offset is the optical Stark shift. At the resonance, an anti-crossing is observed showing that the strong coupling between the laser field and the exciton creates hybrid light-matter states. As presented in the inset of Fig. 2.32(d), a good agreement with the simple dressed atom model is obtain with a Rabi energy of $\hbar\Omega_r$=180μeV. On resonance, the emission from the $|-1,+5/2\rangle$

state splits into a doublet when the power of the control laser is increased, as expected from the Autler-Townes model. The splitting is plotted as a function of the square root of the control laser intensity in Fig. 2.32(f), showing that the splitting linearly depends on the laser field strength. A Rabi splitting larger than 250μeV is obtained at high excitation intensity. It is worth noting that these energy shifts can be easily larger than the magnetic anisotropy of an isolated Mn spin created by the strain in the QD plane ($\approx 50\mu$eV). As we will see in chapter 3, this optical tuning of the fine structure may lead to a control of the coherent dynamics of the isolated Mn spin.

The high energy transition of X-Mn is twice degenerated. The corresponding optical transitions differ by the polarization of the absorbed or emitted photons. The polarization dependence of the laser induced splitting shown in Fig. 2.32(b) confirms the Mn spin selectivity of the strong coupling with the laser field: $\sigma+$ photons couple with the state $|+5/2\rangle$ of the Mn to create two hybrid light-matter states while no splitting of the $\sigma-$ PL line is observed with $\sigma-$ control photons.

2.5.2 Individual addressing of any Mn spin state

The strong coupling with the control laser is also observed in optical transitions that involve the biexciton exchanged coupled to a single Mn (X_2-Mn). This is illustrated in Fig. 2.33 in the case of successive resonant excitations on the X-Mn levels with a Mn spin state S_z=+1/2, +3/2 and +5/2. In these cases, the recombinaison of X_2-Mn probes the laser induced splitting of X-Mn for a given spin states of the Mn. It is shown here that any X-Mn transition, and consequently any Mn spin state, can be optically shifted by a control laser tuned on resonance. As illustrated in Fig. 2.33(c), by coherently driving the X_2-Mn to X-Mn transition, one can also tune the energy of any state of the X-Mn complex. This set of experiment demonstrates that a complete optical control of the exciton-Mn system is possible.

It is also demonstrated here that the use of a resonant strong laser field allows to individually address any spin state of the Mn even if they are coupled by the exciton through the valence band mixing. The particular situation where the Mn spin states $|+1/2\rangle$ and $|+3/2\rangle$ are significantly mixed is presented in Fig. 2.34. The spectrum of this QD (QD2 in Fig. 2.34(a)) differs clearly from the one expected in the pure heavy-hole approximation and presents seven peaks. The valence band mixing couples $|-1,+3/2\rangle$ with $|+2,+1/2\rangle$ and the new eigenstates share the oscillator strength of the bright state $|-1,+3/2\rangle$. The two lines on the right of the low energy state can be attributed to the bright part of these mixed bright-dark excitons. This attribution is confirmed by the calculation of the energy levels presented in Fig. 2.34(b).

As shown in Fig. 2.34(c) and 2.34(d), it is possible to optically address selectively one state (and one only) of the Mn spin in the mixed bright-dark XMn levels. When the $\sigma+$ control laser is tuned on the state $|+1,+3/2\rangle$ (line (d)), a Autler-Townes splitting is observed in $\sigma-$ polarization for both components of the emission of the dark-bright excitonic complexes (lines (a) and (b) in Fig.2.34(c)).

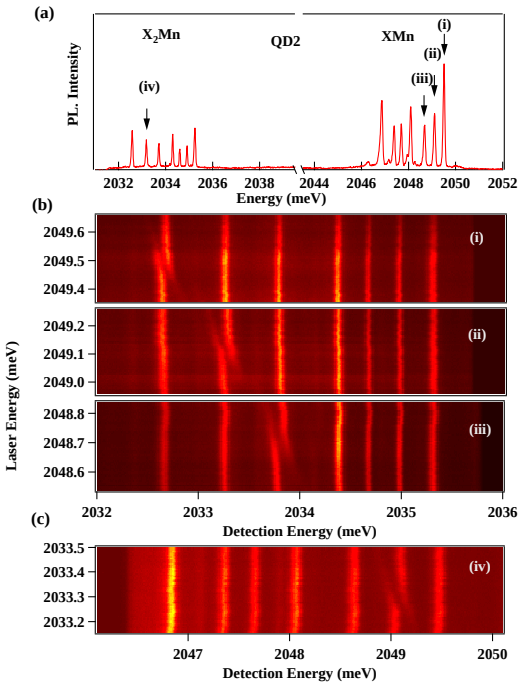

Figure 2.33 (a) PL of the exciton and biexciton in a Mn-doped QD (QD2). (b) Autler-Townes splitting of the exciton in QD2 detected on the biexciton PL under resonant excitation of the ground-to-exciton transition for the spin state of the Mn S_z=+5/2 (i), S_z=+3/2 (ii) and S_z=+1/2 (ii) (arrows in the PL of QD2). (c) Emission of the exciton for a dressed exciton-to-biexciton transition. The excitation is tuned around the state S_z=+3/2 of the biexciton (iv).

This arises from the control laser induced splitting of their common final state with a Mn spin $S_z = +3/2$. With a resonant excitation on the mixed bright-dark states, only the states which share a $S_z = +3/2$ Mn spin are split: the dark part with Mn spin $S_z = +1/2$ is not affected. This is demonstrated in Fig.2.34(d). The $\sigma-$ control laser splits the Mn state $|+3/2\rangle$ which leads to the doublet formation in the $\sigma+$ PL from the state $|+1,+3/2\rangle$ (line (d)) while no splitting of the state $|+1,+1/2\rangle$ (line (c)) is observed. The Mn spin state $S_z = +1/2$ is not affected by the control laser tuned on the dark-bright mixed exciton. This experiment suggests the possibility to optically control the exciton induced coupling between two spin states of the Mn atom, an important step towards coding quantum information on an individual magnetic atom [127].

Finally, it is shown in Fig. 2.35 that, in QDs containing 2 Mn atoms, a selective addressing of the X-2Mn complex can be achieved with a control laser on resonance with one of the PL line and the energy of the 2 Mn spins tuned optically. When a control single mode laser is tuned to the high energy line of X-2Mn in $\sigma+$ polarization, one observes a power-dependent (Fig. 2.35(b)) and

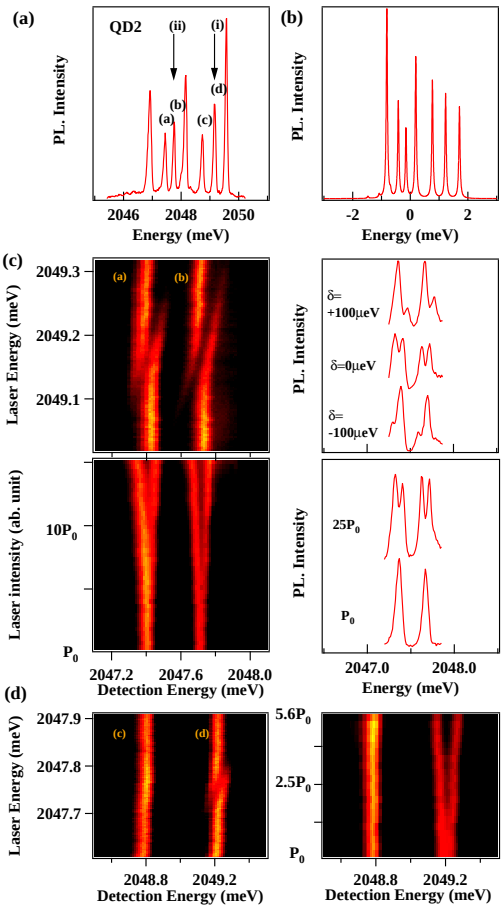

Figure 2.34 Rabi splitting obtained on mixed bright-dark exciton states in QD2. (a) presents the PL of QD2. The intensity of the lines is influenced by the absorption selectivity of the excited state (see ref. [57]). The corresponding theoretical emission spectra is presented in (b). It is calculated with I_{eMn}=- 0.095 meV, I_{hMn}=0.3 meV, I_{eh}=-0,6 meV and $\rho/\Delta_{lh} = 0.1$, δ_2=0.05 meV and T_{eff}=25K. (c) presents the laser detuning dependence and the excitation power dependence of the Rabi splitting obtained on mixed bright-dark exciton under excitation on (i). (d) presents the detuning and excitation intensity dependence measured on the high energy transitions associated with the Mn spin state S_z=+1/2 and S_z=+3/2 under excitation on the mixed dark-bright exciton (ii).

tuning-dependent (Fig. 2.35(c)) splitting of the low energy line of X-2Mn in $\sigma-$ polarization. Since the ground state is the same for both transitions, this shows that the energy of Mn spins of the ground state are tuned by the resonant laser field.

As in the 1 Mn case, the strong electric field of the control laser field mixes the states with a 2 Mn spins component M_z=+5 in the presence (X-2Mn) or absence

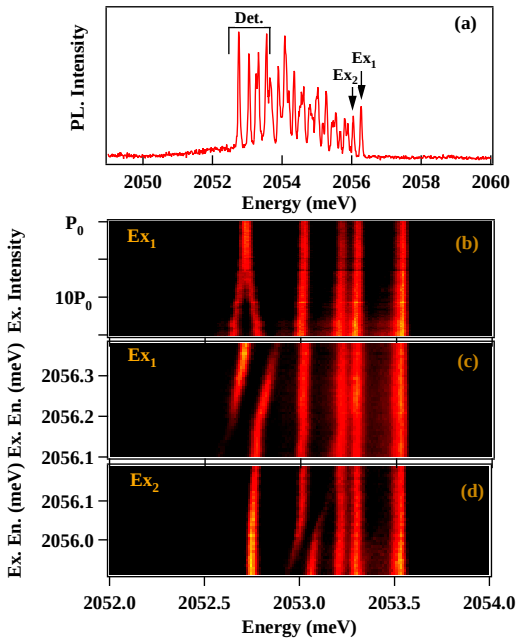

Figure 2.35 (a) Nonresonant PL of the exciton exchanged coupled to two Mn (X-2Mn) in a QD.(b) PL map of the X-2Mn versus the power of the control laser in resonance with Ex1. (c,d) PL maps of the X-2Mn when the control laser energy is tuned around the 2-Mn spin states M_z=+5 (c) and M_z=+4 (d).

(2 Mn alone) of the exciton. At resonance, hybrid matter-field states are created (Fig. 2.35(b)). As the laser detuning increases, the optically active transitions asymptotically approach the original excitonic transitions where the remaining energy offset is the optical Stark shift (Fig. 2.35(d)). The use of a resonant laser field allows to individually address any spin state of the 2 Mn if the corresponding excitonic transition is sufficiently isolated from the others (Fig. 2.35(c) M_z=+5 and Fig. 2.35(d) M_z=+4).

2.5.3 Mn energy levels in the strong coupling regime.

Let us finally analyze the influence of the strong laser field on the Mn fine and hyperfine structure. We start again from the Hamiltonian of the coupled electronic and nuclear Mn spins given in equation (1.21) of chapter 1. This structure is mainly controlled by $\mathcal{A}$, the hyperfine coupling with the nuclear spin, and $\mathcal{D}_0$ the strain induced magnetic anisotropy. We consider, as in the experiments presented previously, that the Mn spin is coherently coupled to a single excited exciton-Mn level $(+1, S_z = 5/2, I_z)$ with a resonant laser field. This is a good approximation if the Rabi splitting induced by the resonant laser is much weaker than the splitting between the lines of the X-Mn complex. This can be verified in most of

the Mn doped QDs as the laser energy shift we need to influence the Mn spin fine structure is typically lower than 50μeV.

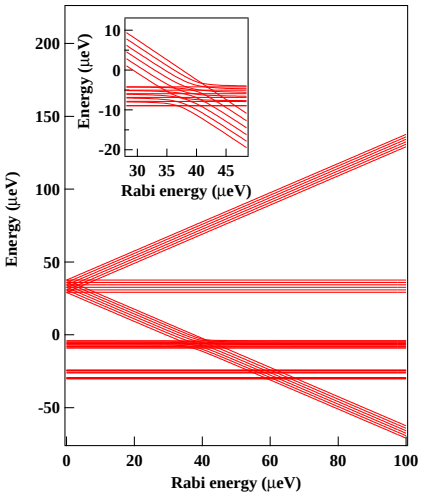

Figure 2.36 Fine structure of the Mn spin in a strained QD as a function of the Raby energy $\hbar\Omega_r$. The enlarged view in the inset shows anti-crossing between the different Mn spin states $S_z = +5/2$ and $S_z = +3/2$. Calculated with $A = 0.7$ μeV, $D_0 = 10$ μeV, $a = 0.32$ μeV.

The Hamiltonian of the coupled light matter systems in the semi-classical limit reads:

$$\mathcal{H}_{lm} = \mathcal{H}_{Mn} + \delta - \hbar\Omega_r(d^\dagger + d) \tag{2.18}$$

where $\delta = \hbar\omega_0 - \hbar\omega_l$ is the detuning between the optical transition and the laser of frequency ω_0 and ω_l respectively. d (resp. $d^\dagger$) is the annihilation (resp. creation) operator of an exciton of energy $\hbar\omega_0$. $\Omega_r = \sqrt{n}g$ is the Raby frequency, with g the electrical dipole matrix element describing the coupling between the dipole of the QD transition and the mode ω_l of the electric field and n the number of photons in the mode. The optically dressed states are found diagonalizing the total Hamiltonian. The result of the diagonalization for different values of Ω_r is presented in Fig. 2.36. As expected, optically dressed states are created for S_z=+5/2 and all the spin states of the nuclei I_z. As observed experimentally (Fig. 2.32), the laser induced splitting can be much larger than the fine structure produced by D_0. Consequently, the degeneracy between S_z=+5/2 and S_z=+3/2 can be optically restored. The strong coupling with the laser field could be used to tune the energy of any other spin state of the Mn and control their degeneracy.

When the light induced energy shift compensate the strain induced magnetic anisotropy, two consecutive spin states of the Mn are coupled by simultaneous electron-nuclei flip-flops, governed by $\mathcal{H}_{Hyper} = \mathcal{A}[I_zS_z + 1/2(I^+S^- + I^-S^+)]$.

This is responsible for the anti-crossing observed between the states S_z=+5/2 and S_z=+3/2 in the inset of Fig. 2.36. At the resonance, as $\mathcal{D}_0$ blocks further evolution in the spin ladder, the electronic and nuclear spins will start to oscillate at the Raby frequency (governed by $\mathcal{A}$). This coherent oscillation killed by the fast dephasing time of the dressed states could perturb significantly the initialization of the electronic spin and lead to a pumping of the nuclear spin. We will discuss the dynamics of these optically dressed states in the next chapter.

2.6 Summary and conclusion

We have shown in this chapter that the optical injection of spin polarized carriers in a QD could be an efficient way to prepare and probe the dynamics of carriers, nuclei and magnetic atoms spins.

We have first evidenced the coherent time-evolution of the electron-nuclei coupled system. Although no hysteresis was observed, the diluted nuclear spins in II-VI QDs present a very rich and complex dynamics. We have observed that unpolarized nuclear spins could cause a rapid decoherence of the resident electron. Under optical pumping conditions, an efficient nuclear spin could be obtained, limiting the electron spin relaxation at zero field. These nuclear effects could in principle be completely avoided in II-VI materials through the use of isotopically purified materials.

Similar time resolved optical pumping experiments have been used to study the dynamics of individual Mn spins embedded in II-VI QDs. We have shown that Mn spin orientation could be achieved using light of a controlled helicity and energy. This was the first demonstration of the optical pumping of a magnetic atom in a solid state environment. Such orientation can be performed in a few tens of ns. The spin distribution obtained by such means is perfectly conserved over a few μs. This is a direct evidence of the long spin memory of an individual Mn atom.

The dynamic of the Mn spin orientation at zero magnetic field is controlled by a magnetic anisotropy produced by the presence of strains at the Mn location. The strain induced fine structure explains the saturation of the efficiency of the pumping process (at $\approx$ 75%, in the best cases) under resonant excitation. We discussed possible processes responsible for the photo-induced spin-orientation involving a hole spin-flip, or carrier-Mn spin-flips. These spin-flips have been evidenced experimentally but their origin needs to be clarified.

We have also demonstrated the possibility to create optically dressed states on a Mn-doped QDs. This signature of a strong light-matter coupling and of an optical Stark shift of the Mn spin is promising for coherent manipulation of the Mn atom. We will discuss in the next chapter the spin dynamics of these optically dressed states and see how the optical tuning of the energy of the Mn electronic spin can be use to control the coupling with its nuclear spin.

Part II

Ongoing work, perspectives

3

Coherent dynamics of few interacting spins in a quantum dot

In this chapter, we discuss ongoing and future experiments for the study of the coherent dynamics of a few interacting spins in a semiconductor host: one or two Mn spins in interaction with their nuclear spins, electron or hole spins in a QD interacting or not with a Mn spin and in contact with a diluted nuclear spin bath. These are ideal objects for the study of the coherent transfer of information between spins subsystems in a quantum object.

We will first present a new technique under development to analyze the optical preparation of the electronic Mn spin and the interaction with its nuclear spin. This technique, based on a two-photon excitation of the biexciton combined with a resonant excitation of the exciton, will be used to analyse the influence of the strong coupling with a laser field on the optical preparation of the Mn spin. We will show that for particular conditions of detuning and Rabi energy, the creation of dressed states in a Mn doped QD can lead to a new way to initialize the Mn spin that we call "population trapping". We will discuss possibilities to optimize this spin preparation. We will also show how the strong coupling with a laser field can be used to optically control the electronic spin / nuclear spin coupling on a Mn atom and how an optical access to the nuclear spin of the Mn should be possible.

We will discuss methods to access the spin dynamics of the optically dressed states of the Mn. The influence of the strong coupling on the Mn spin dynamics will be particularly important for unstrained QDs where the creation of dressed states should block the coherent electron-nuclei flip-flop induced by the hyperfine coupling. First results on the development of unstrained singly Mn-doped QDs will be presented. Strategies to increase the photon collection from Mn-doped QDs in order to access the dynamics of the dressed states with the two-photon technique will also be presented.

An important step for the possible use of magnetic atoms as spin memories in devices would be to be able to coherently couple two or more magnetic atoms. In QDs containing two magnetic atoms, the injection of a carrier during a controlled time could be used to induce a coherent coupling between the localized spins. In a long term perspective, each Mn spin could be addressed with a resonant microwave excitation and their interaction controlled by an injected carrier. As a first step toward this goal, we will study the spin dynamics in QDs containing one or two magnetic atoms and an individual injected carrier. We will analyze how the exchange interaction with a Mn spin can stabilize the confined carrier spin and

study the dynamics of the carrier induced ferromagnetic coupling between two localized spins.

We will in a last section discuss the possibility of a coherent control of an individual carrier or Mn spin exploiting time resolved optical Stark effect in a transverse magnetic field or a direct micro-wave excitation. We will present a protocols for a full optical coherent control of a Mn spin in unstrained QDs and for an optically detected magnetic resonance of a Mn spin.

3.1 Dynamics of coupled electronic and nuclear spins of a Mn atom.

As we have seen in chapter 2, because of the fine and hyperfine structure of the Mn, different S_z of the Mn are coupled by the non-diagonal terms of H_{Mn} (equation 1.21). For instance, the hyperfine terms $\mathcal{A}$ couples two consecutive Mn spin states through an electron-nuclei flip-flop. We can then expect that a non-equilibrium population of the electronic spin of the Mn will be transferred to its nuclear spin. This would lead to a pumping of the nuclear spin under optical pumping of the Mn. However, in the presence of large magnetic anisotropy, these electron-nuclei flip-flops are blocked. An anisotropic strain distribution in the QD plane can also couple spin states separated by two units through the crystal field term $E(S_x^2 - S_y^2)$. These coupling are likely to affect the population redistribution on the different Mn states under resonant optical pumping.

The strong coupling with a resonant laser field can be used to tune the energy of one Mn spin level across the full fine structure of the Mn atom. This gives an optical way to control the flip-flops of the electronic and nuclear spins. The energy tuning of the optically dressed states should then have an influence on the dynamics of the Mn spin. We will see that the detuning and the intensity of the resonant laser can significantly affect the initialization of the electronic Mn spin and could lead to an optical pumping of the Mn nuclear spin. We will discuss methods to probe the dynamics of the optically dressed Mn atom and the dynamics of preparation and relaxation of its nuclear spin.

3.1.1 Spin dynamics of an optically dressed Mn atom: Controlled electron-nuclei flip-flops.

In order to gain knowledge on the repartition of the population on the electronic spin states of the Mn under resonant optical excitation, we are developing a technique allowing probing simultaneously the population of the six spin states of the Mn in the resonant optical excitation regime.

This experiment is based on the two-photon creation of a biexciton under pulsed excitation (see Fig. 3.1). A picosecond pulsed excitation tuned in between the exciton and the biexciton levels can directly create a biexciton in a QD through a two-photon transition [50]. As the biexciton is a spin singlet state it does not interact with the Mn spin and the direct injection of the biexciton in a Mn-doped QD offers a way to observe the six spin population without perturbing

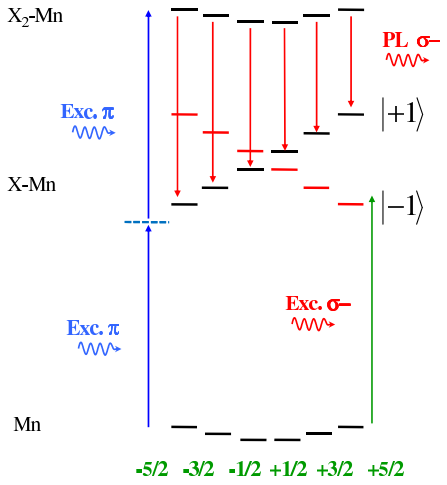

Figure 3.1 Scheme of the optical transitions and their polarization in a QD containing an individual magnetic atom and 0, 1 or 2 excitons. The exciton state is split by the exchange interaction with the Mn spin whereas in the ground and biexciton states the energy levels results from the fine and hyperfine structure of the Mn spin. By a two-photon process, a direct resonant transition from the ground to the biexciton state is possible without the intermediate creation of an exciton.

too much the system. This population can be extracted from the intensity of the PL lines of the biexciton. Moreover, as the emission of the biexciton is shifted by 10 to 14 meV below the resonant excitation on the exciton-Mn levels, it can be easily separated from the scattered photons of a pumping laser tuned on resonance with an exciton-Mn state. The use of a resonant excitation to create the biexciton avoids the injection of free carriers in the vicinity of the QD and consequently limits the spin relaxation of the Mn by exchange coupling with free carriers. Let's note however that the cascade recombination of the biexciton leaves in the QD a maximum of one, in average unpolarized, bright exciton every 13 ns. These exciton can slightly perturb the Mn spin prepared by the resonant optical excitation but, as we will see, a signature of the resonant excitation should in general be observed.

A two-photon PL spectra of a Mn-doped QD is presented in Fig. 3.2. This figure illustrates the experimental configuration. The biexciton is resonantly created by a linearly polarized pulsed excitation tuned at equidistance from the exciton and the biexciton transitions. As expected from the optical selection rules, circularly polarized pulses do not create any PL. This confirms that one can find experimental conditions where the PL signal from the biexciton is fully dominated by the two-photon resonant excitation. Such experimental configuration is necessary to avoid any perturbation of the Mn spin by non-resonantly created free carriers

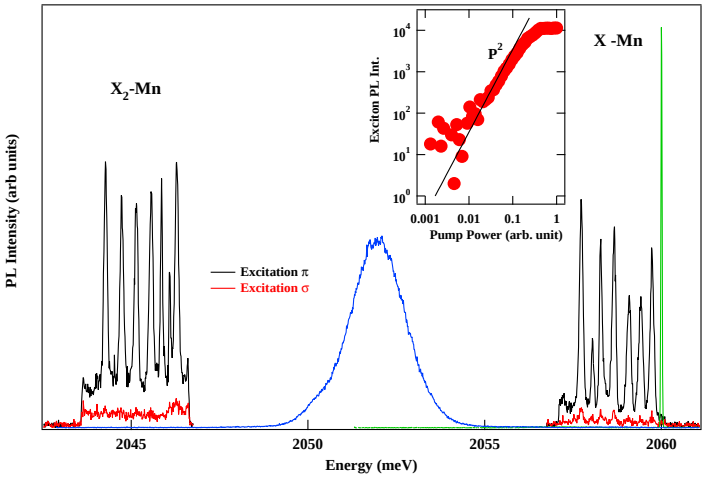

Figure 3.2 Photoluminescence spectra of a Mn-doped QD obtained under a two-photon pulsed resonant excitation. The resonant creation of the biexciton is only possible for a linearly polarized excitation (black) whereas no PL is observed for circularly polarized pulses (red). Inset: PL intensity of the exciton versus pulsed excitation power. The influence on the Mn spin population of a resonant CW excitation on X-Mn (green) can be detected in the intensity distribution of X_2-Mn.

and efficiently use the biexciton intensity distribution as a probe of the Mn spin population.

The first results of a two-photon detection of the resonant Mn spin preparation are presented in Fig. 3.3. These results are obtained under circular polarization for the resonant CW excitation and the optical detection of the biexciton. Without resonant excitation on X-Mn, an equally distributed population is observed in the biexciton PL lines showing that the two-photon excitation does not produce any pumping of the Mn. A strong change in the intensity distribution is observed when a CW laser is scanned on each X-Mn level suggesting a complex dynamics.

Under circular excitation, a resonant excitation on a X-Mn level only address one spin state of the Mn. For co-circular excitation on X-Mn and detection on X_2-Mn, the low energy lines of X and X_2 corresponds to the same spin state of the Mn (Fig. 3.1). As the CW laser is scanned around the low energy line of X, it mainly affects the low energy line of X_2. Similarly, as the high energy line of X is excited, the high energy line of X_2 is perturbed showing that the resonant excitation mainly affects the spin state which is directly addressed.

To illustrate the effect of the resonant laser on the Mn spin population, let's focus on the two outside lines of the biexciton PL. They corresponds to the spin states $S_z = +5/2$ or $S_z = -5/2$. The intensity of these lines is presented in figure 3.3(b) versus the energy of the resonant CW pumping laser scanned on the X-Mn levels. As expected for an optical pumping, one observes a decrease of

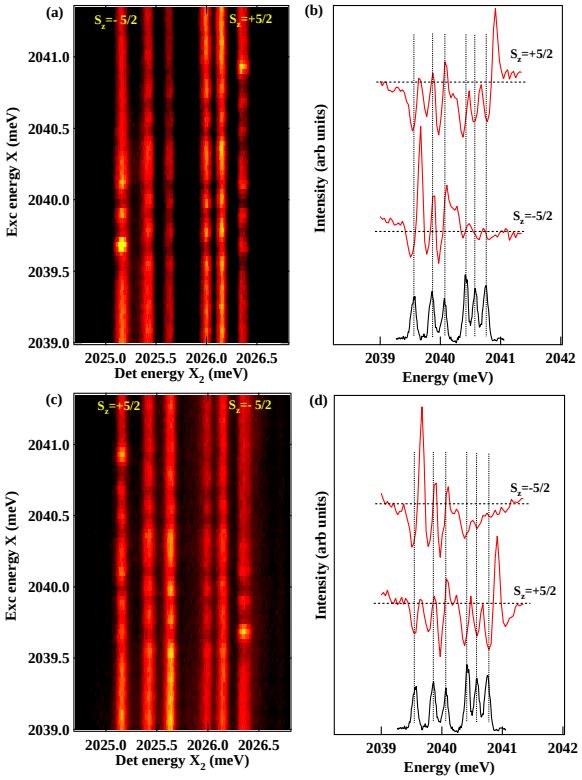

Figure 3.3 Map of the intensity of X_2 versus the energy of the CW resonant excitation on X for co (a) and cross (c) circular excitation on X and detection on X_2. (b) and (d) present the corresponding intensity curves of X_2 for the spin states S_z=+5/2 and S_z=-5/2.

the population of S_z=-5/2 when the laser is tuned on resonance with the level (J_z=+1,S_z=-5/2). However, a strong increase of the population of S_z=-5/2 is observed a soon as soon the pumping laser is slightly detuned on the high energy side of the transition. A similar behavior is observed when the high energy line of X-Mn is excited and the high energy line of X_2-Mn is probed (i.e. exciting and detecting the Mn spin state S_z=+5/2). As expected for a Mn spin dependent phenomena, reversing the circular polarisation of detection (Fig.3.3(c) and (d)) reverses the role played by the high and low energy line of X_2-Mn and a similar strong increase of population is observed on S_z=+5/2 or S_z=-5/2 for a slightly detuned excitation on X-Mn.

A detail of the evolution of the PL intensity distribution obtained by scanning a circularly polarized single mode laser around the low energy line of X-Mn is presented in Fig. 3.4. This detail scan allows to quantify the observed energy shift. For an excitation around (J_z=+1,S_z=-5/2), the maximum of population of S_z=-5/2 is obtained for a laser detuning of about 60 μeV.

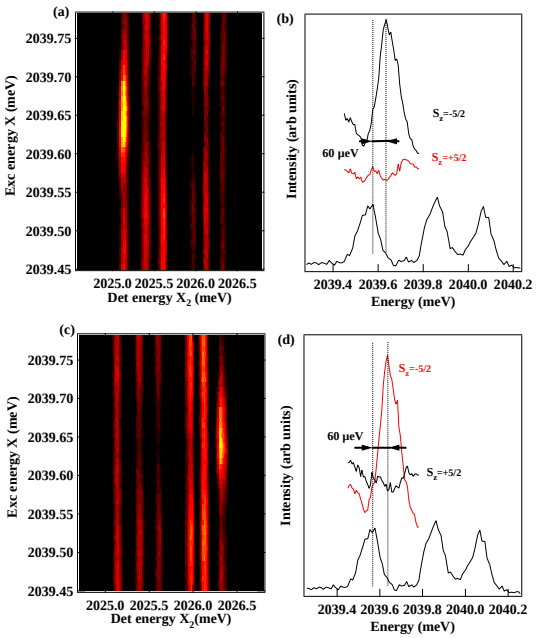

Figure 3.4 Map of the intensity of X_2 versus the energy of a single mode resonant excitation on X for co (a) and cross (c) circular excitation on X and detection on X_2. (b) and (d) present the corresponding intensity curves of X_2 for the spin states S_z=+5/2 and S_z=-5/2.

These first experimental results show that on one hand, as expected from previous resonant optical pumping experiments, a resonant excitation decreases the population of the spin state which is excited. On the other hand, a slight detuning of the laser can, in some of the dots, "trap" the Mn spin population in the state which is excited. We will see in the following that this is a signature of the coherent dynamics of the Mn spin coupled with its nuclear spin in the resonant laser field.

3.1.2 Coherent dynamics of a Mn spin under a resonant laser field.

We present here a model under development that describes the coherent dynamics of an optically dressed Mn atom and discuss the consequence of the coupling with the laser field on the Mn spin optical preparation. We will show in particular how the optical Stark shift induced by a resonant laser will be used in future experiments to control the coupling between the electronic and nuclear spins of a Mn atom and will be exploited to optically pump and probe the nuclear spin of an individual Mn atom.

The optically dressed Mn energy levels obtained under a resonant excitation by a single mode laser were already presented in chapter 2 (Fig. 2.36). The expected coherent dynamics of these dressed states can be calculated using the general

form of master equation for a multi-level system (equation 2.15) also introduced in chapter 2.

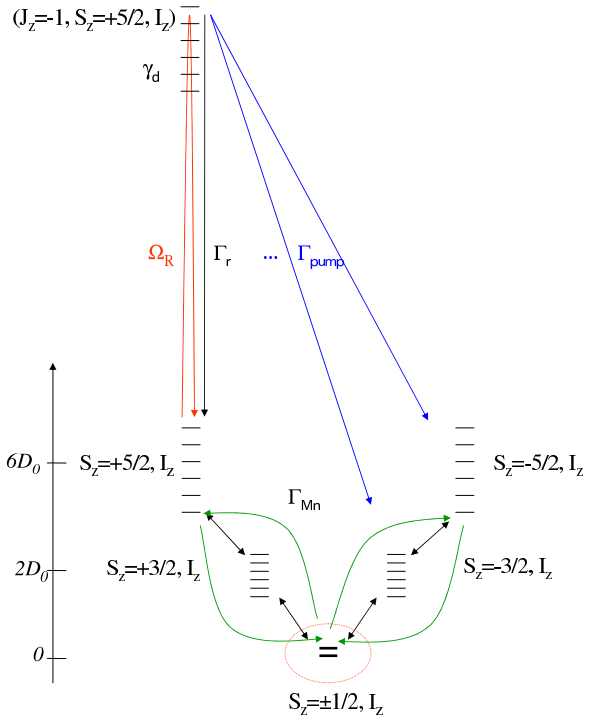

Figure 3.5 Scheme of the energy levels and transitions rates involved in the resonant excitation model presented in the text. Ω_r is the coupling with the laser field, γ_d is a pure dephasing of the exciton, Γ_{Mn} is the relaxation rate of the Mn, Γ_r is the optical recombination rate of the exciton. A relaxation rate of the exciton-Mn complex Γ_{pump} is used for an effective description of the optical pumping effect. Green arrows illustrate some coherent coupling induced by the non-diagonal terms of H_{Mn}.

For a general description, valid from the low to the high excitation intensity regime, we consider that the laser field induces a coherent coupling between the ground and exciton state. The coherent coupling between two levels induced by a strong resonant laser field leads to Rabi oscillations between the populations ϱ_{ii} and ϱ_{jj} and coherence of these levels $\varrho_{ij} = \varrho_{ji}^*$. In the Lindblad equation (2.15), this reversible coupling can be described by the operator:

$$L_{coh,i\leftrightarrow j}\varrho = i\frac{\Omega_{ij}}{2}(|j\rangle\langle i|\varrho + |i\rangle\langle j|\varrho - \varrho|j\rangle\langle i| - \varrho|i\rangle\langle j|) \tag{3.1}$$

where $\Omega_{ij} = P_{ij}\mathcal{E}/\hbar$ is the Rabi frequency with P_{ij} the dipolar moment of the

QD transition and $\mathcal{E}$ the amplitude of the electric field of the control laser. This term, which corresponds to the dipole field coupling, could be included in the Hamiltonian evolution. However, this form of Lindblad operator $L_{coh,i\leftrightarrow j}$ is more practical for programming.

Figure 3.5 presents the energy levels of the simplified system considered in the calculations. The states (S_z=+5/2,I_z) of the Mn are coupled by a resonant laser to the exciton states (J_z=-1,S_z=+5/2,I_z). In a first approximation, we neglect the possible excitation of more than one exciton state by the resonant laser (i.e. the splitting between the X-Mn lines is larger than the Rabi energy or the detuning of the laser). This approximation will be valid in QDs with a large exciton-Mn overlap.

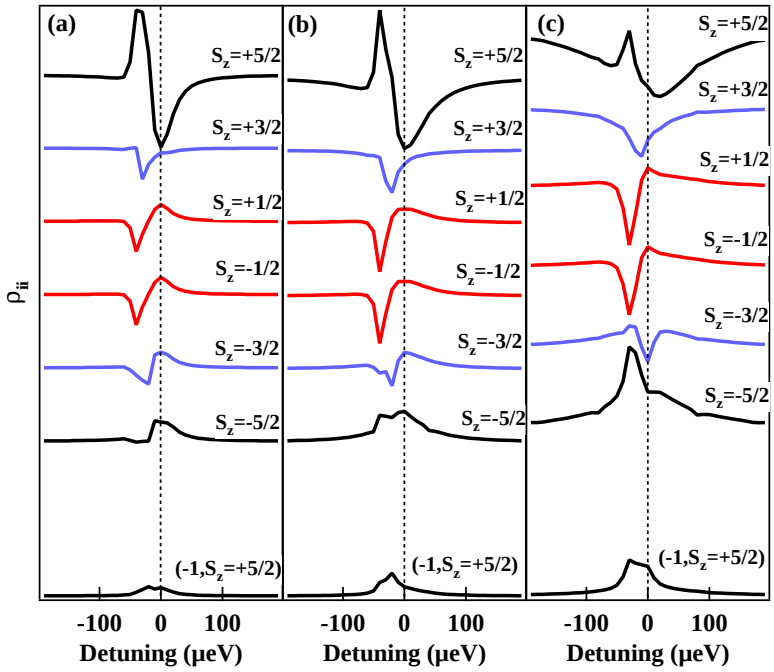

Figure 3.6 Calculated population of the six spin states of a Mn versus the detuning of the excitation laser around the exciton state (J_z=-1,S_z=+5/2,I_z) for different Rabi energies (a) $\Omega_r = 12.5\mu eV$, (b) $\Omega_r = 25\mu eV$ and (c) $\Omega_r = 50\mu eV$. The other parameters are E = $0.35\mu eV$, $\mathcal{A} = 0.7\mu eV$, $\mathcal{D}_0 = 7\mu eV$, a=$0.32\mu eV$, $\tau_{Mn} = 250ns$, $\tau_r = 0.25ns$ and $\tau_{pump} = 60ns$.

The calculated evolution of the population of the different spin states of the Mn with the detuning of a circularly polarized laser around (J_z=-1,S_z=+5/2) is presented in Fig. 3.6 for different Rabi energies. As expected, at low Rabi energies and zero detuning, an optical pumping of the state S_z=+5/2 is obtained. As the laser is detuned, a strong increase of the population of S_z=+5/2 is observed. This evolution is very similar to the one observed in the experiment. Simultaneously,

the population of S_z=±1/2 significantly decreases. This is what we will call the "population trapping". The spectral width of the pumping signal (i.e. decrease of population obtained on resonance with the transition) increases with the Rabi energy and dominates the population trapping at hight excitation intensity.

It appears in the calculation that the states S_z=+5/2 (*i.e.* excited by the laser) and S_z=±1/2 are the most affected by the laser detuning. Let's give a qualitative description of the observed complexe dynamics. As the pumping laser is detuned from the transition, the dressed states associated with S_z=+5/2 can be pushed on resonance with S_z=±1/2. If the QD presents an in plane strain anisotropy, S_z=+5/2 and S_z=+1/2 are coherently coupled by the term E of the crystal field. This coherent coupling produces an enhancement of the population transfer between S_z=+1/2 and the dressed states when they are on resonance (at the resonance, mixed states are created by the coherent coupling term). The optical recombination of the optically dressed state, which is mainly excitonic, induces an irreversible transfer of population from S_z=+1/2 to S_z=+5/2. In addition, S_z=+1/2 and S_z=-1/2 are coherently coupled by the hyperfine interaction which, through electron-nuclei flip-flops, induces an oscillation of population between these two levels. Consequently, both S_z=+1/2 and S_z=-1/2 populations are transferred to S_z=+5/2 through the coherent coupling with the dressed states. The strong influence of the in-plane strain anisotropy E is confirmed by the calculation: if the term E is suppressed, the population trapping regime disappears (not shown). A value of E corresponding to a few percent of D_0 (5% in the calculation presented in Fig. 3.6) can explain the redistribution of population observed in the resonant excitation experiments.

The interest of this trapping mechanism in the case of a Mn atom is that it should permit to prepare the Mn in one given spin state instead of just reducing the population of the state which is resonantly excited like in the optical pumping experiments we used until now. The first results of the model confirms that the dynamics we observe results from a coherent coupling between the Mn spin states induced either by the hyperfine coupling or an in-plane anisotropy in the crystal field. A detailed experimental study of this mechanism will be performed.

The efficiency of the population trapping is conditioned by the overlap of the optically dressed states with the Mn spin states not coupled to light and by the efficiency of the population transfer between these states. Both parameters are controlled by the combination of the laser power and detuning. A systematic study has to be performed to find the optimal excitation conditions to prepare the Mn spin.

Another possibility to affect the coherent coupling between the Mn spin states would be to apply an external magnetic field. In particular, a weak transverse magnetic field induces coherent coupling among the Mn spin states and should enhance the population trapping. However, as we have seen in optical pumping experiments, a transverse field which dominates the magnetic anisotropy, will erase the Mn spin memory. An optimum in the transverse magnetic field dependence of the trapping efficiency should be found to enhance the fidelity of the Mn spin preparation.

3.1.3 Time resolved optical pumping of coupled electronic and nuclear spins.

In the previous modeling, we just considered the steady state population of the Mn. We will now analyze how this stationary state is reached to estimate in which extend time resolved measurements could give the detail of the population transfer involved in the population trapping mechanism.

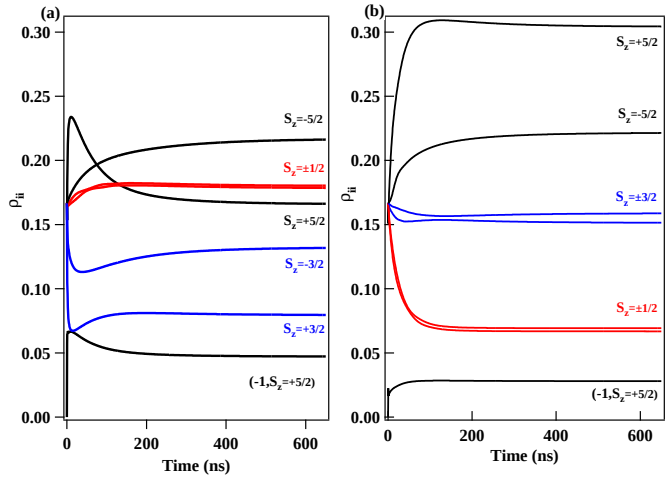

Figure 3.7 Dynamics of the electronic spin of the Mn under excitation around S_z=+5/2. (a) detuning $\delta = -20\mu eV$ and (b) $\delta = -40\mu eV$. The other parameters are $\mathcal{A} = 0.7\mu eV$, $\mathcal{D}_0 = 7\mu eV$, a=$0.32\mu eV$, $E = 0.35\mu eV$, $\tau_{Mn} = 250ns$, $\tau_r = 0.25ns$, $\tau_{pump} = 60ns$ and $\Omega_r = 25\mu eV$. The dynamics strongly depends on the detuning.

The expected dynamics of coupled electronic and nuclear spins under resonant optical excitation including the fine and hyperfine structure of the Mn and the strong coupling with the resonant laser field are presented in Fig. 3.7 for two different detunings. It appears that the dynamics strongly depends on the laser detuning. For a detuning of $\delta = -40\mu eV$ (Fig. 3.7(b)), the steady state is reached in less than 100 ns. For this value of detuning, the S_z=+5/2 dressed states are on resonance with S_z=±1/2 and the rise time of the S_z=+5/2 population measures the fast population transfer between these states.

If the detuning is slightly reduced ($\delta = -20\mu eV$, Fig. 3.7(a)), the S_z=+5/2 population presents a non-monotonic evolution. A fast initial increase in a few tens of ns is followed by a slower decrease and the steady state is reached after 500ns. For this detuning, the optically dressed states are on resonance with S_z=+3/2. The dressed state and S_z=+3/2 are coherently coupled by a flip-flop with the nuclear spin induced by the hyperfine coupling. This coupling associated with the optical recombination of the dressed state leads to a transfer of population from S_z=+3/2 to S_z=+5/2. The increase by one unit of the electronic spin is associated with a reduction by one unit of the nuclear spin. Repetition

of this process can lead to an optical pumping of the nuclear spin. This is responsible for the calculated long timescale decrease of the S_z=+5/2 population: as the nuclear spin get polarized, the coherent transfer induced by the electron-nuclei flip-flop are progressively blocked and the S_z=+5/2 population reaches its steady state. This expected complex spin dynamics will have to be studied in details experimentally.

The recently developed two-photon detection technique will be used to time resolved the population of each Mn spin state under resonant optical pumping conditions to reveal the long time scale dynamics induced by the fine and hyperfine structure of the Mn. These time resolved experiments would benefits from an improvement of the efficiency of the photon collection. Strategies to improve the photon collection from Mn-doped QDs will be presented in the last part of this chapter.

3.1.4 Optical control of the Mn nuclear spin.

Probing a single nuclear spin represents both the ultimate resolution limit of magnetic resonance imaging and a requirement in quantum computing proposals where the nuclear spin is used as a qubit. The idea of storing and manipulating information in nuclear spins goes back to quantum computing proposals based on P donors in Si [71]. Because of their very small coupling to their environment, the nuclear spin coherence time is expected to be very long but, for the same reason, quantum measurement of a single nuclear spin remains a formidable task. However, recent experimental breakthroughs have permitted performing single shot nondestructive measurement of a single nuclear spin by means of optically detected single spin magnetic resonance in NV centers in diamond [115].

We will show here how we can use the resonant optical excitation of a magnetic QD to access to the nuclear spin of an individual Mn atom in its diluted nuclear spin environment. As mentioned previously, the hyperfine interaction couples the electronic and the nuclear spins and an out of equilibrium distribution of the electronic spin should be transferred to the nuclear spin. In strained QDs, electron-nuclei flip-flops are blocked but they could be restored by the Stark shifting of some of the Mn spin states. Can we use this technique to optically induce a pumping and probe the nuclear spin of the Mn?

Figure 3.8(a) presents the calculated dependence of the population of the nuclear spin of the Mn versus the Rabi energy of a laser on resonance with (J_z=-1,S_z=+5/2,I_z). We still use the simplified structure of energy levels displayed in Fig. 3.5. The modeling shows that the nuclear spin population can become highly out of equilibrium when the Rabi energy is large enough to push the dressed states on resonance with the uncoupled states S_z=±3/2 and S_z=±1/2. In this regime, the electronic spin population is trapped in S_z=+5/2. As expected from the electron-nuclei flip-flops involved in the spin population trapping mechanism, the nuclear spin is pumped and the most populated nuclear spin state is I_z=-5/2.

Another way to change the energy of the dressed states is to slightly detune the laser from the excited transition. Fig. 3.8(b) presents the evolution of the nuclear

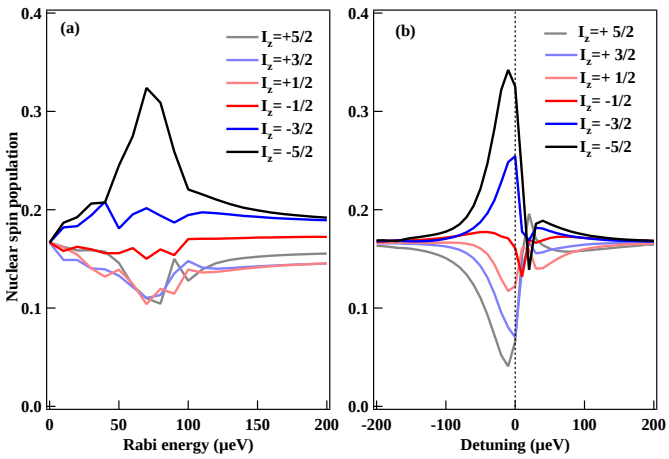

Figure 3.8 Population of the nuclear spin states I_z of the Mn as a function of Rabi energy for an excitation on (J_z=-1,S_z=+5/2,I_z)(a) and as a function of laser detuning from (J_z=-1,S_z=+3/2,I_z) (b). The parameters used in the calculation are $\mathcal{A} = 0.7\mu eV$, $\mathcal{D}_0 = 7\mu eV$, a=$0.32\mu eV$, $E = 0.35\mu eV$, $\tau_{Mn} = 250ns$, $\tau_r = 0.25ns$ et $\tau_{pump} = 60ns$. (a) $\delta = 0$, (b) $\Omega_r = 25\mu eV$.

spin population versus the detuning of the laser around the exciton level (J_z=-1,S_z=+3/2,I_z) for a fixed value of the Rabi energy. A highly out of equilibrium population of the nuclei is obtained for a detuning around δ=-15 μeV. Once again the most populated nuclear spin state is I_z=-5/2. For this particular detuning, the dressed states of S_z=+3/2 is on resonance with S_z=+1/2. The population transfer from S_z=+1/2 to S_z=+3/2 mediated by the hyperfine coupling pump down the nuclear spin. The hyperfine coupling also transfer the population from S_z=-1/2 to S_z=+1/2 through an electron nuclei flip-flop producing an additional channel of pumping for the nuclear spin. It appears that this configuration of excitation, around S_z=+3/2, is the most favorable for an optical preparation of the Mn nuclear spin.

A signature of this efficient pumping of the nuclear spin can be observed in the dynamics of the population of the electronic spin (Fig. 3.7(a)). We will use time resolved experiments in the regime of population trapping to analyze the dynamics of pumping and relaxation of the nuclear spin of the Mn atom. Using the two-photon detection technique, it should be possible to probe both the initialization and relaxation of the nuclear spin. In the absence of resonant optical excitation, the presence of the magnetic anisotropy D_0 will decouple the dynamics of the electronic and nuclear spins and should allow for a long spin memory of the isolated Mn nuclear spin in its diluted nuclear spin environment.

In the population trapping regime, a heating of the nuclear spin by a direct radio-frequency excitation will modify the spin transfer rate between the different electronic spin states. The population of the electronic spin should be modified and consequently change the intensity distribution on the X_2-Mn lines in the

two-photon Mn spin detection scheme. This gives an optical way to detect the magnetic resonance of an individual nuclear spin. A radio-frequency excitation can be tuned on resonance with the nuclear spin level associated with a given electronic spin projection, (S_z=±5/2,I_z) for instance. This resonant frequency is controlled by the hyperfine coupling and should not be significantly affected by much weaker quadripolar splitting of the nuclear spin induced by the strain anisotropy [20]. A change in the population of the Mn electronic spin should then be observed when an equilibrium distribution for the nuclear population will be restored by the radio-frequency excitation.

An experimental set-up combining the resonant optical excitation for the population trapping and Helmoltz coils for the resonant radio-frequency excitation of the nuclear spin will be developed. This set up will also be used to detect the nuclear magnetic resonance of Cd and Te nuclei. These spin I=1/2 are not affected by quadripolar effects in the strained QD and should present sharp magnetic resonance signal. The heating of the nuclear spin by the radio-frequency excitation will be detected in the polarization rate of a negatively charged QD in the optical pumping regime (see chapter 2). As recently demonstrated in InAs/GaAs QDs, this technique will allow probing the QD composition within the extension of the electron wave function [24].

3.1.5 Coherent dynamics of a Mn atom in an unstrained QDs.

We have shown that the strain induced magnetic anisotropy in CdTe/ZnTe Mn-doped QDs blocks the precession of the Mn spin in the hyperfine field of its nuclei. The creation of optically dressed states can restore these electron-nuclei flip-flops and strongly affect the spin dynamics of the magnetic atom. The magnetic anisotropy should be completely suppressed in fully unstrained QDs. In such system, the free coherent evolution of the electronic and nuclear spin prevents any spin memory at zero magnetic field. Unstrained QDs would be however an interesting model system allowing to observe the coherent precession of an individual Mn spin and to externally tune the decoupling between the dynamics of the electronic and nuclear spins with an external magnetic field. For instance, in a large magnetic field along the growth axis, the difference between electronic and nuclear Zeeman energies would suppress flip-flop interaction between the two species and restore a spin memory. On the other hand, even a weak transverse magnetic field will induce a coherent precession of the Mn spin. This precession should be directly observed in the auto-correlation of the emission intensity of an individual line of the sextuplet [13].

Under strong resonant excitation of one X-Mn transition in an unstrained QD, one given spin state of the Mn will be optically dressed. For a Rabi energy larger than the hyperfine interaction, this spin state will be decoupled from the nuclear spin and its coherent precession will stop: a spin memory will be restored. One possibility to probe this optically tunable dynamics is to compare the auto-correlation of the PL of the dressed states a with the spin fluctuation of the undressed states. Undressed states will have a fast dynamics in the *ns* governed

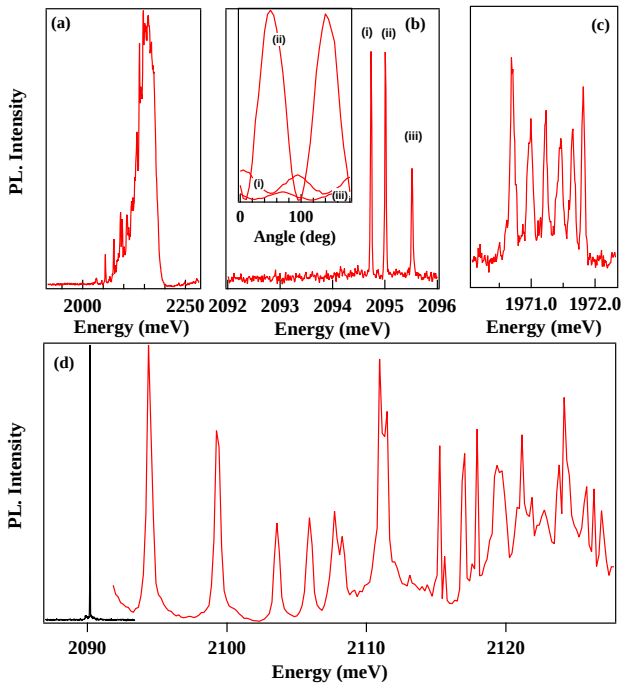

Figure 3.9 (a) Macro-photoluminescence of a thin CdTe/CdMgTe quantum well grown on a CdTe substrate. Individual QDs appears on the low energy side. (b) Photoluminescence of an interface fluctuation QD presenting a large valence band mixing. The three lines originate from the same QD: a mirror structure is observed on the biexciton and they have the same exited states (not presented). The inset shows that the emission of these QDs is highly linearly polarized. (c) A Mn doped interface fluctuation QD. (d) Photoluminescence excitation spectra of the QD presented in (b).

by electron-nuclei flip-flops. On the other hand, the optically dressed states should have a spin dynamics governed by their exciton-Mn component and a bunching in the tens of *ns* range should be observed.

Unstrained Mn-doped QDs already under development are based on interface fluctuations in thin CdTe quantum wells in CdMgTe barriers matched on a CdTe substrate (Fig. 3.9). First optical studies of such QDs show that, despite the absence of strain anisotropy, they present a large valence band mixing. Detailed magneto-optic study will be first performed to understand the origin of this valence band mixing in fully unstrained structures.

The first unstrained QDs containing an individual Mn atom have been observed recently (see Fig. 3.9). The control of incorporation of Mn in these structures will be optimized in close interaction with the MBE growth. Then, the magnetic field dependence of the dynamics of the Mn will be studied using time resolved optical pumping experiments already developed for CdTe/ZnTe strained induced QDs. A completely different optical pumping behavior is expected. Because of the

coupling with the nuclear spin no optical pumping should be observed at zero field and an optical pumping should be restored with an applied magnetic field of a few tens of milli-Teslas. As we have seen in strained dots, the dynamics of this pumping is controlled by exciton-Mn spin flips. Because of a different valence band mixing in unstrained structures, a different dynamics for the pumping could also be expected.

The coherent precession of an individual Mn atom in a transverse field and the dynamics of optically dressed states will then be analyzed using auto-correlation measurements. To observe the dynamics of the Mn alone (empty QD), these auto-correlation measurements have to be performed at low excitation intensity. These experiments require to increase the photon collection efficiency from individual Mn-doped QDs.

We will see in a following section that possible observation of the free precession of the Mn in these unstrained structures could also permit to perform a coherent control of an individual magnetic atom in a weak transverse magnetic field using optical techniques.

3.1.6 Mn-doped QDs in a photonic structure.

The proposed time resolved experiments for the study of the dynamics of the Mn nuclear spin and the autocorrelation measurements in unstrained QDs for the study of the Mn coherent precession would be greatly improved by increasing the photon collection efficiency from Mn-doped QDs. This will be of particular interest to access the long time scale dynamics of the nuclear spin. An efficient way to increase the light collection from an emitting dipole is to put it at the center of a hight index hemispherical lens as most of the photons are emitted in the high index medium [95] and can then be efficiently extracted from the lens shape material [149]. A 99% collection efficiency was predicted for individual molecules on a high index solid immersion lens combined with a dielectric structure [25].

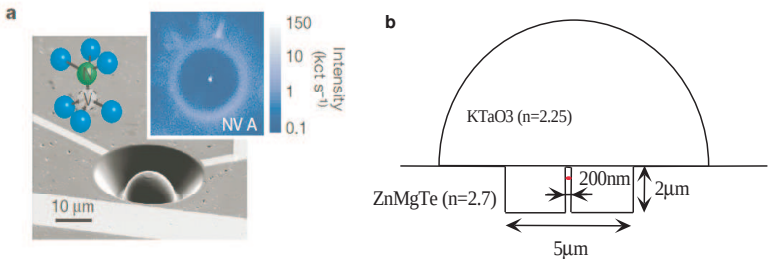

Figure 3.10 (a)Scanning electron microscope image of a solid immersion lens realized on a NV^- center in diamond (from reference [128]). (b) Scheme of a photonic wire structure coupled with a high index hemispherical lens.

To increase the number of collected photons and the light matter interaction, the Mn doped QDs will be introduced in photonic structure based on a single

mode waveguide [29] coupled with a high index (n_lens) micro-lens. The geometry of this simple photonic structure is presented in figure 3.10(b): Half of the emitted light is guided to the top of the wire. In a simplified picture, the top of the wire can be seen as an emitting dipole. This dipole will preferentially radiate light in the high index micro-lens. In term of waveguide optics, the index matching between the guided Gaussian mode and the high index lens suppress the modal reflection which would be around 20% for a radiation in a medium of index 1. The second advantage of the high index lens is that it reduce by a factor n_lens the angle of diffraction at the exit of the single mode fiber. The hemispherical shape of the micro-lens will then permit to efficiently collect the emitted light in a standard NA microscope objective without internal refraction loses.

The increase of the collection efficiency with this technique will first be tested on non-magnetic QDs randomly coupled with a photonic wire. Because of the low density of QDs containing one or two Mn atoms, a technique to position the photonic wire on the good Mn-doped QD will have to be developed. An optical positioning relative to a patterned mask on the sample surface will be tested. An all optical scheme for locating the position of single dots with sub-10 nm accuracy has been recently developed by Thon *et al.* [139]. Although the wavelength of a scanning laser is much larger than the required positioning accuracy, the center of the emission pattern of a QD can be located very precisely by accurately fitting the emission peak and averaging over many scans of the surface. This technique could be sufficient for a rough positioning of the dot in the photonic wire. Positioning of QDs in etched wires will also be used for other projects in the Lab to perform transport through QDs containing an individual Mn atom [47].

Alternatively, if the positioning of a Mn-doped QD in a photonic wire happens to be too difficult, etching an hemispherical lens with focus ion beam directly on the surface of the sample will be preferred [65]. This would be an intermediate solution that would already be better than the high index lens stick on the sample surface we used until now. Etched micro-lenses have been successfully used for the control of the spin of NV^- centers in diamond (Fig. 3.10(a)). Positioning of a Mn-doped QD in the center of a etched micro-lens with typical radius of 10 microns, requires a micrometer resolution which can be easily done with an optical technique.

3.2 Carrier controlled coupling between two Mn spins.

Semiconductors afford the unique opportunity of controlling the exchange interaction between distant magnetic dopants by varying the carrier density of the host. This has been shown in quantum wells [17] but in QDs the effect is expected to be stronger and to take advantage of the discreteness of the charge addition [48, 125].

We recently identified QDs containing two magnetic atoms. Despite the complexity of the optical spectra, in QDs with a weak valence band mixing, each spin state of the two Mn could be addressed optically. The injection of an individual

carrier in a QD containing two Mn could be used to deterministically control their coupling. As a first step towards the development of such device we will analyse the spin dynamics of individual carriers (electron or hole) exchange coupled to 1 or 2 Mn spins. We will analyze how the exchange interaction with a Mn spin stabilize the confined carrier spin and study the dynamics of the carrier induced ferromagnetic coupling between two localized Mn spins.

3.2.1 Dynamics of coupled carrier and Mn spins

In a magnetic QD, the exchange interaction between a confined carrier and the Mn spin lift the degeneracy of the spin of the carrier. In a p-doped Mn doped QD, the exchange coupling of the Mn spin and anisotropic hole spin form a ferromagnet with an easy axis along the QD growth axis and two degenerated ground states that correspond to opposite spins orientations for the hole-Mn system. The combined requirements of energy and spin conservation should make this hybrid spin very stable so that it could be used to store information.

The electron-Mn system, on the other hand, form a paramagnet with J=3 in the ground state. The dynamics of the electron-Mn complex should be controlled by the magnetic anisotropy of the Mn induced by the local strain at the Mn location. For a large magnetic anisotropy, the electron-Mn interaction should decouple the electron spin from the nuclear spin bath and cancel this source of dephasing. The dynamics of the coupled electron/Mn/nuclei spins will be studied in detail.

We will analyze the dynamics of these hybrid spin systems using both negatively charged and positively charged Mn-doped QDs. To avoid fast tunnel coupling with a reservoir that would erase any long spin memory, a chemical doping will be preferred. The chemical doping of these II-VI QDs will have to be improved in close interaction with the MBE growth. Singly charged n-doped QDs obtained with an Al modulation doping have already been realized. This electrical doping will have to be combined with the magnetic doping. For positively charged dots, the nitrogen doping of the ZnMgTe barriers (barrier material usually used to obtain a better hole confinement) will have to be developed.

Time resolved optical pumping experiments will then be carried out on modulation doped magnetic QDs. In negatively charged QDs, we have already shown that the injection of spin polarized carriers above the triplet state of the charged exciton can be used to optically pump the resident electron spin. The magnetic field dependence and the dynamics of the negative polarization rate in these QDs compared with non-magnetic dots (first section of chapter 2) will permit to analyze the influence of the exchange interaction with the Mn on the electron/nuclei spin coupling.

The dynamics of the coupled electron-Mn spins will ultimately control the initialization of hole-Mn complex under resonant optical pumping in p-doped QDs containing a Mn atom. This is illustrated in Fig. 3.11. Under resonant optical excitation of X^+-Mn we expect a very efficient and fast initialization of the hole-Mn complex controlled by electron-Mn spin-flips. On the other hand, the strong anisotropy induced by the hole spin should induce a long spin memory for the cou-

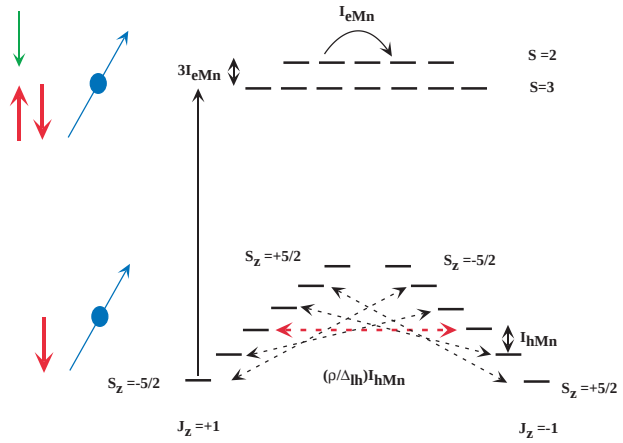

Figure 3.11 Scheme of the energy levels of X^+-Mn. A resonant excitation on one of the X^+-Mn optical transition followed by an electron-Mn spin-flip can be used to optically pump the hole-Mn system.

pled hole-Mn system. This dynamics will be studied with time resolved resonant optical pumping experiments. Mechanisms of hole-Mn spin relaxation should be dominated by the influence of the valence band mixing which couples two by two the different hole-Mn states with a characteristic energy $I_{hMn}(\rho_s/\Delta_{lh})$.

The fluorescence of a resonantly driven positively charged exciton will be used to probe the population of the hole-Mn spin state which is excited. As in the resonant optical pumping experiments performed on X-Mn, one can use the fluorescence signal emitted at slightly lower energy than the excitation after a carrier-Mn spin-flip to probe the resonant absorption. The time evolution of this signal under amplitude or polarization modulation of the excitation will reveal the dynamics of the optical initialization of the hole-Mn complex. The influence of a static magnetic field on the initialization process and on the carrier spin relaxation will be analyzed. The depolarization (decrease of the optical pumping efficiency) in a transverse magnetic field will give access to the stability (controlled by the spin anisotropy) of the hole-Mn complex.

3.2.2 Carrier induced coupling between two Mn spins

In a neutral dot containing two Mn atoms, the spins are only coupled via a very short range anti-ferromagnetic exchange, which would be only relevant for first or second neighbors ($I_{Mn,Mn}$=0.5meV for neighboring atoms) [52, 126]. However, the injection of a single electron, whose wave function is spread along the entire dot, couples the two Mn and the electron spin ferro-magnetically, resulting in a

ground state with $S = 11/2$. This contrasts with the addition of a single exciton on the neutral dot, for which the Mn spins also couple ferromagnetically, but the strong spin-orbit coupling of the hole breaks spin rotational invariance. The addition of an exciton on the negatively charged dot, puts the two electrons in a singlet state so that the two Mn interacts with a single hole.

Coupling between magnetic atoms induced by an injected carrier would be an important step toward electronic coupling of spin memory units based on Mn spins. The pulsed resonant injection and destruction of excitons in a QD containing two Mn atoms could be used to switch on and off their mutual interaction. In a longer time-scale, the fast (gigahertz) electrical injection of an individual carrier from a doped layer could be used [114]. The two Mn atoms could be individually addressed using resonant microwave absorption and their interaction tuned by the injection of individual carriers. In addition, the relative coupling of the two Mn spins with the confined carriers could be tuned by an in-plane uniform electric field which will shift the position of the carrier wave-function providing another tool to control the Mn-Mn coupling.

We will, as a first step, analyze the spin dynamics of two Mn spins exchanged coupled with a confined carrier spin (electron or hole) in modulation doped structures. We will in particular analyze to which extend the higher number of weakly spaced hole-Mn spin levels change the dynamics of the hole compared to the case of non-magnetic or singly Mn-doped QDs.

In a second step, devices with QDs containing 1 or 2 Mn in a transverse electric field will be developed. Etched micro-pillars containing 1Mn or 2Mn QDs will be selected by optical spectroscopy. Then, metallic electrical contacts will be realized on each side of the selected pillars by electron beam lithography. In the 1Mn-doped QDs case, the transverse electric field will shift the position of the carriers wave-function and change their exchange interaction with the Mn spin. The electric field dependence of the X-Mn splitting will permit to estimate the position of the Mn atom in a the QD plane. The DC Stark shift of the exciton could also be used for the fine tuning of the resonance with a single laser in the "optical trapping" experiments. In the 2 Mn case, the transverse field will change the relative coupling of each Mn spin with the confined carriers and then their mutual interaction.

Finally, field effect structures with a low capacitance [114] will be designed and realized to test the effect of fast electrical injection and removal of a single charge on the two Mn spins coupling.

3.3 Coherent control of individual carrier and Mn spins

A quantum computing scheme based on spins in a solid state environment requires to be able to do an initialization of the spin state, to perform a coherent control of an individual spin or of a pair of intricate spins in a time scale shorter than their decoherence time T_2, and finally to read the state of the spin before its relaxation. The most direct way to perform a coherent control is to use a resonant microwave excitation between two spins sublevels. However, an all optical control of

the state of a single spin would allow faster operations thanks to the technique of optical ultrafast coherent control.

We intend to develop the tools for coherent control of individual spins in II-VI semiconductor QDs. We will first discuss a method for the optical detection of the magnetic resonance of an individual Mn atom. We will then analyze the possibility to probe the coherent dynamics of individual electrons in CdTe/ZnTe QDs using time resolved optical Stark effect in a large transverse magnetic field. We will finally discuss a proposal for an optical fast coherent control of an individual Mn spin. It is based on the optical pumping of a Mn spin in an unstrained QD in a transverse magnetic field followed by a free precession and pulsed optical Stark effect.

3.3.1 Direct micro-wave control of a Mn spin.

After having established optical methods to prepare and readout the spin of a single Mn atom, we intend to manipulate the Mn spin using direct microwave excitation. As a first step towards the full coherent control of a Mn spin under microwave excitation we will develop a set-up to optically detect the spin resonance of a Mn atom under excitation with microwaves photons. This will permit to directly access the Mn spin structure induced by the crystal field and the hyperfine coupling with the Mn nuclear spin. The spectral linewidth of the spin resonance signal will also give the coherence time of this isolated spin. In this experiment, the effect of resonant microwaves photons will be detected in the signal of optical pumping already observed under CW or modulated quasi-resonant excitation. This experiment will greatly benefit from the increase of the PL collection efficiency by the used of etched micro-lens. This geometry can be combined with RF lines deposited on the sample surface and has been recently used successfully for NV center in diamonds (see Fig. 3.10). When this technique of electron spin resonance will be controlled, a pulsed microwave excitation could be used to perform a direct coherent control of the localized spin. The high microwave power needed for this coherent control could be achieved using micro-strip resonator deposited atop the semiconductor structure.

3.3.2 Control of electron spin using optical pulses.

As it has been demonstrated recently for individual electron or hole spins in InAs/GaAs QDs [123, 33], a coherent control of an individual spin can be performed with the optical Stark shift induced by resonant picosecond optical pulses excitation. A coherent control protocol similar to the one developed by Press *et al.* [123] including the initialization by optical pumping in a large transverse magnetic field (probed in the resonance fluorescence) and the fast optical control by picosecond pulses will be applied to a strongly confined electron spin in a II-VI self-assembled QDs. This will allow probing the coherent dynamics of the electron spin coupled to a diluted nuclear spin bath with I=1/2 [134].

The weak Overhauser field in II-VI QDs, 10 to 50 times smaller than in InAs

QDs, and the absence of hysteretic behavior should allow more complex optical coherent control operations no longer affected by the complex nuclear spin bath dynamics. Such reduction of the nuclear spin effects has already been observed for hole spins in III-V QDs [83] with coherence times limited by non-nuclear mechanism but similar to the electron. QDs based on II-VI compounds present a very large confinement for electrons, have very good optical properties and ultimately, these nano-structures could offer the possibility of isotopic purification to enhance the coherence time of the localized electron. Thought less popular II-VI semiconductors are then an interesting alternative to III-V materials and the coherent spin dynamics in II-VI nano-structure deserve to be investigated.

3.3.3 Time resolved optical Stark effect on a Mn spin.

Optically induced phase shifts and magnetic anisotropy

The simplified model of coherent Mn spin dynamics presented at the beginning of this chapter can be used to model pulsed optical coherent control experiments on a Mn spin. As we will see, optical coherent control operation on a Mn spin could in principle be performed in unstrained or weakly strained QDs.

A resonant picosecond pulsed excitation of a Mn-doped QD can move the system outside of the Mn spin subspace during its precession in a transverse magnetic field. This excitation introduces a phase shift between each Mn spin component. Such phase shifts can be seen as a rotation of the Mn spin. For instance, in a simple three level system, a 2π pulse induces a π rotation about the z axis (direction of optical propagation).

For a real Mn atom in a semiconductor matrix, the hyperfine coupling with the nuclear spin and the crystal field has to be taken into account to understand its coherent dynamics under pulsed excitation. The precession of a Mn spin in a transverse magnetic field $B_x = 0.25T$ for different values of strained induced magnetic anisotropy is presented in Fig. 3.12(a). After about $1ns$, the precession of the electronic Mn spin is blurred by the hyperfine coupling and influence of crystal field. Consequently, in a transverse field, a coherent control of the Mn can only be performed in the first $1ns$ and in a weakly strained QD resulting in a D_0 typically lower than 1 μeV. Such coherent control is presented in Fig. 3.12(b) for D_0=1μeV and sequences of one or two resonant pulses. This illustrate that optically induced phase shift can in principal be introduced in the precession of the Mn spin during the first ns after its initialization.

Full optical coherent control of a Mn spin.

We will develop an experiment for a complete optical control of a single Mn spin using the combination of narrow-band single mode laser for the spin initialization and picosecond pulses for the spin rotation. Similar optical techniques have been successfully used for the detection and the control of the state of ions in magnetic traps [109], for the control of ensemble of spins localized on donors in GaAs, in InAs QDs and for the control of a single electron or hole spin in an individual

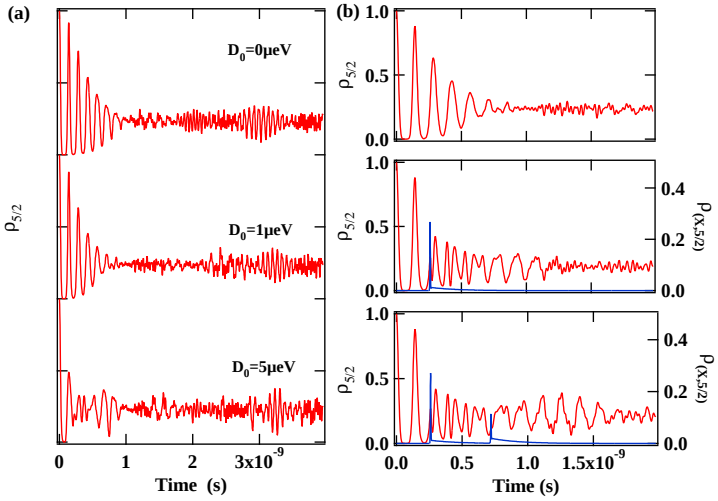

Figure 3.12 (a) Time evolution of $\varrho_{5/2}$ obtained with A=0.7 μeV, a=0.32 μeV and variable D_0 under a transverse magnetic field $B_x = 0.25T$ with $T_{Mn} = 20ns$ and $\varrho_{5/2}(0) = 1$. (b) Time evolution of $\varrho_{5/2}$ in a weakly strained Mn-doped QD ($D_0 = 1\mu$eV) under a transverse magnetic field $B_x = 0.25T$, with $T_{Mn} = 20ns$ and $\varrho_{5/2}(0) = 1$. Zero, one or two 2π Gaussian pulses with a width of $\tau = 10ps$ are sent at t_1= 260 ps and t_2=720 ps. The calculations are performed with τ_r=250 ps and a pure dephasing for the exciton $1/\gamma_d$=100 ps.

InAs QD. The successful implementation of a single Mn spins full optical control would be the first demonstration of a new way of using light to control atoms in a solid state environment.

The scheme proposed for a full fast optical control of an individual Mn spin is summarize in figure 3.13. An unstrained (or weakly strained) QD containing a Mn atom is placed in a weak static transverse magnetic field (typically 0.25 T in the QD plane). In this weak magnetic field regime, the exciton-Mn system remains quantized along the QD growth axis (the exciton-Mn, though spin polarized perpendicular to the magnetic field does not precess for fields up to a few Tesla). In the ground state (empty QD) the Mn spin is quantized along the magnetic field direction and its population is initially thermalized with the lattice. Its Zeeman splitting is in the order of tens of μeV's and all the levels are almost equally populated.

A preparation of a non-equilibrium distribution of the Mn (initialization) can be performed by optical pumping. In a transverse field B_x, each exciton-Mn level (quantized along z) is optically coupled to any of the Mn S_x states: six optical transitions are observed for each exciton-Mn levels. A narrow-band single mode laser can drive one of the lines of the sextuplet associated with a given exciton-Mn level. Let's consider for instance an excitation on the high energy line with $\sigma+$ photon (state (+1,+5/2)). The creation of the exciton-Mn complex followed

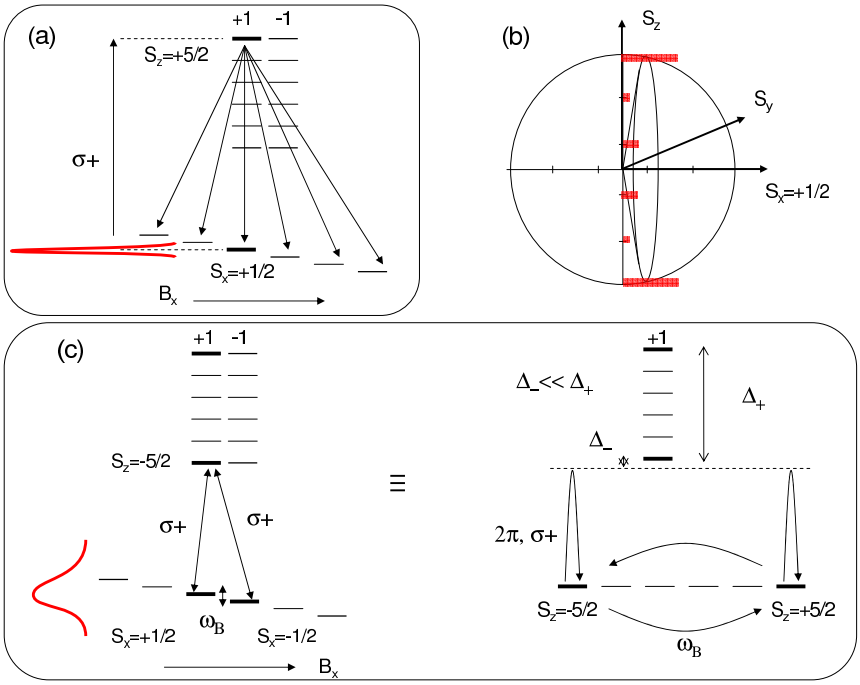

Figure 3.13 (a) Scheme of the optical pumping process for a Mn spin in a weak transverse magnetic field: A narrow-band single mode laser selectively excites the state S_x=+1/2 and creates a exciton-Mn state which spontaneously decays into the different S_x. This process empties the state S_x=+1/2. (b) Scheme of the projection of the spin state S_x=+1/2 on the basis S_z. The coefficients in the decomposition are obtained from the rotation matrix of a spin 5/2. (c) Scheme of the levels involved in the spin rotation protocol described in the text.

by the spontaneous decay into the different S_x quickly empties the state under excitation (S_x=+1/2 in the example presented in figure 3.13(a)).

This initialization process could be probed in the intensity of the resonance fluorescence. For these measurements, a time resolved resonance fluorescence set-up on individual dots under magnetic field will have to be developed. The quantum dot transition will be resonantly driven by a narrow-band frequency stabilized laser and the backscattered photons detected. The interaction of the incident laser beam with the QD and the collection of scattered photons will be enhanced by the use of photonic wires combined with high index solid immersion lenses. A modulation of the exciton energy by a transverse electric field could also be exploited for a lock in detection of the resonant fluorescence signal.

After spin rotation, the population of S_x=+1/2 could be measured using the same technique: if the spin is rotated, the QD will absorb photons and emit a fluorescence signal. A rotation of the Mn spin can be performed with picosecond pulses which will move the system population outside the Mn spin subspace

during the rotation in the transverse B field. This will introduce a phase shift between each Mn spin component S_x. Such phase shifts can be seen as a rotation of the Mn spin. Any direction of the Mn could be targeted with a carefully designed pulse sequence (amplitude and delay).

To illustrate the proposed mechanism, let's consider a simplified picture of the optical transitions in a Mn-doped QD. We will concentrate on the two ground states S_x=+1/2 and S_x=-1/2. They are both coupled by $\sigma+$ photons to any of the exciton-Mn (+1, S_z) states. S_x=+1/2 or S_x=-1/2 states can be expressed in the S_z basis. They are mainly formed of the components S_z=+5/2 and S_z=-5/2 (figure 3.13(b)). In other words, a $\sigma+$ photon will mainly coupled S_x=+1/2 and S_x=-1/2 to the exciton-Mn states (+1, +5/2) and (+1, -5/2). Let's consider the low energy state (+1, -5/2). Together with S_x=+1/2 and S_x=-1/2, they form a Λ system with both transitions having the same polarization and being very close in frequency (figure 3.13(c)).

An alternative depiction of this system is presented in figure 3.13(c) (right scheme): the lower levels are expressed as eigenstates of S_z which are not energy eigenstates since they are perpendicular to the magnetic field. Following the decomposition presented in figure 3.13(b), the main components are S_z=+5/2 and S_z=-5/2, coupled by the transverse magnetic field. When $\sigma+$ polarized light is sent in the bandgap, slightly detuned from the low energy exciton-Mn level, or on resonance with the low energy line, only the spin state S_z=-5/2 couples with the exciton-Mn state (+1, -5/2). The other one (+1, -5/2) is indirectly coupled through the magnetic field. A fast resonant pulse of area 2π will move the population outside the Mn spin subspace (S_z=+5/2 or -5/2) during the rotation in the transverse B field and will induce a phase shift between S_z=+5/2 and S_z=-5/2. This amounts to a rotation of the spin about the z axis if we neglect the phase shift induced by non-resonant coupling between S_z=+5/2 and (+1, +5/2) (i.e. consider a pure three level system).

In the full multilevel system, different phase shift will be introduced in all the S_z components through the non-resonant coupling with all the six exciton-Mn levels. A complete modeling including all the optically active transitions will have to be developed. These experiments will be first performed on individual Mn spins in unstrained interface QDs.

Conclusion

Single dot spectroscopy is a very powerful technique for the study of the spin dynamics at the single spin level. The optical properties of II-VI QDs containing individual carriers and 1 or 2 Mn atoms will now be used for the study of the coherent dynamics and the coherent control of few interacting spins in a solid state environment. The strong coupling with a resonant laser field by creating an optically dressed magnetic atom provides new ways to initialize the Mn spin. It should also permit to optically access the nuclear spin of an individual Mn atom and study its dynamics in its diluted nuclear spin bath. Extension of this work to QDs containing two magnetic atoms would permit to optically control

the electronic coupling between localized spins. The optical properties of these QDs in the strong coupling regime suggest a possible all optical coherent control of an individual Mn spin exploiting the time resolved optical Stark effect.

General conclusion

Using single dot spectroscopy, we studied the spin dynamics of individual carrier and individual Mn atom in II-VI material. The emission of magnetic QDs reveals the interactions between the confined carriers and the Mn spin. The different parameters controlling these interactions were determined by magneto-optical experiments. By analyzing the emission spectrum of some of these magnetic QDs, we can detect directly the spin state of the magnetic atom. The detection conditions are strongly influenced by the dot shape anisotropy or an inhomogeneous distribution of strains in the local environment of the dot. The effects of these phenomena were studied in details. We also studied the magneto-optical properties of the different charged states of magnetic QDs. This shows the possibility to control electrically or optically the magnetic anisotropy of nanoscopic magnetic systems.

Single spin temporal fluctuations were pointed out by analyzing the statistics of photons emitted by single magnetic QDs. We have shown that Mn spin orientation could be achieved using light of a controlled helicity and energy. This was the first demonstration of the optical pumping of a magnetic atom in a solid state environment. The spin distribution obtained by such means is perfectly conserved over a few μs. This is a direct evidence of the long spin memory of an individual Mn atom. The dynamic of the Mn spin orientation at zero magnetic field is controlled by a magnetic anisotropy produced by the presence of strains at the Mn location. We have also demonstrated the possibility to create optically dressed states on a Mn-doped QD. This signature of a strong light-matter coupling, and of an optical Stark shift of the Mn spin is promising for coherent manipulation of the Mn atom. We already shown that the strong coupling with a resonant laser field, by creating an optically dressed magnetic atom, provides new ways to initialize the Mn spin.

It appears that single dot spectroscopy is a very powerful technique for the study of the spin dynamics at the single spin level. The optical properties of II-VI charged and magnetic QDs will now be used for the study of the coherent dynamics and the coherent control of few interacting spins: one or two magnetic atoms in interaction with their nuclear spins, electron or hole spins in a QD interacting or not with a magnetic atom spin and in contact with a diluted nuclear spin bath. All the optical control technique discussed in this manuscript could be easily extended to QDs containing other transition metals (Cr, with 90% of isotopes without nuclear spin could be an interesting alternative system).

Appendix A

Main publications related to presented work

1. *Optical control of the spin state of two Mn atoms in a quantum dot.* L. Besombes, C.L. Cao, S. Jamet, H. Boukari, J. Fernandez-Rossier, Physical Review B 86, 165306 (2012).

2. *Electron-nuclei spin dynamics in II-VI semiconductor quantum dots.* C. Le Gall, A. Brunetti, H. Boukari, L. Besombes, Physical Review B 85, 195312 (2012).

3. *Optical Stark effect and dressed excitonic states in a Mn-doped quantum dot.* C. Le Gall, A. Brunetti, H. Boukari, L. Besombes, Physical Review Letters 107, 057401 (2011).

4. *Spin-phonon coupling in single Mn-doped CdTe quantum dot.* C.L. Cao, L. Besombes, J. Fernandez-Rossier, Physical Review B 84, 205305 (2011).

5. *Optical initialization, readout, and dynamics of a Mn spin in a quantum dot.* C. Le Gall, R.S. Kolodka, C.L. Cao, H. Boukari, H. Mariette, J. Fernandez-Rossier, L. Besombes, Physical Review B 81, 245315 (2010).

6. *Optical spin orientation of a single manganese atom in a semiconductor quantum dot using quasiresonant photoexcitation.* C. Le Gall, L. Besombes, H. Boukari, R. Kolodka, H. Mariette, J. Cibert, Physical Review Letters 102, 127402 (2009).

7. *Optical probing of spin fluctuations of a single paramagnetic Mn atom in a semiconductor quantum dot.* L. Besombes, Y. Leger, J. Bernos, H. Boukari, H. Mariette, J. P. Poizat, T. Clement, J. Fernandez-Rossier, R. Aguado, Physical Review B 78, 125324 (2008).

8. *Spin properties of charged Mn-doped quantum dots.* L. Besombes, Y. Leger, L. Maingault, H. Mariette, Journal of Applied Physics 101, 081713 (2007).

9. *Valence band mixing in neutral, charged, and Mn-doped self-assembled quantum dots.* Y. Leger, L. Besombes, L. Maingault, H. Mariette, Physical Review

B 76, 045331 (2007).

10. *Fine structure of exciton excited levels in a quantum dot with a magnetic ion.* M.M. Glazov, E.L. Ivchenko, L. Besombes, Y. Leger, L. Maingault, H. Mariette, Physical Review B 75, 205313 (2007).

11. *Electrical control of a single Mn atom in a quantum dot.* Y. Leger, L. Besombes, J. Fernandez-Rossier, L. Maingault, H. Mariette, Physical Review Letters 97, 107401 (2006).

12. *Hole spin anisotropy in single Mn-doped quantum dots.* Y. Leger, L. Besombes, L. Maingault, D. Ferrand, H. Mariette, Physical Review B 72 (24), 241309(R) (2005).

13. *Geometrical effects on the optical properties of quantum dots doped with a single magnetic atom.* Y. Leger, L. Besombes, L. Maingault, D. Ferrand, H. Mariette, Physical Review Letters 95, 047403 (2005).

14. *Carriers induced spin splitting of a magnetic atom embedded in a quantum dot.* L. Besombes, Y. Leger, L. Maingault, D. Ferrand, H. Mariette, J. Cibert, Physical Review B 71, 161307(R) (2005).

15. *Probing the spin state of a single magnetic atom in an individual quantum dot.* L. Besombes, Y. Leger, L. Maingault, D. Ferrand, H. Mariette, J. Cibert, Physical Review Letters 93, 207403 (2004).

References

[1] Abragam, A. (ed). 1961. *Principles of nuclear magnetism.* Oxford University Press.

[2] Akimov, I.A., Feng, D.H., and Henneberger, F. 2006. Electron Spin Dynamics in a Self-Assembled Semiconductor Quantum Dot: The Limit of Low Magnetic Fields. *Phys. Rev. Lett.*, **97**, 056602.

[3] Archer, P.I., Santangelo, S.A., and Gamelin, D.R. 2007. Direct Observation of sp-d Exchange Interactions in Colloidal Mn^{2+} and Co^{2+} Doped CdSe Quantum Dots. *Nanoletters*, **7**, 1037.

[4] Autler, S.H., and Townes, C.H. 1955. Stark Effect in Rapidly Varying Fields. *Phys. Rev.*, **100**, 703.

[5] Bacher, G., Maksimov, A. A., Schömig, H., Kulakovskii, V. D., Welsch, M. K., Forchel, A., Dorozhkin, P. S., Chernenko, A. V., Lee, S., Dobrowolska, M., and Furdyna, J. K. 2002. Monitoring Statistical Magnetic Fluctuations on the Nanometer Scale. *Phys. Rev. Lett.*, **89**(12), 127201.

[6] Baudin, E., Benjamin, E., Lemaitre, A., and Krebs, O. 2011. Optical Pumping and a Nondestructive Readout of a Single Magnetic Impurity Spin in an InAs/GaAs Quantum Dot. *Phys. Rev. Lett.*, **107**, 197402.

[7] Bayer, M., Ortner, G., Stern, O., Kuther, A., Gorbunov, A.A., A.Forchel, Hawrylak, P., Fafard, S., Hinzer, K., Reinecke, T.L., Walck, S.N., Reithmaier, J.P., Klopf, F., and Schafer, F. 2002. Fine structure of neutral and charged excitons in self-assembled In(Ga)As/(Al)GaAs quantum dots. *Phys. Rev. B*, **65**, 195315.

[8] Beaulac, R., Schneider, L., Archer, P.I., Bacher, G., and Gamelin, D.R. 2009. Light-Induced Spontaneous Magnetization in Doped Colloidal Quantum Dots. *Science*, **325**(5943), 973–976.

[9] Besombes, L., Marsal, L., Kheng, K., Charvolin, T., Dang, Le Si, Wasiela, A., and Mariette, H. 2000. Fine structure of the exciton in a single asymmetric CdTe quantum dot. *Journal of Crystal Growth*, **214/215**, 742.

[10] Besombes, L., Kheng, K., Marsal, L., and Mariette, H. 2002. Few-particle effects in single CdTe quantum dots. *Phys. Rev. B*, **65**, 121314.

[11] Besombes, L., Léger, Y., Maingault, L., Ferrand, D., Mariette, H., and Cibert, J. 2004. Probing the Spin State of a Single Magnetic Ion in an Individual Quantum Dot. *Phys. Rev. Lett.*, **93**, 207403.

[12] Besombes, L., Leger, Y., Maingault, L., Ferrand, D., Mariette, H., and Cibert, J. 2005. Carrier-induced spin splitting of an individual magnetic atom embedded in a quantum dot. *Phys. Rev. B*, **71**, 161307.

[13] Besombes, L., Léger, Y., Bernos, J., Boukari, H., Mariette, H., Poizat, J.P., Fernandez-Rossier, J., and Aguado, R. 2008. Optical probing of spin fluctuations of a single paramagnetic Mn atom in a semiconductor quantum dot. *Phys. Rev. B*, **78**, 125324.

[14] Bhattacharjee, A. K., and Pérez-Conde, J. 2003. Optical properties of paramagnetic ion-doped semiconductor nanocrystals. *Phys. Rev. B*, **68**(4), 045303.

[15] Bhunia, S., and Bose, D. N. 2000. Schottky barrier studies on single crystal ZnTe and determination of interface index. *J. of Appl. Phys.*, **87**, 2931.

[16] Bockelmann, U., and Bastard, G. 1992. Interband absorption in quantum wires. I. Zero-magnetic-field case. *Phys. Rev. B*, **45**, 1688.

[17] Boukari, H., Kossacki, P., Bertolini, M., Ferrand, D., Cibert, J., Tatarenko, S., Wasiela, A., Gaj, J. A., and Dietl, T. 2002. Light and Electric Field Control of Ferromagnetism in Magnetic Quantum Structures. *Phys. Rev. Lett.*, **88**(20), 207204.

[18] Boyle, S.J., Ramsay, A.J., Fox, A.M., Skolnick, M.S., Heberle, A.P., and Hopkinson, M. 2009. Beating of Exciton-Dressed States in a Single Semiconductor InGaAs/GaAs Quantum Dot. *Phys. Rev. Lett.*, **102**, 207401.

[19] Bracker, A. S., Stinaff, E. A., Gammon, D., Ware, M. E., Tischler, J. G., Shabaev, A., Efros, Al. L., Park, D., Gershoni, D., Korenev, V. L., and Merkulov, I. A. 2005. Optical Pumping of the Electronic and Nuclear Spin of Single Charge-Tunable Quantum Dots. *Phys. Rev. Lett.*, **94**, 047402.

[20] Bulutay, C. 2012. Quadrupolar spectra of nuclear spins in strained $In_xGa_{1-x}As$ quantum dots. *Phys. Rev. B*, **85**, 115313.

[21] Cao, C. L., Besombes, L., and Fernández-Rossier, J. 2011. Spin-phonon coupling in single Mn-doped CdTe quantum dot. *Phys. Rev. B*, **84**, 205305.

[22] Causa, M. T., Tovar, M., Oseroff, S. B., Calvo, R., and Giriat, W. 1980. Spin-Lattice coefficients of Mn^{2+} in II-VI compounds. *Phys. Lett.*, **A77**(6), 473.

[23] Chekhovich, E. A., Makhonin, M. N., Skiba-Szymanska, J., Krysa, A. B., Kulakovskii, V. D. Skolnick, M. S., and Tartakovskii, A. I. 2010. Dynamics of optically induced nuclear spin polarization in individual $InP/Ga_xIn_{1-x}P$ quantum dots. *Phys. Rev. B*, **81**, 245308.

[24] Chekhovich, E. A., Kavokin, K. V., Puebla, J., Krysa, A. B., Hopkinson, M., Andreev, A. D., Sanchez, A. M., Beanland, R., Skolnick, M. S., and Tartakovskii, A. I. 2012. Structural analysis of strained quantum dots using nuclear magnetic resonance. *Nature Nanotechnology*, **7**, 646.

[25] Chen, X-W, Gotzinger, S, and Sandoghdar, V. 2011. 99% efficiency in collecting photons from a single emitter. *Optics Letters*, **36**, 3545.

[26] Cheng, S.-J., and Hawrylak, P. 2008. Controlling magnetism of semi-magnetic quantum dots with odd-even exciton numbers. *Eur. Phys. Lett.*, **81**, 37005.

[27] Cherbunin, R. V., Verbin, S. Yu., Auer, T., Yakovlev, D. R., Reuter, D., Wieck, A. D., Gerlovin, I. Ya., Ignatiev, I. V., Vishnevsky, D. V., and Bayer, M. 2009. Dynamics of the nuclear spin polarization by optically oriented electrons in a (In,Ga)As/GaAs quantum dot ensemble. *Phys. Rev. B*, **80**, 035326.

[28] Chernenko, A. V., Dorozhkin, P. S., Kulakovskii, V. D., Brichkin, A. S., Ivanov, S. V., and Toropov, A. A. 2005. Auger recombination of excitons in semimagnetic quantum dot structure in a magnetic field. *Phys. Rev. B*, **72**(4), 045302.

[29] Claudon, J., Bleuse, J., Malik, N. Singh, Bazin, M., Jaffrennou, P., Gregersen, N., Sauvan, C., Lalanne, P., and Gerard, J.-M. 2010. A highly efficient single-photon source based on a quantum dot in a photonic nanowire. *Nature Photonics*, **4**, 174.

[30] Cortez, S., Krebs, O., and Voisin, P. 2000. In-plane optical anisotropy of quantum well structures: From fundamental considerations to interface characterization and optoelectronic engineering. *J. Vac. Sci. Technol. B*, **18**, 2232.

[31] Cortez, S., Krebs, O., Laurent, S., Senes, M., Marie, X., Voisin, P., Ferreira, R., Bastard, G., Gerard, J-M., and Amand, T. 2002. Optically Driven Spin Memory in n-Doped InAs-GaAs Quantum Dots. *Phys. Rev. Lett.*, **89**, 207401.

[32] Cywinsky, L. 2010. Optical orientation of a single Mn spin in a quantum dot: Role of carrier spin relaxation. *Phys. Rev. B*, **82**, 075321.

[33] De Greve, K., Mcmahon, P.L., Press, D., Ladd, T.D., Bisping, D., Schneider, C., Kamp, M., Worschech, L., Hofling, S., Forchel, A., and Yamamoto, Y. 2011. Ultrafast coherent control and suppressed nuclear feedback of a single quantum dot hole qubit. *Nature Physics*, **7**, 872.

[34] Deng, C., and Hu, X. 2005. Nuclear spin diffusion in quantum dots: Effects of inhomogeneous hyperfine interaction. *Phys. Rev. B*, **72**, 165333.

[35] Desfonds, P., Eble, B., Fras, F., Testelin, C., Bernardot, F., Chamarro, M., Urbaszek, B., Amand, T., Marie, X., Grard, J. M., Thierry-Mieg, V., Miard, A., and Lematre, A. 2010. Electron and hole spin cooling efficiency in InAs quantum dots: The role of nuclear field. *Apll. Phys. Lett.*, **96**, 172108.

[36] Dietl, T., Peyla, P., Grieshaber, W., and d'Aubigne, Y. Merle. 1995. Dynamics of Spin Organization in Diluted Magnetic Semiconductors. *Phys. Rev. Lett.*, **74**, 474.

[37] Dorozhkin, P. S., Chernenko, A. V., Kulakovskii, V. D., Brichkin, A. S., Maksimov, A. A., Schoemig, H., Bacher, G., Forchel, A., Lee, S., Dobrowolska, M., and Furdyna, J. K. 2003. Longitudinal and transverse fluctuations of magnetization of the excitonic magnetic polaron in a semimagnetic single quantum dot. *Phys. Rev. B*, **68**(19), 195313.

[38] Dou, X.M., Sun, B.Q., Jiang, D.S., Ni, H.Q., and Niu, Z.C. 2012. Measurements of a fast nuclear-spin dynamicfs in a single InAs quantum dot with positively charged exciton. *Europeen Physics Letter*, **98**, 17007.

[39] Dreiser, J., Atatre, M., Galland, C., Mller, T., Badolato, A., and Imamoglu, A. 2008. Optical investigations of quantum dot spin dynamics as a function of external electric and magnetic fields. *Phys. Rev. B*, **77**, 075317.

[40] Dyakonov, M. I. 2008. *Spin physics in Semiconductors*. Springer.

[41] Dzhioev, R.I., and Korenev, V.L. 2007. Stabilization of the Electron-Nuclear Spin Orientation in Quantum Dots by the Nuclear Quadrupole Interaction. *Phys. Rev. Lett.*, **99**, 037401.

[42] Eble, B., Krebs, O., Lemaitre, A., Kowalik, K., Kudelski, A., Voisin, P., Urbaszek, B., Marie, X., and Amand, T. 2006. Dynamic nuclear polarization of a single charge-tunable InAs?GaAs quantum dot. *Phys. Rev. B*, **74**, 081306(R).

[43] Erwin, S.C., Zu, L., Haftel, M.I., Efros, A.L., Kennedy, T. A., and Norris, D. J. 2005. Doping semiconductor nanocrystals. *Nature*, **436**, 91–94.

[44] Favero, I., Cassabois, G., Voisin, C., Delalande, C., Roussignol, Ph., Ferreira, R., Couteau, C., Poizat, J. P., and Gérard, J. M. 2005. Fast exciton spin relaxation in single quantum dots. *Phys. Rev. B*, **71**, 233304.

[45] Feng, D.H., Akimov, I.A., and Henneberger, F. 2007. Nonequilibrium Nuclear-Electron Spin Dynamics in Semiconductor Quantum Dots. *Phys. Rev. Lett.*, **99**, 036604.

[46] Fernández-Rossier, J. 2006. Single-exciton spectroscopy of semimagnetic quantum dots. *Phys. Rev. B*, **73**, 045301.

[47] Fernández-Rossier, J., and Aguado, Ramón. 2007. Single-Electron Transport in Electrically Tunable Nanomagnets. *Phys. Rev. Lett.*, **98**, 106805.

[48] Fernandez-Rossier, J., and Brey, L. 2004. Ferromagnetism Mediated by Few Electrons in a Semimagnetic Quantum Dot. *Phys. Rev. Lett.*, **93**, 117201.

[49] Flagg, E.B., Muller, A., Robertson, J.W., Founta, S., Deppe, D. G., Xiao, M., Ma, W., Salamo, G. J., and Shih, C.K. 2009. Resonantly driven coherent oscillations in a solid-state quantum emitter. *Nature Physics*, **5**, 203.

[50] Flissikowski, T., Betke, A., Akimov, I.A., and Henneberger, F. 2004. Two-photon coherent control of a single quantum dot. *Phys. Rev. Lett.*, **92**, 227401.

[51] Fras, F., Eble, B., Desfonds, P., Bernardot, F., Testelin, C., Chamarro, M., Miard, A., and Lemaître, A. 2012. Two-phonon process and hyperfine interaction limiting slow hole-spin relaxation time in InAs/GaAs quantum dots. *Phys. Rev. B*, **86**, 045306.

[52] Furdyna, J.K. 1988. Diluted magnetic semiconductors. *J. Appl. Phys.*, **64**, R29.

[53] Furdyna, J.K., and Kossut, J. (eds). 1988. *Diluted Magnetic Semiconductors*. Semiconductors and Semimetals, vol. 25. Academic Press, Boston.

[54] Gaj, J. A., Planel, R., and Fishman, G. 1979. title. *Solid State Communications*, **29**, 435.

[55] Gammon, D., Efros, Al. L., Kennedy, T. A., Rosen, M., Katzer, D. S., Park, D., Brown, S. W., Korenev, V. L., and Merkulov, I. A. 2001. Electron and Nuclear Spin Interactions in the Optical Spectra of Single GaAs Quantum Dots. *Phys. Rev. Lett.*, **86**, 5176.

[56] Gerardot, JB. D., Brunner, D., Dalgarno, P. A., Ohberg, P., Seidl, S., Kroner, M., Karrai, K., Stoltz, N. G., Petroff, P. M., and Warburton, R. 2008. Optical pumping of a single hole spin in a quantum dot. *Nature*, **451**, 441.

[57] Glazov, M. M., Ivchenko, E. L., Besombes, L., Léger, Y., Maingault, L., and Mariette, H. 2007. Fine structure of exciton excited levels in a quantum dot with a magnetic ion. *Phys. Rev. B*, **75**, 205313.

[58] Goryca, M., Ferrand, D., Kossacki, P., Nawrocki, M., Pacuski, W., Maslana, W., Gaj, J.A., Tatarenko, S., Cibert, J., Wojtowicz, T., and Karczewski, G. 2009a. Magnetization Dynamics Down to a Zero Field in Dilute (Cd,Mn)Te Quantum Wells. *Phys. Rev. Lett.*, **102**, 046408.

[59] Goryca, M., Kazimierczuk, T., Nawrocki, M., Golnik, A., Gaj, J. A., Kossacki, P., Wojnar, P., and Karczewski, G. 2009b. Optical Manipulation of a Single Mn Spin in a CdTe-Based Quantum Dot. *Phys. Rev. Lett.*, **103**, 087401.

[60] Govorov, A. O., and Kalameitsev, A. V. 2005. Optical properties of a semiconductor quantum dot with a single magnetic impurity: photoinduced spin orientation. *Phys. Rev. B*, **71**, 035338.

[61] Govorov, Alexander O. 2004. Optical probing of the spin state of a single magnetic impurity in a self-assembled quantum dot. *Phys. Rev. B*, **70**, 035321.

[62] Gray, Dwight E. (ed). 1972. *American Intitut of Physics Handbook*. McGraw-Hill.

[63] Greenough, R. D., and Palmer, S. B. 1973. The elastic constants and thermal expansion of single-crystal CdTe. *J. Phys. D: Appl. Phys.*, **6**(53), 587.

[64] Greilich, A., Yakovlev, D.R., Shabaev, A., Efros, Al. L, I.A., Yugova, Oulton, R., Stavarache, V., Reuter, D., Wieck, A., and Bayer, M. 2006. Mode locking of electron spin coherence in singly charged quantum dots. *Science*, **313**, 341.

[65] Hadden, J. P., Harrison, J. P., Stanley-Clarke, A. C., Marseglia, L., Ho, Y.-L. D., Patton, B. R., OBrien, J. L., and Rarity, J. G. 2010. Strongly enhanced photon collection from diamond defect centers under microfabricated integrated solid immersion lenses. *Applied Physics Letters*, **97**, 241901.

[66] Hartmann, A., Ducommun, Y., Kapon, E., Hohenester, U., and Molinari, E. 2000. Few-Particle Effects in Semiconductor Quantum Dots: Observation of Multicharged Excitons. *Phys. Rev. Lett*, **84**, 5648.

[67] Hundt, A., Puls, J., and Henneberger, F. 2004. Spin properties of self-organized diluted magnetic $Cd_{1-x}Mn_xSe$ quantum dots. *Phys. Rev. B*, **69**(12), 121309.

[68] Ikezawa, M., Pal, B., Masumoto, Y., Ignatiev, I. V., Verbin, S. Yu., and Gerlovin, Ilya Ya. 2005. Submillisecond electron spin relaxation in InP quantum dots. *Phys. Rev. B*, **72**, 153302.

[69] Jundt, G., Robledo, L., Hgele, A., Flt, S., and Imamoglu, Atac. 2008. Observation of Dressed Excitonic States in a Single Quantum Dot. *Phys. Rev. Lett.*, **100**, 177401.

[70] Kamada, H., Gotoh, H., Temmyo, J., Takagahara, T., and Ando, H. 2001. Exciton Rabi Oscillation in a Single Quantum Dot. *Phys. Rev. Lett.*, **87**, 246401.

[71] Kane, B. E. 1998. A silicon-based nuclear spin quantum computer. *Nature*, **393**, 133.

[72] Keller, D., Yakovlev, D. R., Knig, B., Ossau, W., Gruber, Th., Waag, A., Molenkamp, L. W., and Scherbakov, A. V. 2001. Heating of the magnetic ion system in (Zn, Mn)Se/(Zn, Be)Se semimagnetic quantum wells by means of photoexcitation. *Phys. Rev. B*, **65**, 035313.

[73] Klauser, D., Coish, W.A., and Loss, D. 2006. Nuclear spin state narrowing via gate-controlled Rabi oscillations in a double quantum dot. *Phys. Rev. B*, **73**, 205302.

[74] Klopotowski, L., l. Cywinski, Wojnar, P., Voliotis, V., Fronc, K., Kazimierczuk, T., Golnik, A., Ravaro, M., Grousson, R., Karczewski, G., and Wojtowicz, T. 2011. Magnetic polaron formation and exciton spin relaxation in single Cd1-xMnxTe quantum dots. *Phys. Rev. B*, **83**, 081306(R).

[75] Koenraad, P. M., and Flatte, M. E. 2011. Single dopants in semiconductors. *Nature Materials*, **10**, 91.

[76] Komaronv, A.V., Ryabchenko, S.M., Terletskii, O.V., Zheru, I.I., and Ivanchuk, R.D. 1977. bla. *Sov. Phys. JETP*, **46**, 318.

[77] Koudinov, A. V., Akimov, I. A., Kusrayev, Yu. G., and Henneberger, F. 2004. Optical and magnetic anisotropies of the hole states in Stranski-Krastanov quantum dots. *Phys. Rev. B*, **70**, 241305.

[78] Krebs, O., Maletinsky, P., Amand, T., Urbaszek, B., Lemaitre, A., Voisin, P., Marie, X., and Imamoglu, A. 2010. Anomalous Hanle Effect due to Optically Created Transverse Overhauser Field in Single InAs/GaAs Quantum Dots. *Phys. Rev. Lett.*, **104**, 056603.

[79] Krebs, Olivier, Benjamin, Emile, and Lemaitre, Aristide. 2009. Magnetic anisotropy of singly Mn-doped InAs/GaAs quantum dots. *Phys. Rev. B*, **80**, 165315.

[80] Kroner, M., Lux, C., Seidl, S., Holleitner, A. W., Karrai, K., Badolato, A., Petroff, P. M., and Warburton, R.J. 2008. Rabi splitting and ac-Stark shift of a charged exciton. *Appl. Phys. Lett.*, **92**, 031108.

[81] Kudelski, A., Lemaitre, A., Miard, A., Voisin, P., Graham, T. C. M., Warburton, R. J., and Krebs, O. 2007. Optically Probing the Fine Structure of a Single Mn Atom in an InAs Quantum Dot. *Phys. Rev. Lett.*, **99**, 247209.

[82] Kurtsiefer, Christian, Mayer, Sonja, Zarda, Patrick, and Weinfurter, Harald. 2000. Stable Solid-State Source of Single Photons. *Phys. Rev. Lett.*, **85**, 290.

[83] Ladd, T. D., Press, D., De Greve, K., McMahon, P. L., Friess, B., Schneider, C., Kamp, M., Höfling, S., Forchel, A., and Yamamoto, Y. 2010. Pulsed Nuclear Pumping and Spin Diffusion in a Single Charged Quantum Dot. *Phys. Rev. Lett.*, **105**, 107401.

[84] Lai, C.W., Maletinsky, P., Badolato, A., and Imamoglu, A. 2006. Knight-Field-Enabled Nuclear Spin Polarization in Single Quantum Dots. *Phys. Rev. Lett.*, **96**, 167403.

[85] Latta, C., Hgele, A., Zhao, Y., Vamivakas, A. N., Maletinsky, P., Kroner, M., Dreiser, J., Carusotto, I., Badolato, A., Schuh, D., Wegscheider, W., Atature, M., and Imamoglu1, A. 2009. Confluence of resonant laser excitation and bidirectional quantum-dot nuclear-spin polarization. *Nature Physics*, **5**, 758.

[86] Le Gall, C., Besombes, L., Boukari, H., Kolodka, R., Cibert, J., and Mariette, H. 2009. Optical Spin Orientation of a Single Manganese Atom in a Semiconductor Quantum Dot Using Quasiresonant Photoexcitation. *Phys. Rev. lett.*, **102**, 127402.

[87] Le Gall, C., Kolodka, R. S., Cao, C. L., Boukari, H., Mariette, H., Fernández-Rossier, J., and Besombes, L. 2010. Optical initialization, readout, and dynamics of a Mn spin in a quantum dot. *Phys. Rev. B*, **81**, 245315.

[88] Le Gall, C., Brunetti, A., Boukari, H., and Besombes, L. 2011. Optical Stark effect and dressed exciton states in a Mn-Doped CdTe quantum dot. *Phys. Rev. Lett.*, **107**, 057401.

[89] Le Gall, C., Brunetti, A., Boukari, H., and Besombes, L. 2012. Electron-nuclei spin dynamics in II-VI semiconductor quantum dots. *Phys. Rev. B*, **85**, 195312.

[90] Lee, Y.R., Ramdas, A.K., and Aggarwal, R.L. 1986. Origin of the Mn^{2+} optical transition in Mn-based II-VI diluted magnetic semiconductors. *Phys. Rev. B*, **33**(10), 7383.

[91] Leger, Y., Besombes, L., Maingault, L., Ferrand, D., and Mariette, H. 2005a. Geometrical Effects on the Optical Properties of Quantum Dots Doped with a Single Magnetic Atom. *Phys. Rev. Lett.*, **95**, 047403.

[92] Leger, Y., Besombes, L., Maingault, L., Ferrand, D., and Mariette, H. 2005b. Hole spin anisotropy in single Mn-doped quantum dots. *Phys. Rev. B*, **72**, 241309.

[93] Léger, Y., Besombes, L., Maingault, L., and Mariette, H. 2007. Valence-band mixing in neutral, charged, and Mn-doped self-assembled quantum dots. *Phys. Rev. B*, **76**, 045331.

[94] Loth, S., Baumann, S., Lutz, C. P., Eigler, D. M., and Heinrich, A. J. 2012. Bistability in Atomic-Scale Antiferromagnets. *Science*, **335**, 196.

[95] Luan, L., Sievert, P.R., and Ketterson, J.B. 2006. Near field and far-field electric dipole radiation in the vicinity of a planar dielectric half space. *New Journal of Physics*, **8**, 264.

[96] Mackh, G., Ossau, W., Yakovlev, D.R., Waag, A., Landwehr, G., Hellmann, R., and Gobel, E.O. 1994. Localized exciton magnetic polarons in Cd1-xMnxTe. *Phys. Rev. B*, **49**, 10248.

[97] Maingault, L., Besombes, L., Léger, Y., Bougerol, C., and Mariette, H. 2006. Inserting one single Mn ion into a quantum dot. *Appl. Phys. Lett.*, **89**, 193109.

[98] Makhonin, M. N., Chekhovich, E. A., Senellart, P., Lemaitre, A., Skolnick, M. S., and Tartakovskii, A. I. 2010. Optically tunable nuclear magnetic resonance in a single quantum dot. *Phys. Rev. B*, **82**, 161309.

[99] Maksimov, A. A., Bacher, G., McDonald, A., Kulakovskii, V. D., Forchel, A., Becker, C. R., Landwehr, G., and Molenkamp, L. W. 2000. Magnetic polarons in a single diluted magnetic semiconductor quantum dot. *Phys. Rev. B*, **62**(12), R7767–R7770.

[100] Maletinsky, P., Lai, C.W., Badolato, A., and Imamoglu, A. 2007. Nonlinear dynamics of quantum dot nuclear spins. *Phys. Rev. B*, **75**, 035409.

[101] Maletinsky, P., Kroner, M., and Imamoglu, A. 2009. Breakdown of the nuclear-spin-temperature approach in quantum-dot demagnetization experiments. *Nature Physics*, **5**, 407.

[102] Maletinsky, P., Hong, S., Grinolds, M. S., Hausmann, B., Lukin, M. D., Walsworth, R. L., Loncar, M., and Yacoby, A. 2012. A robust scanning diamond sensor for nanoscale imaging with single nitrogen-vacancy centres. *Nature Nanotech.*, **7**, 320.

[103] Maslana, W., Kossacki, P., Bertolini, M., Boukari, H., Ferrand, D., Tatarenko, S., Cibert, J., and Gaj, J. A. 2003. p-type doping of IIVI heterostructures from surface states: Application to ferromagnetic Cd1-xMnxTe quantum wells. *Appl. Phys. Letters*, **82**, 1875.

[104] Meier, F., and Zakharchenya, B.P. (eds). 1984. *Optical Orientation.* Elsevier, Amsterdam.

[105] Merkulov, I.A., Yakovlev, D. R., Keller, A., Ossau, W., Geurts, J., Waag, A., Landwehr, G., Karczewski, G., Wojtowicz, T., and Kossut, J. 1999. Kinetic Exchange between the Conduction Band Electrons and Magnetic Ions in Quantum-Confined Structures. *Phys. Rev. Lett.*, **83**, 1431.

[106] Merkulov, I.A., Efros, Al.L., and Rosen, M. 2002. Electron spin relaxation by nuclei in semiconductor quantum dots. *Phys. Rev. B*, **65**, 205309.

[107] Merkulov, I.A., Alvarez, G., Yakovlev, D.R., and Schulthess, T.C. 2010. Long-term dynamics of the electron-nuclear spin system of a semiconductor quantum dot. *Phys. Rev. B*, **81**, 115107.

[108] Mollow, B.R. 1972. Stimulated Emission and Absorption near Resonance for Driven Systems. *Phys. Rev. A*, **5**, 2217.

[109] Monroe, C. 2002. Quantum information processing with atoms and photons. *Nature*, **416**, 238.

[110] Moskalenko, E.S., Larsson, L.A., and Holtz, P.O. 2009. Spin polarization of the neutral exciton in a single InAs quantum dot at zero magnetic field. *Phys. Rev. B*, **80**, 193413.

[111] Muller, A., Fang, W., Lawall, J., and Solomon, G.S. 2008. Emission Spectrum of a Dressed Exciton-Biexciton Complex in a Semiconductor Quantum Dot. *Phys. Rev. Lett.*, **101**, 027401.

[112] Muller, A., Fang, W., Lawall, J., and Solomon, G.S. 2009. Creating Polarization-Entangled Photon Pairs from a Semiconductor Quantum Dot Using the Optical Stark Effect. *Phys. Rev. Lett.*, **103**, 217402.

[113] Myers, R. C., Mikkelsen, M. H., Tang, J.-M., Gossard, A. C., Flatt, M. E., and Awschalom, D. D. 2008. Zero-field optical manipulation of magnetic ions in semiconductors. *Nature materials*, **7**, 203.

[114] Nannen, J., Quitsch, W., Eliasson, S., Kummel, T., and Bacher, G. 2012. High-frequency electrical charge and spin control in a single InGaAs quantum dot. *Phys. Rev. B*, **85**, 035325.

[115] Neumann, P., Beck, J., Steiner, M., Rempp, F., Fedder, H., Hemmer, P. R., Wrachtrup, J., and Jelezko, F. 2010. Single-Shot Readout of a Single Nuclear Spin. *Science*, **329**, 542.

[116] Norris, D. J., Yao, Nan, Charnock, F.T., and Kennedy, T. A. 2001. High-Quality Manganese-Doped ZnSe Nanocrystals. *Nanoletters*, **1**, 3.

[117] Oulton, R., Greilich, A., Verbin, S. Yu., Cherbunin, R.V., Auer, T., Yakovlev, D.R., Bayer, M., Merkulov, I.A., Stavarache, V., Reuter, D., and Wieck, A.D. 2007. Subsecond Spin Relaxation Times in Quantum Dots at Zero Applied Magnetic Field Due to a Strong Electron-Nuclear Interaction. *Phys. Rev. Lett.*, **98**, 107401.

[118] Paget, D., Lampel, G., Sapoval, B., and Safarov, V.I. 1977. Low field electron-nuclear spin coupling in gallium arsenide under optical pumping conditions. *Phys. Rev. B*, **15**, 5780.

[119] Patella, F., Nufris, S., Arciprete, F., M., Fanfoni, E., Placidi, Sgarlata, A., and Balzarotti, A. 2003. Tracing the two- to three-dimensional transition in the InAs/GaAs(001) heteroepitaxial growth. *Phys. Rev. B*, **67**, 205308.

[120] Patton, B., Langbein, W., Woggon, U., Maingault, L., and Mariette, H. 2006. Time- and spectrally-resolved four-wave mixing in single CdTe/ZnTe quantum dots. *Phys. Rev. B*, **73**, 235354.

[121] Petrov, M.Y., Ignatiev, I.V., Poltavtsev, S.V., Greilich, A., Bauschulte, A., Yakovlev, D.R., and Bayer, M. 2008. Effect of thermal annealing on the hyperfine interaction in InAs/GaAs quantum dots. *Phys. Rev. B*, **78**, 045315.

[122] Petrov, M.Y., Kozlov, G.G., Ignatiev, I.V., Cherbunin, R.V., Yakovlev, D.R., and Bayer, M. 2009. Coupled electron-nuclear spin dynamics in quantum dots: A graded box model approach. *Phys. Rev. B*, **80**, 125318.

[123] Press, D., Ladd, T.D., Zhang, B., and Yamamoto, Y. 2008. Complete quantum control of a single quantum dot spin using ultrafast optical pulses. *Nature*, **456**, 218.

[124] Qazzaz, M., Yang, G., Xin, S.H., Montes, L., Luo, H., and Furdyna, J.K. 1995. Electron paramagnetic resonance of Mn2+ in strained layer semiconductor superlattices. *Solid State Communications*, **96**, 405.

[125] Qu, F., and Hawrylak, P. 2005. Magnetic Exchange Interactions in Quantum Dots Containing Electrons and Magnetic Ions. *Phys. Rev. Lett.*, **95**, 217206.

[126] Qu, F., and Hawrylak, P. 2006. Theory of Electron Mediated Mn-Mn Interactions in Quantum Dots. *Phys. Rev. Lett.*, **96**, 157201.

[127] Reiter, D. E., Kuhn, T., and Axt, V. M. 2009. All-Optical Spin Manipulation of a Single Manganese Atom in a Quantum Dot. *Phys. Rev. Lett.*, **102**, 177403.

[128] Robledo, L., Childress, L., Bernien, H., Hensen, B., Alkemade, P.F.A, and Hanson, R. 2011. High-fidelity projective read-out of a solid-state spin quantum register. *Nature*, **477**, 574.

[129] Scalbert, D., Cernogora, J., and la Guillaume, C. Benoit . 1988. Spin-lattice relaxation in paramegnetic CdMnTe. *Solid State Commun.*, **66**, 571.

[130] Seufert, J., Bacher, G., Scheibner, M., Forchel, A., Lee, S., Dobrowolska, M., and Furdyna, J. K. 2001. Dynamical Spin Response in Semimagnetic Quantum Dots. *Phys. Rev. Lett.*, **88**(2), 027402.

[131] Shabaev, A., Stinaff, E. A., Bracker, A. S., Gammon, D., Efros, A. L., Korenev, V. L., and Merkulov, I. 2009. Optical pumping and negative luminescence polarization in charged GaAs quantum dots. *Phys. Rev. B*, **79**, 035322.

[132] Smith, J.M., Dalgarno, P. A., Warburton, R.J., Govorov, A.O., Karrai, K., Gerardot, B. D., and Petroff, P. M. 2005. Voltage Control of the Spin Dynamics of an Exciton in a Semiconductor Quantum Dot. *Phys. Rev. Lett.*, **94**, 197402.

[133] Stuhler, J., Schaack, G., Dahl, M., Waag, A., Landwehr, G., Kavokin, K. V., and Merkulov, I. A. 1995. Multiple Mn2+-Spin-Flip Raman Scattering at High Fields via Magnetic Polaron States in Semimagnetic Quantum Wells. *Phys. Rev. Lett.*, **74**, 2567.

[134] Syperek, M., Yakovlev, D. R., Yugova, I. A., Misiewicz, J., Sedova, I. V., Sorokin, S. V., Toropov, A. A., Ivanov, S. V., and Bayer, M. 2011. Long-lived electron spin coherence in CdSe/Zn(S,Se) self-assembled quantum dots. *Phys. Rev. B*, **84**, 085304.

[135] Tanaka, T., Singh, J., Arakawa, Y., and Bhattacharya, P. 1993. Near band edge polarization dependence as a probe of structural symmetry in GaAs/AlGaAs quantum dot structures. *Appl. Phys. Lett.*, **62**, 756.

[136] Tartakovskii, A.I., Wright, T., Russell, A., Falko, V. I., Vankov, A. B., Skiba-Szymanska, J., Drouzas, I., Kolodka, R. S., Skolnick, M. S., Fry, P. W., Tahraoui, A., Liu, H.-Y., and Hopkinson, M. 2007. Nuclear Spin Switch in Semiconductor Quantum Dots. *Phys. Rev. Lett.*, **98**, 026806.

[137] Testelin, C., Eble, B., Bernardot, F., Karczewski, G., and Chamarro, M. 2008. Signature of the Overhauser field on the coherent spin dynamics of donor-bound electrons in a single CdTe quantum well. *Phys. Rev. B*, **77**, 235306.

[138] Testelin, C., Bernardot, F., Eble, B., and Chamarro, M. 2009. Hole˘spin dephasing time associated with hyperfine interaction in quantum dots. *Phys. Rev. B*, **79**, 195440.

[139] Thon, S. M., Rakher, M. T., Kim, H., Gudat, J., Irvine, W.T.M., Petroff, P.M., and Bouwmeester, D. 2009. Strong coupling through optical positioning of a quantum dot in a photonic crystal cavity. *Applied Physics Letters*, **94**, 111115.

[140] Tinjod, F., Gilles, B., Moehl, S., Kheng, K., and Mariette, H. 2003. IIVI quantum dot formation induced by surface energy change of a strained layer. *Appl. Phys. Lett.*, **82**, 4340.

[141] Tonin, C., Hostein, R., Voliotis, V., Grousson, R., Lemaitre, A., and Martinez, A. 2012. Polarization properties of excitonic qubits in single self-assembled quantum dots. *Phys. Rev. B*, **85**, 155303.

[142] Trojnar, A. H., Korkusiński, M., Kadantsev, E. S., Hawrylak, P., Goryca, M., Kazimierczuk, T., Kossacki, P., Wojnar, P., and Potemski, M. 2011. Quantum Interference in Exciton-Mn Spin Interactions in a CdTe Semiconductor Quantum Dot. *Phys. Rev. Lett.*, **107**, 207403.

[143] Twardowski, A., Swiderski, P., von Ortenberg, M., and Pauthenet, R. 1984. title. *Solid State Communications*, **50**, 509.

[144] Tyazhlov, M.G., Filin, A.I., Larionov, A.V., Kulakovskii, V.D., Yakovlev, D.R., Waag, A., and Landwehr, G. 1997. Spin relaxation of Mn ions in CdMnTe/CdMgTe quantum wells under picosecond optical pumping. *JETP*, **85**, 784.

[145] Van Exter, M.P., Gudat, J., Nienhuis, G., and Bouwmeester, D. 2009. Spin quantum jumps in a singly charged quantum dot. *Phys. Rev. A*, **80**, 023812.

[146] Vasanelli, A., Ferreira, R., and Bastard, G. 2002. Continuous Absorption Background and Decoherence in Quantum Dots. *Phys. Rev. Lett.*, **89**, 216804.

[147] Ware, M. E., Stinaff, E. A., Gammon, D., Doty, M. F., Bracker, A. S., Gershoni, D., Korenev, V. L., Badescu, S. C., Lyanda-Geller, Y., and Reinecke, T. L. 2005. Polarized Fine Structure in the Photoluminescence Excitation Spectrum of a Negatively Charged Quantum Dot. *Phys. Rev. Lett.*, **95**, 177403.

[148] Wojnar, P., Bougerol, C., Bellet-Amalric, E., Besombes, L., Mariette, H., and Boukari, H. 2011. Towards vertical coupling of CdTe/ZnTe quantum dots formed by a high temperature tellurium induced process. *J. Crystal Growth*, **335**, 28.

[149] Wrigge, G., Gerhardt, I., Hwang, J., Zumofen, G., and Sandoghdar, V. 2008. Efficient coupling of photons to a single molecule and the observation of its resonance fluorescence. *Nature Physics*, **4**, 60.

[150] Xu, X., Sun, B., Berman, P.R., Steel, D.G., Bracker, A.S., Gammon, D., and Sham, L.J. 2007. Coherent Optical Spectroscopy of a Strongly Driven Quantum Dot. *Science*, **317**, 929.

[151] Xu, X., Sun, Bo, Kim, E. D., Smirl, K., Berman, P.R., Steel, D.G., Bracker, A.S., Gammon, D., and Sham, L.J. 2008. Single Charged Quantum Dot in a Strong Optical Field: Absorption, Gain, and the ac-Stark Effect. *Phys. Rev. Lett.*, **101**, 227401.

[152] Yakovlev, D. R., Kavokin, K. V., Merkulov, I. A., Mackh, G., Ossau, W., Hellmann, R., Göbel, E. O., Waag, A., and Landwehr, G. 1997. Picosecond dynamics of magnetic polarons governed by energy transfer to the Zeeman reservoir. *Phys. Rev. B*, **56**(15), 9782–9788.

[153] Yu, Peter, and Cardona, Manuel. 1996. *Fundammentals of Semiconductors*. Springer.

[154] Zare, R.N. (ed). 1988. *Angular momentum*. Wiley.